

Measurement of $D\bar{D}$ Decays from the $\psi(3770)$ Resonance

A DISSERTATION
SUBMITTED TO THE FACULTY OF THE GRADUATE SCHOOL
OF THE UNIVERSITY OF MINNESOTA
BY

Andy Jarod Julin

IN PARTIAL FULFILLMENT OF THE REQUIREMENTS
FOR THE DEGREE OF
DOCTOR OF PHILOSOPHY

Prof. Ron Poling

May, 2017

© Andy Jarod Julin 2017



The text of this work is licensed under a Creative Commons
Attribution-ShareAlike 4.0 International license.

Acknowledgements

This is where the Acknowledgements go!

Dedication

This is where the Dedications go!

Abstract

We measure the production cross section of $e^+e^- \rightarrow \psi(3770) \rightarrow D\bar{D}$ near the peak of the $\psi(3770)$ resonance. The $(69.80 \pm 0.03)\text{ pb}^{-1}$ of e^+e^- annihilation data used were collected in 2010 over a center-of-mass energy range of 3.735 GeV to 3.870 GeV. From previously observed $e^+e^- \rightarrow D\bar{D}$ cross section measurements, this shape cannot be explained by a single Breit-Wigner. Instead, in this analysis we fitted the cross section by including interference effects from non-resonant $D\bar{D}$ production, and measured the mass and width of the $\psi(3770)$ more precisely than previous results.

Contents

Acknowledgements	i
Dedication	ii
Abstract	iii
List of Tables	viii
List of Figures	xii
1 Introduction	1
1.1 Procedure	3
2 Theoretical Background	5
2.1 Standard Model	5
2.1.1 Electromagnetic Force	5
2.1.2 Weak Force	6
2.1.3 Strong Force	7
2.1.4 Elementary Particles	8
2.2 Charmonium	11
3 Detector and Related Systems	14
3.1 BEPCII Accelerator	15
3.2 BESIII Detector	16
3.2.1 Multi-Layer Drift Chamber	17
3.2.2 Time-of-Flight System	19

3.2.3	Electromagnetic Calorimeter	20
3.2.4	Muon Identifier	22
3.3	Triggering Systems	22
4	Analysis Software	25
4.1	BESIII Offline Software System	25
4.1.1	Framework	25
4.1.2	Simulation	26
4.1.3	Reconstruction	27
4.1.4	Calibration	28
4.2	Detector Simulation	28
4.2.1	Multi-Layer Drift Chamber	28
4.2.2	Time-of-Flight System	29
4.2.3	Electromagnetic Calorimeter	30
4.2.4	Muon Identifier	30
4.3	<i>D</i> -Tagging	31
4.3.1	Selection Cuts	32
4.3.2	Reconstruction	34
5	Measurement of $\sigma(\psi(3770) \rightarrow D\bar{D})$ near $\psi(3770)$	36
5.1	Derivation of $\sigma(\psi(3770) \rightarrow D\bar{D})$	36
5.2	Form Factors	39
5.3	Data and Monte Carlo Samples	40
5.3.1	Data Samples	40
5.3.2	Center-of-Mass Energy Measurement	41
5.3.3	Luminosity Measurement	44
5.3.4	Monte Carlo Generation	46
5.4	Signal Determination	47
5.5	Efficiency Correction	48
5.5.1	CP Violation Correction	54
5.6	Fitting Procedure	55
5.6.1	Coulomb Correction	59
5.7	Systematic Uncertainties	61

5.7.1	$\psi(3770)$ Parameter Systematic Uncertainties	61
5.7.2	Cross Section Systematic Uncertainties	67
5.8	Results	69
6	Measurement of Hadronic Production and $\Gamma(\psi(3770) \rightarrow \text{non-}D\bar{D})$	71
6.1	Data and Monte Carlo Samples	72
6.1.1	Data Samples	72
6.1.2	Center-of-Mass Energy Measurement	72
6.2	Event Selection	73
6.3	Hadron Counting	75
6.4	Background Subtraction	76
6.5	Efficiency Extrapolation	78
6.6	Procedure for $\psi(3770)$ Data	86
6.6.1	$D\bar{D}$ Subtraction	87
6.6.2	Reconstruction Efficiencies	90
6.6.3	Signal Amounts	91
6.6.4	Non- $D\bar{D}$ Branching Fraction Exploration (Breit-Wigner)	92
6.7	$\psi(2S)$ Background Investigation	93
6.7.1	Non- $D\bar{D}$ Branching Fraction Exploration ($\psi(2S)$ from Data)	94
6.7.2	Non- $D\bar{D}$ Branching Fraction Exploration ($\psi(2S)$ Excluded)	98
6.8	Procedure for Scan Data	102
7	Conclusion	107
References		109
Appendix A.	Glossary and Acronyms	113
A.1	Glossary	113
A.2	Acronyms / Initialisms	113
Appendix B.	D^0 Signal Fits	115
Appendix C.	D^+ Signal Fits	127
Appendix D.	Scan Data Hadronic Counting Fits	138

Appendix E. Scan Data Reconstruction Efficiency	150
Appendix F. Scan Data Signal Counts	159

List of Tables

1.1	Previous experimental results for the mass of the $\psi(3770)$	2
4.1	The reconstructed D -tag modes used in this analysis.	32
4.2	The required cuts to identify charged tracks as π^\pm or K^\pm	33
4.3	The required cuts to identify neutral showers as a γ	33
4.4	The required cuts to reconstruct $\gamma\gamma$ pairs as a π^0	33
4.5	The required cuts to reconstruct $\pi^+\pi^-$ pairs as a K_S^0	34
4.6	Cuts to suppress cosmic ray and lepton backgrounds in $D^0 \rightarrow K^-\pi^+$. .	34
5.1	Selection cuts on muon tracks used to determine the center-of-mass energy.	41
5.2	Selection cuts on electron tracks used to determine the luminosity.	44
5.3	Measured integrated luminosities for each energy bin.	45
5.4	Number of events contained in each generated sample.	46
5.5	Mode-by-mode reconstruction efficiencies for D^0 and D^+	49
5.6	Numbers of proper and generated particles for D^0	50
5.7	Numbers of proper and generated particles for D^+ (part 1).	51
5.8	Numbers of proper and generated particles for D^+ (part 2).	52
5.9	The overall reconstruction efficiency of D^0 and D^+ for each energy bin.	53
5.10	The quantum correlated factors for the D^0 modes.	54
5.11	The measured $D\bar{D}$ cross sections at each E_{cm} point.	56
5.12	Single-tag fitting differences by mode.	62
5.13	Comparison of input and output fit parameters.	63
5.14	Comparison of output fit parameters between ISR generators.	64
5.15	Systematic uncertainties relative to the measured parameters of the $\psi(3770)$.	66
5.16	Parameter differences based on the choice of form factor.	66
5.17	Systematics shifts affecting the cross section measurements.	67

5.18	Measurements of the D^0 and D^+ cross sections.	68
5.19	Final results for the $\psi(3770)$ parameters.	69
5.20	Fit results compared to the KEDR results and the PDG.	69
5.21	Comparison of cross section calculations at $E_{\text{cm}} = 3.7732 \text{ GeV}$	70
6.1	Data samples used for the inclusive measurement.	73
6.2	Selection cuts on charged tracks used to count hadronic events.	73
6.3	Selection cuts on neutral tracks used to count hadronic events.	74
6.4	Selection cuts to remove Bhabha and two-photon backgrounds.	74
6.5	Standard selection cuts (SHAD) for counting hadronic events.	74
6.6	Loose selection cuts (LHAD) for counting hadronic events.	75
6.7	Tight selection cuts (THAD) for counting hadronic events.	75
6.8	Reconstruction of background samples for the old continuum data.	77
6.9	Hadronic events selected in the old continuum data.	77
6.10	Reconstruction of background samples for the new continuum data.	80
6.11	Hadronic events selected in the new continuum data.	81
6.12	Selection methods for the $D\bar{D}$ efficiency correction.	87
6.13	Efficiency corrections for the $\psi(3770)$ samples.	87
6.14	Reconstruction of background samples for the $\psi(3770)$ data.	90
6.15	Hadronic events selected in the $\psi(3770)$ data.	91
6.16	Cross sections for $\psi(3770) \rightarrow \text{non-}D\bar{D}$ found using the $\psi(3770)$ data.	92
6.17	Branching fractions for $\psi(3770) \rightarrow \text{non-}D\bar{D}$ found using the $\psi(3770)$ data.	92
6.18	Cross sections of $\psi(2S)$ calculated using two different methods.	93
6.19	Cross sections for $\psi(3770) \rightarrow \text{non-}D\bar{D}$ found using the $\psi(3770)$ data.	94
6.20	Branching fractions for $\psi(3770) \rightarrow \text{non-}D\bar{D}$ found using the $\psi(3770)$ data.	94
6.21	Cross sections for $\psi(3770) \rightarrow \text{non-}D\bar{D}$ found using the $\psi(3770)$ data.	98
6.22	Branching fractions for $\psi(3770) \rightarrow \text{non-}D\bar{D}$ found using the $\psi(3770)$ data.	98
6.23	Energy values and background cross sections for the scan data.	103
A.1	Acronyms and Initialisms	113
E.1	Reconstruction of background samples for the 3734 (Scan) data.	150
E.2	Reconstruction of background samples for the 3736 (Scan) data.	150
E.3	Reconstruction of background samples for the 3744 (Scan) data.	151
E.4	Reconstruction of background samples for the 3748 (Scan) data.	151

E.5	Reconstruction of background samples for the 3750 (Scan) data.	151
E.6	Reconstruction of background samples for the 3751 (Scan) data.	151
E.7	Reconstruction of background samples for the 3753 (Scan) data.	152
E.8	Reconstruction of background samples for the 3755 (Scan) data.	152
E.9	Reconstruction of background samples for the 3756 (Scan) data.	152
E.10	Reconstruction of background samples for the 3759 (Scan) data.	152
E.11	Reconstruction of background samples for the 3762 (Scan) data.	153
E.12	Reconstruction of background samples for the 3765 (Scan) data.	153
E.13	Reconstruction of background samples for the 3767 (Scan) data.	153
E.14	Reconstruction of background samples for the 3771 (Scan) data.	153
E.15	Reconstruction of background samples for the 3774 (Scan) data.	154
E.16	Reconstruction of background samples for the 3777 (Scan) data.	154
E.17	Reconstruction of background samples for the 3780 (Scan) data.	154
E.18	Reconstruction of background samples for the 3782 (Scan) data.	154
E.19	Reconstruction of background samples for the 3786 (Scan) data.	155
E.20	Reconstruction of background samples for the 3789 (Scan) data.	155
E.21	Reconstruction of background samples for the 3792 (Scan) data.	155
E.22	Reconstruction of background samples for the 3797 (Scan) data.	155
E.23	Reconstruction of background samples for the 3800 (Scan) data.	156
E.24	Reconstruction of background samples for the 3802 (Scan) data.	156
E.25	Reconstruction of background samples for the 3807 (Scan) data.	156
E.26	Reconstruction of background samples for the 3809 (Scan) data.	156
E.27	Reconstruction of background samples for the 3813 (Scan) data.	157
E.28	Reconstruction of background samples for the 3815 (Scan) data.	157
E.29	Reconstruction of background samples for the 3822 (Scan) data.	157
E.30	Reconstruction of background samples for the 3832 (Scan) data.	157
E.31	Reconstruction of background samples for the 3839 (Scan) data.	158
E.32	Reconstruction of background samples for the 3849 (Scan) data.	158
E.33	Reconstruction of background samples for the 3855 (Scan) data.	158
E.34	Reconstruction of background samples for the 3863 (Scan) data.	158
F.1	Hadronic events selected in the 3734 (Scan) data.	159
F.2	Hadronic events selected in the 3736 (Scan) data.	159

F.3	Hadronic events selected in the 3744 (Scan) data.	160
F.4	Hadronic events selected in the 3748 (Scan) data.	160
F.5	Hadronic events selected in the 3750 (Scan) data.	160
F.6	Hadronic events selected in the 3751 (Scan) data.	161
F.7	Hadronic events selected in the 3753 (Scan) data.	161
F.8	Hadronic events selected in the 3755 (Scan) data.	161
F.9	Hadronic events selected in the 3756 (Scan) data.	162
F.10	Hadronic events selected in the 3759 (Scan) data.	162
F.11	Hadronic events selected in the 3762 (Scan) data.	162
F.12	Hadronic events selected in the 3765 (Scan) data.	163
F.13	Hadronic events selected in the 3767 (Scan) data.	163
F.14	Hadronic events selected in the 3771 (Scan) data.	163
F.15	Hadronic events selected in the 3774 (Scan) data.	164
F.16	Hadronic events selected in the 3777 (Scan) data.	164
F.17	Hadronic events selected in the 3780 (Scan) data.	164
F.18	Hadronic events selected in the 3782 (Scan) data.	165
F.19	Hadronic events selected in the 3786 (Scan) data.	165
F.20	Hadronic events selected in the 3789 (Scan) data.	165
F.21	Hadronic events selected in the 3792 (Scan) data.	166
F.22	Hadronic events selected in the 3797 (Scan) data.	166
F.23	Hadronic events selected in the 3800 (Scan) data.	166
F.24	Hadronic events selected in the 3802 (Scan) data.	167
F.25	Hadronic events selected in the 3807 (Scan) data.	167
F.26	Hadronic events selected in the 3809 (Scan) data.	167
F.27	Hadronic events selected in the 3813 (Scan) data.	168
F.28	Hadronic events selected in the 3815 (Scan) data.	168
F.29	Hadronic events selected in the 3822 (Scan) data.	168
F.30	Hadronic events selected in the 3832 (Scan) data.	169
F.31	Hadronic events selected in the 3839 (Scan) data.	169
F.32	Hadronic events selected in the 3849 (Scan) data.	169
F.33	Hadronic events selected in the 3855 (Scan) data.	170
F.34	Hadronic events selected in the 3863 (Scan) data.	170

List of Figures

1.1	Measurements of $R = \sigma(e^+e^- \rightarrow (\text{hadrons}))/\sigma(e^+e^- \rightarrow \mu^+\mu^-)$	1
1.2	Measured and predicted charmonium resonances.	2
2.1	The standard model of particle physics.	8
2.2	The Cabibbo-Kobayashi-Maskawa (CKM) Matrix.	9
2.3	The standard form of the Cabibbo-Kobayashi-Maskawa (CKM) Matrix.	10
2.4	An example Feynman diagram for the decay of $\psi(3686)$	12
2.5	An example Feynman diagram for the decay of $\psi(3770)$	13
3.1	A schematic of the BESIII detector.	16
3.2	MDC energy deposition for various particles as a function of momenta. .	19
3.3	ToF measurements for various particles as a function of momenta. . .	20
3.4	EMC energy deposition for various particles as a function of momentum. .	21
3.5	Triggering systems for event filtering at BESIII.	24
5.1	A comparison of online center-of-mass energies and measured $\mu^+\mu^-$ events. .	42
5.2	The values measured for on-peak data center-of-mass energies.	43
5.3	Projections of the 2D (ΔE vs. m_{BC}) signal fit.	47
5.4	Mode-by-mode efficiencies for D^0 and D^+ determined with signal MC. .	49
5.5	The measured $e^+e^- \rightarrow D\bar{D}$ cross sections.	55
5.6	The fit results for the Exponential Model form factor.	57
5.7	The fit results for the Vector Dominance Model form factor.	58
5.8	The Vector Dominance Model fit results with Coulomb interactions. .	59
5.9	The ratio of measured D^+ to D^0 cross sections.	60
5.10	The $K\pi$ vs. $\pi\pi$ invariant masses for the mode $D^+ \rightarrow K^-\pi^+\pi^+$	65
6.1	Fits to determine the number of hadrons in the 3650 (Old) data sample. .	76
6.2	Fits to determine the number of hadrons in the 3500 (New) data sample. .	78

6.3	Fits to determine the number of hadrons in the 3542 (New)) data sample.	78
6.4	Fits to determine the number of hadrons in the 3600 (New) data sample.	79
6.5	Fits to determine the number of hadrons in the 3650 (New) data sample.	79
6.6	Fits to determine the number of hadrons in the 3671 (New) data sample.	79
6.7	The continuum extrapolation for SHAD events.	83
6.8	The continuum extrapolation for LHAD events.	84
6.9	The continuum extrapolation for THAD events.	85
6.10	Fits to determine the number of hadrons in the $\psi(3770)$ (R1) data sample.	86
6.11	Fits to determine the number of hadrons in the $\psi(3770)$ (R2) data sample.	86
6.12	The other-side D^0 tracks and corresponding $D^0\overline{D}^0$ multiplicities for R1.	88
6.13	The other-side D^+ tracks and corresponding D^+D^- multiplicities for R1.	88
6.14	The other-side D^0 tracks and corresponding $D^0\overline{D}^0$ multiplicities for R2.	89
6.15	The other-side D^+ tracks and corresponding D^+D^- multiplicities for R2.	89
6.16	The continuum extrapolation for SHAD events using $\psi(2S)$ data.	95
6.17	The continuum extrapolation for LHAD events using $\psi(2S)$ data.	96
6.18	The continuum extrapolation for THAD events using $\psi(2S)$ data.	97
6.19	The continuum extrapolation for SHAD events without $\psi(2S)$ events.	99
6.20	The continuum extrapolation for LHAD events without $\psi(2S)$ events.	100
6.21	The continuum extrapolation for THAD events without $\psi(2S)$ events.	101
6.22	The inclusive cross sections measured for the scan data region.	104
6.23	The non- $D\overline{D}$ cross sections measured for the scan data region.	105
6.24	The non- $D\overline{D}$ branching fractions measured for the scan data region.	106
B.1	Projections of the 2D signal fit (ΔE vs. m_{BC}) for D^0 in Bin 0.	115
B.2	Projections of the 2D signal fit (ΔE vs. m_{BC}) for D^0 in Bin 1.	115
B.3	Projections of the 2D signal fit (ΔE vs. m_{BC}) for D^0 in Bin 2.	116
B.4	Projections of the 2D signal fit (ΔE vs. m_{BC}) for D^0 in Bin 3.	116
B.5	Projections of the 2D signal fit (ΔE vs. m_{BC}) for D^0 in Bin 4.	116
B.6	Projections of the 2D signal fit (ΔE vs. m_{BC}) for D^0 in Bin 5.	117
B.7	Projections of the 2D signal fit (ΔE vs. m_{BC}) for D^0 in Bin 6.	117
B.8	Projections of the 2D signal fit (ΔE vs. m_{BC}) for D^0 in Bin 7.	117
B.9	Projections of the 2D signal fit (ΔE vs. m_{BC}) for D^0 in Bin 8.	118
B.10	Projections of the 2D signal fit (ΔE vs. m_{BC}) for D^0 in Bin 9.	118

B.11	Projections of the 2D signal fit (ΔE vs. m_{BC}) for D^0 in Bin 10	118
B.12	Projections of the 2D signal fit (ΔE vs. m_{BC}) for D^0 in Bin 11	119
B.13	Projections of the 2D signal fit (ΔE vs. m_{BC}) for D^0 in Bin 12	119
B.14	Projections of the 2D signal fit (ΔE vs. m_{BC}) for D^0 in Bin 13	119
B.15	Projections of the 2D signal fit (ΔE vs. m_{BC}) for D^0 in Bin 14	120
B.16	Projections of the 2D signal fit (ΔE vs. m_{BC}) for D^0 in Bin 15	120
B.17	Projections of the 2D signal fit (ΔE vs. m_{BC}) for D^0 in Bin 16	120
B.18	Projections of the 2D signal fit (ΔE vs. m_{BC}) for D^0 in Bin 17	121
B.19	Projections of the 2D signal fit (ΔE vs. m_{BC}) for D^0 in Bin 18	121
B.20	Projections of the 2D signal fit (ΔE vs. m_{BC}) for D^0 in Bin 19	121
B.21	Projections of the 2D signal fit (ΔE vs. m_{BC}) for D^0 in Bin 20	122
B.22	Projections of the 2D signal fit (ΔE vs. m_{BC}) for D^0 in Bin 21	122
B.23	Projections of the 2D signal fit (ΔE vs. m_{BC}) for D^0 in Bin 22	122
B.24	Projections of the 2D signal fit (ΔE vs. m_{BC}) for D^0 in Bin 23	123
B.25	Projections of the 2D signal fit (ΔE vs. m_{BC}) for D^0 in Bin 24	123
B.26	Projections of the 2D signal fit (ΔE vs. m_{BC}) for D^0 in Bin 25	123
B.27	Projections of the 2D signal fit (ΔE vs. m_{BC}) for D^0 in Bin 26	124
B.28	Projections of the 2D signal fit (ΔE vs. m_{BC}) for D^0 in Bin 27	124
B.29	Projections of the 2D signal fit (ΔE vs. m_{BC}) for D^0 in Bin 28	124
B.30	Projections of the 2D signal fit (ΔE vs. m_{BC}) for D^0 in Bin 29	125
B.31	Projections of the 2D signal fit (ΔE vs. m_{BC}) for D^0 in Bin 30	125
B.32	Projections of the 2D signal fit (ΔE vs. m_{BC}) for D^0 in Bin 31	125
B.33	Projections of the 2D signal fit (ΔE vs. m_{BC}) for D^0 in Bin 32	126
B.34	Projections of the 2D signal fit (ΔE vs. m_{BC}) for D^0 in Bin 33	126
C.1	Projections of the 2D signal fit (ΔE vs. m_{BC}) for D^+ in Bin 2	127
C.2	Projections of the 2D signal fit (ΔE vs. m_{BC}) for D^+ in Bin 3	127
C.3	Projections of the 2D signal fit (ΔE vs. m_{BC}) for D^+ in Bin 4	128
C.4	Projections of the 2D signal fit (ΔE vs. m_{BC}) for D^+ in Bin 5	128
C.5	Projections of the 2D signal fit (ΔE vs. m_{BC}) for D^+ in Bin 6	128
C.6	Projections of the 2D signal fit (ΔE vs. m_{BC}) for D^+ in Bin 7	129
C.7	Projections of the 2D signal fit (ΔE vs. m_{BC}) for D^+ in Bin 8	129
C.8	Projections of the 2D signal fit (ΔE vs. m_{BC}) for D^+ in Bin 9	129

C.9	Projections of the 2D signal fit (ΔE vs. m_{BC}) for D^+ in Bin 10.	130
C.10	Projections of the 2D signal fit (ΔE vs. m_{BC}) for D^+ in Bin 11.	130
C.11	Projections of the 2D signal fit (ΔE vs. m_{BC}) for D^+ in Bin 12.	130
C.12	Projections of the 2D signal fit (ΔE vs. m_{BC}) for D^+ in Bin 13.	131
C.13	Projections of the 2D signal fit (ΔE vs. m_{BC}) for D^+ in Bin 14.	131
C.14	Projections of the 2D signal fit (ΔE vs. m_{BC}) for D^+ in Bin 15.	131
C.15	Projections of the 2D signal fit (ΔE vs. m_{BC}) for D^+ in Bin 16.	132
C.16	Projections of the 2D signal fit (ΔE vs. m_{BC}) for D^+ in Bin 17.	132
C.17	Projections of the 2D signal fit (ΔE vs. m_{BC}) for D^+ in Bin 18.	132
C.18	Projections of the 2D signal fit (ΔE vs. m_{BC}) for D^+ in Bin 19.	133
C.19	Projections of the 2D signal fit (ΔE vs. m_{BC}) for D^+ in Bin 20.	133
C.20	Projections of the 2D signal fit (ΔE vs. m_{BC}) for D^+ in Bin 21.	133
C.21	Projections of the 2D signal fit (ΔE vs. m_{BC}) for D^+ in Bin 22.	134
C.22	Projections of the 2D signal fit (ΔE vs. m_{BC}) for D^+ in Bin 23.	134
C.23	Projections of the 2D signal fit (ΔE vs. m_{BC}) for D^+ in Bin 24.	134
C.24	Projections of the 2D signal fit (ΔE vs. m_{BC}) for D^+ in Bin 25.	135
C.25	Projections of the 2D signal fit (ΔE vs. m_{BC}) for D^+ in Bin 26.	135
C.26	Projections of the 2D signal fit (ΔE vs. m_{BC}) for D^+ in Bin 27.	135
C.27	Projections of the 2D signal fit (ΔE vs. m_{BC}) for D^+ in Bin 28.	136
C.28	Projections of the 2D signal fit (ΔE vs. m_{BC}) for D^+ in Bin 29.	136
C.29	Projections of the 2D signal fit (ΔE vs. m_{BC}) for D^+ in Bin 30.	136
C.30	Projections of the 2D signal fit (ΔE vs. m_{BC}) for D^+ in Bin 31.	137
C.31	Projections of the 2D signal fit (ΔE vs. m_{BC}) for D^+ in Bin 32.	137
C.32	Projections of the 2D signal fit (ΔE vs. m_{BC}) for D^+ in Bin 33.	137
D.1	Fits to determine the number of hadrons in the 3734 (Scan) data sample.	138
D.2	Fits to determine the number of hadrons in the 3736 (Scan) data sample.	139
D.3	Fits to determine the number of hadrons in the 3744 (Scan) data sample.	139
D.4	Fits to determine the number of hadrons in the 3748 (Scan) data sample.	139
D.5	Fits to determine the number of hadrons in the 3750 (Scan) data sample.	140
D.6	Fits to determine the number of hadrons in the 3751 (Scan) data sample.	140
D.7	Fits to determine the number of hadrons in the 3753 (Scan) data sample.	140
D.8	Fits to determine the number of hadrons in the 3755 (Scan) data sample.	141

D.9	Fits to determine the number of hadrons in the 3756 (Scan) data sample.	141
D.10	Fits to determine the number of hadrons in the 3759 (Scan) data sample.	141
D.11	Fits to determine the number of hadrons in the 3762 (Scan) data sample.	142
D.12	Fits to determine the number of hadrons in the 3765 (Scan) data sample.	142
D.13	Fits to determine the number of hadrons in the 3767 (Scan) data sample.	142
D.14	Fits to determine the number of hadrons in the 3771 (Scan) data sample.	143
D.15	Fits to determine the number of hadrons in the 3774 (Scan) data sample.	143
D.16	Fits to determine the number of hadrons in the 3777 (Scan) data sample.	143
D.17	Fits to determine the number of hadrons in the 3780 (Scan) data sample.	144
D.18	Fits to determine the number of hadrons in the 3782 (Scan) data sample.	144
D.19	Fits to determine the number of hadrons in the 3786 (Scan) data sample.	144
D.20	Fits to determine the number of hadrons in the 3789 (Scan) data sample.	145
D.21	Fits to determine the number of hadrons in the 3792 (Scan) data sample.	145
D.22	Fits to determine the number of hadrons in the 3797 (Scan) data sample.	145
D.23	Fits to determine the number of hadrons in the 3800 (Scan) data sample.	146
D.24	Fits to determine the number of hadrons in the 3802 (Scan) data sample.	146
D.25	Fits to determine the number of hadrons in the 3807 (Scan) data sample.	146
D.26	Fits to determine the number of hadrons in the 3809 (Scan) data sample.	147
D.27	Fits to determine the number of hadrons in the 3813 (Scan) data sample.	147
D.28	Fits to determine the number of hadrons in the 3815 (Scan) data sample.	147
D.29	Fits to determine the number of hadrons in the 3822 (Scan) data sample.	148
D.30	Fits to determine the number of hadrons in the 3832 (Scan) data sample.	148
D.31	Fits to determine the number of hadrons in the 3839 (Scan) data sample.	148
D.32	Fits to determine the number of hadrons in the 3849 (Scan) data sample.	149
D.33	Fits to determine the number of hadrons in the 3855 (Scan) data sample.	149
D.34	Fits to determine the number of hadrons in the 3863 (Scan) data sample.	149

Chapter 1

Introduction

Since the discovery of the J/ψ resonance in 1974, the charm energy range (3.0 GeV to 4.5 GeV) has been investigated by many experiments in particle physics. This has led to the further discovery of many more resonances, as shown in Figure 1.1.

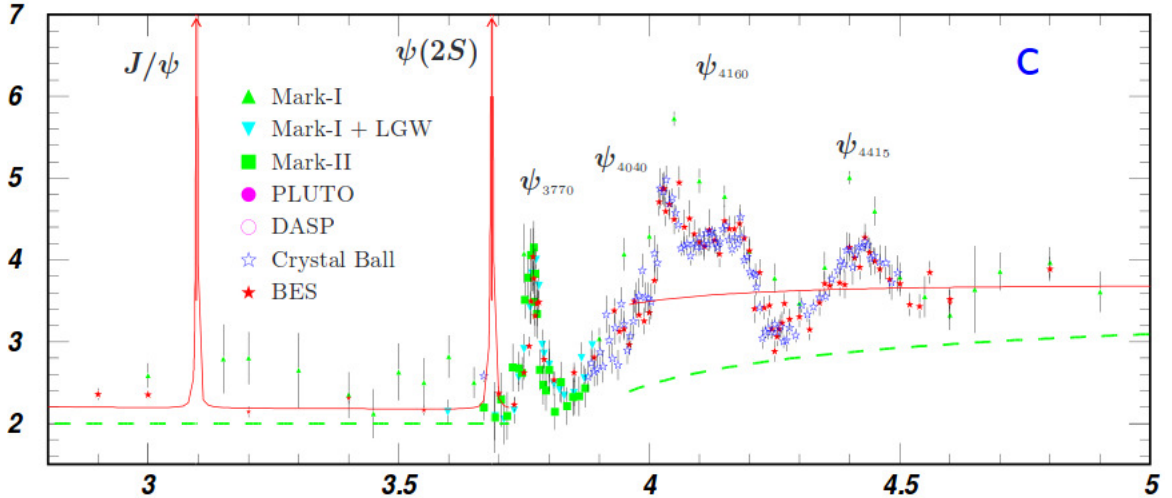


Figure 1.1: Measurements of $R = \sigma(e^+e^- \rightarrow (\text{hadrons})) / \sigma(e^+e^- \rightarrow \mu^+\mu^-)$.

Many of the lower mass resonances are predictable within the context of the quark model. However, there are a number of states which have been predicted, but not yet discovered. There are also states which were discovered experimentally without any corresponding predictions. A variety of these particles are shown in Figure 1.2.

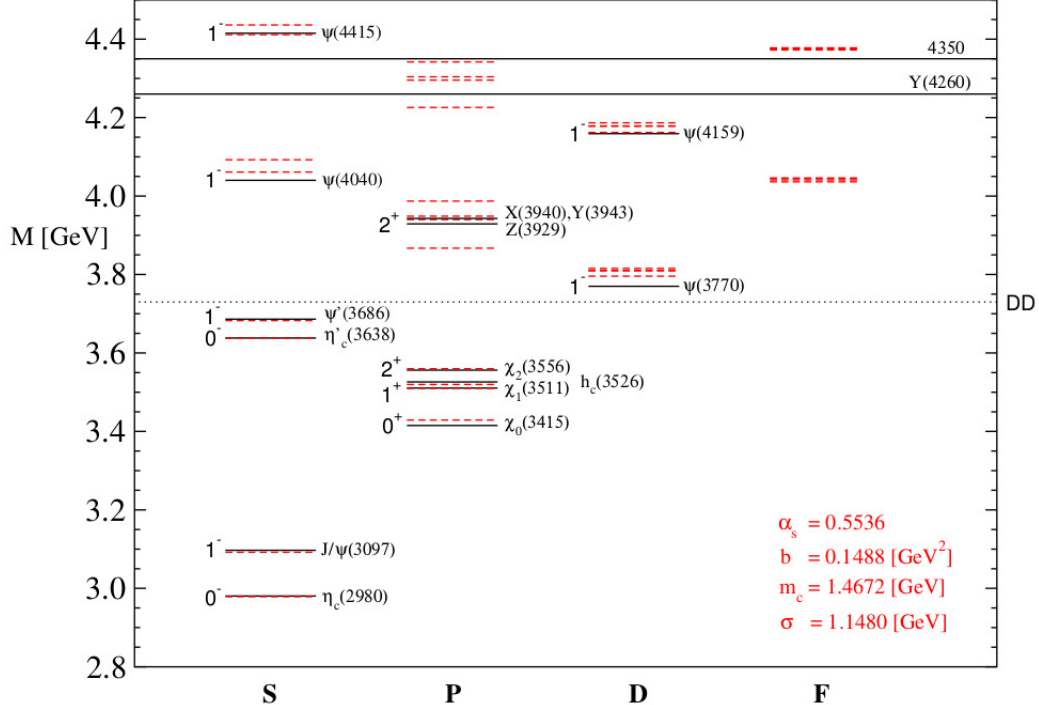


Figure 1.2: Measured and predicted charmonium resonances.
 Solid black lines represent measurements while the dashed red lines are predictions.

The resonances below the $D\bar{D}$ threshold, like the J/ψ and the $\psi(2S)$, show solid agreement with theoretical predictions. However, many of the ones above, such as the $\psi(3770)$, still show some disagreement. This is likely due to the more complicated interactions introduced from $D\bar{D}$ decays. Several experiments have attempted to measure the shape of the $\psi(3770)$ based on different assumptions. Many did not account for interference effects, which can notably alter the measured parameters of the $\psi(3770)$, such as the mass, shown in Table 1.1.

$M^{\psi(3770)} [\text{MeV}] (\text{No Interference})$	$M^{\psi(3770)} [\text{MeV}] (\text{With Interference})$
BES-II [1] 3772.0 ± 1.9	BaBar [4] $3778.8 \pm 1.9 \pm 0.9$
Belle [2] $3776.0 \pm 5.0 \pm 4.0$	KEDR [5] $3779.2^{+1.8+0.5+0.3}_{-1.7-0.7-0.3}$
BaBar [3] $3775.5 \pm 2.4 \pm 0.5$	

Table 1.1: Previous experimental results for the mass of the $\psi(3770)$. Where applicable, the first errors are statistical, the second are systematic, and the third are model-dependent.

Both BaBar [4] and KEDR [5] found it necessary to include interference effects in $D\bar{D}$ production in order to fit to the cross sections of $e^+e^- \rightarrow \gamma D\bar{D}$ and $e^+e^- \rightarrow (\text{hadrons})$, respectively. In the case of the KEDR measurement, the statistics were insufficient to fully resolve the discrepancies seen with other experiments that ignored interference. **Using the larger data sample available at BESIII, we have precisely measured and analyzed the shape of the $D\bar{D}$ spectrum around the $\psi(3770)$ resonance.** We have also used this measurement to probe the branching fraction of non- $D\bar{D}$ decays in this region.

1.1 Procedure

The basis of this measurement involves identifying $D\bar{D}$ pairs produced in $\psi(3770)$ decays. All data used in this analysis were collected from e^+e^- collisions analyzed by the BESIII detector. The e^- and e^+ annihilate through a virtual photon, meaning the total energy is transferred to the final state. Because the input energy can be precisely tuned, specific states with the right quantum numbers, such as the $\psi(3770)$, can be produced. However, resonances like this will decay almost instantaneously. For example, the $\psi(3770)$ has an average lifetime of $\sim 10^{-23}$ s, and disappears far too quickly to be directly observed. Even the initial decay into $D\bar{D}$ pairs is too fast to precisely measure, as the average lifetime ($\tau_D \approx 4 \times 10^{-13}$ s) would correspond to a distance of ~ 1 mm if it were traveling at c . Because the available energy in these decays is small ($m_{\psi(3770)} - 2 \times m_D \approx 40$ MeV), even the maximum velocity ($\beta \approx 0.15$) is too small to observe any displacement in the detector.

Instead, the reconstruction of candidate D particles relies on measuring their decays into other known modes. While dozens of decays modes have been measured, we focus on those which have high branching fractions, and are comprised of particles identifiable by the BESIII detector. For our purposes, these are π^\pm, K^\pm, π^0 , and K_S^0 . Each of these particles leaves ‘tracks’ within the detector; charged particles travel along curved paths and interact electromagnetically with charged wires along their trajectory, while neutral particles travel along straight paths and deposit energy in the detector crystals located outside the tracking region. The various components of the BESIII detector analyze these tracks to determine the type of particle, as well as its momentum and energy. By

analyzing sets of particles corresponding to the chosen decay modes, we can reconstruct the possible combinations and select those most likely to have originated from a D based on their total energy and momentum.

To determine the $\psi(3770) \rightarrow D\bar{D}$ cross section, we need to count the number of $D\bar{D}$ pairs produced, as well as measure the total quantity of e^+e^- collisions (the integrated luminosity, \mathcal{L}), at each energy point in our data sample. This counting is done not only for the actual collision data collected, but also for simulated samples, known as Monte Carlo (MC), to estimate detection efficiencies and backgrounds in our measurement. Each potential background corresponds to a particular event type which may be mistaken as signal, such as $e^+e^- \rightarrow \tau^+\tau^-$. We subtract these misidentified contributions from the total amount found in data to determine the actual number of reconstructed $D\bar{D}$ events. The detection efficiency of reconstructing $D\bar{D}$ is determined by counting the number of simulated signal events that pass our selection criteria and dividing by the number of events generated. Then, using the measured luminosity for each energy point, we determine the cross section as a function of center-of-mass energy.

The specific details of this analysis start with Chapter 2, which provides a discussion of relevant theoretical concepts. Next, Chapter 3 lists the specifications for the collider and detector which collected the data used for these measurements while Chapter 4 describes some of the related analysis software and reconstruction methods. From here, Chapter 5 describes the procedure for determining the $\psi(3770) \rightarrow D\bar{D}$ cross section and shows our measured $\psi(3770)$ parameters with systematic uncertainties. Finally, Chapter 6 examines the current progress of a related investigation for measuring the non- $D\bar{D}$ branching fraction of the $\psi(3770)$.

Chapter 2

Theoretical Background

2.1 Standard Model

Developed throughout the 1960s and 1970s, the Standard Model provides the most complete description of observable matter in the universe to date. It is a classification of all confirmed subatomic particles currently known, and predicts the most accurate results of any scientific theory ever measured. Each of the electromagnetic, weak, and strong fundamental forces are well described by this formulation. These three are described by an $SU(3) \times SU(2) \times U(1)$ group, where the $SU(3)$ corresponds to the strong force, the $SU(2)$ corresponds to the weak force, and the $U(1)$ corresponds to the electromagnetic force. The remaining fundamental force, gravity, is not included in the Standard Model. It is negligible on the scale of the masses of fundamental particles, and will be ignored in the discussions that follow.

2.1.1 Electromagnetic Force

The electromagnetic force is responsible for the forces between objects with electric charge, most notably binding together electrons and protons to form atoms and the structures they comprise. The theory of electromagnetic interactions is known as Quantum Electrodynamics (QED). Within this theory, the mediator of this force is the photon, a massless vector boson. As there is only a single mediator, and a single conserved quantity (electric charge), the formulation of QED is relatively simple compared to

the other forces. Still, the predictions it makes show astounding consistency with experiment, such as correctly calculating the anomalous magnetic dipole moment of the electron to more than 10 significant figures. Much of this success is due to QED being calculable through perturbation theory, where corrections are applied in terms of higher order factors of the coupling constant, α . This is possible due to its relatively small value ($\alpha \approx 1/137$), as the terms are convergent below very high orders of α .

2.1.2 Weak Force

The weak force is responsible for radioactive decay and other subatomic phenomena. This is distinct from the electromagnetic and strong interactions, where the constituent particles cannot change their types (or flavors). The mediators of this force are the W and Z , which are massive vector bosons. Not only are each of their masses non-zero, they are extremely heavy particles at 80.4 GeV and 90.2 GeV, respectively [6]. The unit of energy, eV, represents the amount of energy required to move a charge of e through a potential difference of 1 V. These large masses not only limit the interaction distance of the weak force, but also minimize the interaction strength (which is inversely proportion to mass). Furthermore, the large W and Z masses also lead to much slower interaction times, further reducing the effects of the weak force in comparison to the strong and electromagnetic forces.

In addition to transforming particle flavor, the weak force is also unique in its violation of various symmetries. The first discovery of symmetry violation came in 1957, when Wu and others [8] discovered the weak force did not behave identically under parity (P) transformations (i.e., mirror reflection). To account for this, a new theory conserving a compound symmetry was proposed. This combined charge conjugation (C), the swapping of particles with their antiparticles, with parity to form CP parity. However, in 1964, evidence of CP violation was also discovered by Cronin and Fitch [9]. The resolution to this symmetry conservation involves yet a third symmetry, time reversal (T), in which time is replaced with its negative ($t \rightarrow -t$). While the weak force violates these symmetries individually, the application of all three (CPT) is conserved across all known processes, and is known as the CPT Theorem.

At higher energy scales, the electromagnetic and weak forces unify into the electroweak force. In this theory, there are initially four massless gauge bosons mediating

the interactions. As a result of the Higgs mechanism, the initial gauge symmetry is broken at lower energies, and three of these bosons acquire a mass. These three bosons are the W^\pm and Z , while the remaining massless boson is the γ . The energies scales required for this unification were only present in the early universe. Before this, it is also believed there was an epoch of even higher energy, in which the electroweak force merged with the strong force.

2.1.3 Strong Force

The strong force is responsible for binding together particles known as hadrons. The theory of strong interactions is known as Quantum Chromodynamics (QCD). Like the electromagnetic force, the mediator of the strong force is also a massless vector boson, the gluon. However, while massless particles typically correspond to an infinite interaction range, the strong potential becomes very large at higher separations. This prevents the most fundamental particles which interact through the strong force, known as quarks (see Section 2.1.4), from existing as isolated entities in a process known as confinement. The typical interaction range is on the order of the proton radius, around 10^{-15} m. QCD calculations face serious challenges, however, as the coupling constant is not small ($\alpha_S \gtrsim 1$). This excludes the use of perturbation theory for most cases, as the higher order terms do not converge.

Strong interactions are associated with a corresponding conserved quantity known as the color charge. Despite its name, however, the term 'color' has no association with light, which is a purely electromagnetic phenomena. There are three colors associated with this charge, red (r), green (g), and blue (b). For anti-particles, there are oppositely charged values (\bar{r} , \bar{g} , and \bar{b}). In order for hadrons to be formed, the total color values of the constituents must be colorless. This means the total sum must involve all three colors (rgb or $\bar{r}\bar{g}\bar{b}$) or pairs of opposite colors ($r\bar{r}$, $g\bar{g}$, or $b\bar{b}$). However, these individual colors are not observable in nature. Because particles with different color values are distinct, this effectively triples the number of possible particle combinations, due to combinatorics.

Unlike the photon, which does not carry an electric charge, gluons do possess a color charge. There are eight possible color combinations which a gluon may possess, which are typically expressed using the Gell-Mann representation of $SU(3)$. With this basis,

each gluon is linearly independent, and no combination of gluons can be used to form a color singlet state. This non-zero charge of the force carrier makes QCD significantly more complex than QED. In fact, carrying color charge means gluons can also interact with each other directly, leading to certain theoretical states such as glueballs.

2.1.4 Elementary Particles

There are two primary groups contained in the Standard Model, fermions and bosons. This division is based on the Spin Statistics theorem, where fermions (bosons) have half-integer (integer) spins. As described by the Pauli Exclusion principle, nature restricts fermions from occupying the same quantum state. Bosons, however, do not have this restriction, and can have any number occupying the same state.

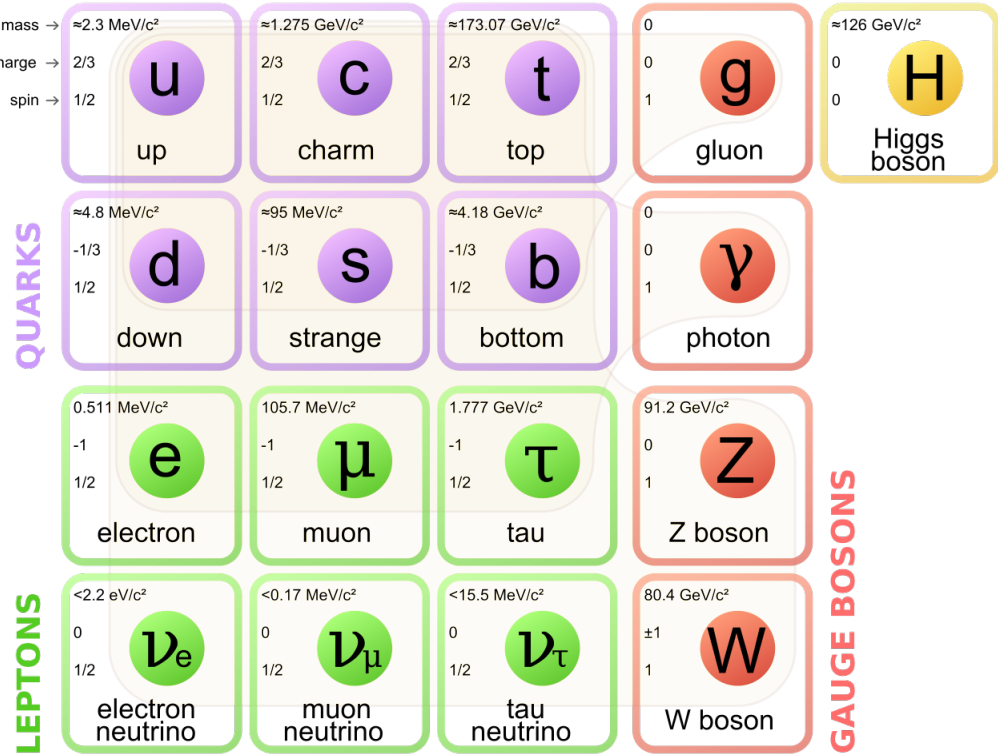


Figure 2.1: The standard model of particle physics.

It is comprised of two main groups: fermions, which includes the quarks and leptons, and bosons, which includes the gauge bosons and the Higgs boson. Image reproduced courtesy of [7].

Fermions

The fermions are divided by their interaction types into two major groups, quarks (q) and leptons (l). Each of these groups contains six particles with their corresponding antiparticles. These can be grouped into three generations, which aligns particles with the same electric charges, but greatly differing masses. As an example, the up (u), charm (c), and top (t) quarks all have an electric charge of $+2/3$ (in terms of the electron charge, e), but t is approximately five orders of magnitude more massive than u . For the quarks and fermions in Figure 2.1, rows indicate particles with the same electric charge, while columns represent each generation of particles.

While all fundamental fermions interact weakly, and all charged fermions interact electromagnetically, only the quarks interact strongly. Because of confinement, quarks cannot exist as isolated particles, and are only found in nature as groups of particles called hadrons. The most common types of hadrons exist as quark-antiquark pairs, known as mesons, or as groups of three quarks (or antiquarks), known as baryons. There are, however, indications of more exotic combinations of quarks, such as tetra- ($qq\bar{q}\bar{q}$) or penta-quark ($qqqq\bar{q}$) states seen by recent experiments [10, 11, 12].

While the negatively charged quarks (d , s , and b) are labeled as definite states, the quarks are actually mixed states. Through weak interactions, each of these quarks can transform into other quarks. The probabilities for these transformations are expressed by the Cabibbo-Kobayashi-Maskawa (CKM) Matrix [13], shown in Figure 2.2. From the experimentally measured values [6], it is evident the matrix is nearly diagonal. It is also clear that correlations are strongest within each generation, as the off-diagonal terms are generally smaller than the diagonal ones. Additionally, though the convention splits the negatively charged quarks into mixed states (leaving the positively charged quarks fixed), this choice has no physical basis. The reverse choice of having mixed positively charged quarks is equivalent.

$$\begin{bmatrix} |V_{ud}| & |V_{us}| & |V_{ub}| \\ |V_{cd}| & |V_{cs}| & |V_{cb}| \\ |V_{td}| & |V_{ts}| & |V_{tb}| \end{bmatrix} = \begin{bmatrix} 0.97427 \pm 0.00014 & 0.22536 \pm 0.00061 & 0.00355 \pm 0.00015 \\ 0.22522 \pm 0.00061 & 0.97343 \pm 0.00015 & 0.0414 \pm 0.0012 \\ 0.00886^{+0.00033}_{-0.00032} & 0.0405^{+0.0011}_{-0.0012} & 0.99914 \pm 0.00005 \end{bmatrix}$$

Figure 2.2: The Cabibbo-Kobayashi-Maskawa (CKM) Matrix.
Each coefficient represents the coupling of quark flavor to the observable mass state.

The values of the CKM matrix are typically parameterized using three Euler angles ($\theta_{12}, \theta_{23}, \theta_{13}$) and a CP-violating phase parameter (δ_{13}), where the indices represent the three generations of quarks. This formulation allows the matrix to be cast in the “standard” parametrization, shown in Figure 2.3. The form with three separated matrices clearly shows the connections between the generations of quarks. Namely, the third shows the original formulation in terms of a single rotation, the Cabibbo angle (θ_{12}). This theory is known as the Glashow-Iliopoulos-Maiani (GIM) mechanism [[14]] and was used to explain the suppression of flavor-changing neutral currents (FCNC) before the discovery of the charm quark.

$$\begin{aligned}
& \begin{bmatrix} 1 & 0 & 0 \\ 0 & c_{23} & s_{23} \\ 0 & -s_{23} & c_{23} \end{bmatrix} \begin{bmatrix} c_{13} & 0 & s_{13}e^{-i\delta_{13}} \\ 0 & 1 & 0 \\ -s_{13}e^{i\delta_{13}} & 0 & c_{13} \end{bmatrix} \begin{bmatrix} c_{12} & s_{12} & 0 \\ -s_{12} & c_{12} & 0 \\ 0 & 0 & 1 \end{bmatrix} \\
&= \begin{bmatrix} c_{12}c_{13} & s_{12}c_{13} & s_{13}e^{-i\delta_{13}} \\ -s_{12}c_{23} - c_{12}s_{23}s_{13}e^{i\delta_{13}} & c_{12}c_{23} - s_{12}s_{23}s_{13}e^{i\delta_{13}} & s_{23}c_{13} \\ s_{12}s_{23} - c_{12}c_{23}s_{13}e^{i\delta_{13}} & -c_{12}s_{23} - s_{12}c_{23}s_{13}e^{i\delta_{13}} & c_{23}c_{13} \end{bmatrix}
\end{aligned}$$

Figure 2.3: The standard form of the Cabibbo-Kobayashi-Maskawa (CKM) Matrix. The parameterization is in terms of three angles ($\theta_{12}, \theta_{23}, \theta_{13}$) and a phase angle (δ_{13}).

Here, $c_{ij} = \cos \theta_{ij}$ and $s_{ij} = \sin \theta_{ij}$.

The leptons are also organized into generations consisting of particles with two distinct charges. The electron (e^-), muon (μ^-), and tau (τ^-) are all negatively charged particles. There is also a neutral particle, a neutrino (ν), corresponding to each of the charged leptons (ν_e, ν_μ, ν_τ). These are very small mass (< 1 eV) particles with extremely low interactions. With the exception of mass, the interaction properties of each flavor are very similar. However, the three flavors themselves are treated as separate conserved quantities.

The Standard Model assumes neutrinos to be massless particles. However, this was violated by the discovery of neutrino oscillations, where transformations occur between neutrino flavor states due to differences in their masses. As with the quarks, the flavor states, ν_e, ν_μ , and ν_τ , are not the states observed in nature. Rather, the states with definite mass, labeled ν_1, ν_2 , and ν_3 , are linear combinations of the three flavor states. This can be expressed in a rotation of bases called the Pontecorvo-Maki-Nakagawa-Sakata (PMNS) matrix [15, 16]. Its formulation is analogous to the CKM Matrix.

Bosons

For each of the three forces included in the Standard Model, there are accompanying gauge bosons. These are the photon (γ) for electromagnetic force, the W^\pm and Z for the weak force, and the gluon (g) for the strong force. Each of the gauge bosons is a spin-1 vector boson, which means there are three available polarization states (-1, 0, +1). However, since the photon and gluon are both massive, gauge invariance requires these to have transverse polarizations. This means the spin-0 state is eliminated, and there are only two polarization states for each. There is also the Higgs boson (H), which unifies the electromagnetic and weak forces, and whose interactions with other particles are responsible for their mass. This is the only known fundamental spin-0 particle, which means it has only one polarization state.

Even with the amazing success of the Standard Model, the theory is not complete. Along with neutrino oscillations, other effects, such as dark matter and dark energy, remain major obstacles to constructing a unified theory. Such a theory must also include gravity, but there remain significant difficulties in explaining its effects through a quantum field theory. There also remains no conclusive explanation for various constants, such as the masses of the fundamental particles. Still, the Standard Model remains the most precise description of the universe to date, and continues to provide the basis for much current and future experimental and theoretical work.

2.2 Charmonium

The majority of this analysis focuses on a specific group of particles known as Charmonium. These particles are resonances formed by a $c\bar{c}$ pair, and can be treated analogously to the hydrogen atom. Namely, there is a spectrum of various excited states in the Charmonium region, just as the spectrum of states associated with the emission lines of hydrogen. The first three charmonium states to be discovered were the J/ψ , ψ' , and ψ'' . The ' and '' marks indicate their initial interpretations as the first and second excited states of the J/ψ , respectively. In the current terminology, the ψ' is denoted $\psi(3686)$ and the ψ'' is denoted $\psi(3770)$. The numbers in parentheses represent the masses of the particles in MeV.

An alternative labeling scheme for these states uses the quantum numbers for each

particle. This is written in the form $N^{2s+1}L_J$, where N refers to the principal quantum number, s refers to the total spin angular momentum of the particle, L refers to the orbital angular momentum, and J refers to the total angular momentum. Here, the values of L are in spectroscopic notation, where $L = 1, 2, 3, 4 \dots$ is denoted $S, P, D, F \dots$, and higher values follow alphabetically (excluding J). As each of these states is comprised of two spin- $\frac{1}{2}$ particles, the value of s in this case can only be 0 (opposite) or 1 (aligned). With this, the J/ψ , $\psi(3686)$, and $\psi(3770)$ can be denoted 1^3S_1 , 2^3S_1 , and 1^3D_1 . The values of n and L are used for the alternate notation of $\psi(2S)$ representing $\psi(3686)$. However, the notation of $\psi(1D)$ is not used for $\psi(3770)$ due to evidence of mixing in $\psi(3770)$ between the 2^3S_1 and 1^3D_1 states that suggests more complicated underlying interactions [17, 18].

In fact, while this model works well for states less massive than the $\psi(3770)$, the predictions made above this often break down. This likely reflects the greater complexity of states with energy values above that required to produce the open-charm D mesons $D^+(c\bar{u})$ and $D^0(c\bar{d})$. The $D\bar{D}$ threshold (twice the mass of the D^0) is just above the $\psi(2S)$ mass, and slightly below the $\psi(3770)$ mass. Therefore, the decay products of the two are drastically different, even while the available phase space is similar. Example Feynman diagrams for these two states can be seen in Figures 2.4 and 2.5.

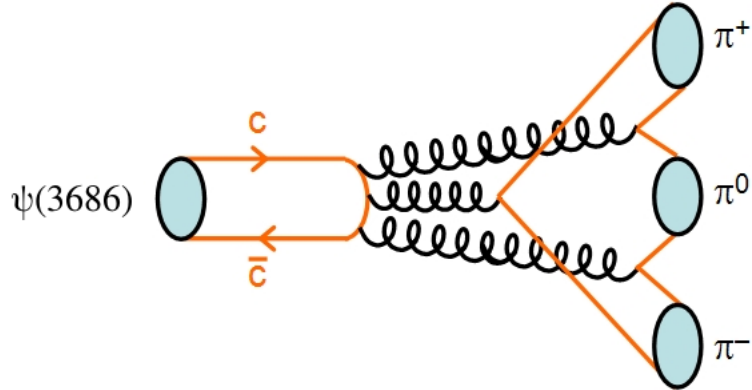


Figure 2.4: An example Feynman diagram for the decay of $\psi(3686)$.

Without sufficient energy to produce D mesons, the decays of $\psi(3686)$ must be mediated by three hard gluons and are suppressed, as described by the OZI rule.

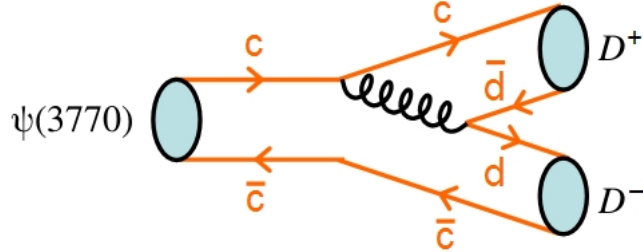


Figure 2.5: An example Feynman diagram for the decay of $\psi(3770)$. With sufficient energy to produce D mesons, the open-charm decays of $\psi(3770)$ are allowed to proceed, greatly increasing the total decay width.

The difference is also clearly seen in the total decay widths, where the most recent experimental averages [6] are $\Gamma^{\psi(2S)} = 286 \text{ keV}$ and $\Gamma^{\psi(3770)} = 27.5 \text{ MeV}$. An explanation for this difference is provided by the OZI Rule, proposed independently in the 1960s by Okubo [19], Zweig [20], and Iizuka [21]. This states that any Feynman Diagram where the initial and final particles can be connected only by energetic gluons represents a suppressed decay. In this process, the momentum transfer from the initial particles must occur entirely through these gluons, and because of the decreasing strength of the strong interaction with higher momentum transfer, the rate of these decays is inhibited. This is further compounded by the need for three gluons in such an interaction, as one gluon could not conserve color charge, and two could not converse C-parity. Once above the $D\bar{D}$ threshold, the allowed open-charm decays dominate, and the total width is greatly increased. This dominance points to a high branching fraction expected for decays of the type $\psi(3770) \rightarrow D\bar{D}$.

Chapter 3

Detector and Related Systems

All data used for this analysis were collected at the third Beijing Spectrometer (BESIII), located in Beijing, China, at the Institute of High Energy Physics (IHEP) campus. This detector records e^+e^- collision events provided by the second Beijing Electron-Positron Collider (BEPCII). The center-of-mass energy range for this facility was selected to concentrate on $\tau^+\tau^-$ and $c\bar{c}$ production, from about 2.0 GeV to 4.6 GeV. Both of these machines are upgrades from previous versions built on the same site. The first BEPC and BES were originally constructed in 1989, while the upgrade to BESII occurred in 1996. Their operation was terminated in 2004 to prepare for the upgrades to the current systems.

In 2009, BEPCII and BESIII began operation with the goal of utilizing greatly increased luminosity. For example, instead of the single-bunch electron collisions of BEPC, the new design utilized multiple bunch collisions. This creates many groups of electrons and positrons which are tightly packed during run time. BEPCII also utilizes a dual-storage ring for the electrons and positrons, compared to the single-ring available at BEPC. The improvements provide BEPCII with a design luminosity of $10^{33} \text{ cm}^{-2} \text{ s}^{-1}$, two orders of magnitude larger than the maximum of BEPC. This luminosity is optimized for energies near the $\psi(3770)$ resonance, as BESIII conducts many precision measurements and rare decay searches around this region. A detailed description of the BESIII detector can be found in Ref. [24].

3.1 BEPCII Accelerator

The setup for collisions in BEPCII begins with bombarding a fixed target with electrons in a linear accelerator. This generates high energy photons which interact with the target material to form e^+e^- pairs. The positrons from these pairs are then separated magnetically. These positrons are then injected into one of the two storage rings and accumulate up to the desired beam current. Following positron injection, electrons are accelerated in the linear accelerator and injected into oppositely circulating orbits in the second storage ring. These injections occur at a rate of 50 mA/min for positrons and 200 mA/min for electrons.

To achieve the necessary beam currents, many bunches of electrons and positrons are packed into the evacuated rings. During operation, each ring contains 93 bunches of length 1.5 cm separated by 8 ns (2.4 m). These provide a maximum beam current of 0.91 A while operating in collision mode. At the interaction point, each beam is focused using super-conducting quadrupole magnets to compress the beam size to about 5.7 μm vertically, while the horizontal beam size is about 380 μm . For collisions, each beam is also angled towards the center of the storage rings with an angle of 11 mrad. Though head-on collisions increase the instantaneous luminosity, this also results in beam-beam interactions spread through the confines of the electron and positron bunches which quickly degrade the beam current. Having this angle ensures more collisions occur at the targeted interaction point and results in an increased total integrated luminosity.

For a normal run, collisions continue occurring until the instantaneous luminosity falls below useful levels. While this is typically depleted due to the collisions between the e^+e^- particles, other unwanted interactions (such as those with residual gas in the storage rings) also reduce these currents. When this happens, BEPCII can replenish the beams using top-off injections. This allows the collider to continue utilizing the remaining particles within the storage rings without dumping the beams completely. Recycling these leftover electrons and positrons saves considerable time, and allows for more efficient data taking.

3.2 BESIII Detector

Centered around the interaction point of BEPCII, the BESIII detector records information about the particles produced by the e^+e^- collisions. Each collision occurs within the beam-pipe of the detector, which has inner and outer radii of 31.5 mm and 57.0 mm, and is evacuated to 5×10^{-10} Torr. Most of the apparatus is a region of uniform 1.0 T magnetic field provided by a super-conducting solenoid with a mean radius of 1.482 m and a length of 3.53 m. The field points in the z -direction, which is along the direction of the e^+ beam. The x -direction points towards the center of the storage rings, while the y -direction is vertically upwards. This magnetic field is used to allow measurement of the momenta of charged particles based on the curvature of their trajectories. It allows typical charged particles to sufficiently interact with much of the tracking volume, while minimizing those which curl too much to reach all layers of the detector.

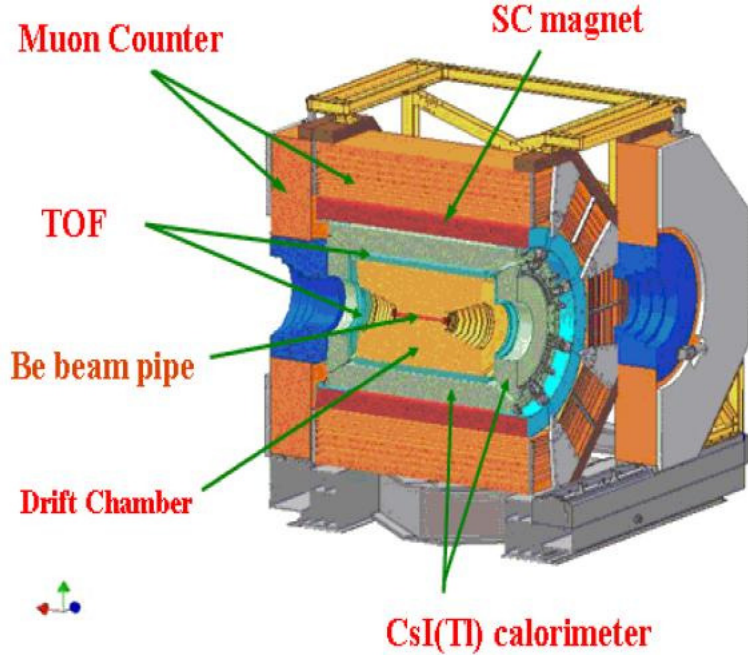


Figure 3.1: A schematic of the BESIII detector.

There are four main layers surrounding the beam-pipe: the Main Drift Chamber (MDC), the Time-of-Flight (ToF), the Electromagnetic Calorimeter (EMC), and the Muon Chamber (MUC). All but the MUC are surrounded by a uniform 1.0 T magnetic field produced by the super-conducting solenoidal magnet.

The BESIII detector, shown in Figure 3.1, consists of four main components which address different aspects of measuring and identifying particles. Starting from the most interior, these layers are the Multi-Layer Drift Chamber (MDC), the Time-of-Flight System (ToF), the Electromagnetic Calorimeter (EMC), and the Muon Identifier (MUC). Using the information provided by each of these, the tracks seen in the detector are given a particle hypothesis for their most likely identity. Only charged particles stable enough to traverse the detector volume are identifiable in this way. The charged particles identified at BESIII are electrons (e), muons (μ), pions (π), kaons (K), and protons (p). Short-lived particles, such as D^0 and D^+ , must be reconstructed from their decays into these constituents, as well as neutral shower energy from photons (γ).

3.2.1 Multi-Layer Drift Chamber

The purpose of the Multi-Layer Drift Chamber is to determine the momenta and trajectories of charged particles. Because of the magnetic field, charged particles travel in helical trajectories. The direction of curvature is used to determine the charge, while the radius of curvature of the track is used to determine the momentum.

The MDC is comprised of many layers of tungsten sense wires to detect the ionization of particles which pass through its gas-filled volume. The sense and field wires create an electric field which causes ionization electrons to drift towards the sense wires. This field is tuned to a strength which minimizes secondary ionization, except in the immediate vicinity of the sense wire. This produces an avalanche of secondary ionizations which creates a measurable current pulse in the sense wire. The amount of energy deposited by this process is proportional to the primary ionization produced by the track. Tracing the path of energy depositions over time allows for the reconstruction of each charged particle trajectory.

The main design of the MDC focuses on cylindrical layers of drift cells comprised of sense wires running coaxial to the beam pipe. The inner and outer radii of the MDC are 59 mm and 810 mm, respectively. There are 43 layers of sense wires which cover 93% of the 4π solid angle in the detector. These include 8 layers in the inner chamber, and 35 in the outer chamber. Each of the layers in the inner chamber are stereo layers (for measuring along the z -axis), while the 16 stereo layers and 19 axial layers (for measuring along the $x-y$ plane) are interleaved in the outer chamber. This arrangement

provides position resolutions of 130 μm and 2 mm in the $r - \phi$ plane and beam direction, respectively, for each hit. The uncertainty in the transverse plane measurements is dominated by electron diffusion and the readout time uncertainty for the electronics. For the transverse momentum, the resolution is about 0.5 % for tracks with momenta of 1 GeV, with uncertainties coming mainly from wire position measurements, and multiple scattering from material in the MDC.

The gas used for ionization is a mixture of 60% helium (He) and 40% propane (C_3H_8). Helium, because of its low atomic number, and thus, long radiation length, also minimizes the multiple scattering that degrades the momentum resolution. Propane, with extra rotational and vibrational degrees of freedom not accessible to helium, quenches the ionization energy. Without this effect, electrons would be accelerated by the electric field, produced secondary ionization energy, and lead to electric breakdown.

In addition to trajectory, the MDC also measures the rate of energy loss over distance for a particle traveling through a material [25], as described by the Bethe-Bloch equation,

$$-\frac{dE}{dx} = 4\pi N \frac{z^2 e^4}{m_e \beta^2} \left[\log \left(\frac{2m_e \beta^2}{I(1 - \beta^2)} \right) - \beta^2 \right], \quad (3.1)$$

where N is the electron number density of the material, z is the charge of the particle in terms of e , the charge of the electron, m_e is the mass of the electron, β is the velocity of the particle, and I is the mean excitation potential for electrons in the material being traversed. The resolution of dE/dx in the MDC is about 6 % for particles incident 90° to the beam-axis. The uncertainty is due to fluctuations in the number of primary ionizations along the flight path, fluctuations in the avalanche process, as well as from edge effects on each cell.

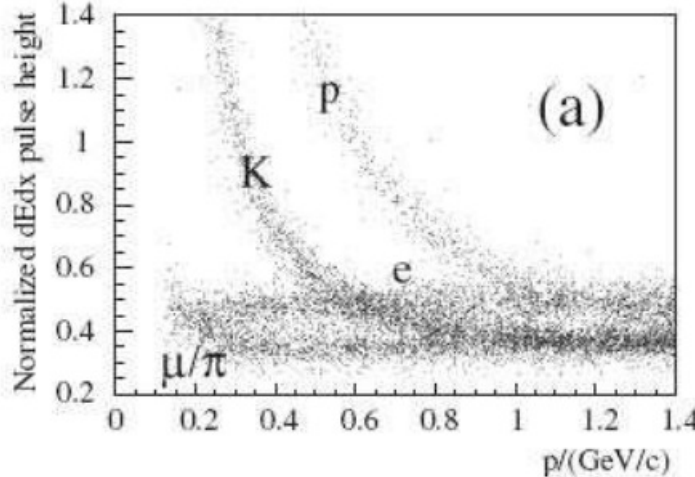


Figure 3.2: MDC energy deposition for various particles as a function of momenta. Distinction between K^\pm and π^\pm tracks is easier for low momenta, but becomes very difficult for higher values.

The energy deposition provides a method of determining particle identity, as this quantity depends on the velocity of the particle. An example of this behavior for multiple types of particles can be seen in Figure 3.2. To identify a particle from the various candidates, the measured energy deposition (dE/dx_{meas}) is compared against the expected value (dE/dx_{exp}) of each hit used to reconstruct the particle's trajectory (i):

$$\chi^2 = \sum_i \chi_i^2 = \left(\frac{dE/dx_{\text{meas}} - dE/dx_{\text{exp}}}{\sigma} \right)_i^2, \quad (3.2)$$

where σ represents the uncertainty on the measured energy deposition. This process provides a separation of 3σ between K^\pm and π^\pm tracks with momenta up to 770 MeV.

3.2.2 Time-of-Flight System

The purpose of the Time-of-Flight System is to determine the velocity of charged particles. This is useful for distinguishing particles with similar momenta, but different masses, as shown in Figure 3.3. It uses information provided by the MDC to determine the probability for each charged track to match the possible particle hypotheses. Namely, this includes the measured momentum, the expected time interval based on its

trajectory, and the mass for each particle hypothesis. This process provides a separation of 3σ between K^\pm and π^\pm tracks with momenta up to 900 MeV.

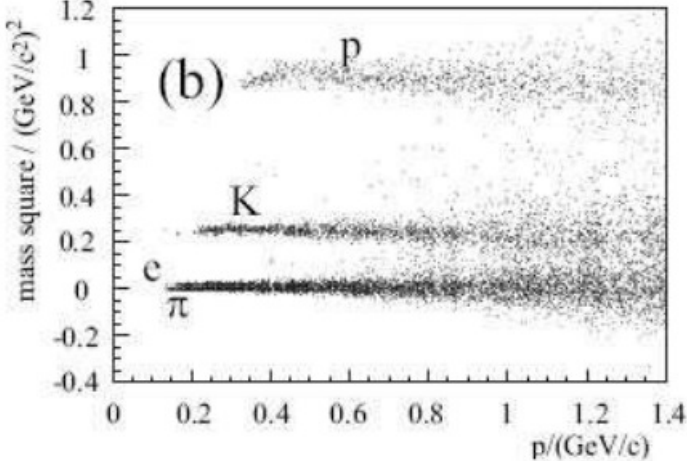


Figure 3.3: ToF measurements for various particles as a function of momenta. Distinction between K^\pm and π^\pm tracks is very easy for low momenta, but becomes more difficult for higher values.

The main body of the ToF is comprised of two bands of staggered plastic scintillators attached to photomultiplier tubes (PMTs). These two bands, located at 0.81 m and 0.86 m from the beam-pipe, provide two time measurements of the travel time from the interaction point. These measurements are used to determine the speed of each charged particle. The resolution is about 100 ps, and is largely limited by the scintillation light rise time, as well as fluctuations associated with the PMTs. The ToF is split into two regions, barrel and endcap, which cover the ranges $|\cos \theta| < 0.82$ and $0.85 < |\cos \theta| < 0.95$, respectively. The former is dual-layer with each containing 88 scintillators of 5 cm thickness arranged in a trapezoidal cross section, while the latter contains two single layers of 48 fan-shaped scintillators. Between the two are support structures for the MDC as well as other service lines.

3.2.3 Electromagnetic Calorimeter

The purpose of the Electromagnetic Calorimeter is to measure the energy deposited by photons and electrons. Since most of the charged tracks identified in the detector

are relativistic, they are minimum ionizing particles. This causes each to deposit a relatively constant value of energy, independent of the measured momenta. However, electrons, with their extremely small mass, will deposit significant amounts of energy due to Bremsstrahlung radiation and subsequent secondary e^+e^- pair production. This provides a clear distinction in the detector between e^- and π^-/μ^- tracks above 200 MeV, as seen in Figure 3.4. Energy measurements from the EMC are also useful for identifying neutral particles which decay only to photons, such as π^0 .

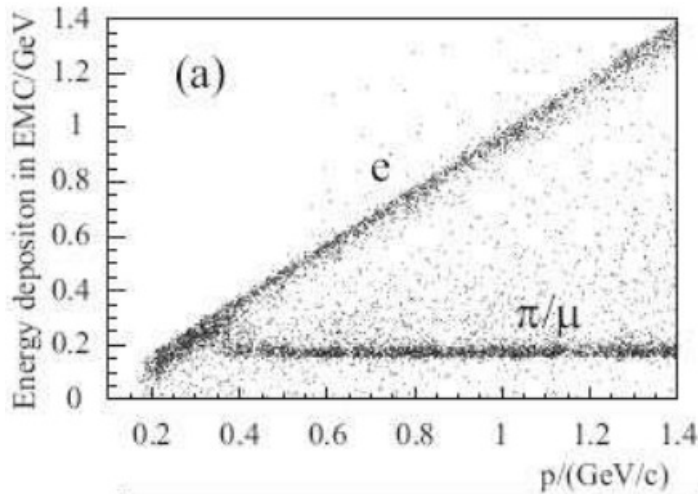


Figure 3.4: EMC energy deposition for various particles as a function of momentum. As the mass of e^- is so small, it deposits virtually all of its energy in the EMC. Both μ^- and π^- are generally minimum ionizing particles in this momenta range, and their similar masses make them difficult to distinguish with the EMC measurements alone.

The EMC is comprised of tellurium-doped cesium iodide ($\text{CsI}(\text{Tl})$) crystals with square front faces attached to two photodiodes. Each of the 6240 crystals is 5.2 cm long on the square edges and 28 cm (15 radiation lengths) deep. To prevent photons from aligning with the gaps between crystals, each one is offset with a tilt of 1.5° in the ϕ -direction and 1.5° to 3° in the θ -direction. These crystals provide an energy resolution (σ/E) of 2.5% at 1 GeV and 4% down to 100 MeV. This is limited by energy leaking out of the back of the crystals, the gaps between crystals, and by non-uniform light production. Only measurements of energy above 20 MeV are considered, because of the irreducible noise level in the detector. The position resolution is $\sigma = 0.6 \text{ cm}/\sqrt{E \text{ [GeV]}}$, and is limited by the crystal segmentation. The EMC has an inner radius of 94 cm and

a total weight of approximately 24 tons. It covers the regions $|\cos \theta| < 0.83$ (barrel) and $0.85 < |\cos \theta| < 0.93$ (endcap), with a gap in between that does not provide reliable energy measurements.

3.2.4 Muon Identifier

The purpose of the Muon Identifier is to determine the likelihood of a charged particle being a muon. Since electrons are significantly lower mass, they deposit virtually all of their remaining energy in the EMC. Additionally, since muons do not interact strongly, they will penetrate notably further than will pions, kaons, or protons. This provides a clear indication of a muon when a particle penetrates into the MUC. However, due to the magnetic field, only muons with $p > 0.4 \text{ GeV}$ can traverse deep enough to be identifiable.

The MUC is comprised of resistive plate counters (RPC) which are interspersed between the steel plates of the super-conducting solenoid's flux-return iron. The steel layers increase in thickness working outwards from the center: 3 cm, 3 cm, 3 cm, 4 cm, 4 cm, 8 cm, 8 cm, 8 cm, and 15 cm. Like the other components, the MUC is split into a barrel and an endcap region. The barrel has nine RPC layers of 4 cm thickness. In the endcap, the first RPC layer is after the first steel layer, leaving only eight RPC layers. Each of these layers has RPC strips oriented along only one direction. For the barrel, the z (ϕ) orientation is read out for only the odd (even) layers. Conversely, the endcap only reads out the x (y) orientation in the odd (even) layers.

3.3 Triggering Systems

In order to maintain a high efficiency for selecting physics events, many backgrounds must be filtered out. At BESIII, this is done through a triggering system with two-tiers: a hardware trigger (L1) and a software event filter (L3). This process is illustrated in Figure 3.5. The filtered background events are primarily from beam-related sources, such as beam-gas or beam-wall interactions, and occur at a rate of about 13 MHz. To assist with this process, collimators and masks are used to prevent lost electrons from interacting with the detector. However, there are also other sources of backgrounds, such as cosmic rays, which occur at a rate of about 1.5 kHz. The total backgrounds

must be suppressed to a rate which does not overwhelm the recording of events by the readout systems. This rate is roughly 2 kHz at the J/ψ peak, and 600 Hz for the $\psi(2S)$ when running near peak luminosity. For Bhabha events ($e^+e^- \rightarrow e^+e^-$), which are used for calibration and luminosity measurements, this rate is 800 Hz within the detector acceptance.

The first step (L1) reads out every clock cycle (24 ns) at a rate of 41.65 MHz. It uses information from the MDC, ToF, and EMC collectively to reduce the rates of beam-related backgrounds to 1.84 kHz and cosmic rays to about 200 Hz. However, L1 has a maximum rate of about 4 kHz. Because of this, when the buffer holding the subdetector data is around 80 % full, L1 triggering is halted until the buffer drops below 10 % full.

From the MDC, L1 gathers information about each charged track. The main parameter examined is the number of superlayers a track passed through. Here, a superlayer is the collection of wires at the same radial distance away from the center of the detector. Tracks are defined as ‘short’ if they deposit energy in segments of superlayers 3-5, or ‘long’ for superlayers 3-5 and 10. To ensure a sufficient momentum to reach the outer superlayers while originating at the interaction point, a minimum transverse momentum cut is applied to each track. This cut is 90 MeV and 120 MeV for short and long tracks, respectively. In addition to the numbers of short and long tracks for an event, the information about back-to-back tracks is also used.

From the ToF, L1 gathers information about the number of hits in the barrel and end-cap regions. It also examines the number of back-to-back hits in each of the two regions. Here, ‘back-to-back’ is defined as having hits within a range of 9 counters on the opposite side of the detector.

From the EMC, L1 gathers information about the clustering of energies around a local maximum-energy crystal. This includes the number of isolated clusters, as well as the information about back-to-back hits in the barrel and end-cap. Additionally, the balance of energy in the ϕ -direction (barrel) and in the z -direction (endcap) is also used.

The subdetector information gathered during L1 is then passed off to an online computer farm (L3) where the event is assembled. This step reduces backgrounds from a rate of about 2 kHz to about 1 kHz. Combined with the signal rate at the J/ψ peak (2 kHz), this corresponds to a total maximum event rate of 3 kHz, or a tape write speed of 40 MB/s.

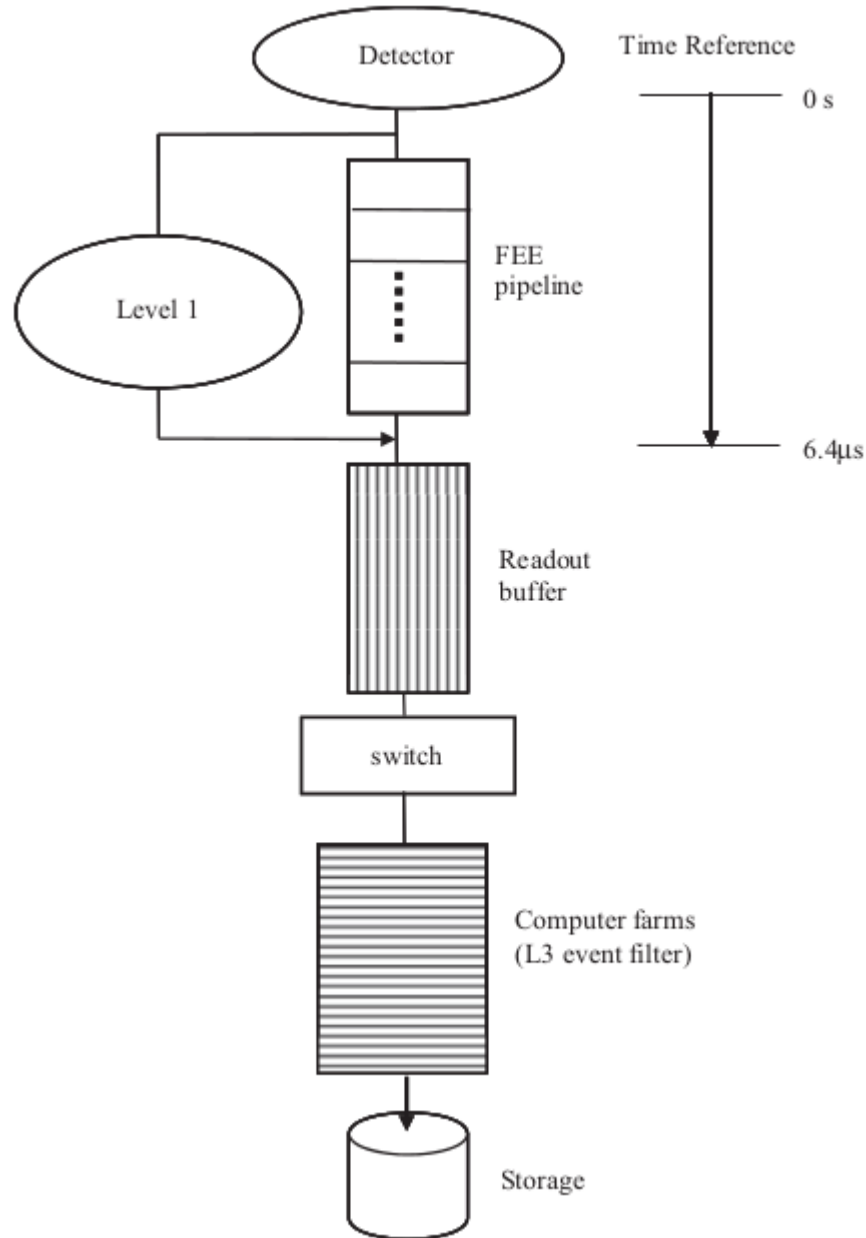


Figure 3.5: Triggering systems for event filtering at BESIII.

To prevent overloading the event recording system, non-physics background events must be eliminated from the data stream. This processing uses simple read-out information from each layer of the detector to quickly and efficiently determine whether or not events should be further considered for analysis.

Chapter 4

Analysis Software

4.1 BESIII Offline Software System

Reconstructing and processing event data gathered by the BESIII detector is done using the BESIII Offline Software System (BOSS) [26]. This is an analysis software distribution written using the C++ language and running primarily on the Scientific Linux CERN operating system [27]. There are five main parts to BOSS: framework, simulation, reconstruction, calibration, and analysis.

4.1.1 Framework

The framework is built on the Gaudi software architecture [28], which provides a standard interface and utilities for things such as event simulation, data processing, and physics analysis. The software is managed using the Configuration Management Tool [29], which provides a method for creating packages, handling package dependencies, and producing executables from source code. There are three main filetypes for data stored by the framework: raw data (`.raw`), reconstructed data (`.rec`), and Data-Summary-Tape (`.dst`). The latter two of these file types are derived from the ROOT [30] format (`.root`) for easy management and usage in various analyses.

4.1.2 Simulation

There are four main parts to the simulation process: event generation, detector description, particle tracking, and detector response. Event generation is primarily handled by the Monte Carlo (MC) generators KKMC, BesEvtGen, and Babayaga, which are described below. To model its geometry and materials, a unique description of the detector has been created using a format based on XML. This allows both simulation and reconstruction packages to appropriately model the behavior of events within the specific environment of BESIII. For particle tracking, interactions with detector materials are handled by GEANT4 [31]. Lastly, detector responses are modeled by the so-called ‘digitization code’. This takes into account each detector component, as well as readout electronics, and realistic situations such as noise or dead channels. There is also a simulation of the triggering system implemented.

KKMC

Originally developed for the LEP and SLC colliders, KKMC [32] is a generator used to model electroweak interactions. Namely, the processes generated are of the form $e^+e^- \rightarrow f\bar{f} + (n)\gamma$, where $f = \{\mu, \tau, u, d, s, c, b\}$, and $(n)\gamma$ represents any number of additional photons. These are modeled taking into account second-order sub-leading corrections, as well as initial-state radiation (ISR), and interference between initial- and final-state radiation (FSR). The effects of beam energy spread, typically on the order of 1 MeV near the $\psi(3770)$, can also be included.

After generation, the $f\bar{f}$ pair is decayed by models depending on the fermions involved. The TAUOLA library [33] is used to decay $\tau^+\tau^-$ pairs, and takes into account spin-polarization effects. The PYTHIA model [34] is used to hadronize final-state $q\bar{q}$ continuum production using the parton shower model. For resonances like the $\psi(3770)$, the only action performed by KKMC is the generation of ISR. After this, the virtual photon produced is handed off to BesEvtGen.

BesEvtGen

Originally developed for the CLEO and BaBar collaborations, EvtGen [35] is another widely used generator. It is the basis for BesEvtGen [36], which incorporates many

different decay models into a single utility. Over 30 exclusive decay models are available in BesEvtGen, as well as the capability to incorporate user-created models.

The simulation process occurs sequentially using dynamic information from decay amplitude probabilities and forward/backward spin-density matrices. From this, final state radiation is handled by the PHOTOS model [37]. To generate unknown decays of charmonium resonances, the LundCharm model [38] is used, while other unknown hadronic decays are handled by PYTHIA. For radiative processes, such as radiative return to J/ψ or $\psi(2S)$, the VECTORISR model [39] is used. This occurs when one particle in the initial e^+e^- pair radiates a photon of high enough energy that only lower mass resonances can be produced from the reduced center-of-mass energy. When the radiation is less energetic, the $\psi(3770)$ resonance is directly produced through the combination of KKMC and BesEvtGen.

Babayaga

Production of QED processes is done using the Babayaga generator [40]. This includes $e^+e^- \rightarrow \{e^+e^-, \mu^+\mu^-, \gamma\gamma\}$. The results are very accurate, with an estimated theoretical uncertainty of 0.1%. It also matches exact next-to-leading-order corrections from the parton shower algorithm. The high precision is important for determination of the efficiencies and acceptances required to precisely measure the integrated luminosity.

4.1.3 Reconstruction

Reconstruction primarily involves information about specific types of particles from each of the four main detector subsystems. These sources of information are as follows:

- a charged track finding algorithm and a Kalman-filter-based track-fitter
- a particle identifying algorithm based on dE/dx and time-of-flight measurements
- a shower- and cluster-finding algorithm for EMC energy and position
- a muon track finding algorithm

Further descriptions of each of these processes can be found in Sec. 4.2. Additionally, algorithms for determining the corresponding beam bunch crossing, as well as for secondary vertex and track refitting, are also utilized.

4.1.4 Calibration

To maintain consistent production and analysis of datasets, a centralized source of run-dependent information is maintained by BOSS. This includes algorithms which determine the calibration constants for each sub-detector, as well as a centralized database to store the results. Each of the calibration outputs are stored in a ROOT file along with other details such as the beam energy, luminosity, magnetic field information, trigger conditions, and hardware/software versions. While all of this information is stored by a central MySQL [41] server at IHEP, other institutions in BESIII regularly synchronize with this server to create mirrored copies of these databases.

4.2 Detector Simulation

The following sections detail the simulation, calibration, and reconstruction processes for each detector subsystem. Each of these relies on a geometry description created using GEANT4.

4.2.1 Multi-Layer Drift Chamber

Simulating events in the MDC accounts for axial layers, stereo layers, and endplates. The simulation also relies on the calibration parameters to determine things such as wire efficiency and resolution as a function of drift distance for each wire, noise in each layer, and possible misalignment.

Calibration of the MDC relies on $J/\psi \rightarrow \mu^+ \mu^-$ for both position and dE/dx . Using J/ψ events allows for quickly obtaining sufficient statistics due to the very large production cross section at that peak. The information determined includes constants such as $x - t$ relations, timing, alignment, and absolute wire efficiency. These values are stored in the database for each run. Special-purpose runs with the magnetic field turned off allow precise determination of wire positions.

Reconstructing MDC events starts by finding axial track segments using raw hits. These are found by searching for matches to pre-determined patterns. Next, these segments are fitted to circular tracks using the least-squares method. Stereo segments are then added using an iterative helix fit. Lastly, additional hits which were possibly

missed from the initial reconstruction are added to the track using a Kalman-filter process. This process determines the track parameters for multiple particle hypotheses. The reconstruction is remarkably efficient, with over 98 % of tracks with $p_T > 150$ MeV being reconstructed, even amidst high backgrounds. From this, the charge, momentum, and trajectory can be determined for each track.

In addition to tracking, the MDC also measures the ionization energy deposited per unit length, dE/dx , for each particle. The energy deposition of each track as it passes through the chamber is compared to expectations to determine a probability for each particle hypothesis. Corrections applied account for things such as multiple scatterings, magnetic deflection, and ionization. This likelihood from dE/dx is combined with information from the ToF to determine the type of particle that best matches the track properties.

4.2.2 Time-of-Flight System

Simulating events in the ToF accounts for the scintillator, wrapping materials, and photomultiplier tubes (PMTs). The process converts the energy deposited in the scintillator into photons, then propagates the shape of a photon pulse (rather than individual photons) to the PMTs in order to generate an electronic signal. A discriminator is applied to each pulse to determine the analog-to-digital conversion (ADC) and time-to-digital conversion (TDC) outputs. The algorithm was designed and tested with dedicated test beam data, however, each new data set requires updated tuning. A full simulation tracking each optical photon is also available for detailed study of the timing measurements.

Calibration of the ToF also uses J/ψ decays to dileptons for both timing and energy measurements. The information determined includes effective velocity, attenuation length, and muon energy loss. The status and performance of the ToF are regularly monitored by a laser-fiberoptics pulsing system.

Reconstructing ToF events starts by using tracks with trajectories extrapolated from the MDC. Each track is matched with a particular ToF module; either the two layers of the barrel, or the single-layer endcap. The travel time for each hypothesis is then calculated using weighted-average times from PMTs at both ends of the scintillator. Corrections are also applied to account for aspects like the effective light velocity in the scintillator and the light attenuation length. Measurements of deposited energy are

obtained for both charged and neutral particles, and are added to the EMC to improve the shower energy resolution.

4.2.3 Electromagnetic Calorimeter

Simulating events in the EMC accounts for the crystals, casing, silicon photodiodes, preamplifier boxes, cables, and the support system. For each of the crystals and photodiodes, hit information is recorded, and the deposited energy is summed. From this, photon statistics are computed, and the resulting photodiode response is converted into electronic signals. To obtain the waveform in the time domain, an inverse Laplace transform is applied. Then, a sampling and peak searching process is simulated to yield energy and time information. For each bin, Gaussian-type electronic noise is added, and the background is produced by summing over the waveforms.

Calibration of the EMC uses Bhabha electrons with $E > 1.55 \text{ GeV}$ for the high energy response, and $\pi^0 \rightarrow \gamma\gamma$ decays for the low energy response. The responses for individual crystals must be analyzed separately, due to their potential intrinsic variations. As a result, they are monitored frequently by a LED light pulser, and periodically recalibrated. Corrections due to temperature variations are also applied.

Reconstructing EMC events starts by converting the ADC value of each crystal into energy based on the calibration constants. After this, clusters in both the barrel and endcaps are formed by analyzing local maximum energy deposits, called seeds. A clustering algorithm then aggregates hits around these seeds and sums the values for a particular shower. The position of each shower is then calculated using the energy-weighted first moment. If multiple seeds are found in one cluster, a splitting algorithm is invoked to split the cluster into multiple showers. Additionally, matching energy deposits from the ToF are also added back into the total shower energy. This improves the energy resolution, particularly for low energy photons.

4.2.4 Muon Identifier

Simulating events in the MUC accounts for forming each RPC, creating sets of strips to form each read-out plane, combining each of these with aluminum boxes to form a muon counter module, and interleaving the modules between layers of iron plates.

The digitization from the read-out planes is selected to fire based on the distance to each track. Noise is simulated using Poisson distributions initially determined from measurements made during the construction of the chamber, and updated during actual data taking.

Calibration of the MUC analyzes RPC detection efficiencies as function of area. The cluster sizes and noise levels are also studied.

Reconstructing MUC events starts by searching for collected hits in each of the barrel and endcap orientations. The two collections are then matched with reconstructed tracks from the MDC. Since low momentum muons may cause only a few layers to fire, a subsequent search is performed over unused hits based on the extrapolated trajectories of MDC tracks. The reconstruction process primarily analyzes the depth of the track in the MUC, the maximum number of hits in the layers fired by a track, and the matching between a MDC track with the MUC stand-alone track. These parameters, along with the track momentum and MDC exit angle, are input into an Artificial Neural Network in order to distinguish between hadron and muon tracks. The identification process is quite effective, generally removing $\sim 96\%$ of pions and retaining $\sim 90\%$ of muons.

4.3 *D*-Tagging

From the decay of the $\psi(3770)$, the most commonly produced particles are $D^0\overline{D}^0$ or D^+D^- pairs. Since the $D\overline{D}$ pairs are produced in two-body decays, the energy of each D is half of the center-of-mass energy (in the center-of-mass reference frame). Each of these D mesons then quickly decays to certain sets of particles. Reconstructing one of these decays requires assembling the right combination of such particles under the constraint of 4-momentum conservation.

This reconstruction technique is known as ‘*D*-Tagging’, and was pioneered by the MARK-III collaboration [42, 43]. For our analysis, the particles analyzed in the detector include π^\pm , K^\pm , π^0 , and K_S^0 , and the decay modes used are shown in Table 4.1. There are three D^0 modes and six D^+ modes, where charge conjugation (converting all particles to their anti-particles) is implied throughout the analysis. The modes used are chosen for their overall efficiency of reconstruction in the detector; they generally have higher branching fractions and manageable multiplicity (the number of tracks in the final state).

For the neutral modes, this procedure also includes the doubly-Cabbibo suppressed decays (DCSD), such as $D^0 \rightarrow K^+ \pi^-$, which have small and well-measured branching fractions.

(0) $D^0 \rightarrow K^- \pi^+$	(200) $D^+ \rightarrow K^- \pi^+ \pi^+$	(203) $D^+ \rightarrow K_S^0 \pi^+ \pi^0$
(1) $D^0 \rightarrow K^- \pi^+ \pi^0$	(201) $D^+ \rightarrow K^- \pi^+ \pi^+ \pi^0$	(204) $D^+ \rightarrow K_S^0 \pi^+ \pi^+ \pi^-$
(3) $D^0 \rightarrow K^- \pi^+ \pi^+ \pi^-$	(202) $D^+ \rightarrow K_S^0 \pi^+$	(205) $D^+ \rightarrow K^+ K^- \pi^+$

Table 4.1: The reconstructed D -tag modes used in this analysis.

The numerical values are shorthand codes used by the reconstruction software.

This process occurs for each event and searches over each decay mode for each charm state (D^+ and D^-). The combinations chosen for reconstruction are those with the smallest energy difference from the expected value. More than one D combination can be extracted from a given event, as long as it satisfies all other requirements (see Section 4.3.1). While this may sound like it overestimates the number of actual D particles found, the process is also used to calculate reconstruction efficiency, thereby eliminating any bias.

4.3.1 Selection Cuts

Before being considered as potential reconstruction candidates, each track in the detector must also pass other cuts specific to its identified particle type. The following describes the criteria required for the particles in the decay modes we are using.

π^\pm/K^\pm Selection

Each of the reconstructed charged tracks must pass vertex cuts in both the transverse ($x - y$) and beam (z) directions relative to the interaction point. This requires that tracks originate sufficiently close to the interaction point to ensure they are not other backgrounds, such as cosmic rays, or daughters of tracks which have decayed in flight. There is also a cut on the polar angle measured within the MDC (θ) to ensure the track can reliably be reconstructed. Lastly, from the particle identification process, the probability of being a pion (kaon) must be greater than that for being a kaon (pion). The specific cuts for each of these requirements can be found in Table 4.2.

Vertex (xy)	$V_{xy} < 1 \text{ cm}$
Vertex (z)	$ Vz < 10 \text{ cm}$
MDC Angle	$ \cos \theta < 0.93$
Pion Probability	$P(\pi) > 0, P(\pi) > P(K)$
Kaon Probability	$P(K) > 0, P(K) > P(\pi)$

Table 4.2: The required cuts to identify charged tracks as π^\pm or K^\pm .

γ Selection

To distinguish photon energy from noise, each shower in the EMC is required to have a certain amount of deposited energy. These cuts are different for the barrel ($|\cos \theta| < 0.80$) and endcap ($0.84 < |\cos \theta| < 0.92$) regions. Each photon must also pass a timing cut to ensure they are consistent with actual physics events, and not originating at other times. The values for each of these requirements can be found in Table 4.3.

Minimum Energy (Barrel)	$E_{\text{EMC}} > 25 \text{ MeV}$	$(\cos \theta < 0.80)$
Minimum Energy (Endcap)	$E_{\text{EMC}} > 50 \text{ MeV}$	$(0.84 < \cos \theta < 0.92)$
TDC Timing	$(0 \leq t \leq 14) \times 50 \text{ ns}$	

Table 4.3: The required cuts to identify neutral showers as a γ .

π^0 Selection

Reconstructing π^0 mesons involves finding $\gamma\gamma$ pairs, as this the most dominant decay ($\sim 99\%$). Each of the γ showers must pass the cuts described above. Additionally, at least one photon in the pair must be found in the barrel region. Each of the two photons are then kinematically fitted to compare with the invariant mass of the π^0 , and must also pass a proper fit cut. The resulting momentum from this fit is used for reconstructing D -tag candidates. The values used for each of these requirements are shown in Table 4.4.

Nominal Mass	$115 \text{ MeV} < m_{\pi^0} < 150 \text{ MeV}$
Fit Quality	$\chi^2 < 200, \text{Converged}$

Table 4.4: The required cuts to reconstruct $\gamma\gamma$ pairs as a π^0 .

K_S^0 Selection

Reconstructing K_S^0 mesons involves finding $\pi^+\pi^-$ pairs, as this is its most common decay ($\sim 70\%$). While $\pi^0\pi^0$ pairs are also a substantial decay mode ($\sim 30\%$), these are not considered due to the difficulty of correctly reconstructing the 4γ final state. To account for the K_S^0 decaying in flight, each of the charged pions considered are not subjected to the vertex or probability cuts in Table 4.2. Instead, the two found pions are kinematically constrained to a common vertex. The results must pass a nominal mass cut ($\sim 3\sigma$) and a proper fit cut to be deemed a K_S^0 . From this, the resulting momentum from the vertex fit is used for reconstructing D -tag candidates. The values used for each of these requirements are shown in Table 4.5.

Nominal Mass	$487 \text{ MeV} < m_{K_S^0} < 511 \text{ MeV}$
Fit Quality	$\chi^2 < 100$, Converged

Table 4.5: The required cuts to reconstruct $\pi^+\pi^-$ pairs as a K_S^0 .

Cosmic Ray and Lepton Veto

When reconstructing the mode $D^0 \rightarrow K^-\pi^+$, an additional veto is used. Since this mode has only two charged tracks, it is common to misidentify particles which come from cosmic ray and backgrounds like $e^+e^- \rightarrow \{\gamma e^+e^-, \gamma\mu^+\mu^-\}$. To prevent this, cuts on the timing difference between the tracks, as well as on the particle identification variables, are imposed. The values used for these requirements are shown in Table 4.6.

Timing (TDC)	$ t_1 - t_2 < 5 \times 50 \text{ ns}$
Particle Identification	$(\chi_{e^-}^2 + \chi_{e^+}^2) - (\chi_{K^-}^2 + \chi_{\pi^+}^2) > 10$

Table 4.6: Cuts to suppress cosmic ray and lepton backgrounds in $D^0 \rightarrow K^-\pi^+$.

4.3.2 Reconstruction

After all of the constituent particles are identified, reconstructed D candidates are characterized by two main kinematic quantities:

$$\Delta E = |E_{\text{beam}} - E_{\text{tag}}|, \quad m_{\text{BC}} = \sqrt{E_{\text{beam}}^2 - |\vec{p}_{\text{tag}}|^2}. \quad (4.1)$$

These are the energy difference (ΔE) and the beam-constrained mass (m_{BC}), and effectively represent the energy and momentum of the D -tag, respectively. As the candidate with the smallest ΔE for each decay mode in each event is selected, the values will peak near 0 MeV. Distributions of m_{BC} peak near the respective D masses, $m_{D^0} = 1.865$ GeV or $m_{D^+} = 1.870$ GeV. While invariant mass ($m_{\text{inv}} = \sqrt{E_{\text{tag}}^2 - |\vec{p}_{\text{tag}}|^2}$) is an alternative selection variable, m_{BC} is preferred because the beam energy is more precisely known than the 4-momenta of the individual particles comprising the D candidate.

Chapter 5

Measurement of $\sigma(\psi(3770) \rightarrow D\bar{D})$ near $\psi(3770)$

The main objective of this analysis is to measure the $\sigma(\psi(3770) \rightarrow D\bar{D})$ cross section at center-of-mass energies around the $\psi(3770)$. While the cross section very near the $\psi(3770)$ mass has been measured with excellent precision [44], the shape over a wider energy range has not been measured as precisely. As such, it has been impossible to fully determine the functional form that best describes the cross section or to definitively determine the extent which interference effects must be included. Fits to this region with a single Breit-Wigner shape (i.e., no interference) have provided a unsatisfactory description of the $\psi(3770)$. The most straightforward modification of this assumption is to incorporate a contribution from the $\psi(2S)$. This is the form considered here, where the procedure largely follows the methodology of the KEDR collaboration [5]. With the larger statistics available at BESIII, however, an inclusive cross section measurement (such as performed by KEDR) is not required. Instead, we measure the production of $\psi(3770) \rightarrow D\bar{D}$ events directly.

5.1 Derivation of $\sigma(\psi(3770) \rightarrow D\bar{D})$

The production rate for a pair of D mesons coming from $\psi(3770)$ at a given center-of-mass energy can be calculated following an approach of Kuraev and Fadin [22]. This method includes Initial State Radiation (ISR), which effectively replaces the well-defined

e^+e^- center-of-mass energy of the accelerator with a distribution of energies, is given by the following:

$$\sigma_{D\bar{D}}^{RC}(W) = \int z_{D\bar{D}}(W\sqrt{1-x}) \sigma_{D\bar{D}}(W\sqrt{1-x}) \mathcal{F}(x, W^2) dx. \quad (5.1)$$

Here, W is the center-of-mass energy after the collision, x parametrizes the fraction of radiated energy, and $\mathcal{F}(x, W^2)$ is the probability of losing this energy by ISR:

$$\begin{aligned} \mathcal{F}(x, W^2) &= \beta x^{\beta-1} \left[1 + \frac{\alpha}{\pi} \left(\frac{\pi^2}{3} - \frac{1}{2} \right) + \frac{3}{4}\beta + \beta^2 \left(\frac{37}{96} - \frac{\pi^2}{12} - \frac{L}{72} \right) \right] = \beta x^{\beta-1} F(W^2), \\ \beta &= \frac{2\alpha}{\pi}(L-1), \quad L = \log \left(\frac{W^2}{m_e^2} \right). \end{aligned} \quad (5.2)$$

The factor $z_{D\bar{D}}$ accounts for the expected Coulomb interaction between the mesons for the charged mode (D^+D^-),

$$z_{D^+D^-} = \frac{\pi\alpha/\beta_{D^+}}{1 - \exp(-\pi\alpha/\beta_{D^+})} \times \theta(W - 2m_{D^+}), \quad (5.3)$$

but only accounts for the $D\bar{D}$ energy threshold in the neutral mode ($D^0\bar{D}^0$),

$$z_{D^0\bar{D}^0} = \theta(W - 2m_{D^0}). \quad (5.4)$$

The theta function imposes the step in the cross section at the production threshold.

The integral in Eq. 5.1 can be simplified by taking advantage of the relatively constant values of $z_{D\bar{D}}$ and $\sigma_{D\bar{D}}$ over sufficiently small intervals. By splitting the full W range into such intervals approximating the integral over each, this becomes

$$\int \mathcal{F}(x, W^2) dx \approx \sum_{n=0}^N F(W^2) \int_{\frac{n}{N}}^{\frac{n+1}{N}} \beta x^{\beta-1} dx = \sum_{n=0}^N F(W^2) \left[x_{\text{upper}}^\beta - x_{\text{lower}}^\beta \right]. \quad (5.5)$$

The upper, lower, and mid-point values are given by

$$x_i = \left[1 - \left(\frac{2m_D}{W} \right)^2 \right] \left(\frac{n_i}{N} \right), \quad n_i : \begin{cases} n_{\text{lower}} &= n \\ n_{\text{mid}} &= n + \frac{1}{2} \\ n_{\text{upper}} &= n + 1 \end{cases}. \quad (5.6)$$

The bracketed expression in Eq. 5.6 represents the maximum value of x determined by the theta functions of Eqs. 5.3 and 5.4. To maintain sufficient precision with this interval approximation, the value of $N = 1024$ is used. Combining this with the other factors in Eq. 5.1, the cross section including the effect of ISR becomes

$$\sigma_{D\bar{D}}^{RC}(W) = \sum_{n=0}^N z_{D\bar{D}}(W') \sigma_{D\bar{D}}(W') F(W^2) \left[1 - \left(\frac{2m_D}{W} \right)^2 \right]^\beta \left[\frac{[(n+1)^\beta - n^\beta]}{N^\beta} \right], \quad (5.7)$$

where $W' = W\sqrt{1-x_{\text{mid}}}$. The Born level (lowest order) $D\bar{D}$ cross section is given by

$$\sigma_{D\bar{D}} = \frac{\pi\alpha^2}{3W^2} \beta_D^3 |F_D(W)|^2, \quad \beta_D = \sqrt{1 - \frac{4m_D^2}{W^2}}. \quad (5.8)$$

Here, β_D is the velocity of the D meson in the center-of-mass system. The form factor F_D governs the contributions of each individual resonant (R) component and the total non-resonant (NR) component. Each resonant piece is parametrized with a phase angle relative to the non-resonant contribution:

$$F_D(W) = F_D^{NR}(W) + \sum_r F_D^{R_r}(W) e^{i\phi_r}. \quad (5.9)$$

Each resonant contribution to the form factor is modeled by a Breit-Wigner amplitude,

$$F_D^R(W) = \frac{6W\sqrt{(\Gamma_{ee}/\alpha^2)(\Gamma_{D\bar{D}}(W)/\beta_D^3)}}{M^2 - W^2 - iM\Gamma(W)}, \quad (5.10)$$

where Γ_{ee} is the dielectron partial width, and $\Gamma(W)$ represents the total width of the resonance with mass M :

$$\Gamma(W) = \left(\frac{M}{W} \right) \left[\frac{z_{D\bar{D}}(W) d_{D\bar{D}}(W)}{z_{D^0\bar{D}^0}(M) d_{D^0\bar{D}^0}(M) + z_{D^+D^-}(M) d_{D^+D^-}(M)} \right] \Gamma(M). \quad (5.11)$$

The value of $\Gamma(M)$ represents the total width at the nominal mass of the resonance, while $d_{D^+D^-}$ and $d_{D^0\bar{D}^0}$ are the Blatt-Weisskopf damping factors [23] for a vector resonance:

$$d_{D\bar{D}} = \frac{\rho_{D\bar{D}}^3}{\rho_{D\bar{D}}^2 + 1}, \quad \rho_{D\bar{D}} = q_D R_0 = \left(\frac{\beta_D W}{2} \right) R_0. \quad (5.12)$$

Here, q_D is the D momentum in the center-of-mass frame, while R_0 represents the radius of the parent particle. The $D\bar{D}$ partial width listed in Eq. 5.10 is the total width rescaled according to $\mathcal{B}_{nD\bar{D}}$, the sum of all non- $D\bar{D}$ decay modes of $\psi(3770)$:

$$\Gamma_{D\bar{D}}(W) = \Gamma(W) \times (1 - \mathcal{B}_{nD\bar{D}}). \quad (5.13)$$

Theoretical calculations of $\mathcal{B}_{nD\bar{D}}$ place the value on the order of a few percent. However, experimental results have measured values throughout the range of 0% to 16%. Without a trustworthy measurement to use for our analysis, we elect to define the fit parameter $\Gamma_{ee}^{\psi(3770)}$ to include the product with $(1 - \mathcal{B}_{nD\bar{D}})$. While this does not provide an immediate result, future values for either parameter allows the other to be easily determined. More information about the branching fraction is discussed in Chapter 6.

5.2 Form Factors

To apply the cross section formula derived above, the relevant form factors (Equation (5.9)) must now be specified. We assume the $\psi(2S)$ resonant contribution is negligible in the energy range of our measurements, so the only significant resonant contribution is from the $\psi(3770)$:

$$F_D(W) = F_D^{\text{NR}}(W) + F_D^{\psi(3770)}(W) e^{i\phi^{\psi(3770)}}. \quad (5.14)$$

Currently, there is no definitive model for the non-resonant term, so we use two alternative parameterizations. The first is a simple exponential model:

$$F_D^{\text{NR}} = F_{\text{NR}} \exp(-q_D^2/a_{\text{NR}}^2), \quad (5.15)$$

where both F_{NR} and a_{NR} are left free in the fit to the cross section. The second treatment implements a Vector Dominance Model (VDM). This assumes the interference effects are due to the $\psi(2S)$ mediating $D\bar{D}$ production above threshold,

$$F_D^{\text{NR}}(W) = F_D^{\psi(2S)}(W) + F_0, \quad (5.16)$$

and that the effective properties of the $\psi(2S)$ are similar to those of the $\psi(3770)$. The

real constant F_0 represents the potential effect of higher resonances, like the $\psi(4040)$. The first term is similar to Equation (5.10), but with a modification to the total width,

$$\Gamma^{\psi(2S)}(W) = \left(\frac{M^{\psi(2S)}}{W} \right) \left[\frac{zd_{D^0\bar{D}^0}(W) + zd_{D^+D^-}(W)}{zd_{D^0\bar{D}^0}(M^{\psi''}) + zd_{D^+D^-}(M^{\psi''})} \right] \Gamma^{\psi(2S)}(M), \quad (5.17)$$

where $zd_{D\bar{D}}(W) = zd_{D\bar{D}}(W) \times d_{D\bar{D}}(W)$. Without this modification, the mass of the $\psi(2S)$ would be below the $D\bar{D}$ threshold, and thus, the vanishing $z_{D\bar{D}}$ terms would cause a singularity in the width. Therefore, we use the mass of the $\psi(3770)$ in its place to estimate the effects in this region. While it may behave like the total width in Equation (5.17), the true physical meaning of the parameter $\Gamma^{\psi(2S)}(W)$ is unclear.

For the radii in Equation (5.12), however, the values used are distinct for each meson: $R_{\psi(2S)} = 0.75$ fm and $R_{\psi(3770)} = 1.00$ fm. These are the same values as used in the KEDR procedure [5], where each is quoted with an uncertainty of 25%. This provides one of the largest sources of systematic uncertainty, and is discussed in Section 5.7.

5.3 Data and Monte Carlo Samples

5.3.1 Data Samples

This analysis primarily uses scan data produced by BEPCII and collected by BESIII in 2010 over an energy range of 3.643 GeV to 3.890 GeV. These data are partitioned into 34 center-of-mass energy (E_{cm}) bins of variable size over a range of 3.735 GeV to 3.870 GeV. The bin partitioning was determined from measurements of center-of-mass energies (Section 5.3.2). The total range was chosen to be above the $D^0\bar{D}^0$ threshold (3.730 GeV) and below the $D^{*0}\bar{D}^0$ threshold (3.872 GeV). Note, this includes values below the D^+D^- threshold (3.739 GeV), with production beginning in the third bin.

Additionally, there are three higher statistics points used for comparison. These include an ‘On-Peak $\psi(3770)$ ’ sample of 2.93 fb^{-1} at $E_{\text{cm}} = 3.7732$ GeV, an ‘XYZ-scan’ sample of 50.54 pb^{-1} at $E_{\text{cm}} = 3.810$ GeV, and an ‘ R -scan’ sample of 7.95 pb^{-1} at $E_{\text{cm}} = 3.850$ GeV. The first of these is the high statistics measurement very near the $\psi(3770)$ peak that was used for a double-tag reconstruction (both D and \bar{D} reconstructed in a single event) measurement performed by Derrick Toth [44]. The other two samples were analyzed using the same procedure as for the scan data (See Sections 5.4 to 5.6).

None of these points are used to determine the final results, as the differences between samples introduce additional systematics which degrade any statistical improvement. However, these provide useful comparisons of cross section measurements at important energy points for the primary scan sample.

5.3.2 Center-of-Mass Energy Measurement

To precisely determine the values of center-of-mass energy along the scan data region, $e^+e^- \rightarrow \mu^+\mu^-$ events were analyzed to determine their invariant mass (m_{inv}). Assuming that minimal energy is radiated by the muons, this value is effectively equal to the energy produced by the collider. The selection process for such events is shown in Table 5.1. The statistics of the scan data are too small to precisely determine the energy for individual runs. Therefore, multiple runs were combined together into bins based on the assumption that run groups were taken at nearly identical energies. A comparison of the measured values to the less well calibrated beam energies measured by BEPCII during runtime is shown in Figure 5.1.

Vertex (xy)	$V_{xy} < 1 \text{ cm}$
Vertex (z)	$ Vz < 10 \text{ cm}$
MDC Angle	$ \cos \theta ^{\mu^\pm} < 0.80$
Muon Opening Angle	$\cos(179.64^\circ) < \cos \theta_{\mu\mu} < \cos(178.60^\circ)$
Energy-Momentum Ratio	$0.05 \leq (E/p)^{\mu^\pm} < 0.15$
Shower Energy	$0.0 \text{ GeV} < E_{EMC}^{\mu^\pm} < 0.3 \text{ GeV}$

Table 5.1: Selection cuts on muon tracks used to determine the center-of-mass energy.

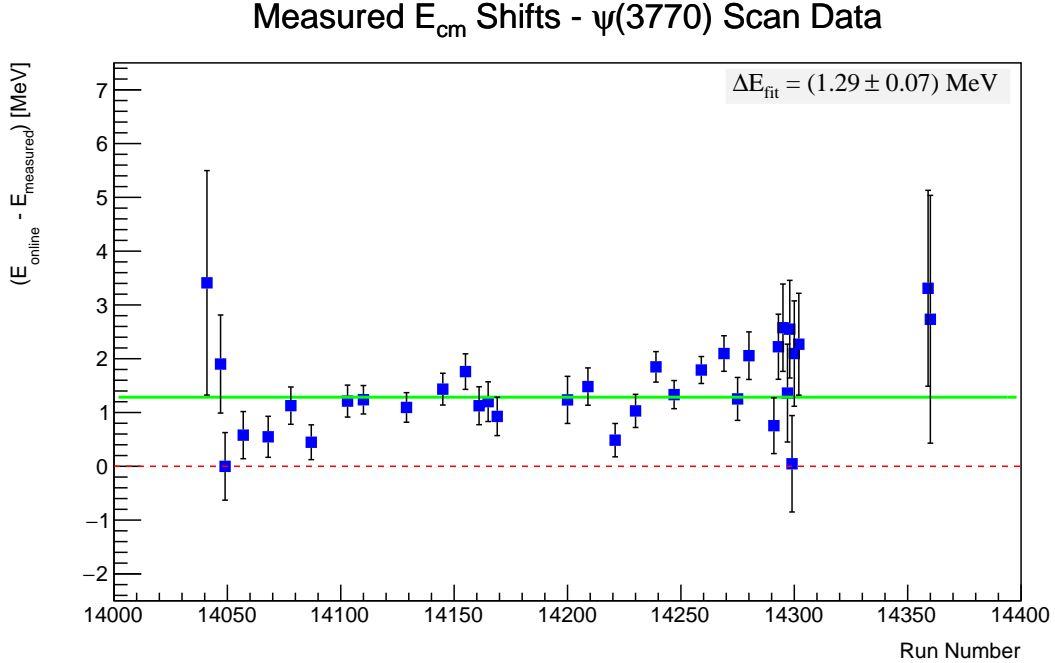


Figure 5.1: A comparison of online center-of-mass energies and measured $\mu^+\mu^-$ events. The average value of the $\mu^+\mu^-$ pair measurements (green) is higher than the average value of the online BEPCII measurements taken during run-time (red) by about 1.29 MeV.

The use of muons to determine energy is subject to an overall scale shift due to potentially miscalibrated momentum measurements, most likely due to the magnetic field. This requires a point of reference to ensure that the measured values are correctly determined. We use the first round of the on-peak $\psi(3770)$ sample for this comparison, as its center-of-mass energy has been measured very precisely using an independent technique involving $D\bar{D}$ events [45]. The results of this method compared to our own are shown in Figure 5.2. It is evident the procedure using $D\bar{D}$ events provides more stability over the run range than using dimuon events.

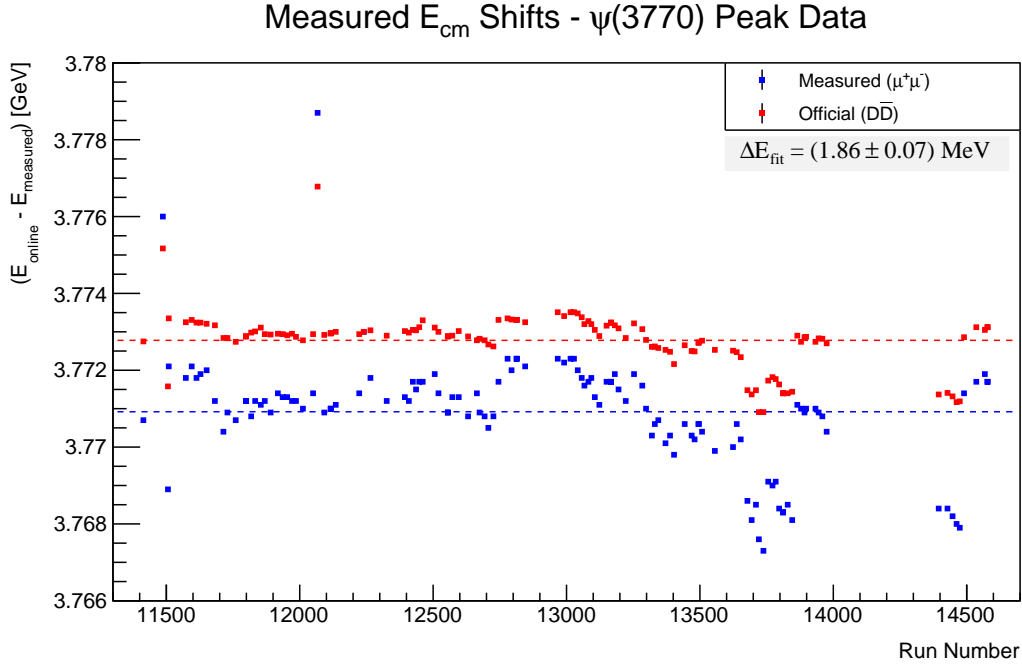


Figure 5.2: The values measured for on-peak data center-of-mass energies. The difference between our measured values (blue) and the $D\bar{D}$ -based measurement values (red) is used to shift the results of the measured scan data energy values.

To correct our measurements for the scan data, we use the difference in average values between the two methods, $\Delta E_{D\bar{D}} - \Delta E_{\mu^+\mu^-} \approx 1.86$ MeV (see Figure 5.1). Adding this difference to each scan data measurements, we obtain the center-of-mass values used in this analysis. Comparing this to the initial scan data center-of-mass energies, which were higher than the measured values by 1.29 MeV (see Figure 5.2), we find the initial values of the scan data were notably low (1.86 MeV – 1.29 MeV ≈ 0.7 MeV). In regions where the cross section rapidly changes, this can have a dramatic effect on determining the functional shape. Namely, this would correspond to a measured mass for the $\psi(3770)$ which is off by 0.7 MeV. The final center-of-mass energies of the scan data, along with the luminosity of each bin, are shown in Table 5.3.

5.3.3 Luminosity Measurement

To precisely determine the values of integrated luminosity for each bin, radiative Bhabha events ($e^+e^- \rightarrow e^+e^-(\gamma)$) were analyzed following the procedure of Ref. [46]. For each run, 1.4×10^6 simulated events were generated using Babayaga 3.5 to characterize the detector response. We select events with only two (oppositely) charged tracks, satisfying the criteria shown in Table 5.2.

Vertex (xy)	$V_{xy} < 1 \text{ cm}$
Vertex (z)	$ Vz < 10 \text{ cm}$
MDC Angle	$ \cos \theta < 0.80$
Exclude $e^+e^- \rightarrow \mu^+\mu^-(\gamma)$ Events	$E_{\text{EMC}} > 0.73 \times E_{\text{beam}}$
Exclude $e^+e^- \rightarrow \gamma J/\psi, J/\psi \rightarrow e^+e^-$ Events	$p > 0.93 \times E_{\text{beam}}$

Table 5.2: Selection cuts on electron tracks used to determine the luminosity.

Applying these cuts to both data and MC identically, we use the resulting number of events found in the MC divided by the number of total generated events to determine the efficiency (ϵ_{MC}). From this, and using the cross section provided by the generator (σ_{Bhabha}), we can determine the integrated luminosity (\mathcal{L}) of each run from the number of events passing the same cuts in data (N_{data}):

$$\mathcal{L} = \frac{N_{\text{data}}}{\sigma_{\text{Bhabha}} \epsilon_{MC}} \quad (5.18)$$

The integrated luminosity for each bin is shown in Table 5.3. The total luminosity for the scan data used is $(69.80 \pm 0.03 \pm 0.70) \text{ pb}^{-1}$, where the errors are statistical and systematic, respectively. Effects from the systematic error are examined in Section 5.7.

Bin	Run Range	E_{cm} Range [GeV]	\mathcal{L} [pb $^{-1}$]
0	14041 - 14046	3.734 - 3.736	0.8293(30)
1	14360 - 14360	3.736 - 3.744	0.3287(19)
2	14047 - 14048	3.744 - 3.748	0.9524(32)
3	14049 - 14053	3.748 - 3.750	1.4055(39)
4	14057 - 14067	3.750 - 3.751	2.2717(50)
5	14068 - 14077	3.751 - 3.753	2.9702(57)
6	14078 - 14086	3.753 - 3.755	3.3080(60)
7	14087 - 14101	3.755 - 3.756	3.4162(61)
8	14103 - 14109	3.756 - 3.759	3.8712(65)
9	14110 - 14123	3.759 - 3.762	4.4382(70)
10	14129 - 14144	3.762 - 3.765	4.4896(70)
11	14145 - 14154	3.765 - 3.767	3.2828(60)
12	14155 - 14160	3.767 - 3.771	2.4418(52)
13	14161 - 14164	3.771 - 3.774	2.0151(47)
14	14165 - 14168	3.774 - 3.777	1.8261(45)
15	14169 - 14174	3.777 - 3.780	1.8237(45)
16	14200 - 14203	3.780 - 3.782	1.9505(46)
17	14209 - 14217	3.782 - 3.787	2.1500(49)
18	14221 - 14226	3.787 - 3.789	2.5488(53)
19	14230 - 14238	3.789 - 3.792	2.8320(56)
20	14239 - 14246	3.792 - 3.797	3.5310(63)
21	14247 - 14258	3.797 - 3.800	4.0479(67)
22	14259 - 14268	3.800 - 3.802	3.9284(66)
23	14269 - 14274	3.802 - 3.807	2.6929(55)
24	14275 - 14279	3.807 - 3.809	1.7604(44)
25	14280 - 14290	3.809 - 3.813	1.2539(38)
26	14291 - 14292	3.813 - 3.815	0.8969(32)
27	14293 - 14294	3.815 - 3.823	0.6803(28)
28	14295 - 14296	3.823 - 3.832	0.3997(21)
29	14297 - 14297	3.832 - 3.839	0.2846(18)
30	14298 - 14298	3.839 - 3.849	0.2802(18)
31	14299 - 14299	3.849 - 3.855	0.2764(18)
32	14300 - 14301	3.855 - 3.863	0.3188(19)
33	14302 - 14303	3.863 - 3.870	0.3002(19)

Table 5.3: Measured integrated luminosities for each energy bin.
The uncertainties listed are statistical errors from the data selection, as uncertainties from the MC statistics are negligible.

5.3.4 Monte Carlo Generation

To analyze the detection efficiencies and background levels of the detector, several MC samples were produced. For the signal determination, samples of generic $D^0\overline{D}^0$ and D^+D^- from $\psi(3770)$ were generated with 2×10^5 events per center-of-mass energy bin. In addition, $100\times$ data-size samples were produced for $q\bar{q}$, $\tau^+\tau^-$, radiative return to J/ψ (denoted $\gamma J/\psi$), and radiative return to $\psi(2S)$ (denoted $\gamma\psi'$). Each of these samples was generated at the University of Minnesota in July of 2014 using BOSS version 6.6.4.p02. The $D^0\overline{D}^0$, D^+D^- , $q\bar{q}$, and $\tau^+\tau^-$ states were generated using KKMC, while the $\gamma J/\psi$ and $\gamma\psi'$ were generated with BesEvtGen. All except $q\bar{q}$ were then decayed with BesEvtGen. The total numbers of events in each sample is shown in Table 5.4.

Sample	Number of Events
$\psi(3770) \rightarrow D^0\overline{D}^0$	6.800×10^6
$\psi(3770) \rightarrow D^+D^-$	6.400×10^6
$q\bar{q}$	8.916×10^7
$\gamma J/\psi$	7.307×10^6
$\gamma\psi'$	2.457×10^7
$\tau^+\tau^-$	2.164×10^7

Table 5.4: Number of events contained in each generated sample.

In general, all MC samples were generated based on decay tables developed and maintained within BESIII based on world-average branching fraction measurements. The $D\overline{D}$ samples were generated by implementing the Born level shape measured in this analysis into KKMC. This procedure was iterated five times to provide a data-driven basis for the ISR corrections. The effects of this process are examined in Section 5.7.

5.4 Signal Determination

We measure the yields of both $D^0\overline{D}^0$ and D^+D^- events with two-dimensional fits to ΔE and m_{BC} , as defined in 4.3.2. MC samples are partitioned into the following four groups: proper D -tags ($N_{D\bar{D}}$), misreconstructed D -tags (N_{misrec}), continuum ($N_{q\bar{q}}$), and other (N_{other}). The first two groups are obtained using truth information from the $D\bar{D}$ samples, while the last group is a combination of the $\tau^+\tau^-$, $\gamma J/\psi$, and $\gamma\psi'$ samples. These groups are fitted to data using the RooFit [47] package to perform a negative log-likelihood minimization for each energy bin (E_i) separately for both D^0 and D^+ . For each fit, the four MC sample groups are used to construct 2D (ΔE vs. m_{BC}) PDF functions that are used to fit the corresponding data histograms. The proper $D\bar{D}$ shape is treated as signal, and its integral after fitting (N_D) is used for determining the signal yields and cross sections. An example fit is shown in Figure 5.3, while the complete set of these plots can be found in Appendices B and C.

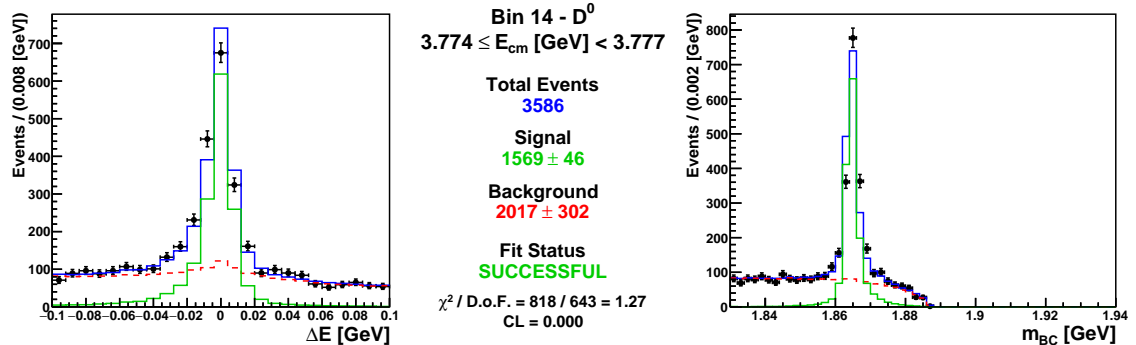


Figure 5.3: Projections of the 2D (ΔE vs. m_{BC}) signal fit.

This covers D^0 events in the region $3.774 \text{ GeV} \leq E_{\text{cm}} < 3.777 \text{ GeV}$. The data points (black) are fitted by the total MC shape (blue), which is the sum of the signal (green) and background (red) components.

The m_{BC} signal component is formed from two sources: events which are produced by Born level direct production (which peak at m_D) and events which are affected by ISR (which peak at E_{beam}). For most of the lower energy points, these values are similar, and the peaks are generally indistinguishable. However, starting around 3.8 GeV, the splitting becomes more visible (see Figures B.21 to B.23). This trend continues for the higher energy points, though it is somewhat difficult to distinguish given the statistics

of the scan data. Regardless, this effect provides further constraints on potential fit shapes (see Section 5.6).

5.5 Efficiency Correction

In addition to the parameters gathered during reconstruction, truth information was taken from the generic $D\bar{D}$ samples to determine the mode-by-mode reconstruction efficiencies. To be deemed proper, a reconstruction must pass not only the standard D -tag cuts, but also match the generator information for the event. This process removes backgrounds contributed by modes with similar constituents that tend to peak in the signal region. The total number of proper D -tag reconstructions is then divided by the number of D particles generated for each mode, and the mode-by-mode efficiencies are weighted by the world-average (PDG) branching ratios [6] to determine the overall efficiency (ϵ_D) for each of D^0 and D^+ :

$$\epsilon_D = \sum_i \epsilon_{i \text{ rec}} \mathcal{B}_i = \sum_i \left(\frac{N_{i \text{ prop}}}{N_{i \text{ gen}}} \right) \mathcal{B}_i. \quad (5.19)$$

Each D^0 efficiency also includes the corresponding DCSD terms for its decay (see Section 4.3).

The efficiencies for D^+ and D^0 calculated for the total sample are shown for each mode in Table 5.5 and Figure 5.4. However, for the determination of the cross section, this procedure was applied separately for each energy bin. The numbers of proper and generated particles are shown in Table 5.6 for D^0 and Tables 5.7 and 5.8 for D^+ while the total efficiencies for both D^0 and D^+ are shown in Table 5.9.

Decay Mode (i)	PDG \mathcal{B}_i [%]	MC Efficiency ϵ_i
$D^0 \rightarrow K^- \pi^+$	3.89 ± 0.05	0.7002 ± 0.0011
$D^0 \rightarrow K^- \pi^+ \pi^0$	13.93 ± 0.50	0.3794 ± 0.0004
$D^0 \rightarrow K^- \pi^+ \pi^+ \pi^-$	8.11 ± 0.21	0.3988 ± 0.0006
$\epsilon_{D^0} = (11.245 \pm 0.020)\%$		
$D^+ \rightarrow K^- \pi^+ \pi^+$	9.13 ± 0.19	0.5471 ± 0.0007
$D^+ \rightarrow K^- \pi^+ \pi^+ \pi^0$	5.99 ± 0.18	0.2739 ± 0.0006
$D^+ \rightarrow K_S^0 \pi^+$	1.47 ± 0.07	0.3883 ± 0.0014
$D^+ \rightarrow K_S^0 \pi^+ \pi^0$	6.99 ± 0.27	0.2079 ± 0.0005
$D^+ \rightarrow K_S^0 \pi^+ \pi^+ \pi^-$	3.12 ± 0.11	0.2237 ± 0.0007
$D^+ \rightarrow K^+ K^- \pi^+$	0.95 ± 0.03	0.4317 ± 0.0018
$\epsilon_{D^+} = (9.770 \pm 0.063)\%$		

Table 5.5: Mode-by-mode reconstruction efficiencies for D^0 and D^+ .

The values shown are over the entire data sample, while calculations for the cross sections use the values for each energy point individually (see Table 5.9). The errors listed for the PDG branching fractions are shown for reference, and are not included in the efficiency errors (see Section 5.7.1).

Monte Carlo Efficiency per Mode

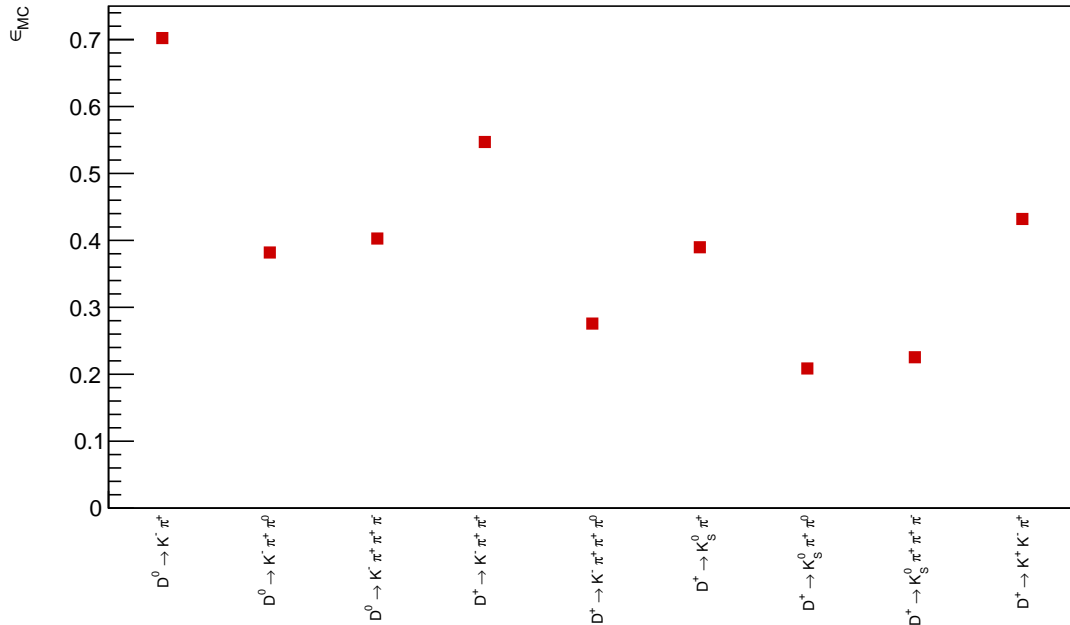


Figure 5.4: Mode-by-mode efficiencies for D^0 and D^+ determined with signal MC.
The error bars are negligible on the scale shown.

Bin	$D^0 \rightarrow K^- \pi^+$			$D^0 \rightarrow K^- \pi^+ \pi^0$			$D^0 \rightarrow K^- \pi^+ \pi^+ \pi^-$		
	N_{prop}	N_{gen}	ϵ_{rec}	N_{prop}	N_{gen}	ϵ_{rec}	N_{prop}	N_{gen}	ϵ_{rec}
0	11197	15757	0.711	21600	55815	0.387	13592	33714	0.403
1	11266	15713	0.717	21735	56189	0.387	13651	33621	0.406
2	11065	15557	0.711	21683	55791	0.389	13984	33431	0.418
3	10748	15501	0.693	21114	55767	0.379	13168	33505	0.393
4	11176	15779	0.708	21922	55873	0.392	13613	33410	0.407
5	10984	15722	0.699	21366	56027	0.381	13483	33748	0.400
6	10837	15507	0.699	21144	55551	0.381	13738	33639	0.408
7	10707	15645	0.684	20889	56193	0.372	13074	33494	0.390
8	11031	15585	0.708	21788	55891	0.390	13967	33826	0.413
9	10994	15485	0.710	21978	56012	0.392	14020	33601	0.417
10	10952	15497	0.707	21400	56126	0.381	13727	33591	0.409
11	11025	15535	0.710	21700	55919	0.388	13980	33706	0.415
12	10909	15593	0.700	21713	55876	0.389	13787	33335	0.414
13	11088	15826	0.701	21696	55758	0.389	14013	33805	0.415
14	10975	15620	0.703	21576	55591	0.388	14039	33581	0.418
15	10965	15672	0.700	21501	55647	0.386	13777	33644	0.409
16	10803	15438	0.700	21505	55667	0.386	13832	33822	0.409
17	10913	15473	0.705	21574	56023	0.385	14163	34131	0.415
18	11156	15856	0.704	21461	55706	0.385	13725	33321	0.412
19	11124	15728	0.707	21775	56192	0.388	13930	33935	0.410
20	10837	15530	0.698	21149	55737	0.379	13883	33703	0.412
21	10756	15397	0.699	21212	55815	0.380	13577	33907	0.400
22	10986	15582	0.705	21178	56343	0.376	13352	33773	0.395
23	11147	15861	0.703	21088	56167	0.375	13200	33680	0.392
24	10785	15633	0.690	20763	55952	0.371	12651	33660	0.376
25	10972	15490	0.708	20687	55957	0.370	12841	33512	0.383
26	11016	15645	0.704	20707	55785	0.371	12563	33615	0.374
27	10800	15420	0.700	20244	55748	0.363	12362	33359	0.371
28	10939	15694	0.697	20077	55550	0.361	12507	33497	0.373
29	10839	15689	0.691	20685	56386	0.367	12575	33551	0.375
30	10798	15766	0.685	20238	55433	0.365	12526	33885	0.370
31	10568	15438	0.685	20533	55825	0.368	12901	33745	0.382
32	10820	15679	0.690	20706	55823	0.371	13155	33810	0.389
33	10643	15736	0.676	20488	55672	0.368	12875	33547	0.384

Table 5.6: Numbers of proper and generated particles for D^0 . The mode-by-mode numbers of particles used in the efficiency calculations for $D^0 \rightarrow K^- \pi^+$, $D^0 \rightarrow K^- \pi^+ \pi^0$, and $D^0 \rightarrow K^- \pi^+ \pi^+ \pi^-$.

Bin	$D^+ \rightarrow K^- \pi^+ \pi^+$			$D^+ \rightarrow K^- \pi^+ \pi^+ \pi^0$			$D^+ \rightarrow K_S^0 \pi^+$		
	N_{prop}	N_{gen}	ϵ_{rec}	N_{prop}	N_{gen}	ϵ_{rec}	N_{prop}	N_{gen}	ϵ_{rec}
2	20643	37609	0.549	6853	24250	0.283	2302	5900	0.390
3	19935	37582	0.530	6569	24235	0.271	2335	6114	0.382
4	20859	37915	0.550	6653	24216	0.275	2291	5879	0.390
5	20193	37647	0.536	6611	24051	0.275	2292	5965	0.384
6	20484	37814	0.542	6616	24184	0.274	2292	5924	0.387
7	19635	37462	0.524	6411	24708	0.259	2127	5815	0.366
8	20876	37758	0.553	6867	24343	0.282	2328	5841	0.399
9	20873	37739	0.553	6754	24284	0.278	2377	5911	0.402
10	20571	37487	0.549	6604	24249	0.272	2360	6010	0.393
11	20669	37468	0.552	6818	24268	0.281	2296	5904	0.389
12	20843	37838	0.551	6783	24247	0.280	2401	6074	0.395
13	20486	37286	0.549	6942	24582	0.282	2335	6184	0.378
14	20935	37961	0.551	6836	24467	0.279	2282	5963	0.383
15	20543	37458	0.548	6769	24135	0.280	2295	5889	0.390
16	20713	37543	0.552	6758	24376	0.277	2356	5921	0.398
17	21016	37757	0.557	6949	24470	0.284	2302	5903	0.390
18	21123	38024	0.556	6635	24111	0.275	2320	5889	0.394
19	20708	37357	0.554	6662	24240	0.275	2204	5855	0.376
20	20760	37761	0.550	6768	24395	0.277	2263	5883	0.385
21	20860	37893	0.550	6668	24216	0.275	2296	5996	0.383
22	20827	37820	0.551	6673	24421	0.273	2353	5997	0.392
23	20796	37554	0.554	6723	24377	0.276	2290	5957	0.384
24	20058	37410	0.536	6415	24310	0.264	2341	5966	0.392
25	20677	37552	0.551	6462	24245	0.267	2364	5987	0.395
26	20300	37491	0.541	6539	24405	0.268	2356	5993	0.393
27	20754	37704	0.550	6530	24295	0.269	2288	5969	0.383
28	20213	37428	0.540	6362	24146	0.263	2341	5988	0.391
29	20565	37545	0.548	6495	24257	0.268	2262	5916	0.382
30	20313	37773	0.538	6535	24167	0.270	2323	6075	0.382
31	20322	37280	0.545	6566	24389	0.269	2378	5927	0.401
32	20883	37992	0.550	6594	24249	0.272	2306	5855	0.394
33	20645	37738	0.547	6560	24195	0.271	2269	5945	0.382

Table 5.7: Numbers of proper and generated particles for D^+ (part 1). The mode-by-mode numbers of particles used in the efficiency calculations for $D^+ \rightarrow K^- \pi^+ \pi^+$, $D^+ \rightarrow K^- \pi^+ \pi^+ \pi^0$, and $D^+ \rightarrow K_S^0 \pi^+$.

Bin	$D^+ \rightarrow K_S^0 \pi^+ \pi^0$			$D^+ \rightarrow K_S^0 \pi^+ \pi^+ \pi^-$			$D^+ \rightarrow K^+ K^- \pi^+$		
	N_{prop}	N_{gen}	ϵ_{rec}	N_{prop}	N_{gen}	ϵ_{rec}	N_{prop}	N_{gen}	ϵ_{rec}
2	5742	27235	0.211	3562	15019	0.237	1720	4019	0.428
3	5668	27699	0.205	3169	14877	0.213	1637	3970	0.412
4	5710	27527	0.207	3358	14750	0.228	1791	4016	0.446
5	5614	27654	0.203	3282	14696	0.223	1748	3981	0.439
6	5656	27475	0.206	3392	14823	0.229	1771	4075	0.435
7	5481	27597	0.199	3293	14860	0.222	1593	3951	0.403
8	5827	27975	0.208	3462	15035	0.230	1736	4042	0.429
9	6003	27589	0.218	3427	14906	0.230	1716	3940	0.436
10	5722	27751	0.206	3327	14854	0.224	1690	3941	0.429
11	5888	27649	0.213	3385	14837	0.228	1672	3930	0.425
12	5731	27651	0.207	3370	14926	0.226	1718	3889	0.442
13	5792	27618	0.210	3336	14669	0.227	1696	3958	0.428
14	5745	27608	0.208	3288	14702	0.224	1712	3904	0.439
15	5832	27480	0.212	3384	14808	0.229	1649	3855	0.428
16	5891	27758	0.212	3443	14845	0.232	1783	3947	0.452
17	5954	27639	0.215	3484	14910	0.234	1804	3941	0.458
18	5875	27669	0.212	3366	14913	0.226	1700	3968	0.428
19	5773	27838	0.207	3371	14782	0.228	1766	4037	0.437
20	6024	28019	0.215	3367	14801	0.227	1709	3903	0.438
21	5804	27645	0.210	3306	14819	0.223	1688	3863	0.437
22	5893	27692	0.213	3304	14949	0.221	1741	3975	0.438
23	5780	27865	0.207	3313	14981	0.221	1670	3891	0.429
24	5623	27811	0.202	3161	14867	0.213	1667	3954	0.422
25	5684	27490	0.207	3250	14794	0.220	1711	3966	0.431
26	5704	27829	0.205	3137	14811	0.212	1641	3958	0.415
27	5630	27497	0.205	3132	14881	0.210	1678	3972	0.422
28	5724	28006	0.204	3271	14828	0.221	1690	3931	0.430
29	5693	27554	0.207	3272	15009	0.218	1772	3994	0.444
30	5574	27717	0.201	3308	14730	0.225	1673	4026	0.416
31	5556	27556	0.202	3288	15049	0.218	1746	3965	0.440
32	5785	27634	0.209	3259	14840	0.220	1680	3923	0.428
33	5653	27528	0.205	3287	14959	0.220	1734	4031	0.430

Table 5.8: Numbers of proper and generated particles for D^+ (part 2). The mode-by-mode numbers of particles used in the efficiency calculations for $D^+ \rightarrow K_S^0 \pi^+ \pi^0$, $D^+ \rightarrow K_S^0 \pi^+ \pi^+ \pi^-$, and $D^+ \rightarrow K^+ K^- \pi^+$.

E_{bin}	ϵ_{D^0}	ϵ_{D^+}
0	0.1146 ± 0.0005	-
1	0.1151 ± 0.0005	-
2	0.1161 ± 0.0005	0.0990 ± 0.0005
3	0.1119 ± 0.0005	0.0952 ± 0.0005
4	0.1156 ± 0.0005	0.0983 ± 0.0005
5	0.1131 ± 0.0005	0.0964 ± 0.0005
6	0.1137 ± 0.0005	0.0972 ± 0.0005
7	0.1104 ± 0.0005	0.0934 ± 0.0005
8	0.1157 ± 0.0005	0.0991 ± 0.0005
9	0.1165 ± 0.0005	0.0996 ± 0.0005
10	0.1141 ± 0.0005	0.0977 ± 0.0005
11	0.1157 ± 0.0005	0.0990 ± 0.0005
12	0.1152 ± 0.0005	0.0986 ± 0.0005
13	0.1154 ± 0.0005	0.0985 ± 0.0005
14	0.1157 ± 0.0005	0.0984 ± 0.0005
15	0.1146 ± 0.0005	0.0986 ± 0.0005
16	0.1146 ± 0.0005	0.0992 ± 0.0005
17	0.1151 ± 0.0005	0.1003 ± 0.0005
18	0.1148 ± 0.0005	0.0990 ± 0.0005
19	0.1151 ± 0.0005	0.0984 ± 0.0005
20	0.1138 ± 0.0005	0.0988 ± 0.0005
21	0.1129 ± 0.0005	0.0982 ± 0.0005
22	0.1122 ± 0.0005	0.0984 ± 0.0005
23	0.1118 ± 0.0005	0.0982 ± 0.0005
24	0.1094 ± 0.0005	0.0953 ± 0.0005
25	0.1105 ± 0.0005	0.0975 ± 0.0005
26	0.1098 ± 0.0005	0.0962 ± 0.0005
27	0.1082 ± 0.0005	0.0969 ± 0.0005
28	0.1081 ± 0.0005	0.0961 ± 0.0005
29	0.1087 ± 0.0005	0.0971 ± 0.0005
30	0.1078 ± 0.0005	0.0959 ± 0.0005
31	0.1092 ± 0.0005	0.0969 ± 0.0005
32	0.1104 ± 0.0005	0.0978 ± 0.0005
33	0.1090 ± 0.0005	0.0971 ± 0.0005

Table 5.9: The overall reconstruction efficiency of D^0 and D^+ for each energy bin. These values are used to calculate the corresponding cross sections at each energy point. The listed errors are statistical only.

5.5.1 CP Violation Correction

Due to CP violation in the $D^0\overline{D}^0$ system, each of the neutral decay modes must be corrected to account for quantum correlations arising from production through a $J^{PC} = 1^{--}$ state. This is done by applying scaling factors to the efficiency for each of the three modes used in reconstruction. The corrections are parameterized for each mode (m) by the following form [48]:

$$\alpha_{D^0 \rightarrow m} = 1 + r_m^2 + 2 \times y \times r_m \times R_m \times \cos(\delta_m). \quad (5.20)$$

Here, r_m and δ_m represent the relative magnitudes and phases between the Cabibbo-favored and doubly-Cabibbo-suppressed modes, respectively, while the factor of R_m represents a coherence factor characterizing the variation of δ_m over phase space. Note, there is no such variation for a two-body decay (like $D^0 \rightarrow K^- \pi^+$), so $R_{D^0 \rightarrow K^- \pi^+} = 1$. The value of y represents the difference in total width components of the $D^0\overline{D}^0$ system, $y = (\Gamma_2 - \Gamma_1)/(\Gamma_2 + \Gamma_1)$, where 1 and 2 represent the CP-odd and CP-even states, respectively.

The mode-dependent values for these factors are listed in Table 5.10. These are taken from the *CPV*-allowed values in [49] for $D^0 \rightarrow K^- \pi^+$, and from [50] for $D^0 \rightarrow K^- \pi^+ \pi^0$ and $D^0 \rightarrow K^- \pi^+ \pi^+ \pi^-$. The value $y = 0.0066^{+0.0007}_{-0.0010}$ is also from [49], and is the same for all modes. After applying each of the mode-dependent corrections, the efficiency for the full sample changes from $\epsilon_{D^0} = (11.320 \pm 0.213)\%$ to $\epsilon_{D^0} = (11.352 \pm 0.213)\%$, and similarly for the efficiencies of each E_{cm} bin.

Mode	r_m	R_m	$\delta_m [\circ]$	α_m
$D^0 \rightarrow K^- \pi^+$	0.0591 ± 0.0063	1	$11.8^{+9.5}_{-14.7}$	1.00426 ± 0.00083
$D^0 \rightarrow K^- \pi^+ \pi^0$	0.0447 ± 0.0012	0.81 ± 0.06	18^{+14}_{-15}	1.00248 ± 0.00014
$D^0 \rightarrow K^- \pi^+ \pi^+ \pi^-$	0.0549 ± 0.0006	$0.43^{+0.17}_{-0.13}$	-52^{+28}_{-17}	$1.00270^{+0.00014}_{-0.00012}$

Table 5.10: The quantum correlated factors for the D^0 modes.

5.6 Fitting Procedure

After applying the correction in Section 5.5.1, the efficiency values (Table 5.9) were combined with the luminosity (Table 5.3) and the signal values from each 2D fit (Table 5.11) to determine the cross section at each energy point. Since each $\psi(3770)$ produces a $D\bar{D}$ pair, a factor of 2 is included in the denominator to correct for double counting:

$$\sigma_{D\bar{D}}^{RC}(E_i) = \frac{N_D(E_i)}{2\epsilon_D(E_i)\mathcal{L}(E_i)}. \quad (5.21)$$

The resulting cross sections for D^0 and D^+ are shown in Figure 5.5 and Table 5.11.

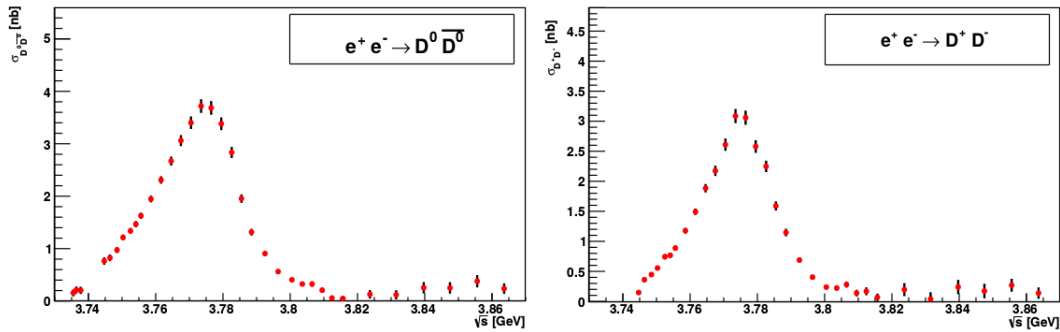


Figure 5.5: The measured $e^+e^- \rightarrow D\bar{D}$ cross sections.

The $D^0\bar{D}^0$ cross section is shown on the left and $D^+\bar{D}^-$ is shown on the right.

These cross sections are fit to Equation (5.7) using each form factor choice described in Section 5.2. There are four common fit parameters, $M^{\psi(3770)}$, $\Gamma^{\psi(3770)}$, $\Gamma_{ee}^{\psi(3770)}$, and $\phi^{\psi(3770)}$, representing the mass, total width, electron partial width, and relative phase to the non-resonant contribution for the $\psi(3770)$, respectively. The total width corresponds to $\Gamma(M)$ in Section 5.1. Two additional parameters are form factor dependent: F_{NR} and a_{NR} for the exponential, or $\Gamma^{\psi(2S)}$ and F_0 for the VDM. For the former, these represent the amplitude and exponent normalization for the non-resonant contribution. For the latter, these represent the modified total width for the $\psi(2S)$ above resonance (see Section 5.2) and the constant contribution of resonances above the $\psi(3770)$. The fitting is done simultaneously for D^0 and D^+ with identical parameters using TMinuit [51]. The minimized χ^2 is the total contribution from both D^0 and D^+ . Results for the Exponential and VDM form factors are shown in Figures 5.6 and 5.7, respectively.

E_{mid}	$N_{D^0\overline{D}^0}$	$\sigma_{D^0\overline{D}^0}^{RC}$ [nb]	$N_{D^+D^-}$	$\sigma_{D^+D^-}^{RC}$ [nb]
3.7342	32 ± 9	0.169 ± 0.046	-	-
3.7368	16 ± 5	0.218 ± 0.068	-	-
3.7447	169 ± 16	0.765 ± 0.070	28 ± 7	0.150 ± 0.038
3.7483	264 ± 20	0.838 ± 0.064	96 ± 13	0.360 ± 0.048
3.7501	509 ± 28	0.968 ± 0.053	196 ± 18	0.439 ± 0.040
3.7517	831 ± 34	1.237 ± 0.052	329 ± 23	0.574 ± 0.040
3.7534	1036 ± 38	1.377 ± 0.051	481 ± 27	0.748 ± 0.042
3.7556	1182 ± 41	1.566 ± 0.055	508 ± 28	0.797 ± 0.045
3.7562	1459 ± 45	1.629 ± 0.051	701 ± 32	0.914 ± 0.042
3.7592	2014 ± 52	1.948 ± 0.052	1054 ± 39	1.192 ± 0.045
3.7624	2444 ± 58	2.385 ± 0.058	1346 ± 44	1.534 ± 0.051
3.7650	2062 ± 53	2.715 ± 0.071	1223 ± 42	1.882 ± 0.066
3.7676	1746 ± 48	3.102 ± 0.087	1059 ± 39	2.200 ± 0.081
3.7713	1585 ± 46	3.406 ± 0.101	1045 ± 38	2.634 ± 0.098
3.7742	1569 ± 46	3.714 ± 0.111	1103 ± 40	3.067 ± 0.111
3.7775	1543 ± 46	3.692 ± 0.111	1108 ± 39	3.078 ± 0.111
3.7802	1539 ± 46	3.444 ± 0.104	1006 ± 38	2.599 ± 0.100
3.7829	1381 ± 44	2.791 ± 0.090	951 ± 38	2.206 ± 0.088
3.7869	1167 ± 42	1.995 ± 0.072	821 ± 36	1.627 ± 0.073
3.7891	888 ± 38	1.361 ± 0.058	656 ± 34	1.178 ± 0.062
3.7926	739 ± 36	0.920 ± 0.045	475 ± 32	0.680 ± 0.045
3.7970	514 ± 34	0.562 ± 0.037	329 ± 31	0.414 ± 0.039
3.8003	374 ± 31	0.424 ± 0.035	186 ± 28	0.241 ± 0.037
3.8024	196 ± 23	0.325 ± 0.038	125 ± 23	0.236 ± 0.043
3.8070	136 ± 19	0.352 ± 0.050	97 ± 17	0.289 ± 0.051
3.8093	65 ± 14	0.233 ± 0.050	32 ± 13	0.132 ± 0.055
3.8135	12 ± 10	0.060 ± 0.049	26 ± 11	0.153 ± 0.066
3.8153	8 ± 7	0.056 ± 0.051	12 ± 8	0.089 ± 0.063
3.8229	12 ± 7	0.140 ± 0.083	15 ± 8	0.197 ± 0.107
3.8320	4 ± 5	0.069 ± 0.086	3 ± 5	0.046 ± 0.099
3.8390	14 ± 6	0.237 ± 0.105	14 ± 7	0.254 ± 0.124
3.8494	11 ± 6	0.186 ± 0.104	10 ± 6	0.186 ± 0.118
3.8555	24 ± 8	0.337 ± 0.111	17 ± 6	0.273 ± 0.104
3.8632	22 ± 8	0.340 ± 0.127	6 ± 5	0.099 ± 0.091

Table 5.11: The measured $D\overline{D}$ cross sections at each E_{cm} point.

The numbers of data events ($N_{D^0\overline{D}^0}$ and $N_{D^+D^-}$) observed in each E_{cm} bin are also shown. The uncertainties on the cross sections are statistical only and come from the signal fitting (N_D), PDG values (Table 5.5), and MC reconstruction efficiencies (Table 5.9). The data event values are taken from the signal fits shown in Appendices B and C.

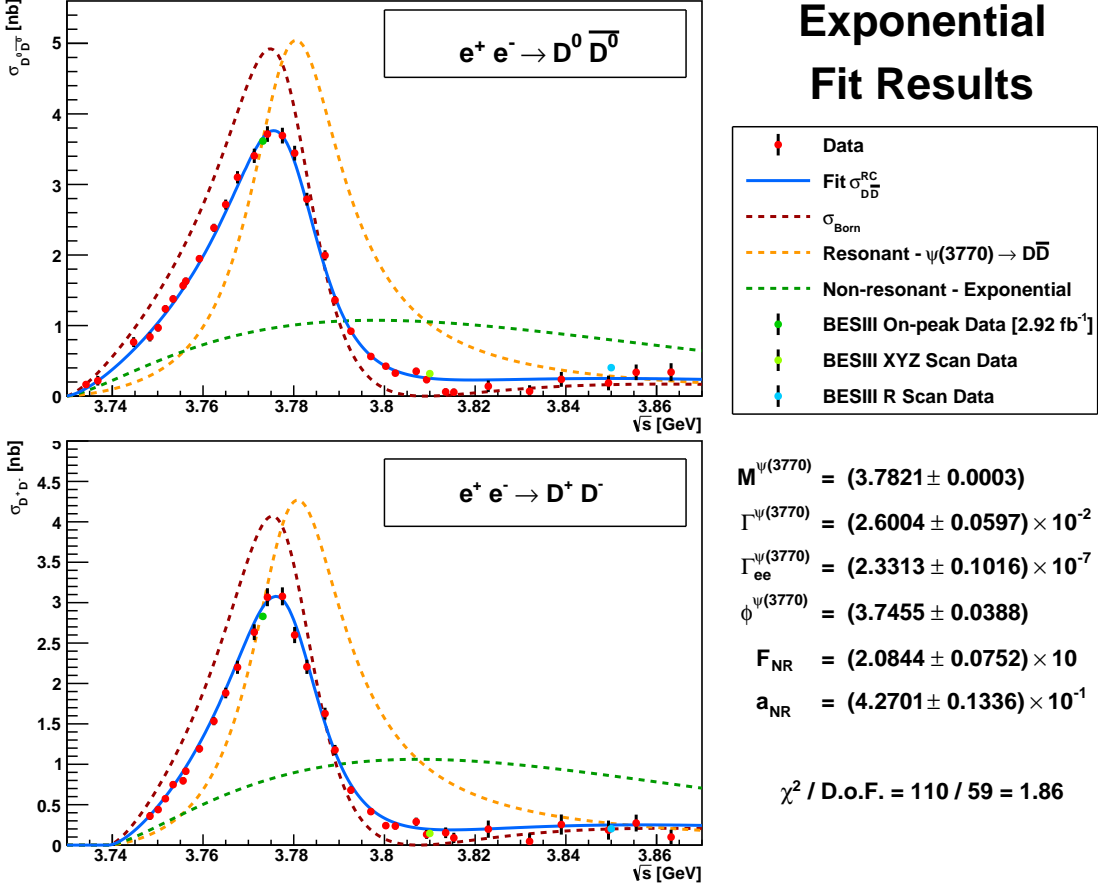


Figure 5.6: The fit results for the Exponential Model form factor. Both the D^0 (top) and the D^+ (bottom) use a fit shape (blue) calculated from Equation (5.1) using the non-resonant component from Equation (5.15).

Both form factor choices show generally good agreement with their theoretical formulation. While a value of $\chi^2 / \text{D.o.F.}$ (degrees of freedom) ≈ 2 is a bit higher than desired, much of this excess is due to a small set of points. Namely, the two points within 3.81 GeV to 3.82 GeV for the D^0 cross section are well below the predicted shape. This could indicate the model used in our analysis does not well cover this region, and more information is needed to better understand the shape. Still, the parameters for the $\psi(3770)$ are heavily dominated by the energy points in the peak region, and the overall consistency shown in this range provides confidence in the values obtained.

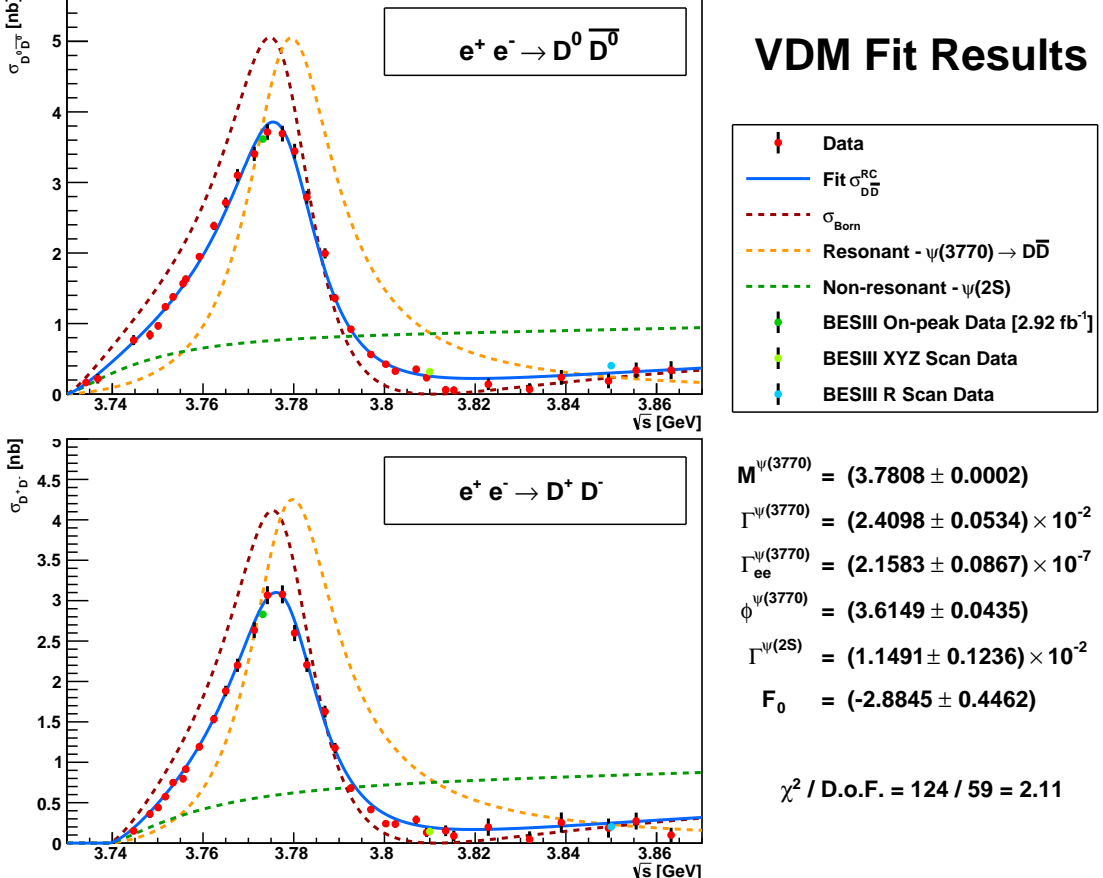


Figure 5.7: The fit results for the Vector Dominance Model form factor. Both the D^0 (top) and the D^+ (bottom) use a fit shape (blue) calculated from Equation (5.1) using the non-resonant component from Equation (5.16).

Another crucial aspect revealed by these fits is the behavior of the Born level cross section (shown in dark red on Figures 5.6 and 5.7). Namely, there is a minimum in the shape near 3.81 GeV which then increases for higher energies. This is also clearly seen from the behavior of the Born level peak in the m_{BC} distributions; these events vanish over this range (see Figures B.25 to B.28) then reappear above (see Figures B.29 to B.34). Such behavior is a strong indication for needing interference, as this shape would be impossible to model with only two non-interfering Breit-Wigner components.

5.6.1 Coulomb Correction

In the development of this analysis, it was discovered that the unmodified theoretical formulation in Section 5.1 did not lead to a successful fit of the $D\bar{D}$ cross sections, as shown in Figure 5.8. Namely, including the Coulomb effect pulls the $D^0\bar{D}^0$ and $D^+\bar{D}^-$ cross sections in opposite directions. We found the best fits were achieved by altering Equation (5.3) to set the Coulomb factor to 1. While this disagrees with conventional theoretical wisdom, it is consistent with studies of $\Upsilon(4S) \rightarrow B\bar{B}$ where applying a Coulomb correction for the charged final state also leads to inconsistency with data.

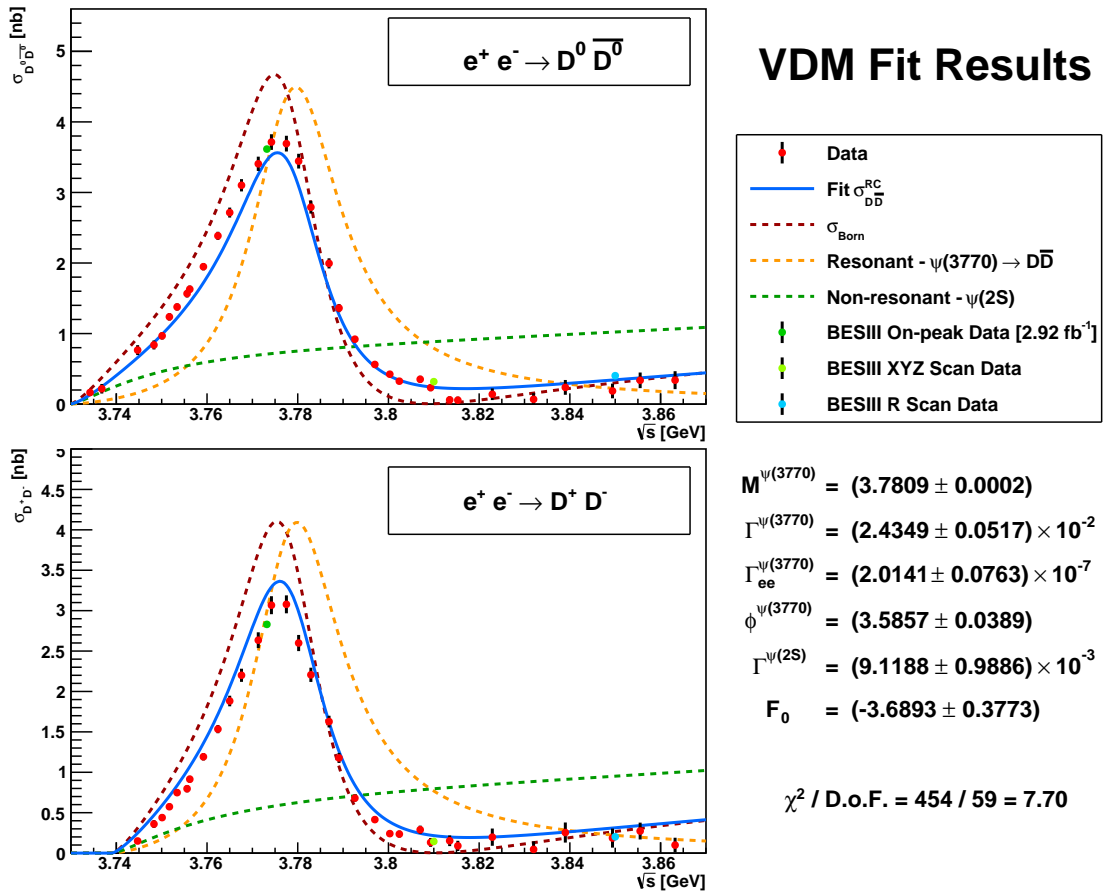


Figure 5.8: The Vector Dominance Model fit results with Coulomb interactions. Including this factor provides notably worse results than when excluding it (see Figure 5.7).

This is most clearly seen in the ratio of D^+D^- and $D^0\bar{D}^0$ cross sections, shown in Figure 5.9, where the ‘No Coulomb’ method sets $z_{D^+D^-}$ in Equations (5.7) and (5.11) to unity, the ‘Partial Coulomb’ sets this factor to unity only for Equation (5.7), and the ‘Full Coulomb’ is the default assumption. Agreement of the measured cross section ratio with the ‘No Coulomb’ calculation is substantially better. This is also true for the high statistics points measured at the $\psi(3770)$ peak by Derrick Toth [44] (light blue). As the data tend to follow the ‘No Coulomb’ method, we choose this as our nominal method for the results, presented in Section 5.8. However, the explanation for this behavior is still undetermined.

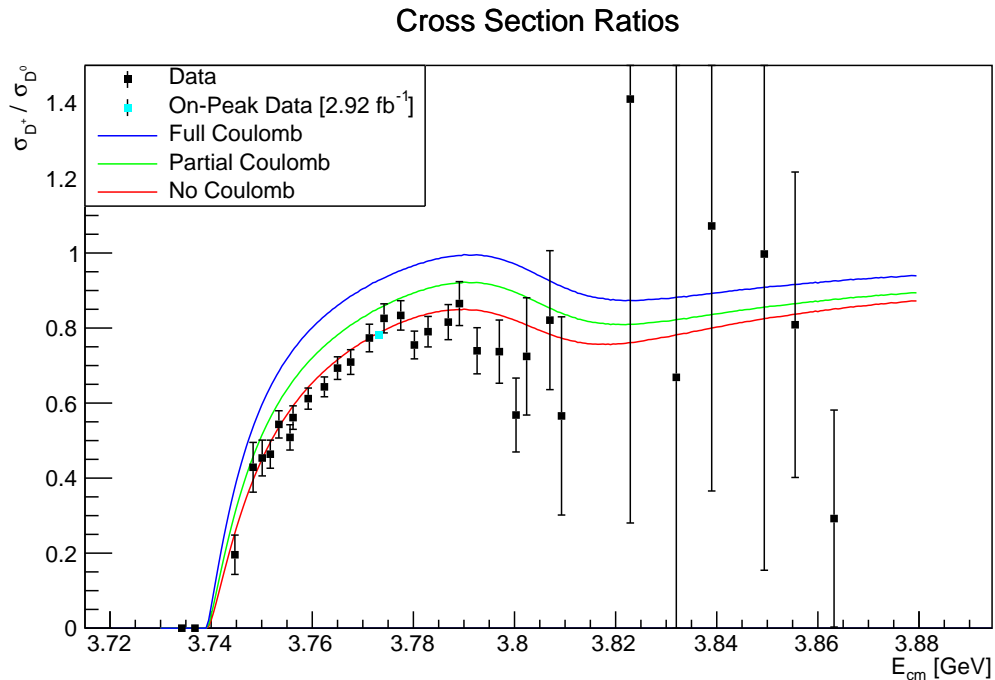


Figure 5.9: The ratio of measured D^+ to D^0 cross sections.

Several levels of Coulomb interactions are examined based on modifications to Equation (5.7) and Equation (5.17). ‘Partial Coulomb’ refers to setting the numerical value of $z_{D^+D^-} = 1$ in the former, while ‘No Coulomb’ refers to applying this change in both. ‘Full Coulomb’ refers to the original formulation described in Section 5.1, and shows substantial disagreement with the data.

5.7 Systematic Uncertainties

To assess the systematic uncertainties in our results, we look at a variety of factors. Many of these affect all BESIII analyses, such as luminosity and tracking. Others, like the modification to KKMC generation (see Section 5.3.4), are specific to this analysis. Additional analysis-specific systematics are typically due to less well-known parameters, like the radii used to describe the $\psi(2S)$ and $\psi(3770)$ (see Section 5.2). Each of these contributions, as well as their total, can be found in Table 5.15.

5.7.1 $\psi(3770)$ Parameter Systematic Uncertainties

Each systematic is obtained by changing a specific assumption, selection criteria, or another analysis feature and re-fitting to the altered cross section distribution using the VDM method. The uncertainties for each parameter are obtained by taking the difference between this result and the nominal fit (Figure 5.7). Generally, each change was done both positively and negatively, and the values used are the largest differences seen between the two changes. The systematics examined in this analysis are summarized below, where a * denotes potential sources that were found to be negligible.

Luminosity

A 1 % change [52] was applied to \mathcal{L} in Equation (5.21). As this is an overall scale change, the only variable significantly affected is $\Gamma_{ee}^{\psi(3770) \rightarrow D\bar{D}}$.

π^\pm/K^\pm Tracking

A 1.0 % efficiency change [53] was applied for each π^\pm or K^\pm in a given decay mode. The summed contribution for each mode is applied to ϵ_m in Equation (5.19). As this is an overall scale change, the only variable significantly affected is $\Gamma_{ee}^{\psi(3770) \rightarrow D\bar{D}}$.

π^0 Tracking

A 2.0 % efficiency change [54] was applied for each π^0 in a given decay mode. The summed contribution for each mode is applied to ϵ_m in Equation (5.19). As this is an overall scale change, the only variable significantly affected is $\Gamma_{ee}^{\psi(3770) \rightarrow D\bar{D}}$.

K_S^0 Tracking

A 1.5% efficiency change [55] was applied for each K_S^0 in a given decay mode. The summed contribution for each mode is applied to ϵ_m in Equation (5.19). As this is an overall scale change, the only variable significantly affected is $\Gamma_{ee}^{\psi(3770) \rightarrow D\bar{D}}$.

Single Tag Fitting

A mode-dependent change [44] was applied to N in Equation (5.21). Differences from fitting were obtained by Derrick Toth after examining the use of single-Gaussian convolved signal shapes as alternatives to the standard procedure, and are shown in Table 5.12. The changes applied were obtained from the sums of the mode-dependent values averaged over their efficiencies. As this is an overall scale change, the only variable significantly affected is $\Gamma_{ee}^{\psi(3770) \rightarrow D\bar{D}}$.

Tag Mode	Difference (%)	Tag Mode	Difference (%)
$D^0 \rightarrow K^- \pi^+$	0.27	$D^+ \rightarrow K^- \pi^+ \pi^+$	0.20
$D^0 \rightarrow K^- \pi^+ \pi^0$	0.10	$D^+ \rightarrow K^- \pi^+ \pi^+ \pi^0$	0.00
$D^0 \rightarrow K^- \pi^+ \pi^+ \pi^-$	0.47	$D^+ \rightarrow K_S^0 \pi^+$	0.17
		$D^+ \rightarrow K_S^0 \pi^+ \pi^0$	0.29
		$D^+ \rightarrow K_S^0 \pi^+ \pi^+ \pi^-$	0.17
		$D^+ \rightarrow K^+ K^- \pi^+$	0.74
D^0 Average: 0.25 %		D^+ Average: 0.20 %	

Table 5.12: Single-tag fitting differences by mode.
The total D^0 and D^+ values are averaged over the efficiencies for each mode.

PDG Branching Fractions

A mode-dependent change based on the PDG branching fractions (Table 5.5) was applied to ϵ_m in Equation (5.19). The branching fraction for each mode was changed by its error. As this is an overall scale change, the only variable significantly affected is $\Gamma_{ee}^{\psi(3770) \rightarrow D\bar{D}}$.

Meson Radii

The most uncertain parameters used in the analysis are the radii of the mesons $\psi(2S)$ and $\psi(3770)$, which enter through the cross section parametrization. We take the same values as used by KEDR, however, each of these is quoted to have an $\sim 25\%$ uncertainty. With this, we adjust the two radii values up or down by 25% over the four possible combinations (both up, both down, and each opposite). The maximum deviations from the nominal method seen across all four cases are used as the systematic uncertainties. Due to the high level of uncertainty on these parameters, this effect is one of the largest sources of systematic uncertainty in the analysis.

MC Iteration*

In generating MC for this analysis, the $D\bar{D}$ samples used a modified form of KKMC which generates events based on an input Born level shape for the $\psi(3770)$. However, as this shape is also the final output of the analysis, only an estimate is available for generation. To assess the variation from the input shape, we compared the output fit parameters to those used in the generation process. This process used the Exponential method, and the results are shown in Table 5.13. The numbers listed are from an earlier iteration of the MC than shown in Section 5.6, but the consistency seen is representative of all iterations. Very little difference is seen in the primary fit output parameters of the $\psi(3770)$. These similarities show the fit values converging, even after only a single iteration. From this, we treat variations due to MC iteration as negligible.

Parameter		KKMC Input	Fit Results	Difference
$M^{\psi(3770)}$	[GeV]	3.7815 ± 0.0003	3.7814 ± 0.0003	0.0001
$\Gamma^{\psi(3770)}$	[MeV]	24.887 ± 0.686	24.839 ± 0.681	0.048
$\Gamma_{ee}^{\psi(3770) \rightarrow D\bar{D}}$	[eV]	217.55 ± 11.18	214.65 ± 11.10	2.90
$\phi^{\psi(3770)}$		3.6374 ± 0.0513	3.6375 ± 0.0518	0.0001
F_{NR}		21.394 ± 1.866	20.147 ± 1.765	0.992
a_{NR}		-1.6202 ± 0.5271	-1.5265 ± 0.5119	0.0937

Table 5.13: Comparison of input and output fit parameters.

The MC generation is done using the Exponential form factor model as an input Born level shape to generate $D\bar{D}$ events using KKMC.

MC ISR Generation*

To compare to the generation process of KKMC, we also generated alternative MC samples of $D\bar{D}$ using the ConExc [56] ISR generator. This process used an input Born level shape identical to a previous iteration produced with KKMC. Each of the background samples used (such as $q\bar{q}$ and $\tau^+\tau^-$) were the same as in the nominal procedure. The cross section results using the VDM model are shown in Table 5.14, and provide $\psi(3770)$ fit parameters that are within the statistical errors of the nominal method. From this, we treat variations due to the MC ISR generator as negligible.

Parameter		ConExc Fit Results	KKMC Fit Results
$M^{\psi(3770)}$	[GeV]	3.7803 ± 0.0003	3.7804 ± 0.0003
$\Gamma^{\psi(3770)}$	[MeV]	23.784 ± 0.616	23.732 ± 0.612
$\Gamma_{ee}^{\psi(3770) \rightarrow D\bar{D}}$	[eV]	204.68 ± 10.28	207.35 ± 10.02
$\phi^{\psi(3770)}$		3.5954 ± 0.0559	3.5952 ± 0.0525
$\Gamma_{ee}^{\psi(2S)}$	[MeV]	12.229 ± 1.336	14.070 ± 1.431
F_0		-2.3415 ± 0.4898	-2.0768 ± 0.4924

Table 5.14: Comparison of output fit parameters between ISR generators.

The MC generation is done using both the ConExc and KKMC generators and the final VDM fit results are shown. The values shown are from an earlier iteration than the final results, but the output from each method remains very similar.

Intermediate Resonances*

In looking at the mode $D^+ \rightarrow K^- \pi^+ \pi^+$, we also analyzed the contribution of intermediate resonances to the $\pi^+ \pi^-$ system, like the ρ^0 . Using the 2.93 fb^{-1} data sample of $\psi(3770)$ events at $E_{\text{cm}} = 3.773 \text{ GeV}$, we split the signal region of this mode based on 1.0 GeV^2 cuts for each of the invariant masses of $K\pi$ and $\pi\pi$. These cuts were chosen to separate the sample into distinctly different regions, as can be seen in Figure 5.10. Fitting the signal distributions for each of these subsamples, we found no statistically significant deviations in the measured yields, and treat this contribution as negligible.

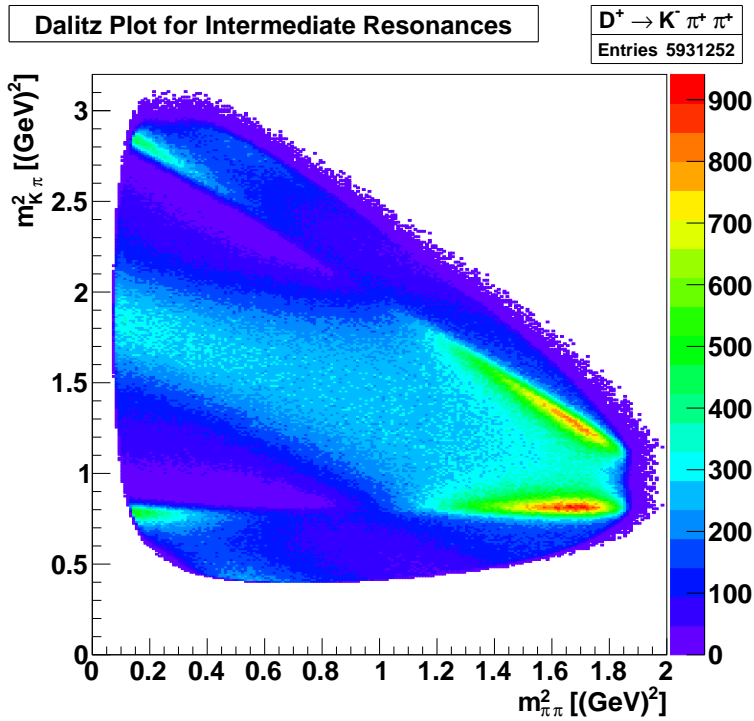


Figure 5.10: The $K\pi$ vs. $\pi\pi$ invariant masses for the mode $D^+ \rightarrow K^- \pi^+ \pi^+$. The on-peak $\psi(3770)$ data was used due to its significantly higher statistics.

Total Systematic Uncertainties

Each of the systematic uncertainty sources considered are assumed to be independent, meaning they are combined in quadrature for the total value. The results are shown in Table 5.15 along with a comparison to the statistical error. Because of the large uncertainty on the meson radii, our measurements are systematics limited, even given the relatively small data sample used.

Systematic	$M^{\psi(3770)}$ [%]	$\Gamma^{\psi(3770)}$ [%]	$\Gamma_{ee}^{\psi(3770) \rightarrow D\bar{D}}$ [%]	$\phi^{\psi(3770)}$ [%]
Luminosity	0.000	0.004	1.005	0.014
K^\pm/π^\pm Tracking	0.000	0.008	2.646	0.033
π^0 Tracking	0.000	0.012	0.746	0.028
K_S^0 Tracking	0.000	0.004	0.260	0.019
Single Tag Fits	0.000	0.012	0.213	0.008
PDG Errors	0.000	0.017	2.840	0.036
Meson Radii	0.016	2.411	3.512	1.477
Total [%]	0.016	2.411	5.389	1.479
Relative Stat. Error [σ]	3.000	1.088	1.342	1.229

Table 5.15: Systematic uncertainties relative to the measured parameters of the $\psi(3770)$.

Non-Resonant Form Factor

In addition to the systematics described above, there is a significant source of uncertainty coming from the non-resonant form factor used. Both models examined, Exponential and VDM, provided quality fit results for the cross section shapes. From this, we conservatively assign an uncertainty equal to the differences in fit parameters provided by these two methods, as shown in Table 5.16. Following the example of KEDR, we treat this as a model-dependent uncertainty separate from the other systematics.

Form Factor	$M^{\psi(3770)}$ [GeV]	$\Gamma^{\psi(3770)}$ [MeV]	$\Gamma_{ee}^{\psi(3770) \rightarrow D\bar{D}}$ [eV]	$\phi^{\psi(3770)}$ [°]
VDM	3.7821	26.004	233.13	214.60
VDM	3.7808	24.098	215.83	207.12
Difference	0.0013	1.906	17.30	7.48

Table 5.16: Parameter differences based on the choice of form factor. These are treated as model-dependent errors, not as part of the total systematics.

5.7.2 Cross Section Systematic Uncertainties

In addition to the statistical uncertainties provided in Table 5.11, we also provide systematic uncertainties on the cross section measurements. These are calculated from the systematic shifts (ΔS) which affect Equation (5.21): Luminosity, K^\pm/π^\pm Tracking, π^0 Tracking, K_S^0 Tracking, and Single Tag Fits. For the luminosity, this is the same as the $\pm 1\%$ shift used previously. The others are calculated by weighting the efficiency over decay modes:

$$\Delta S = \frac{\sum_m \epsilon_m \Delta S_m}{\sum_m \epsilon_m} \quad (5.22)$$

The value of ΔS_m for K^\pm/π^\pm Tracking is 1.0% per K^\pm or π^\pm , and is defined similarly for the other systematics using the previously listed values. The calculated shifts are listed in Table 5.17, and the resulting cross section values are listed in Table 5.18.

Systematic	$\Delta S (D^0) [\%]$	$\Delta S (D^+) [\%]$
Luminosity	1.00	1.00
K^\pm/π^\pm Tracking	2.58	2.59
π^0 Tracking	0.94	0.63
K_S^0 Tracking	0.00	0.42
Single Tag Fits	0.25	0.20
PDG Error	0.31	0.18
Total	2.95	2.89

Table 5.17: Systematics shifts affecting the cross section measurements.
The total shifts are used to calculate the systematic uncertainties of the D^0 and D^+ cross sections.

E_{mid} [GeV]	$\sigma_{D^0\bar{D}^0}^{RC}$ [nb]	$\sigma_{D^+\bar{D}^-}^{RC}$ [nb]
3.7342	$0.164 \pm 0.046 \pm 0.005$	-
3.7368	$0.218 \pm 0.068 \pm 0.006$	-
3.7447	$0.765 \pm 0.070 \pm 0.023$	$0.150 \pm 0.038 \pm 0.004$
3.7483	$0.838 \pm 0.064 \pm 0.025$	$0.360 \pm 0.048 \pm 0.010$
3.7501	$0.968 \pm 0.053 \pm 0.029$	$0.439 \pm 0.040 \pm 0.013$
3.7517	$1.237 \pm 0.052 \pm 0.036$	$0.574 \pm 0.040 \pm 0.017$
3.7534	$1.377 \pm 0.051 \pm 0.041$	$0.748 \pm 0.042 \pm 0.022$
3.7556	$1.566 \pm 0.055 \pm 0.046$	$0.797 \pm 0.045 \pm 0.023$
3.7562	$1.629 \pm 0.051 \pm 0.048$	$0.914 \pm 0.042 \pm 0.026$
3.7592	$1.948 \pm 0.052 \pm 0.057$	$1.192 \pm 0.045 \pm 0.034$
3.7624	$2.385 \pm 0.058 \pm 0.070$	$1.534 \pm 0.051 \pm 0.044$
3.7650	$2.715 \pm 0.071 \pm 0.080$	$1.882 \pm 0.066 \pm 0.054$
3.7676	$3.102 \pm 0.087 \pm 0.092$	$2.200 \pm 0.081 \pm 0.064$
3.7713	$3.406 \pm 0.101 \pm 0.100$	$2.634 \pm 0.098 \pm 0.076$
3.7742	$3.714 \pm 0.111 \pm 0.110$	$3.067 \pm 0.111 \pm 0.089$
3.7775	$3.692 \pm 0.111 \pm 0.109$	$3.078 \pm 0.111 \pm 0.089$
3.7802	$3.444 \pm 0.104 \pm 0.102$	$2.599 \pm 0.100 \pm 0.075$
3.7829	$2.791 \pm 0.090 \pm 0.082$	$2.206 \pm 0.088 \pm 0.064$
3.7869	$1.995 \pm 0.072 \pm 0.059$	$1.627 \pm 0.073 \pm 0.047$
3.7891	$1.361 \pm 0.058 \pm 0.040$	$1.178 \pm 0.062 \pm 0.034$
3.7926	$0.920 \pm 0.045 \pm 0.027$	$0.680 \pm 0.045 \pm 0.020$
3.7970	$0.562 \pm 0.037 \pm 0.017$	$0.414 \pm 0.039 \pm 0.012$
3.8003	$0.424 \pm 0.035 \pm 0.013$	$0.241 \pm 0.037 \pm 0.007$
3.8024	$0.325 \pm 0.038 \pm 0.010$	$0.236 \pm 0.043 \pm 0.007$
3.8070	$0.352 \pm 0.050 \pm 0.010$	$0.289 \pm 0.051 \pm 0.008$
3.8093	$0.233 \pm 0.050 \pm 0.007$	$0.132 \pm 0.055 \pm 0.004$
3.8135	$0.060 \pm 0.049 \pm 0.002$	$0.153 \pm 0.066 \pm 0.004$
3.8153	$0.056 \pm 0.051 \pm 0.002$	$0.089 \pm 0.063 \pm 0.003$
3.8229	$0.140 \pm 0.083 \pm 0.004$	$0.197 \pm 0.107 \pm 0.006$
3.8320	$0.069 \pm 0.086 \pm 0.002$	$0.046 \pm 0.099 \pm 0.001$
3.8390	$0.237 \pm 0.105 \pm 0.007$	$0.254 \pm 0.124 \pm 0.007$
3.8494	$0.186 \pm 0.104 \pm 0.005$	$0.186 \pm 0.118 \pm 0.005$
3.8555	$0.337 \pm 0.111 \pm 0.010$	$0.273 \pm 0.104 \pm 0.008$
3.8632	$0.340 \pm 0.127 \pm 0.010$	$0.099 \pm 0.091 \pm 0.003$

Table 5.18: Measurements of the D^0 and D^+ cross sections. The first errors are statistical and the second are systematic.

5.8 Results

After incorporating the systematic and model uncertainties, the total results for the main $\psi(3770)$ parameters are shown in Table 5.19. The results shown are from the VDM model, as we treat this as the nominal results. The Exponential model is used as a measure of uncertainty, however, the quality of fits found by this approach means it cannot be excluded as a viable option.

$M^{\psi(3770)}$	$3780.8 \pm 0.2 \pm 0.6 \pm 1.3$	[MeV]
$\Gamma^{\psi(3770)}$	$24.1 \pm 0.5 \pm 0.6 \pm 1.9$	[MeV]
$\Gamma_{ee}^{\psi(3770) \rightarrow D\bar{D}}$	$216 \pm 9 \pm 11 \pm 17$	[eV]
$\phi^{\psi(3770)}$	$207 \pm 3 \pm 3 \pm 7$	[$^\circ$]

Table 5.19: Final results for the $\psi(3770)$ parameters.

The first error listed is statistical, the second is systematic, and the third is from the form factor model.

Additionally, since this analysis is based on an approach developed by the KEDR collaboration, a comparison to their results is also shown in table 5.20. For their measurement of $\Gamma_{ee}^{\psi(3770)}$, two solutions were found with very close χ^2 values, so both are quoted in their final results. With the larger statistics available at BESIII, no alternate solution was found during searches over the parameter space. It is clear the VDM results are well in line with the parameters found by the KEDR collaboration, but with significantly smaller statistical errors. Each of these measurements are also highly discrepant with the current PDG world averages.

Method	$M^{\psi(3770)}$ [MeV]	$\Gamma^{\psi(3770)}$ [MeV]	$\Gamma_{ee}^{\psi(3770) \rightarrow D\bar{D}}$ [eV]
Exponential	$3782.1 \pm 0.3 \pm 0.6$	$26.0 \pm 0.6 \pm 0.7$	$233 \pm 10 \pm 13$
VDM	$3780.8 \pm 0.2 \pm 0.6$	$24.1 \pm 0.6 \pm 0.6$	$216 \pm 9 \pm 12$
KEDR	$3779.2^{+1.8+0.5+0.3}_{-1.7-0.7-0.3}$	$24.9^{+4.6+0.5+0.2}_{-4.0-0.6-0.9}$	$154^{+79+17+13}_{-58-9-25},$ $414^{+72+24+90}_{-80-26-10}$
PDG	3773.15 ± 0.33	27.2 ± 0.9	$[262 \pm 18] \times \mathcal{B}_{D\bar{D}}$

Table 5.20: Fit results compared to the KEDR results and the PDG. The first errors listed are statistical, while the second are systematic. In the case of KEDR, the third error is from the model.

We can also compare our results to the cross section values found in the previous analysis of BESIII's on-peak $\psi(3770)$ data sample of 2.93 fb^{-1} by Derrick Toth [44]. The values displayed on Figures 5.6 and 5.7 are his double-tag (DT) values. Each of these cross sections are shown in Table 5.21. Further analysis to better understand the differences seen is still in progress, however both methods used in this analysis are within $\sim 1\sigma$ of the high statistics method.

Model	$\sigma_{D^0\overline{D^0}}$ [nb]	$\sigma_{D^+D^-}$ [nb]
Derrick (DT)	$3.615 \pm 0.010 \pm 0.035$	$2.830 \pm 0.011 \pm 0.026$
Exponential	$3.662 \pm 0.131 \pm 0.108$	$2.947 \pm 0.118 \pm 0.085$
VDM	$3.748 \pm 0.131 \pm 0.111$	$2.951 \pm 0.118 \pm 0.085$

Table 5.21: Comparison of cross section calculations at $E_{\text{cm}} = 3.7732\text{ GeV}$. The values measured previously used a 2.93 fb^{-1} data sample of $\psi(3770)$ events to reconstruct double-tag (DT) decays. The first errors listed are statistical, while the second is systematic.

Chapter 6

Measurement of Hadronic Production and $\Gamma(\psi(3770) \rightarrow \text{non-}D\bar{D})$

The second half of this analysis describes progress on measuring of the branching fraction for non- $D\bar{D}$ events coming from the $\psi(3770)$. While multiple other experiments have performed measurements of this quantity, the results have been highly discrepant with one another. For instance, in 2008 BESII [57] measured a value of $(15.1 \pm 5.6 \pm 1.8)\%$, while in 2010 CLEO [58] measured a value of $(-3.3 \pm 1.4 \pm 6.6)\%$. With the high statistics available at BESIII, we aim to obtain more precise results to conclusively settle this controversy.

In order to determine the branching fraction, we measure the total production rate of multihadronic events. From this, we subtract all non- $\psi(3770)$ background components leaving only the contribution of events produced by the $\psi(3770)$. Subtracting the measured $\sigma(\psi(3770) \rightarrow D\bar{D})$ gives the cross section for non- $D\bar{D}$ events from $\psi(3770)$ ($\sigma(\psi(3770) \rightarrow \text{non-}D\bar{D})$), and the branching fraction follows immediately:

$$\Gamma(\psi(3770) \rightarrow \text{non-}D\bar{D}) = \frac{\sigma(\psi(3770) \rightarrow \text{non-}D\bar{D})}{\sigma(\psi(3770) \rightarrow D\bar{D}) + \sigma(\psi(3770) \rightarrow \text{non-}D\bar{D})}. \quad (6.1)$$

The total hadronic production rate in this region is dominated by events of the

form $e^+e^- \rightarrow q\bar{q}$, where $q\bar{q}$ fragments into any number of hadrons comprised of u , d , or s quarks. However, a precise determination of this contribution at $\psi(3770)$ is impossible, because these multihadronic events cannot be reliably separated from $\psi(3770)$ decays. Instead, we extrapolate measurements made at lower energies, not only below the $D\bar{D}$ threshold, but also below the $\psi(2S)$ peak. Under the physics assumption that $e^+e^- \rightarrow q\bar{q}$ scales as a simple function of energy ($\frac{1}{s}$, as required by QCD), we can determine the contribution of these events near $\psi(3770)$, as long as the detector response and backgrounds are well understood. The measured value for the non- $D\bar{D}$ branching fraction is highly dependent on the accuracy of this extrapolation. From our investigation, the primary determinant of this accuracy is the energy dependence of the $\psi(2S)$ cross section, which we have learned will require more careful study to determine a precise measurement.

6.1 Data and Monte Carlo Samples

6.1.1 Data Samples

The data used for this analysis was also produced by BEPCII and collected by BESIII. The samples used include continuum data taken at 3.650 GeV in 2009 (old continuum), as well as multiple other continuum points taken around this energy in 2013 (new continuum). We also use Round 1 (R1) and Round 2 (R2) of the high-statistics $\psi(3770)$ data taken in 2010 and 2011, respectively. Each of these samples, and their integrated luminosities, can be seen in Table 6.1. The values of luminosity were measured during a previous version of this analysis using the procedure described in Section 5.3.3. The labels given to each continuum point are the nominal center-of-mass energies set during BEPCII operation, which were subsequently discovered through our more precise calibration to differ from the true values. In addition to these datasets, the scan data described previously (Section 5.3.1) is also used.

6.1.2 Center-of-Mass Energy Measurement

As before, a precise measurement of each energy point is vital to the accuracy of the final results. Most notably, due to the rapidly increasing $\psi(2S)$ cross section near the

high end of the continuum points, the value at the 3671 (New) point is highly dependent on the assumed cross section of the $\psi(2S)$. Following the procedure of Section 5.3.2, we measured the E_{cm} value of each continuum point. This resulted in a 4 MeV to 6 MeV shift downwards for each point in the new continuum data, but virtually no shift for the old continuum data point. The measured energies and luminosities of each sample are shown in Table 6.1.

Sample Name	E_{cm} [GeV]	Luminosity pb^{-1}
3500 (New)	3.496	3.680 ± 0.009
3542 (New)	3.538	3.481 ± 0.009
3600 (New)	3.596	0.395 ± 0.019
3650 (New)	3.644	5.420 ± 0.009
3671 (New)	3.665	4.669 ± 0.009
3650 (Old)	3.650	44.334 ± 0.009
$\psi(3770)$ (R1)	3.773	926.922 ± 0.092
$\psi(3770)$ (R2)	3.773	1978.920 ± 0.091

Table 6.1: Data samples used for the inclusive measurement.

While the 3600 (New) sample was intended to be similar in luminosity to the other new continuum points, accelerator issues inhibited the data collection. The new continuum points have a much smaller luminosity compared to the other datasets used in this analysis.

6.2 Event Selection

In order to determine the number of hadronic events in each sample, we apply a variety of cuts. For charged tracks in the MDC, these include the cuts shown in Table 6.2.

Vertex (xy)	$V_{xy} < 1 \text{ cm}$
Vertex (z)	$ Vz < 10 \text{ cm}$
MDC Angle	$ \cos \theta < 0.93$

Table 6.2: Selection cuts on charged tracks used to count hadronic events.

For neutral tracks in the EMC, these include the cuts shown in Table 6.3.

Minimum Energy (Barrel)	$E_{\text{EMC}} > 25 \text{ MeV}$	$(\cos \theta < 0.80)$
Minimum Energy (Endcap)	$E_{\text{EMC}} > 50 \text{ MeV}$	$(0.86 < \cos \theta < 0.92)$
TDC Timing	$(0 \leq t \leq 14) \times 50 \text{ ns}$	

Table 6.3: Selection cuts on neutral tracks used to count hadronic events.

To reject background events from $e^+e^- \rightarrow e^+e^-$ or $e^+e^- \rightarrow \gamma\gamma$, we also employ cuts on the highest energy and highest momentum tracks in the event. These are listed in Table 6.4.

Highest Energy	$\cos \theta_+^{\max} < 0.8$	$(N_{\text{tracks}} = 2)$
	$\cos \theta_-^{\max} > -0.8$	
	$\cos \theta_+^{\max} < 0.8 \text{ or } (p/E_{\text{cm}})_+^{\max} \leq 0.3$	$(N_{\text{tracks}} = 3, 4)$
	$\cos \theta_-^{\max} > -0.8 \text{ or } (p/E_{\text{cm}})_-^{\max} \leq 0.3$	
Highest Momentum	$0.8 \leq (E_{\text{EMC}}/p)_+^{\max} \leq 1.1$	
	$0.8 \leq (E_{\text{EMC}}/p)_-^{\max} \leq 1.1$	

Table 6.4: Selection cuts to remove Bhabha and two-photon backgrounds.

The $+$ and $-$ denote positively and negatively charged tracks, respectively. The $^{\max}$ notation indicates the highest energy or momenta track for the corresponding charge. The energy cuts depend on the total number of charged tracks in the event, N_{tracks} .

After applying these preliminary cuts, there are three groups of selection criteria for multihadronic events: Standard (SHAD), Loose (LHAD), and Tight (THAD). For the nominal procedure, SHAD is used, while LHAD and THAD are for systematic considerations. The cuts included in each of these sets are shown in Tables 6.5 to 6.7. These apply to the number of charged tracks (N_{tracks}), the visible energy (E_{vis}), the total visible momentum in the z -direction ($p_{z \text{ vis}}$), the maximum shower energy (E_{EMC}^{\max}), and the total shower energy ($E_{\text{EMC}}^{\text{tot}}$). Here, ‘visible’ refers to the sum over charged and neutral tracks.

Number of Tracks	$N_{\text{tracks}} > 2$	
Visible Energy	$(E_{\text{vis}}/E_{\text{cm}}) > 0.3$	
Visible Momentum	$(p_{z \text{ vis}}/E_{\text{vis}}) < 0.6$	$(N_{\text{tracks}} = 3, 4)$
Maximum Shower Energy	$(E_{\text{EMC}}^{\max}/E_{\text{beam}}) < 0.75$	$(N_{\text{tracks}} = 3, 4)$
Total Shower Energy	$0.25 < (E_{\text{EMC}}^{\text{tot}}/E_{\text{cm}}) < 0.75$	$(N_{\text{tracks}} = 3)$
	$0.15 < (E_{\text{EMC}}^{\text{tot}}/E_{\text{cm}}) < 0.75$	$(N_{\text{tracks}} = 4)$

Table 6.5: Standard selection cuts (SHAD) for counting hadronic events.

Number of Tracks	$N_{\text{tracks}} > 1$	
Visible Energy	$(E_{\text{vis}}/E_{\text{cm}}) > 0.4$	$(N_{\text{tracks}} = 2)$
	$(E_{\text{vis}}/E_{\text{cm}}) > 0.3$	$(N_{\text{tracks}} \geq 3)$
Visible Momentum	$(p_z^{\text{vis}}/E_{\text{vis}}) < 0.3$	$(N_{\text{tracks}} = 2)$
	$(p_z^{\text{vis}}/E_{\text{vis}}) < 0.6$	$(N_{\text{tracks}} = 3, 4)$
Maximum Shower Energy	$(E_{\text{EMC}}^{\text{max}}/E_{\text{beam}}) < 0.50$	$(N_{\text{tracks}} = 2)$
	$(E_{\text{EMC}}^{\text{max}}/E_{\text{beam}}) < 0.75$	$(N_{\text{tracks}} = 3, 4)$
Total Shower Energy	$0.25 < (E_{\text{EMC}}^{\text{tot}}/E_{\text{cm}}) < 0.75$	$(N_{\text{tracks}} = 2, 3)$
	$0.15 < (E_{\text{EMC}}^{\text{tot}}/E_{\text{cm}}) < 0.75$	$(N_{\text{tracks}} = 4)$

Table 6.6: Loose selection cuts (LHAD) for counting hadronic events.

Number of Tracks	$N_{\text{tracks}} > 3$	
Visible Energy	$(E_{\text{vis}}/E_{\text{cm}}) > 0.4$	
Visible Momentum	$(p_z^{\text{vis}}/E_{\text{vis}}) < 0.6$	$(N_{\text{tracks}} = 4)$
Maximum Shower Energy	$(E_{\text{EMC}}^{\text{max}}/E_{\text{beam}}) < 0.75$	$(N_{\text{tracks}} = 4, 5)$
Total Shower Energy	$0.15 < (E_{\text{EMC}}^{\text{tot}}/E_{\text{cm}}) < 0.75$	$(N_{\text{tracks}} = 4)$
	$0.00 < (E_{\text{EMC}}^{\text{tot}}/E_{\text{cm}}) < 0.75$	$(N_{\text{tracks}} = 5)$

Table 6.7: Tight selection cuts (THAD) for counting hadronic events.

6.3 Hadron Counting

In order to determine the total number of hadronic events in each data sample, we average the charged tracks in each event over their distance of closest approach in the z -direction (V_z). Signal tracks should originate within a few centimeters of the collision point. Backgrounds tracks, such as from cosmic rays or beam-gas interactions, can originate away from the collision point, and will therefore have a much broader distribution. Fits are performed using a double Gaussian shape for the signal and a 2nd order polynomial for the background. These are shown in Figure 6.1 and the resulting signal amounts for each are listed in Table 6.9.

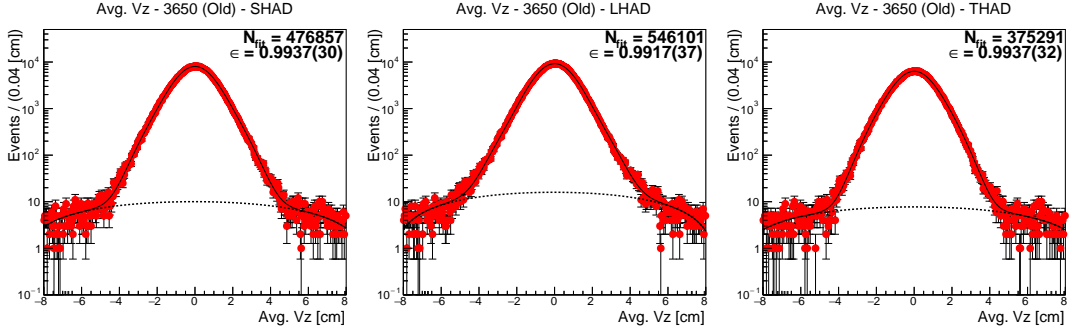


Figure 6.1: Fits to determine the number of hadrons in the 3650 (Old) data sample. The results for SHAD (left), LHAD (middle), and THAD (right) are shown in log scale.

6.4 Background Subtraction

To precisely determine the actual number of hadronic events in the old continuum data, we must subtract off a variety of backgrounds from the total number of hadronic events passing our selection criteria. The samples considered for this measurement include two-track QED processes (e^+e^- , $\mu^+\mu^-$, $\tau^+\tau^-$, $\gamma\gamma$), radiative J/ψ ($\gamma J/\psi$), two photon fusion (2γ), and events coming from $\psi(2S)$. Initially, we assume the $\psi(2S)$ has a standard Breit-Wigner shape.

Each background contributes to the total number of reconstructed events based on their cross section (σ) and reconstruction efficiency (ϵ_{MC}):

$$N_{\text{had}} = \mathcal{L} \times \sigma \times \epsilon_{\text{MC}}. \quad (6.2)$$

The efficiency is simply the fraction of reconstructed tracks compared to the total generated in a given MC sample:

$$\epsilon_{\text{MC}} = \left(\frac{N_{\text{rec}}}{N_{\text{gen}}} \right). \quad (6.3)$$

The MC samples were generated with 2.5×10^3 events for each of the 79 runs in the old continuum data for each of the included backgrounds. Each sample was analyzed with all three cut selection groups (see Section 6.2). The reconstruction efficiencies for each, along with their cross sections at 3.650 GeV are shown in Table 6.8.

3650 (Old) Reconstruction				
Sample	σ [nb]	ϵ_{MC} (SHAD) [%]	ϵ_{MC} (LHAD) [%]	ϵ_{MC} (THAD) [%]
e^+e^-	554.562	0.0006 ± 0.0002	0.0008 ± 0.0002	0.0001 ± 0.0001
$\mu^+\mu^-$	5.560	0.0033 ± 0.0004	0.0044 ± 0.0005	0.0029 ± 0.0004
$\tau^+\tau^-$	1.844	12.8351 ± 0.0255	28.7692 ± 0.0382	9.9371 ± 0.0224
$\gamma J/\psi$	1.260	45.9222 ± 0.0482	55.1722 ± 0.0529	34.1250 ± 0.0416
$\gamma\gamma$	21.530	0.0009 ± 0.0002	0.0010 ± 0.0002	0.0005 ± 0.0002
2γ	1.257	2.4109 ± 0.0110	4.6297 ± 0.0153	1.6468 ± 0.0091
$\psi(2S)^{\dagger}$	0.150	62.9891 ± 0.0078	69.2882 ± 0.0082	51.6942 ± 0.0071

Table 6.8: Reconstruction of background samples for the old continuum data. These include standard QED two-track processes (e^+e^- , $\mu^+\mu^-$, $\tau^+\tau^-$, $\gamma\gamma$), radiative J/ψ ($\gamma J/\psi$) and two photon fusion (2γ) events, and a contribution coming from $\psi(2S)$.

[†]The $\psi(2S)$ is assumed to have a standard Breit-Wigner shape.

Using each of these values, we can determine the total number of hadronic events in the data. This is done by subtracting the expected amount of background from the measured number of events passing each selection method in data. The results for the old continuum data are shown in Table 6.9. Given that the e^+e^- , $\mu^+\mu^-$, and $\gamma\gamma$ samples have contributions much smaller than the uncertainty on the total result, we elect to exclude these samples for the rest of the procedure.

3650 (Old) Results			
Sample	N_{had} (SHAD)	N_{had} (LHAD)	N_{had} (THAD)
Data	477001 ± 691	546546 ± 739	375380 ± 613
e^+e^-*	149 ± 43	187 ± 48	12 ± 12
$\mu^+\mu^-*$	8 ± 1	11 ± 1	7 ± 1
$\tau^+\tau^-$	10490 ± 30	23514 ± 59	8122 ± 25
$\gamma J/\psi$	25658 ± 60	30826 ± 71	19067 ± 46
$\gamma\gamma^*$	9 ± 2	10 ± 2	4 ± 1
2γ	1443 ± 7	2771 ± 11	986 ± 6
$\psi(2S)^{\dagger}$	4175 ± 9	4593 ± 10	3427 ± 7
Hadrons	435234 ± 694	484842 ± 745	343779 ± 615

Table 6.9: Hadronic events selected in the old continuum data. As expected, SHAD finds less events than LHAD and more than THAD.

*The contribution is neglected for the total results.

[†]The $\psi(2S)$ is assumed to have a standard Breit-Wigner shape.

6.5 Efficiency Extrapolation

Due to the increase in event complexity above the $D\bar{D}$ threshold, $q\bar{q}$ events not coming from $\psi(3770)$ are not well modeled by our MC generators. In order to accurately estimate these events, we repeat the procedure for the lower-energy points (below $\psi(3770)$), and extrapolate to the $\psi(3770)$ region. Measuring the hadronic events for the new continuum data follows exactly as for the old continuum data, but with the negligible backgrounds excluded. The number of hadrons found in each data sample are determined from the fits shown in Figures 6.2 to 6.6. Reconstruction efficiencies are shown in Table 6.10 with the total results listed in Table 6.11.

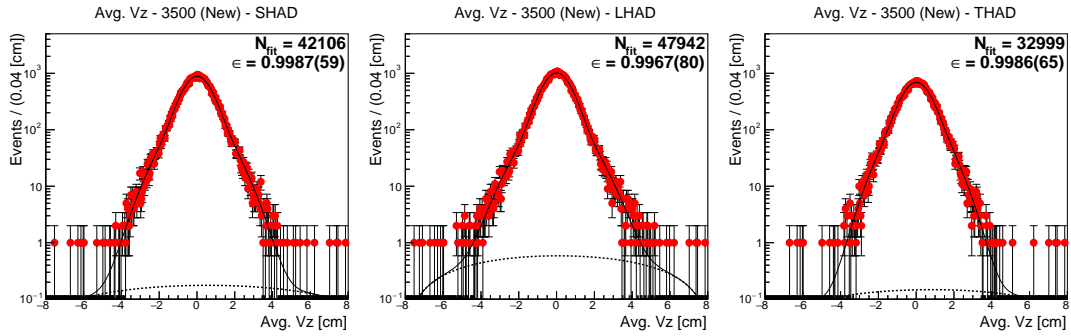


Figure 6.2: Fits to determine the number of hadrons in the 3500 (New) data sample. The results for SHAD (left), LHAD (middle), and THAD (right) are shown in log scale.

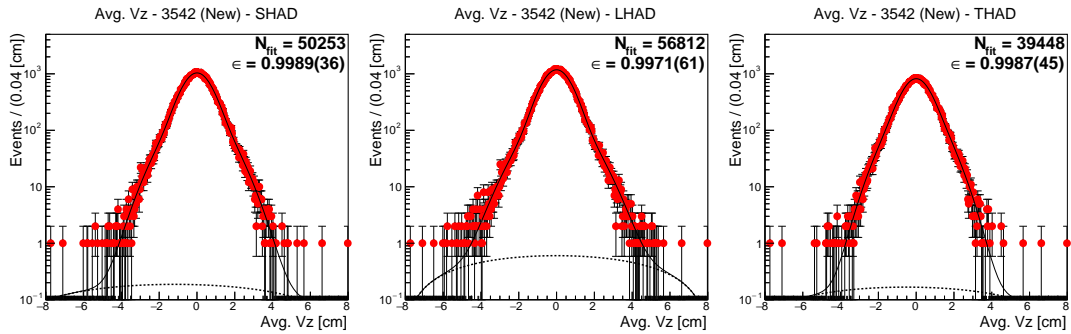


Figure 6.3: Fits to determine the number of hadrons in the 3542 (New) data sample. The results for SHAD (left), LHAD (middle), and THAD (right) are shown in log scale.

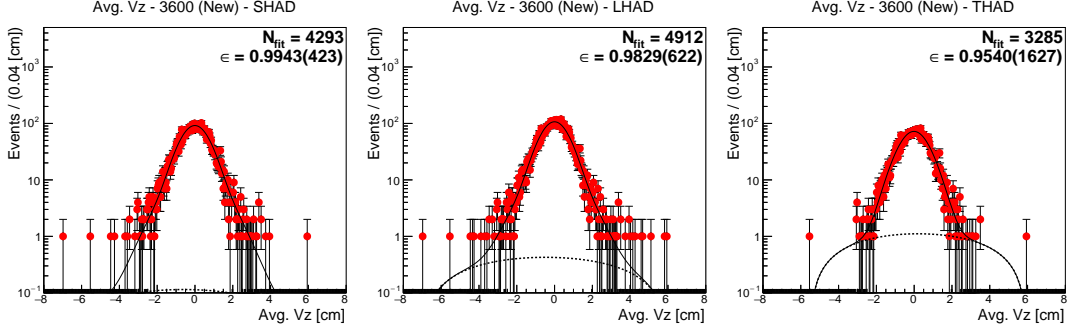


Figure 6.4: Fits to determine the number of hadrons in the 3600 (New) data sample. The results for SHAD (left), LHAD (middle), and THAD (right) are shown in log scale.

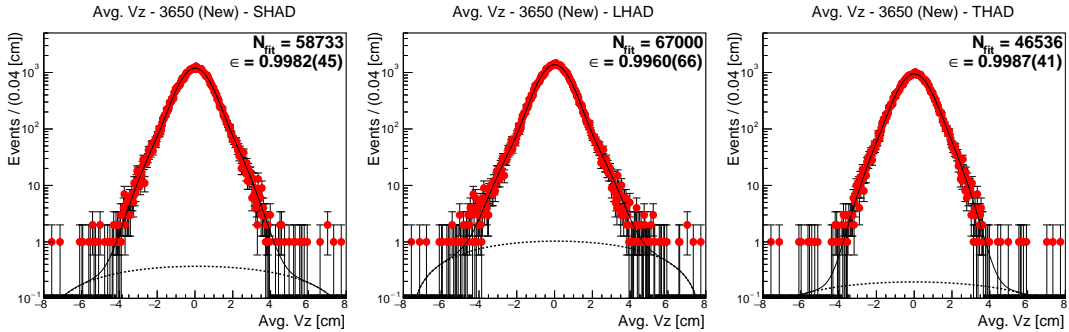


Figure 6.5: Fits to determine the number of hadrons in the 3650 (New) data sample. The results for SHAD (left), LHAD (middle), and THAD (right) are shown in log scale.

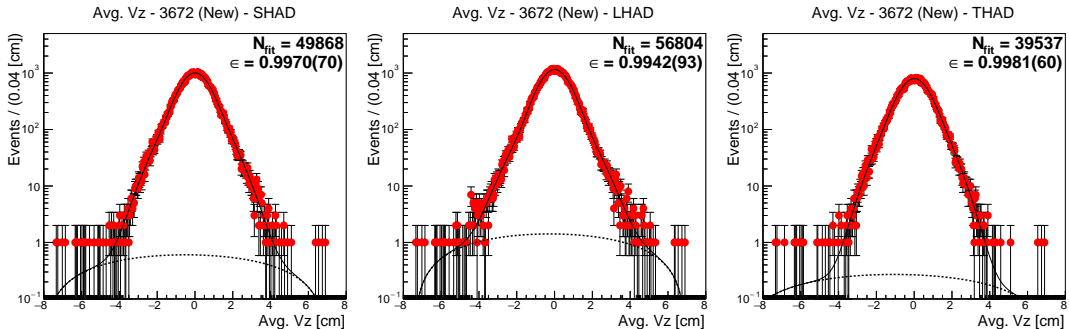


Figure 6.6: Fits to determine the number of hadrons in the 3671 (New) data sample. The results for SHAD (left), LHAD (middle), and THAD (right) are shown in log scale.

3500 (New) Reconstruction				
Sample	σ [nb]	ϵ_{MC} (SHAD) [%]	ϵ_{MC} (LHAD) [%]	ϵ_{MC} (THAD) [%]
$\tau^+\tau^-$	0.000	-	-	-
$\gamma J/\psi$	1.831	47.079 ± 0.077	56.117 ± 0.084	35.320 ± 0.066
2γ	1.240	2.380 ± 0.017	4.924 ± 0.025	1.644 ± 0.014
$\psi(2S)^{\dagger}$	0.006	62.989 ± 0.008	69.288 ± 0.008	51.694 ± 0.007

3542 (New) Reconstruction				
Sample	σ [nb]	ϵ_{MC} (SHAD) [%]	ϵ_{MC} (LHAD) [%]	ϵ_{MC} (THAD) [%]
$\tau^+\tau^-$	0.000	-	-	-
$\gamma J/\psi$	1.632	47.188 ± 0.072	56.430 ± 0.079	35.355 ± 0.063
2γ	1.270	2.386 ± 0.016	5.046 ± 0.024	1.633 ± 0.013
$\psi(2S)^{\dagger}$	0.009	62.989 ± 0.008	69.288 ± 0.008	51.694 ± 0.007

3600 (New) Reconstruction				
Sample	σ [nb]	ϵ_{MC} (SHAD) [%]	ϵ_{MC} (LHAD) [%]	ϵ_{MC} (THAD) [%]
$\tau^+\tau^-$	1.262	12.851 ± 0.080	29.096 ± 0.121	10.040 ± 0.071
$\gamma J/\psi$	1.412	47.524 ± 0.154	56.902 ± 0.169	35.703 ± 0.134
2γ	1.311	2.651 ± 0.036	5.089 ± 0.050	1.897 ± 0.031
$\psi(2S)^{\dagger}$	0.024	62.989 ± 0.008	69.288 ± 0.008	51.694 ± 0.007

3650 (New) Reconstruction				
Sample	σ [nb]	ϵ_{MC} (SHAD) [%]	ϵ_{MC} (LHAD) [%]	ϵ_{MC} (THAD) [%]
$\tau^+\tau^-$	1.844	12.964 ± 0.033	28.939 ± 0.049	10.154 ± 0.029
$\gamma J/\psi$	1.260	47.414 ± 0.063	57.043 ± 0.069	35.701 ± 0.055
2γ	1.346	2.410 ± 0.014	4.675 ± 0.020	1.682 ± 0.012
$\psi(2S)^{\dagger}$	0.110	62.989 ± 0.008	69.288 ± 0.008	51.694 ± 0.007

3671 (New) Reconstruction				
Sample	σ [nb]	ϵ_{MC} (SHAD) [%]	ϵ_{MC} (LHAD) [%]	ϵ_{MC} (THAD) [%]
$\tau^+\tau^-$	2.026	12.997 ± 0.047	28.851 ± 0.069	10.169 ± 0.041
$\gamma J/\psi$	1.205	47.496 ± 0.089	57.237 ± 0.098	35.745 ± 0.077
2γ	1.361	2.473 ± 0.020	4.787 ± 0.028	1.698 ± 0.017
$\psi(2S)^{\dagger}$	0.436	62.989 ± 0.008	69.288 ± 0.008	51.694 ± 0.007

Table 6.10: Reconstruction of background samples for the new continuum data. Cross sections for $\tau^+\tau^-$ are zero below its production threshold at 3.554 GeV.

[†]The $\psi(2S)$ is assumed to have a standard Breit-Wigner shape.

3500 (New) Results			
Sample	N_{had} (SHAD)	N_{had} (LHAD)	N_{had} (THAD)
Data	42106 ± 205	47942 ± 219	32999 ± 182
$\gamma J/\psi$	3173 ± 10	3782 ± 11	2380 ± 8
2γ	109 ± 1	225 ± 1	75 ± 1
$\psi(2S)^{\dagger}$	13 ± 1	14 ± 1	14 ± 1
Hadrons	38812 ± 205	43921 ± 219	30533 ± 182
3542 (New) Results			
Sample	N_{had} (SHAD)	N_{had} (LHAD)	N_{had} (THAD)
Data	50253 ± 224	56812 ± 238	39448 ± 199
$\gamma J/\psi$	3450 ± 9	4126 ± 10	2585 ± 7
2γ	136 ± 1	287 ± 1	93 ± 1
$\psi(2S)^{\dagger}$	26 ± 1	28 ± 1	21 ± 1
Hadrons	46641 ± 224	52371 ± 239	36749 ± 199
3600 (New) Results			
Sample	N_{had} (SHAD)	N_{had} (LHAD)	N_{had} (THAD)
Data	4293 ± 66	4912 ± 70	3285 ± 57
$\tau^+\tau^-$	64 ± 3	145 ± 7	50 ± 2
$\gamma J/\psi$	265 ± 13	317 ± 16	199 ± 10
2γ	14 ± 1	26 ± 1	10 ± 1
$\psi(2S)^{\dagger}$	6 ± 1	7 ± 1	5 ± 1
Hadrons	3944 ± 67	4417 ± 72	3023 ± 58
3650 (New) Results			
Sample	N_{had} (SHAD)	N_{had} (LHAD)	N_{had} (THAD)
Data	58733 ± 242	67000 ± 259	46536 ± 216
$\tau^+\tau^-$	1295 ± 4	2892 ± 7	1015 ± 3
$\gamma J/\psi$	3239 ± 7	3896 ± 8	2439 ± 6
2γ	176 ± 1	341 ± 2	123 ± 1
$\psi(2S)^{\dagger}$	376 ± 1	414 ± 1	309 ± 1
Hadrons	53647 ± 242	59458 ± 259	42652 ± 216
3671 (New) Results			
Sample	N_{had} (SHAD)	N_{had} (LHAD)	N_{had} (THAD)
Data	49868 ± 223	56804 ± 238	39537 ± 199
$\tau^+\tau^-$	1229 ± 5	2729 ± 8	962 ± 4
$\gamma J/\psi$	2671 ± 7	3219 ± 8	2010 ± 6
2γ	157 ± 1	304 ± 2	108 ± 1
$\psi(2S)^{\dagger}$	1282 ± 3	1410 ± 3	1052 ± 2
Hadrons	44528 ± 224	49141 ± 239	35405 ± 199

Table 6.11: Hadronic events selected in the new continuum data.

[†]The $\psi(2S)$ is assumed to have a standard Breit-Wigner shape.

Assuming the rate of $q\bar{q}$ production varies smoothly with energy ($\frac{1}{s}$), the reconstruction efficiency (relative to the old continuum data) for a given E_{cm} point (in MeV) can be determined from the ratio of yields as follows:

$$\frac{\epsilon(E_{\text{cm}})}{\epsilon(3650)} = \left[\frac{N_{\text{had}}(E_{\text{cm}})}{N_{\text{had}}(3650)} \right] \left[\frac{\mathcal{L}(3650)}{\mathcal{L}(E_{\text{cm}})} \right] \left[\frac{E_{\text{cm}}}{3650} \right]^2. \quad (6.4)$$

This efficiency ratio is calculated for each point in the new continuum data, and a linear fit is performed for each of the selection cut methods. We use this slope to extrapolate and find the expected number of hadronic events for the $\psi(3770)$ data. As the old continuum data was taken under conditions more similar to R1 of the $\psi(3770)$ data taking than the new continuum data, we use it as a normalization point for the efficiency extrapolation. The results for each cut are shown in Figures 6.7 to 6.9.

From these extrapolations, it is evident the highest energy new continuum point (3.665 GeV) falls below the trend suggested by the other new continuum points and is inconsistent with the assumed linear behavior. We hypothesize that this reflects a $\psi(2S)$ line shape which differs from the expected Breit-Wigner shape. Recent experimental evidence indicates this resonance may be susceptible to interference effects which distort the shape away from its peak. If the actual shape is lower than expected for the higher energy continuum points, it would decrease the background contribution thereby raising the efficiency ratio. This behavior is discussed further in Section 6.7, and BESIII plans to take considerably more data across this region in the near future. For now, we continue with the default Breit-Wigner assumption, and apply the procedure for the $\psi(3770)$ data. All results presented here should be viewed as illustrative of the procedure and not be construed as BESIII measurements of the non- $D\bar{D}$ decays of $\psi(3770)$.

Efficiency Extrapolation - SHAD

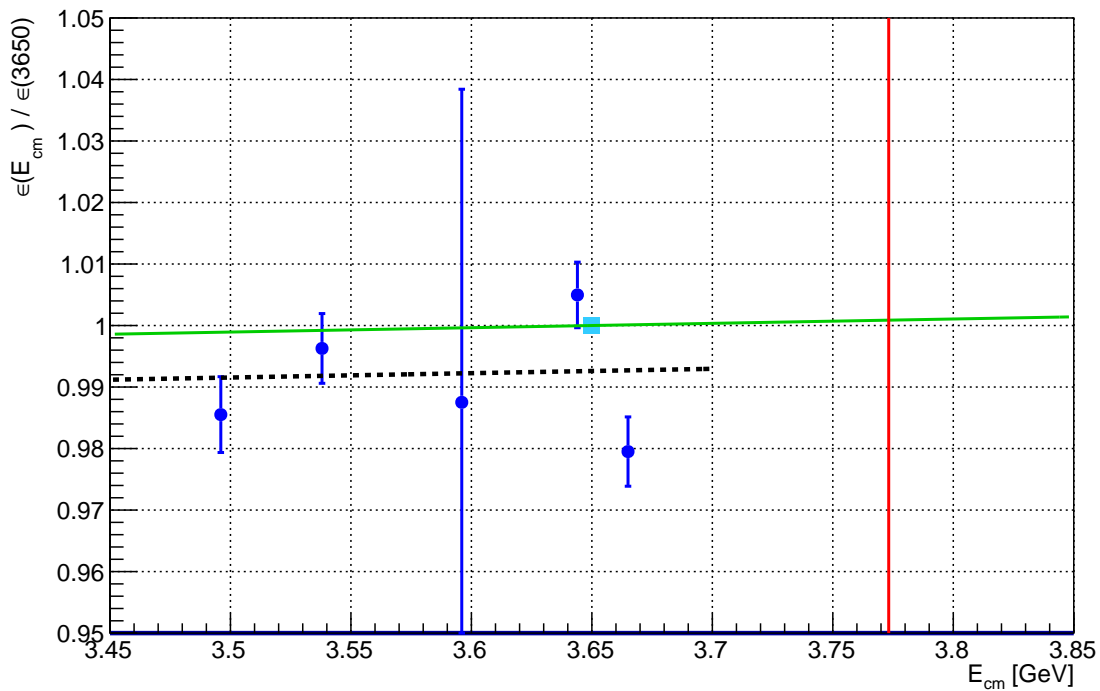


Figure 6.7: The continuum extrapolation for SHAD events.

The new continuum points (blue) are fit using a straight line (dashed black), then extrapolated to higher energies (solid green) based on the old continuum energy point at 3.650 GeV (cyan). The energy point for the $\psi(3770)$ samples at 3.773 GeV is also shown (solid red).

Efficiency Extrapolation - LHAD

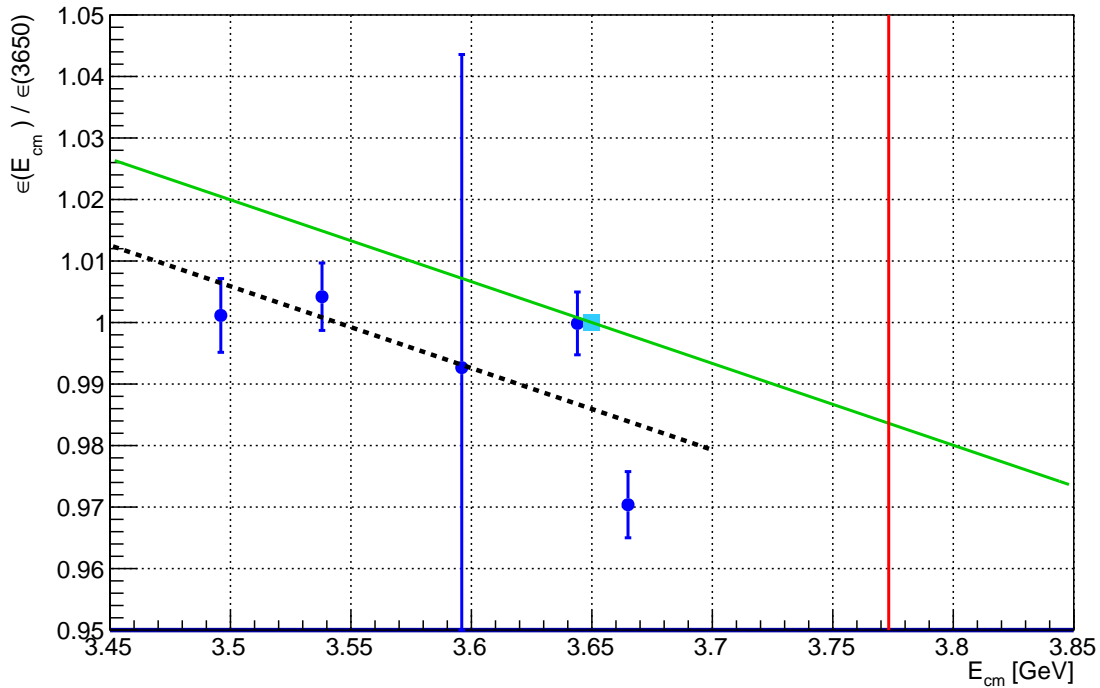


Figure 6.8: The continuum extrapolation for LHAD events.

The new continuum points (blue) are fit using a straight line (dashed black), then extrapolated to higher energies (solid green) based on the old continuum energy point at 3.650 GeV (cyan). The energy point for the $\psi(3770)$ samples at 3.773 GeV is also shown (solid red).

Efficiency Extrapolation - THAD

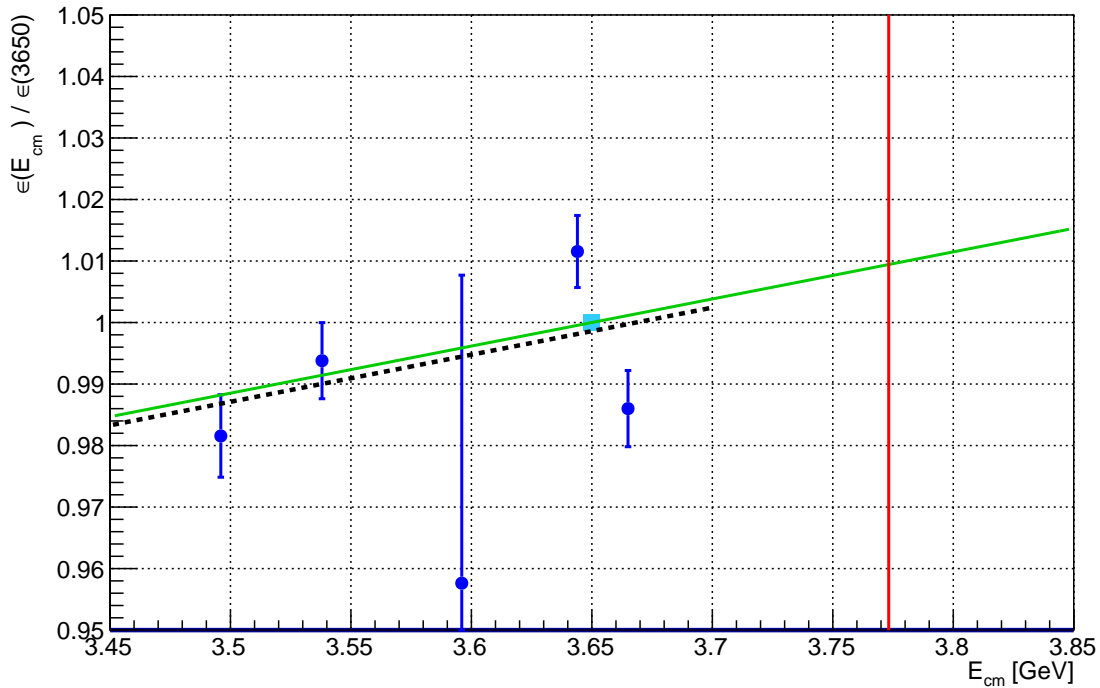


Figure 6.9: The continuum extrapolation for THAD events.

The new continuum points (blue) are fit using a straight line (dashed black), then extrapolated to higher energies (solid green) based on the old continuum energy point at 3.650 GeV (cyan). The energy point for the $\psi(3770)$ samples at 3.773 GeV is also shown (solid red).

6.6 Procedure for $\psi(3770)$ Data

The procedure for determining the hadronic events in the $\psi(3770)$ data is similar to the continuum region, but with modifications required for the backgrounds introduced in this region. Most notably, we utilize the measured $\psi(3770) \rightarrow D\bar{D}$ cross section to subtract off the contributions from $D^0\bar{D}^0$ and $D^+\bar{D}^-$. Instead of the direct $\psi(2S)$ component, there is instead a background from radiative $\psi(2S)$ production ($\gamma\psi(2S)$). Lastly, due to the minimal contribution of two photon fusion events (2γ) in this region, this component is neglected for the $\psi(3770)$ samples. The counting of total hadronic events, however, functions identically to the continuum data, and the results are shown in Figures 6.10 and 6.11.

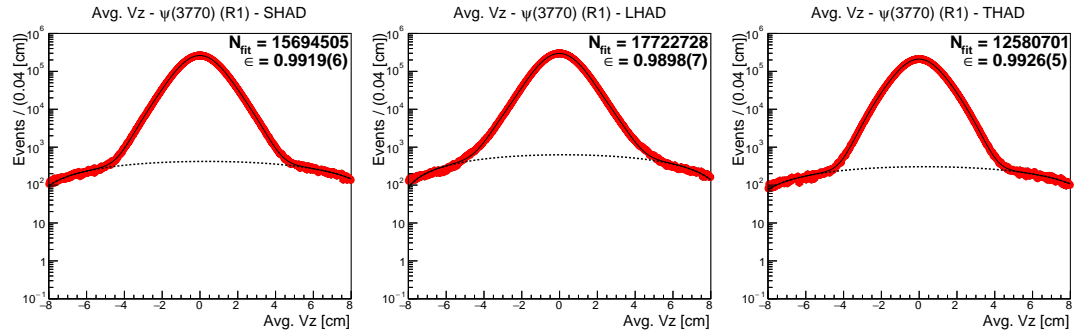


Figure 6.10: Fits to determine the number of hadrons in the $\psi(3770)$ (R1) data sample. The results for SHAD (left), LHAD (middle), and THAD (right) are shown in log scale.

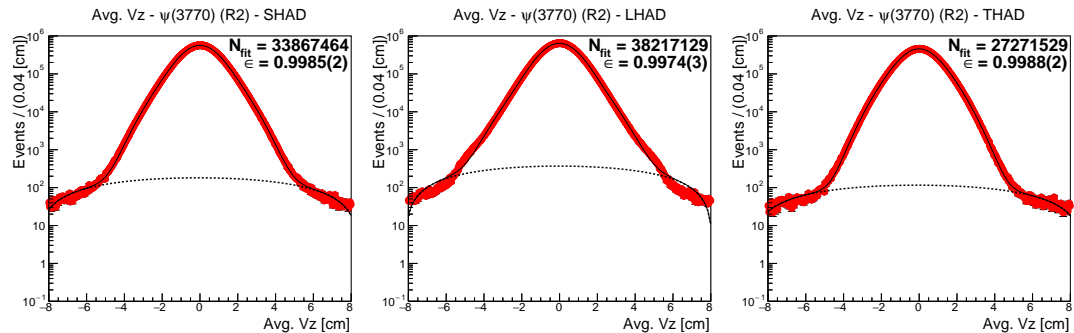


Figure 6.11: Fits to determine the number of hadrons in the $\psi(3770)$ (R2) data sample. The results for SHAD (left), LHAD (middle), and THAD (right) are shown in log scale.

6.6.1 $D\bar{D}$ Subtraction

To subtract the $D\bar{D}$ component from the hadronic cross section, we must have a data-driven procedure for determining the efficiencies of these events passing the SHAD, LHAD, and THAD cuts. MC samples are not reliable for this, largely due to poor modeling of the charged and neutral track multiplicities. Instead, our procedure is to re-weight the MC samples in order to better reflect the data distribution. This is done by finding single-tagged D candidates and counting the number of tracks not used for reconstruction. By randomly sampling pairs of points from this distribution, and assuming the decays are uncorrelated, we can produce an average representation of multiplicity in $D\bar{D}$ events. From this new distribution, selections with SHAD, LHAD, and THAD are performed based off number of tracks selected by the simplified cut criteria shown in Table 6.12 relative to the total. The corrections applied to each efficiency are the ratios of these selections in data and MC. As the $\psi(3770)$ samples for R1 and R2 were taken at different times, they are treated separately for this process. The results for each are shown in Table 6.13 with the corresponding distributions shown in Figures 6.12 to 6.15.

Selection Method	Number of Tracks
SHAD	$N_{\text{tracks}} > 2$
LHAD	$N_{\text{tracks}} > 1$
THAD	$N_{\text{tracks}} > 3$

Table 6.12: Selection methods for the $D\bar{D}$ efficiency correction.

Selection	$\psi(3770)$ R1		$\psi(3770)$ R2	
	$(\epsilon_{\text{Data}}/\epsilon_{\text{MC}}) D^0$	$(\epsilon_{\text{Data}}/\epsilon_{\text{MC}}) D^+$	$(\epsilon_{\text{Data}}/\epsilon_{\text{MC}}) D^0$	$(\epsilon_{\text{Data}}/\epsilon_{\text{MC}}) D^+$
SHAD	0.9751	0.9992	0.9759	0.9999
LHAD	0.9930	1.0018	0.9935	1.0024
THAD	0.9662	1.0064	0.9684	1.0108

Table 6.13: Efficiency corrections for the $\psi(3770)$ samples.

The corrections are impactful for D^0 , but minimal for D^+ . This is due to the differences in their low-side other D multiplicities, as seen in Figures 6.12 to 6.15.

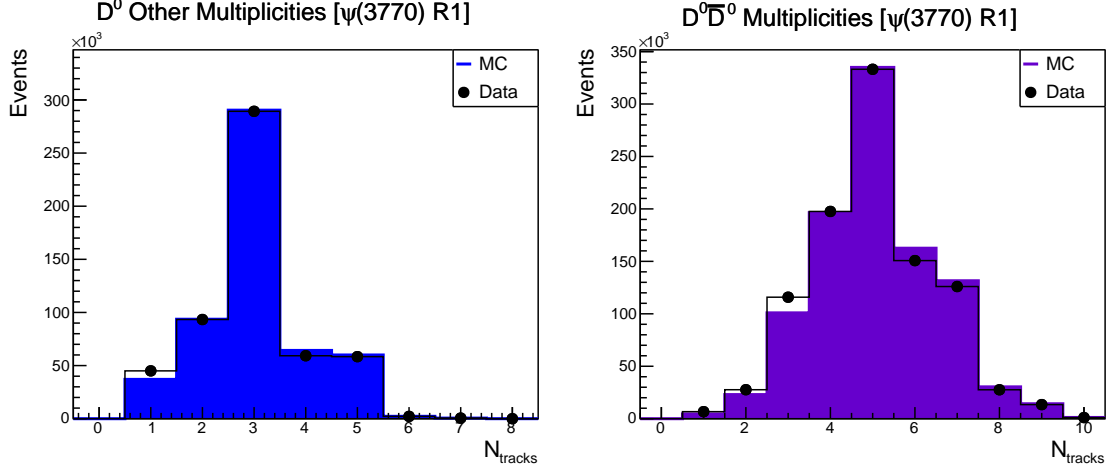


Figure 6.12: The other-side D^0 tracks and corresponding $D^0\overline{D}^0$ multiplicities for R1. The distribution of good tracks not used for reconstruction of single-tagged D^0 particles (left) is randomly sampled for pairs of points which comprise the total multiplicity distribution (right). The tracks in the $D^0\overline{D}^0$ multiplicity distribution are used to determine the efficiency correction based off the cuts in Table 6.12.

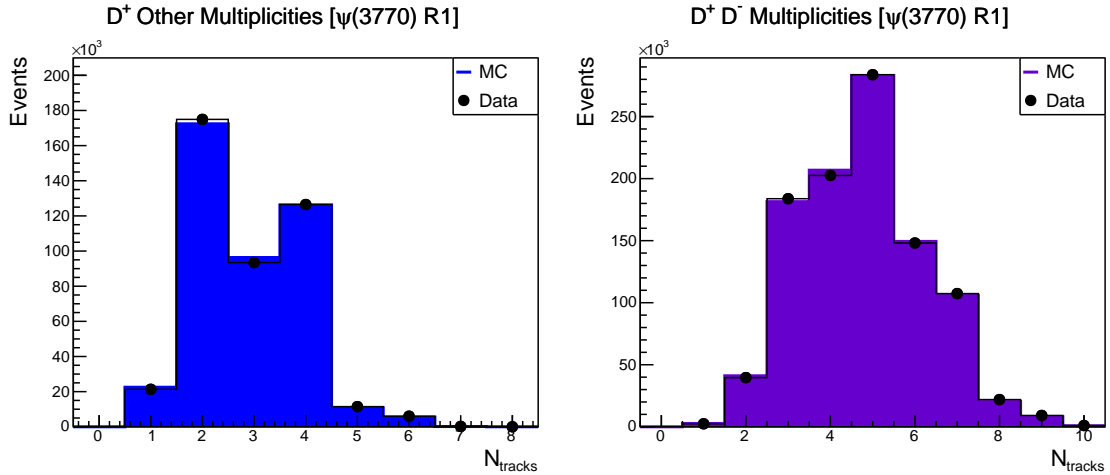


Figure 6.13: The other-side D^+ tracks and corresponding D^+D^- multiplicities for R1. The distribution of good tracks not used for reconstruction of single-tagged D^+ particles (left) is randomly sampled for pairs of points which comprise the total multiplicity distribution (right). The tracks in the D^+D^- multiplicity distribution are used to determine the efficiency correction based off the cuts in Table 6.12.

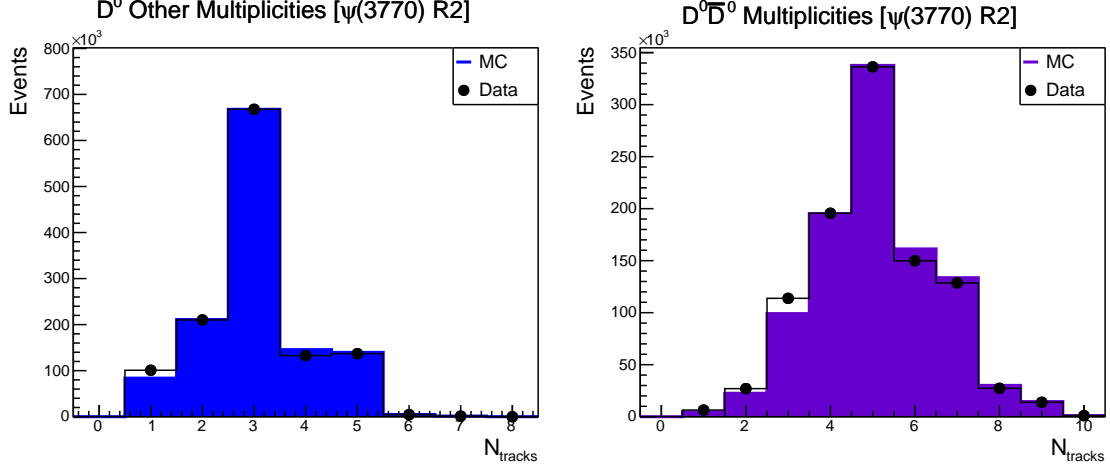


Figure 6.14: The other-side D^0 tracks and corresponding $D^0\bar{D}^0$ multiplicities for R2. The distribution of good tracks not used for reconstruction of single-tagged D^0 particles (left) is randomly sampled for pairs of points which comprise the total multiplicity distribution (right). The tracks in the $D^0\bar{D}^0$ multiplicity distribution are used to determine the efficiency correction based off the cuts in Table 6.12.

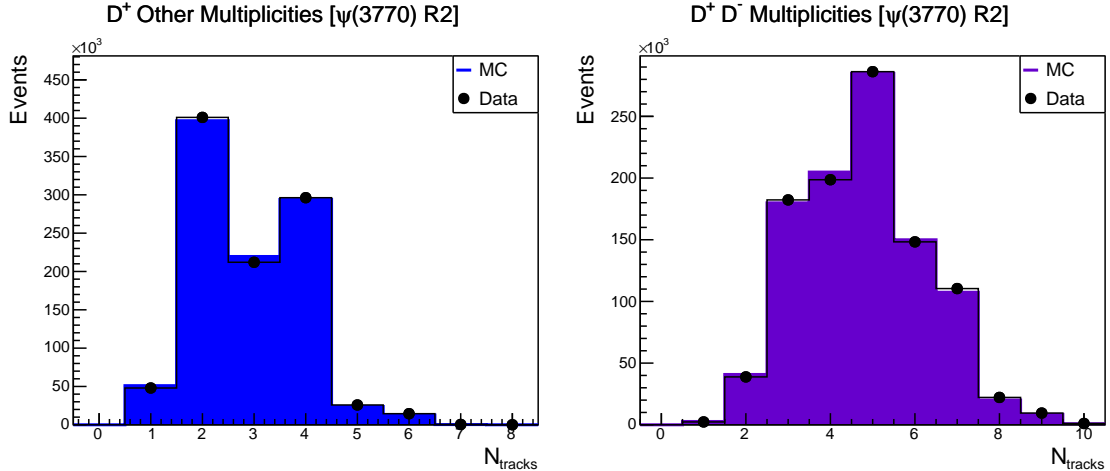


Figure 6.15: The other-side D^+ tracks and corresponding D^+D^- multiplicities for R2. The distribution of good tracks not used for reconstruction of single-tagged D^+ particles (left) is randomly sampled for pairs of points which comprise the convolved distribution (right). The number of tracks in the D^+D^- multiplicity distribution is used to determine the efficiency correction based off the cuts in Table 6.12.

6.6.2 Reconstruction Efficiencies

MC samples for each of the new processes introduced above the $D\bar{D}$ threshold were generated in the same way as for the continuum data. The reconstruction efficiencies for each are shown in Table 6.14. Values for $D^0\bar{D}^0$ and D^+D^- have been multiplied by the correction factors discussed in Section 6.6.1.

For the cross section of $\gamma\psi(2S)$, rather than the radiative return formula (as used with $\gamma J/\psi$), we use cross section results from CLEO-c [59] and BESIII [60]. These values are $\sigma(e^+e^- \rightarrow \gamma\psi(2S), \psi(2S) \rightarrow \pi^+\pi^-J/\psi) = (1036 \pm 13 \pm 23) \text{ pb}$ from the CLEO-c measurement, and $\Gamma(\psi(2S) \rightarrow \pi^+\pi^-J/\psi) = (34.43 \pm 0.30) \%$ after averaging the BESIII measurement with the value from the PDG. From this, we determine

$$\sigma(e^+e^- \rightarrow \gamma\psi') = \frac{\sigma(e^+e^- \rightarrow \gamma\psi', \psi' \rightarrow \pi^+\pi^-J/\psi)}{\Gamma(\psi' \rightarrow \pi^+\pi^-J/\psi)} = (3009 \pm 81) \text{ pb}. \quad (6.5)$$

Additionally, the $D^0\bar{D}^0$ and D^+D^- cross sections are taken from the BESIII on-peak $\psi(3770)$ measurement performed by Derrick Toth [44].

$\psi(3770)$ (R1) Reconstruction				
Sample	σ [nb]	ϵ_{MC} (SHAD) [%]	ϵ_{MC} (LHAD) [%]	ϵ_{MC} (THAD) [%]
$D^0\bar{D}^0$	3.615	73.9324 ± 0.0142	79.8496 ± 0.0147	60.3601 ± 0.0128
D^+D^-	2.830	61.4048 ± 0.0146	68.8212 ± 0.0154	49.4007 ± 0.0131
$\tau^+\tau^-$	2.652	12.7566 ± 0.0253	28.0142 ± 0.0374	9.8776 ± 0.0222
$\gamma J/\psi$	0.986	46.6185 ± 0.0206	56.2494 ± 0.0227	34.7544 ± 0.0178
$\gamma\psi(2S)$	3.009	63.2551 ± 0.0137	69.9696 ± 0.0144	51.5643 ± 0.0123

$\psi(3770)$ (R2) Reconstruction				
Sample	σ [nb]	ϵ_{MC} (SHAD) [%]	ϵ_{MC} (LHAD) [%]	ϵ_{MC} (THAD) [%]
$D^0\bar{D}^0$	3.615	74.5111 ± 0.0097	80.3399 ± 0.0101	61.0386 ± 0.0088
D^+D^-	2.830	61.8444 ± 0.0100	69.1974 ± 0.0106	49.9163 ± 0.0090
$\tau^+\tau^-$	2.652	12.8646 ± 0.0254	28.2140 ± 0.0376	10.0198 ± 0.0224
$\gamma J/\psi$	0.986	47.0066 ± 0.0146	56.6679 ± 0.0161	35.1951 ± 0.0127
$\gamma\psi(2S)$	3.009	63.7345 ± 0.0097	70.4050 ± 0.0102	52.1189 ± 0.0088

Table 6.14: Reconstruction of background samples for the $\psi(3770)$ data.

6.6.3 Signal Amounts

Using the reconstruction efficiencies from Section 6.6.2, we can compute the contribution for each sample. For the $q\bar{q}$ component, we scale the number of hadronic events found in the old continuum data based on Equation (6.4) for both R1 and R2 separately. Due to the uncertainty on the extrapolation procedure, this becomes the dominant source of error in the resulting hadronic event yield. This is also highly susceptible to the assumption of the $\psi(2S)$ shape when analyzing the new continuum points for the extrapolation fit. The resulting numbers of hadronic events are shown in Table 6.15.

$\psi(3770)$ (R1) Results			
Sample	N_{had} (SHAD)	N_{had} (LHAD)	N_{had} (THAD)
Data	15694505 ± 3962	17722728 ± 4210	12580701 ± 3547
$q\bar{q}^\dagger$	8522688 ± 71353	9330411 ± 76320	6789405 ± 61599
$D^0\bar{D}^0$	2477345 ± 534	2675620 ± 560	2022561 ± 473
D^+D^-	1610764 ± 414	1805311 ± 442	1295875 ± 366
$\tau^+\tau^-$	313542 ± 622	688559 ± 922	242781 ± 547
$\gamma J/\psi$	425891 ± 193	513875 ± 213	317504 ± 166
$\gamma\psi(2S)$	1764254 ± 419	1951528 ± 445	1438185 ± 372
Hadrons	490569 ± 71795	658730 ± 76807	401064 ± 61995

$\psi(3770)$ (R2) Results			
Sample	N_{had} (SHAD)	N_{had} (LHAD)	N_{had} (THAD)
Data	33867464 ± 5820	38217129 ± 6182	27271529 ± 5222
$q\bar{q}^\dagger$	18314683 ± 154300	20015495 ± 164688	14644571 ± 133785
$D^0\bar{D}^0$	5330375 ± 738	5747352 ± 770	4366577 ± 662
D^+D^-	3463499 ± 583	3875291 ± 620	2795485 ± 520
$\tau^+\tau^-$	675063 ± 1331	1480514 ± 1972	525781 ± 1175
$\gamma J/\psi$	916819 ± 288	1105253 ± 317	686446 ± 249
$\gamma\psi(2S)$	3795113 ± 603	4192317 ± 636	3103459 ± 541
Hadrons	1179686 ± 155135	1589187 ± 165610	991049 ± 134532

Table 6.15: Hadronic events selected in the $\psi(3770)$ data.

[†]The $q\bar{q}$ contribution is obtained using an extrapolation from the continuum region in which the $\psi(2S)$ is assumed to have a standard Breit-Wigner shape.

6.6.4 Non- $D\bar{D}$ Branching Fraction Exploration (Breit-Wigner)

Illustrative results have been obtained using the Breit-Wigner line shape for $\psi(2S)$ in the continuum subtraction procedure. However, these are not official BESIII results, which will be finalized only after additional data are collected. As the resulting hadronic production is assumed to result only from non- $D\bar{D}$ decays of the $\psi(3770)$, We can determine the cross section as follows:

$$\sigma(\psi(3770) \rightarrow \text{non-}D\bar{D}) = \frac{N_{\text{non-}D\bar{D}}}{\epsilon_{\text{non-}D\bar{D}} \times \mathcal{L}}. \quad (6.6)$$

For the efficiency of non- $D\bar{D}$ events, the value of ϵ_{MC} for $\gamma\psi(2S)$ is used based on an assumption of similar behavior in their decays. Using the standard Breit-Wigner assumption for the $\psi(2S)$, the results for the cross section and branching fraction of non- $D\bar{D}$ decays from $\psi(3770)$ are shown in Tables 6.16 and 6.17.

Sample	$\sigma_{\text{non-}D\bar{D}}$ (SHAD)	$\sigma_{\text{non-}D\bar{D}}$ (LHAD)	$\sigma_{\text{non-}D\bar{D}}$ (THAD)
$\psi(3770)$ (R1)	0.9892 ± 0.1219	1.1679 ± 0.1179	0.9925 ± 0.1291
$\psi(3770)$ (R2)	1.0877 ± 0.1224	1.2926 ± 0.1183	1.1142 ± 0.1298
Lum. Weighted	1.0563 ± 0.1223	1.2528 ± 0.1182	1.0754 ± 0.1296

Table 6.16: Cross sections for $\psi(3770) \rightarrow \text{non-}D\bar{D}$ found using the $\psi(3770)$ data. The $q\bar{q}$ contributions were calculated using the Breit-Wigner formulation for the $\psi(2S)$ component in the continuum extrapolation. Each cross section is in units of [nb]. These results are presented only to illustrate the procedure, and are not official BESIII measurements.

Sample	$\Gamma_{\text{non-}D\bar{D}}$ (SHAD)	$\Gamma_{\text{non-}D\bar{D}}$ (LHAD)	$\Gamma_{\text{non-}D\bar{D}}$ (THAD)
$\psi(3770)$ (R1)	0.1331 ± 0.0183	0.1534 ± 0.0185	0.1334 ± 0.0190
$\psi(3770)$ (R2)	0.1444 ± 0.0186	0.1671 ± 0.0189	0.1474 ± 0.0193
Lum. Weighted	0.1408 ± 0.0185	0.1627 ± 0.0187	0.1430 ± 0.0192

Table 6.17: Branching fractions for $\psi(3770) \rightarrow \text{non-}D\bar{D}$ found using the $\psi(3770)$ data. The $q\bar{q}$ contributions were calculated using the Breit-Wigner formulation for the $\psi(2S)$ component in the continuum extrapolation. These results are presented only to illustrate the procedure, and are not official BESIII measurements.

6.7 $\psi(2S)$ Background Investigation

The most impactful assumption for the measurement of the branching fraction is the cross section shape of $\psi(2S)$ in the continuum region. For the procedure thus far, we have assumed this shape to be a standard Breit-Wigner. Given the drop in relative efficiency for the 3671 (New) data point (see Figure 6.7), it is likely this overestimates the branching fraction (see Table 6.17) by subtracting off too large of a background component for the $\psi(2S)$.

As an alternative comparison, we use the ratio of cross section productions at the resonance peak compared to continuum values,

$$\frac{\sigma_{\text{res}}}{\sigma_{\text{cont}}(E_{\text{cm}})} = \frac{\sqrt{2\pi} (M_{\text{res}} - E_{\text{cm}})^2}{\Gamma_{\text{res}} \times \sigma_{E_{\text{cm}}}}, \quad (6.7)$$

where M_{res} and Γ_{res} are the mass and total width of the resonance, respectively, and $\sigma_{E_{\text{cm}}}$ is the center-of-mass energy spread during collection of the data. For the $\psi(2S)$, with $M_{\psi(2S)} = 3686.1 \text{ MeV}$ and $\Gamma_{\psi(2S)} = 0.299 \text{ MeV}$, assuming an energy spread of $\sigma_{E_{\text{cm}}} = 1.5 \text{ MeV}$ gives $\sigma_{\psi(2S)} \sim 2500 \times \sigma_{\text{cont}}(E_{\text{cm}})$ at $E_{\text{cm}} = 3.665 \text{ GeV}$.

In 2009, BESIII collected 166.25 pb^{-1} of data at $E_{\text{cm}} = 3.686 \text{ GeV}$ and found $(106.41 \pm 0.86) \times 10^6$ events of $\psi(2S)$ decays [61], corresponding to $\sigma_{\psi(2S)} \sim 640 \text{ nb}$. Using Equation (6.7) for each of the continuum points, we obtain the cross section values shown in Table 6.18, where each generally is notably smaller than from the Breit-Wigner assumption.

Sample	E_{cm} [GeV]	$\sigma_{\psi(2S)}$ [nb] (Ratio)	$\sigma_{\psi(2S)}$ [nb] (BW)
3500 (New)	3.496	0.0032	0.0056
3542 (New)	3.538	0.0052	0.0092
3600 (New)	3.596	0.0141	0.0244
3650 (New)	3.644	0.0646	0.1101
3671 (New)	3.665	0.2572	0.4359
3650 (Old)	3.650	0.0879	0.1495

Table 6.18: Cross sections of $\psi(2S)$ calculated using two different methods.

6.7.1 Non- $D\bar{D}$ Branching Fraction Exploration ($\psi(2S)$ from Data)

We repeat the procedure using the cross sections calculated based off Equation (6.7) in place of the Breit-Wigner values (see Table 6.18). This leads to the continuum extrapolations shown in Figures 6.16 to 6.18. The non- $D\bar{D}$ results are shown in Tables 6.19 and 6.20, where the branching fractions are lower on average by around 1.6% compared to the original method.

Sample	$\sigma_{\text{non-}D\bar{D}}$ (SHAD)	$\sigma_{\text{non-}D\bar{D}}$ (LHAD)	$\sigma_{\text{non-}D\bar{D}}$ (THAD)
$\psi(3770)$ (R1)	0.8367 ± 0.1224	1.0157 ± 0.1184	0.8391 ± 0.1297
$\psi(3770)$ (R2)	0.9353 ± 0.1230	1.1406 ± 0.1189	0.9609 ± 0.1304
Lum. Weighted	0.9039 ± 0.1228	1.1008 ± 0.1187	0.9220 ± 0.1302

Table 6.19: Cross sections for $\psi(3770) \rightarrow \text{non-}D\bar{D}$ found using the $\psi(3770)$ data. The $q\bar{q}$ contributions were calculated using $\psi(2S)$ data for the $\psi(2S)$ components in the continuum extrapolation. Each cross section is in units of [nb]. These results are presented only to illustrate the procedure, and are not official BESIII measurements.

Sample	$\Gamma_{\text{non-}D\bar{D}}$ (SHAD)	$\Gamma_{\text{non-}D\bar{D}}$ (LHAD)	$\Gamma_{\text{non-}D\bar{D}}$ (THAD)
$\psi(3770)$ (R1)	0.1149 ± 0.0180	0.1361 ± 0.0181	0.1152 ± 0.0188
$\psi(3770)$ (R2)	0.1267 ± 0.0183	0.1504 ± 0.0185	0.1297 ± 0.0190
Lum. Weighted	0.1230 ± 0.0182	0.1458 ± 0.0183	0.1251 ± 0.0190

Table 6.20: Branching fractions for $\psi(3770) \rightarrow \text{non-}D\bar{D}$ found using the $\psi(3770)$ data. The $q\bar{q}$ contributions were calculated using $\psi(2S)$ data for the $\psi(2S)$ components in the continuum extrapolation. These results are presented only to illustrate the procedure, and are not official BESIII measurements.

Efficiency Extrapolation - SHAD

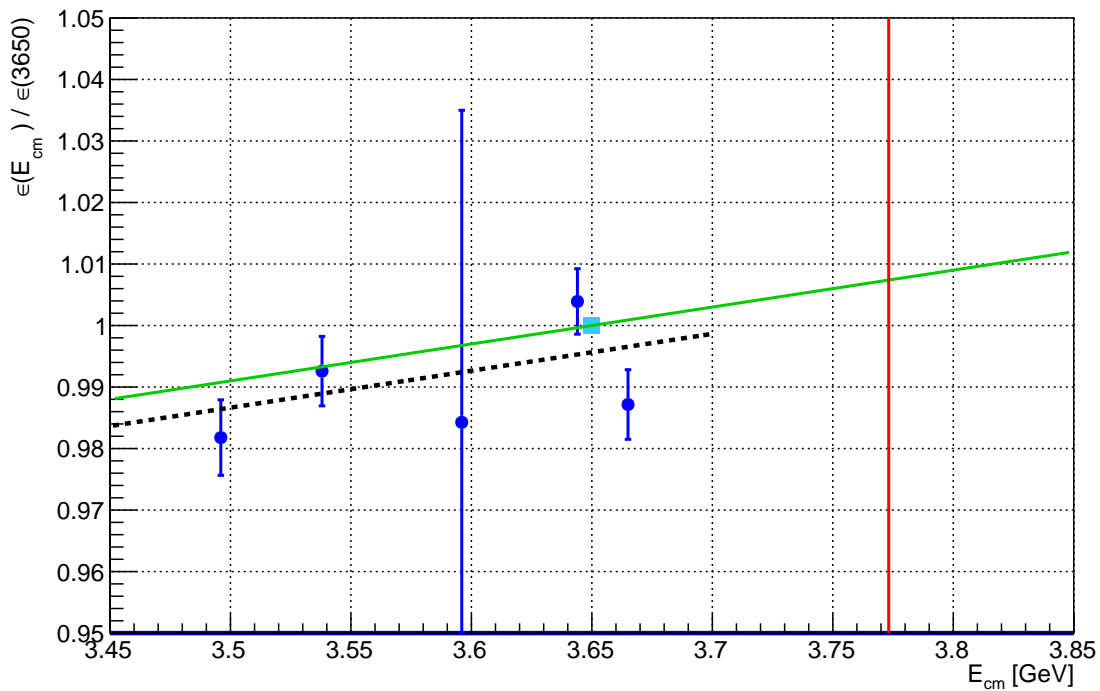


Figure 6.16: The continuum extrapolation for SHAD events using $\psi(2S)$ data. The new continuum points (blue) are fit using a straight line (dashed black), then extrapolated to higher energies (solid green) based on the old continuum point (cyan). The energy point for the $\psi(3770)$ samples at 3.773 GeV is also shown (solid red).

Efficiency Extrapolation - LHAD

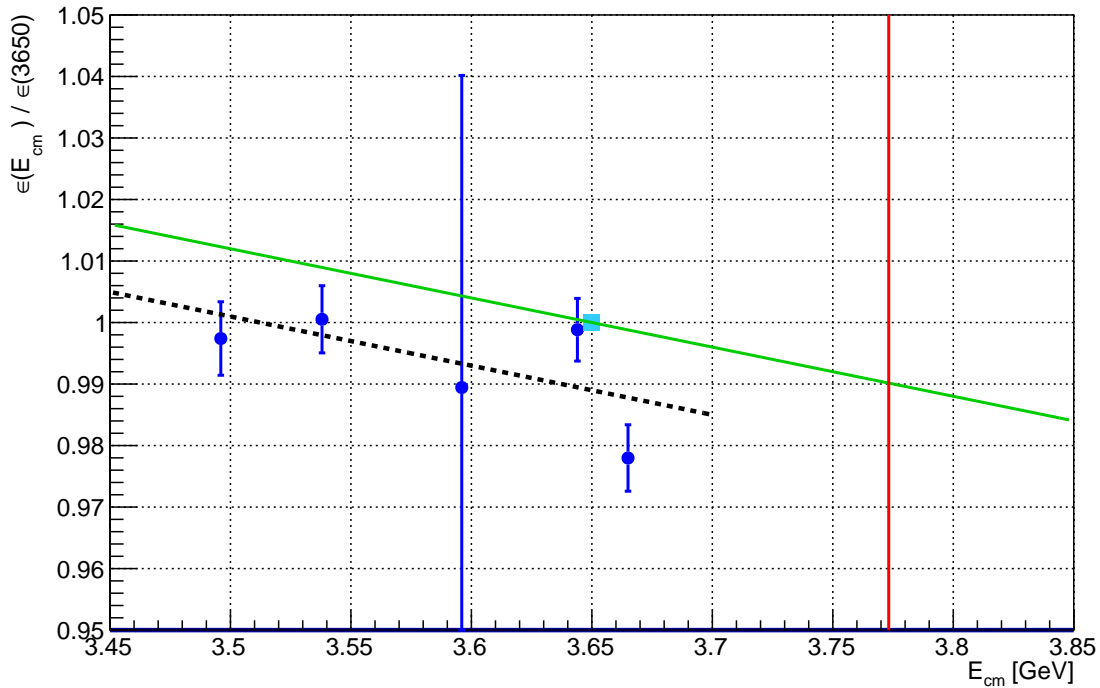


Figure 6.17: The continuum extrapolation for LHAD events using $\psi(2S)$ data. The new continuum points (blue) are fit using a straight line (dashed black), then extrapolated to higher energies (solid green) based on the old continuum point (cyan). The energy point for the $\psi(3770)$ samples at 3.773 GeV is also shown (solid red).

Efficiency Extrapolation - THAD

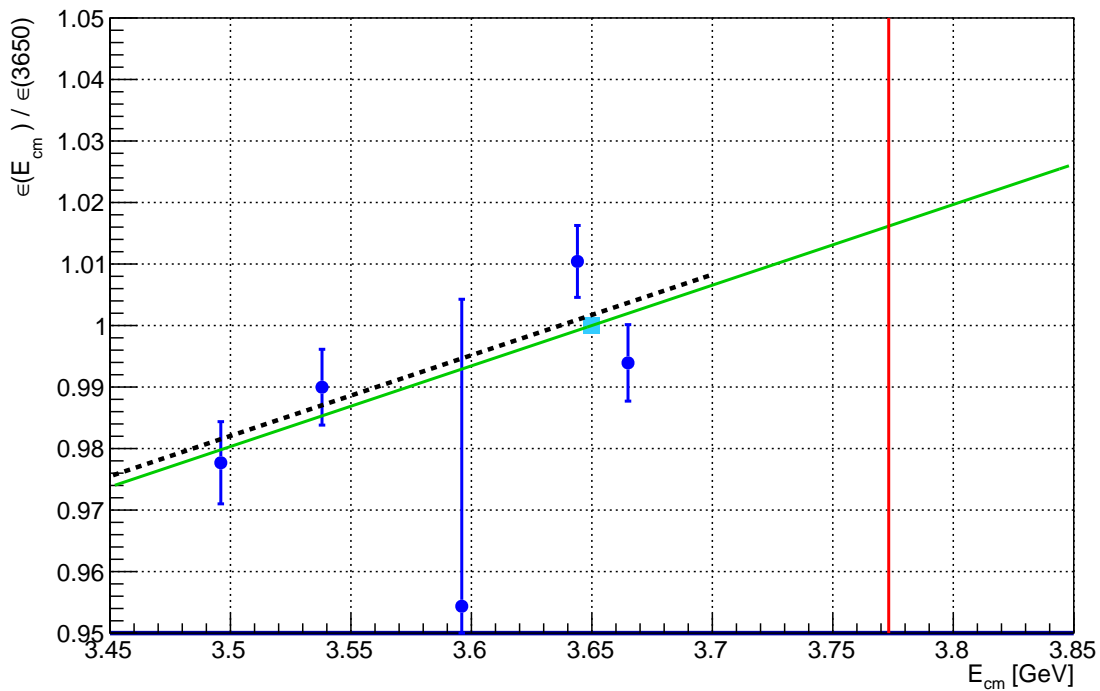


Figure 6.18: The continuum extrapolation for THAD events using $\psi(2S)$ data. The new continuum points (blue) are fit using a straight line (dashed black), then extrapolated to higher energies (solid green) based on the old continuum point (cyan). The energy point for the $\psi(3770)$ samples at 3.773 GeV is also shown (solid red).

6.7.2 Non- $D\bar{D}$ Branching Fraction Exploration ($\psi(2S)$ Excluded)

From our initial procedure, the Breit-Wigner formulation likely provides an upper bound to the non- $D\bar{D}$ branching fraction. Additionally, the modification detailed in Section 6.7 provides an estimation of the actual value, but neither of these is sufficiently reliable to present a definitive BESIII result. However, we can obtain a lower bound on the branching fraction by repeating the measurement without including a contribution from $\psi(2S)$ events. This will increase the extrapolated reconstruction efficiency fits, as seen in Figures 6.19 to 6.21. As a result, more hadrons are subtracted from the $\psi(3770)$ data, and the corresponding branching fraction is lower, as shown in Tables 6.21 and 6.22.

Sample	$\sigma_{\text{non-}D\bar{D}}$ (SHAD)	$\sigma_{\text{non-}D\bar{D}}$ (LHAD)	$\sigma_{\text{non-}D\bar{D}}$ (THAD)
$\psi(3770)$ (R1)	0.6190 ± 0.1232	0.7986 ± 0.1192	0.6203 ± 0.1305
$\psi(3770)$ (R2)	0.7179 ± 0.1238	0.9239 ± 0.1197	0.7421 ± 0.1313
Lum. Weighted	0.6864 ± 0.1236	0.8839 ± 0.1195	0.7033 ± 0.1311

Table 6.21: Cross sections for $\psi(3770) \rightarrow \text{non-}D\bar{D}$ found using the $\psi(3770)$ data. The $q\bar{q}$ contributions were calculated after excluding the $\psi(2S)$ components in the continuum extrapolation. Each cross section is in units of [nb]. These results are presented only to illustrate the procedure, and are not official BESIII measurements.

Sample	$\Gamma_{\text{non-}D\bar{D}}$ (SHAD)	$\Gamma_{\text{non-}D\bar{D}}$ (LHAD)	$\Gamma_{\text{non-}D\bar{D}}$ (THAD)
$\psi(3770)$ (R1)	0.0876 ± 0.0178	0.1102 ± 0.0176	0.0878 ± 0.0187
$\psi(3770)$ (R2)	0.1002 ± 0.0180	0.1254 ± 0.0179	0.1033 ± 0.0188
Lum. Weighted	0.0962 ± 0.0179	0.1205 ± 0.0178	0.0983 ± 0.0188

Table 6.22: Branching fractions for $\psi(3770) \rightarrow \text{non-}D\bar{D}$ found using the $\psi(3770)$ data. The $q\bar{q}$ contributions were calculated after excluding the $\psi(2S)$ components in the continuum extrapolation. These results are presented only to illustrate the procedure, and are not official BESIII measurements.

Efficiency Extrapolation - SHAD

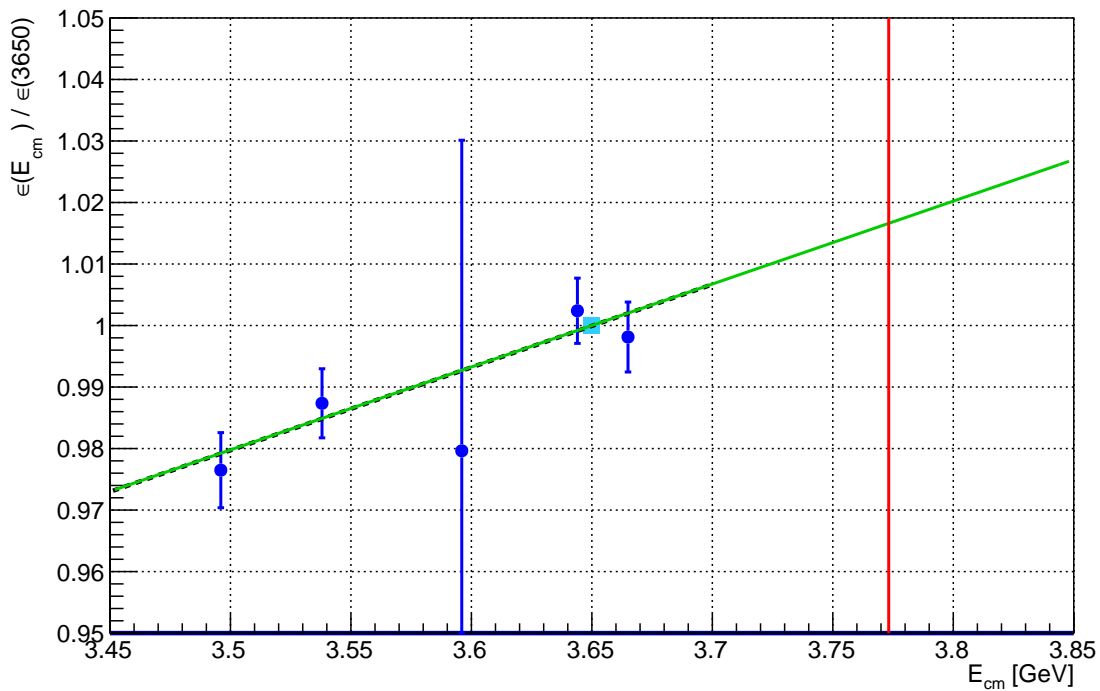


Figure 6.19: The continuum extrapolation for SHAD events without $\psi(2S)$ events. The new continuum points (blue) are fit using a straight line (dashed black), then extrapolated to higher energies (solid green) based on the old continuum point (cyan). The energy point for the $\psi(3770)$ samples at 3.773 GeV is also shown (solid red).

Efficiency Extrapolation - LHAD

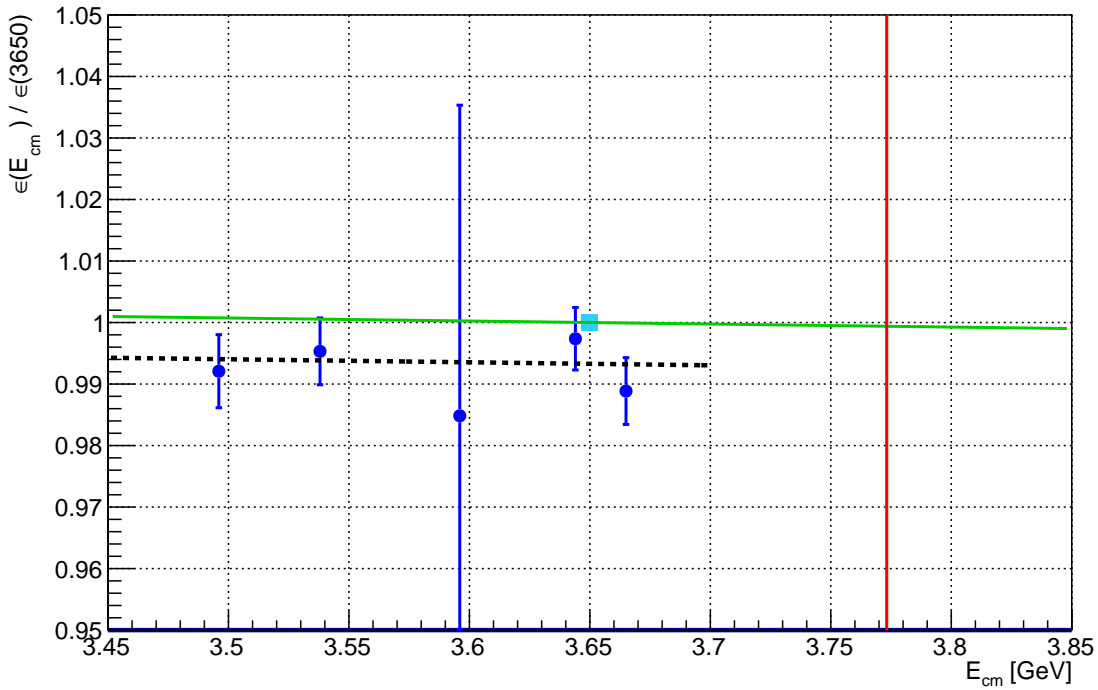


Figure 6.20: The continuum extrapolation for LHAD events without $\psi(2S)$ events. The new continuum points (blue) are fit using a straight line (dashed black), then extrapolated to higher energies (solid green) based on the old continuum point (cyan). The energy point for the $\psi(3770)$ samples at 3.773 GeV is also shown (solid red).

Efficiency Extrapolation - THAD

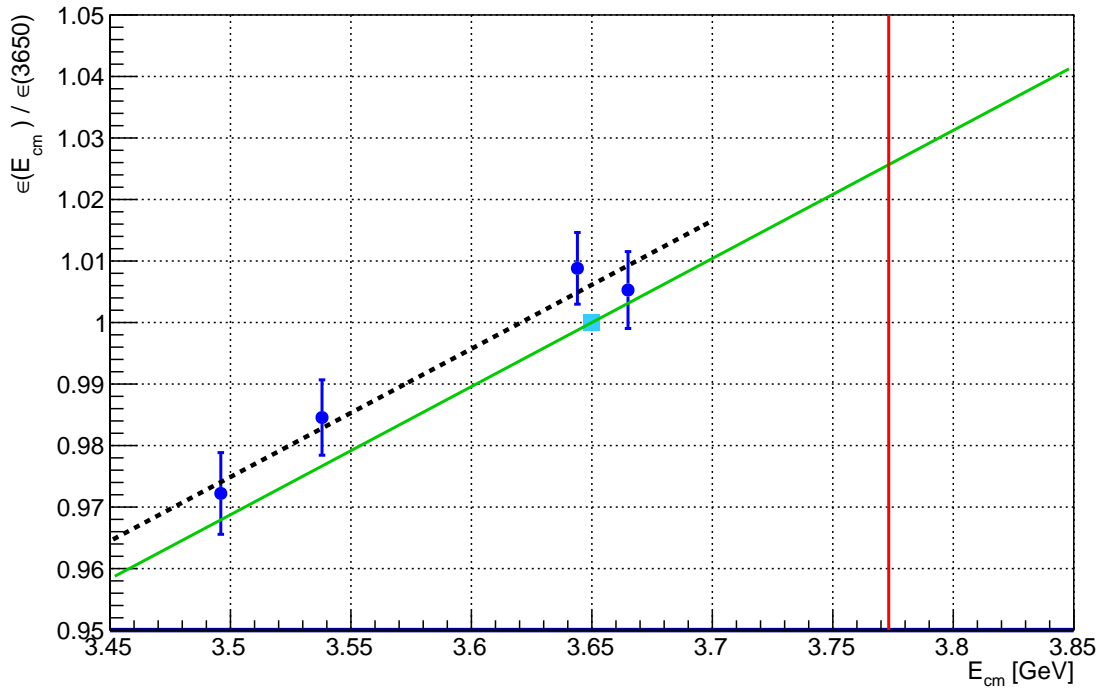


Figure 6.21: The continuum extrapolation for THAD events without $\psi(2S)$ events. The new continuum points (blue) are fit using a straight line (dashed black), then extrapolated to higher energies (solid green) based on the old continuum point (cyan). The energy point for the $\psi(3770)$ samples at 3.773 GeV is also shown (solid red).

6.8 Procedure for Scan Data

In addition to the $\psi(3770)$ data, we also examine the energy points of the scan data. While the statistics for these points are far lower, it will provide insight for the behavior of hadronic production with changing center-of-mass energy. We use $\psi(2S)$ data in order to extrapolate the $q\bar{q}$ events throughout this region (see Section 6.7.1).

Each scan data point used will be referred to by its name listed in Table 6.23. The cross sections for all background samples are also listed, where the $D\bar{D}$ values are taken from the results in Table 5.18. To determine the cross sections of $\gamma\psi(2S)$ at each point, the values were calculated using the standard radiative formula (as for $\gamma J/\psi$), then scaled by the ratio of the data-driven value from Equation (6.5) to the value of this formula at 3.773 GeV.

The total hadronic counting fits for the scan data can be found in Appendix D. As the $\psi(3770)$ R1 data was taken at a similar time as the scan data, we use the same $D\bar{D}$ corrections from R1 for all of the scan data sample points. The reconstruction efficiencies and signal amounts can be found in Appendices E and F, respectively.

In addition to the non- $D\bar{D}$ branching fraction, we can also examine the inclusive hadronic cross section as a function of center-of-mass energy: Dividing the fit counts for each selection method from Appendix D by the luminosities from Table 5.3, we find the inclusive cross sections shown in Figure 6.22. These values are independent of the extrapolation procedure.

The non- $D\bar{D}$ cross sections and branching ratios calculated for each scan point are shown in Figures 6.23 and 6.24, respectively. For comparison, the same calculation for the $\psi(3770)$ data is also shown on each of these plots. Due to the uncertain cross section shape of the $\psi(2S)$ required to properly extrapolate to the scan data region, these values are not representative of a true measurement for the branching fraction. For now, we have done our best to ensure the accuracy of all other background components analyzed. This means, with an improved understanding of the $\psi(2S)$ cross section in the continuum region (likely to be analyzed in the very near future, as BESIII has data taking planned for this region), the branching fraction value can easily be updated for a final result.

Sample	E_{cm} [GeV]	$D^0 \bar{D}^0$	$D^+ D^-$	$\tau^+ \tau^-$	$\gamma J/\psi$	$\gamma \psi(2S)$
3734 (Scan)	3.7342	0.164	0.000	2.467	1.060	5.359
3736 (Scan)	3.7368	0.218	0.000	2.475	1.055	5.094
3744 (Scan)	3.7447	0.765	0.150	2.514	1.039	4.428
3748 (Scan)	3.7483	0.838	0.360	2.522	1.032	4.180
3750 (Scan)	3.7501	0.968	0.439	2.533	1.029	4.065
3751 (Scan)	3.7517	1.237	0.574	2.542	1.025	3.969
3753 (Scan)	3.7534	1.377	0.748	2.553	1.022	3.871
3755 (Scan)	3.7556	1.566	0.797	2.562	1.018	3.752
3756 (Scan)	3.7562	1.629	0.914	2.573	1.017	3.721
3759 (Scan)	3.7592	1.948	1.192	2.584	1.011	3.572
3762 (Scan)	3.7624	2.385	1.534	2.598	1.005	3.426
3765 (Scan)	3.7650	2.715	1.882	2.613	1.000	3.315
3767 (Scan)	3.7676	3.102	2.200	2.627	0.995	3.212
3771 (Scan)	3.7713	3.406	2.634	2.641	0.989	3.075
3774 (Scan)	3.7742	3.714	3.067	2.656	0.983	2.975
3777 (Scan)	3.7775	3.692	3.078	2.669	0.978	2.870
3780 (Scan)	3.7802	3.444	2.599	2.683	0.973	2.788
3782 (Scan)	3.7829	2.791	2.206	2.696	0.968	2.712
3786 (Scan)	3.7869	1.995	1.627	2.709	0.961	2.605
3789 (Scan)	3.7891	1.361	1.178	2.722	0.957	2.550
3792 (Scan)	3.7926	0.920	0.680	2.739	0.951	2.467
3797 (Scan)	3.7970	0.562	0.414	2.755	0.944	2.370
3800 (Scan)	3.8003	0.424	0.241	2.771	0.938	2.301
3802 (Scan)	3.8024	0.325	0.236	2.784	0.935	2.260
3807 (Scan)	3.8070	0.352	0.289	2.795	0.927	2.174
3809 (Scan)	3.8093	0.233	0.132	2.807	0.923	2.133
3813 (Scan)	3.8135	0.060	0.153	2.819	0.917	2.063
3815 (Scan)	3.8153	0.056	0.089	2.829	0.914	2.034
3822 (Scan)	3.8229	0.140	0.197	2.859	0.902	1.920
3832 (Scan)	3.8320	0.069	0.046	2.887	0.888	1.799
3839 (Scan)	3.8390	0.237	0.254	2.914	0.877	1.716
3849 (Scan)	3.8494	0.186	0.186	2.939	0.862	1.604
3855 (Scan)	3.8555	0.337	0.273	2.967	0.853	1.545
3863 (Scan)	3.8632	0.340	0.099	2.988	0.843	1.476

Table 6.23: Energy values and background cross sections for the scan data.
Each cross section listed is in units of [nb].

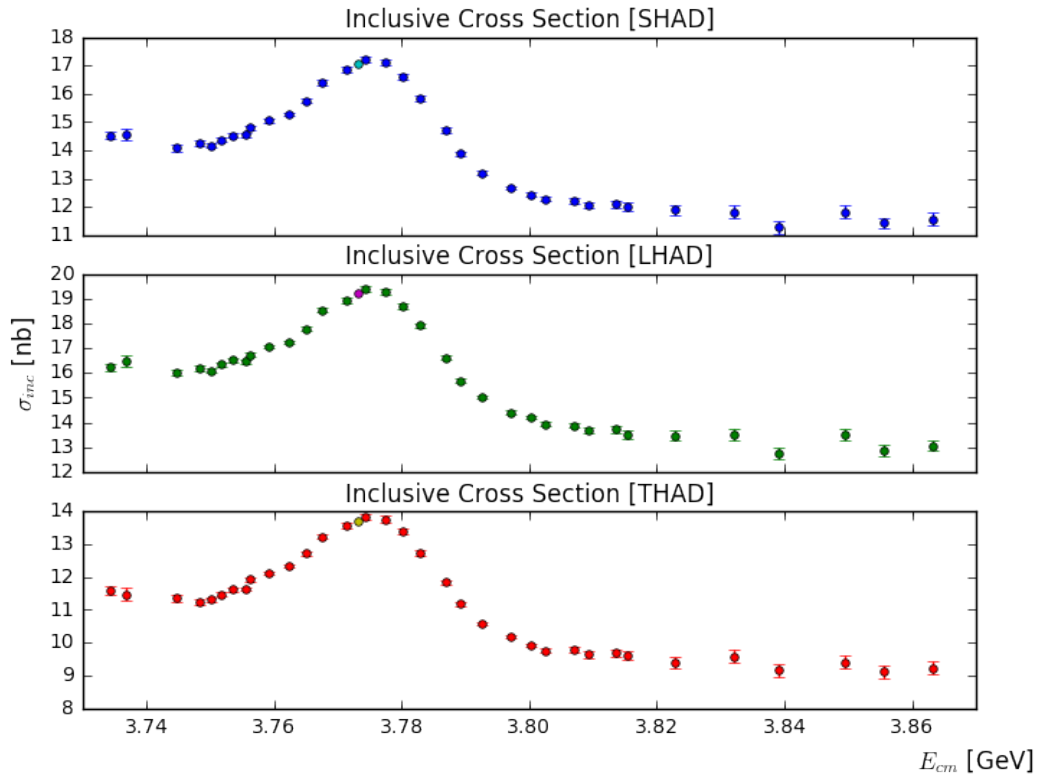


Figure 6.22: The inclusive cross sections measured for the scan data region. The cyan, purple, and yellow points correspond to the luminosity-averaged inclusive cross sections measured for the $\psi(3770)$ data.

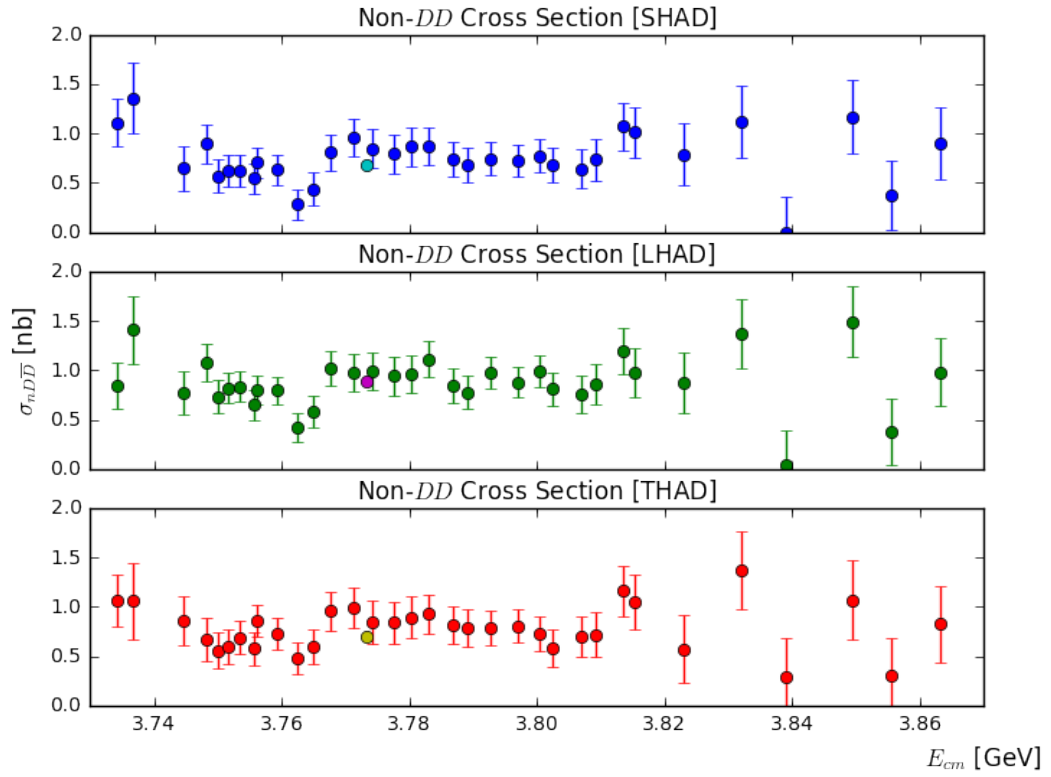


Figure 6.23: The non- $D\bar{D}$ cross sections measured for the scan data region. The cyan, purple, and yellow points correspond to the luminosity-averaged non- $D\bar{D}$ cross sections measured for the $\psi(3770)$ data.

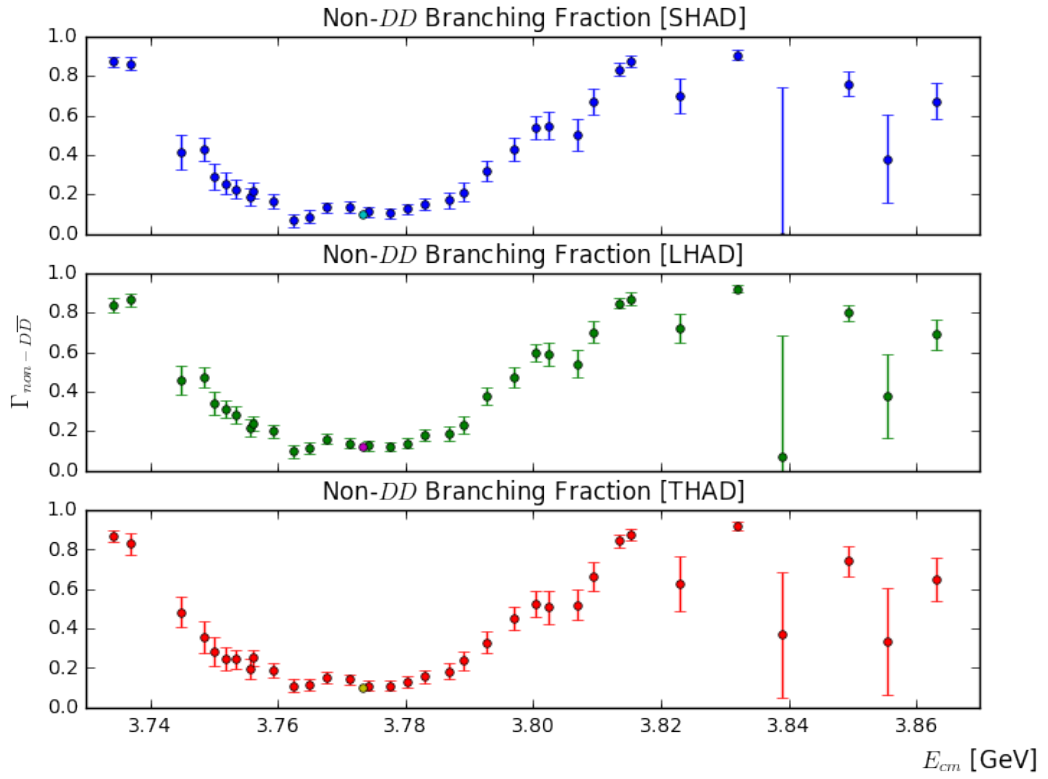


Figure 6.24: The non- $D\bar{D}$ branching fractions measured for the scan data region. The cyan, purple, and yellow points correspond to the luminosity-averaged non- $D\bar{D}$ branching fractions measured for the $\psi(3770)$ data.

Chapter 7

Conclusion

Using the high statistics $e^+e^- \rightarrow \psi(3770)$ collision data available at BESIII, we have measured $\sigma(\psi(3770) \rightarrow D\bar{D})$ as a function of center-of-mass energy more precisely than ever before. In this analysis, we have verified the necessity of including the effect of interference from the $\psi(2S)$. Namely, the vanishing Born cross section near 3.81 GeV can only be fitted with destructive interference. Our measured $\psi(3770)$ parameters differ from world averages while being consistent with the much less precise measured values from KEDR.

While the results for the $\psi(3770) \rightarrow D\bar{D}$ cross section are significant, there are certain aspects which indicate the need for future study. Most notably, while the form factors used both show excellent agreement in the peak region of the $\psi(3770)$, several points at higher energies, namely in the range 3.81 GeV to 3.82 GeV, show significant discrepancy. However, the difficulty fitting the high-side energy dependence has minimal effect on measuring the parameters of the $\psi(3770)$, which are dominated by the cross section shape near the peak. A more sophisticated analysis would improve the model in the higher energy region, such as by using a Breit-Wigner shape for the $\psi(4040)$ instead of a constant parameter, or by exploring potential contributions from other resonances, such as near 3.9 GeV. Other improvements would require minimizing the uncertainty on the cross section parameters involved in the fit, namely the meson radii. The question of how to incorporate Coulomb interactions, if at all, also remains open.

The information provided by the $D\bar{D}$ cross section has also allowed us to investigate $\Gamma(\psi(3770) \rightarrow \text{non-}D\bar{D})$. As it is not feasible to directly distinguish between $q\bar{q}$ and $D\bar{D}$

events produced above the open-charm threshold, obtaining this component must use information from below this region. Based on the data available at BESIII, our methodology for this process involved extrapolating from center-of-mass energies just below the $\psi(2S)$ resonance. However, this procedure is heavily reliant on our understanding of the $\psi(2S)$ cross section shape. Without additional experimental information, the final results are not well constrained. Instead, the best we can provide at this time are bounds on the non- $D\bar{D}$ branching fraction. The results are consistent with previous measurements from BESII, though the uncertainties on their measurements are large. However, the non- $D\bar{D}$ results presented here are preliminary, and should not be quoted as official BESIII results.

Better understanding the $\psi(3770) \rightarrow$ non- $D\bar{D}$ branching fraction requires a precise study of the $\psi(2S)$ cross section in the range of the continuum data. BESIII has plans for data taking in this region during the 2017-2018 run. This will help determine the effects of interference between the $\psi(2S)$ resonance and the continuum region around it. Once precise $\psi(2S)$ cross section values are obtained at each of the continuum energy points, our analysis will be updated to produce a measurement of the branching fraction based on the current BESIII $\psi(3770)$ data sample. It remains to be seen, however, if the understanding of the continuum subtraction will be sufficient to reduce the systematic uncertainty appreciably from the current preliminary result.

For now, we have found very precise measurements of $\sigma(\psi(3770) \rightarrow D\bar{D})$ and $\sigma(e^+e^- \rightarrow (\text{hadrons}))$ over the energy range near the $\psi(3770)$. The former determines multiple parameters of the $\psi(3770)$, such as $M^{\psi(3770)}$, $\Gamma^{\psi(3770)}$, and $\Gamma_{ee}^{\psi(3770) \rightarrow D\bar{D}}$. Each of these can immediately benefit other analyses throughout this region. While not as imminent, combining our results with additional knowledge of the $\psi(2S)$ cross section should also lead to a more precise determination of $\Gamma(\psi(3770) \rightarrow \text{non-}D\bar{D})$. This not only can be used to determine the value of $\Gamma_{ee}^{\psi(3770)}$, but will also greatly benefit theories about strong interactions involving mixed state resonances.

References

- [1] M. Ablikim et al. [BES Collaboration], eConf C070805 (2007) 02 [Phys. Lett. B 660 (2008) 315].
- [2] J. Brodzicka et al. [Belle Collaboration], Phys. Rev. Lett. 100 (2008) 092001.
- [3] B. Aubert et al. [BABAR Collaboration], Phys. Rev. D 77 (2008) 011102.
- [4] B. Aubert et al., Phys. Rev. D 76 (2007) 111105(R).
- [5] V. V. Anashin *et al.*, Phys. Lett. B **711**, 292 (2012) [arXiv:1109.4205 [hep-ex]].
- [6] K.A. Olive et al. (Particle Data Group), Chin. Phys. C, **38**, 090001 (2014).
- [7] Wikimedia Commons. Standard model of elementary particles. 2006.
- [8] C. S. Wu, E. Ambler, R. W. Hayward, D. D. Hoppes, and R. P. Hudson Phys. Rev. **105**, 1413 (1957).
- [9] J. H. Christenson, J. W. Cronin, V. L. Fitch, and R. Turlay Phys. Rev. Lett. **13**, 138 (1964).
- [10] M. Ablikim et al. (BESIII Collaboration) Phys. Rev. Lett. **110**, 252001 (2013).
- [11] Z. Q. Liu et al. (Belle Collaboration) Phys. Rev. Lett. **110**, 252002 (2013).
- [12] R. Aaij et al. (LHCb Collaboration) Phys. Rev. Lett. **115**, 072001 (2015).
- [13] M. Kobayashi and T. Maskawa, “CP-Violation in the Renormalizable Theory of Weak Interaction”. Prog. Theor. Phys. 1973; 49 (2): 652-657. [doi: 10.1143/PTP.49.652]

- [14] S. L. Glashow, J. Iliopoulos, and L. Maiani Phys. Rev. D **2**, 1285 (1970).
- [15] B. Pontecorvo. (1957). “Inverse beta processes and nonconservation of lepton charge”. Zhurnal eksperimentalno i Teoreticheskogo Fiziki. **34**: 247. reproduced and translated in Soviet Physics JETP. 7: 172. 1958.
- [16] Z. Maki, M. Nakagawa, S. Sakata. (1962). “Remarks on the Unified Model of Elementary Particles”. Progress of Theoretical Physics. **28**: 870.
- [17] J. L. Rosner, Phys. Rev. D **64**, 094002 (2001) [hep-ph/0105327].
- [18] J. L. Rosner, Annals Phys. **319**, 1 (2005) [hep-ph/0411003].
- [19] S. Okubo, Phys. Lett. **5**, 165 (1963).
- [20] G. Zweig, Developments in the Quark Theory of Hadrons, Volume 1. Edited by D. Lichtenberg and S. Rosen. pp. 22-101
- [21] J. Iizuka, K. Okada and O. Shito, Prog. Theor. Phys. **35**, 1061 (1966).
- [22] E. A. Kuraev and V. S. Fadin, Sov. J. Nucl. Phys. **41**, 466 (1985) [Yad. Fiz. **41**, 733 (1985)].
- [23] J. M. Blatt and V. F. Weisskopf, Theoretical Nuclear Physics, Wiley, New York, (1952).
- [24] M. Ablikim *et al.* [BESIII Collaboration], Nucl. Instrum. Meth. A **614**, 345 (2010) [arXiv:0911.4960 [physics.ins-det]].
- [25] J. D. Jackson. *Classical Electrodynamics (3rd ed.)*. Wiley. (Section 13.2)
- [26] W. Li, *et al.*, Proc. Int. Conf. Comput. High Energy and Nucl. Phys. 225 (2006).
- [27] See <http://linux.web.cern.ch/linux/scientific5>.
- [28] G. Barrand, I. Belyaev, P. Binko, M. Cattaneo, R. Chytracek, G. Corti, M. Frank and G. Gracia *et al.*, Comput. Phys. Commun. **140**, 45 (2001).
- [29] C. Arnault, “CMT: A software configuration management tool,” (2000).

- [30] See <http://root.cern.ch>.
- [31] S. Agostinelli, *et al.*, Nucl. Instr. and Meth. **506**, (3), 250 (2003); J. Allison, *et al.*, IEEE Trans. Nucl. Sci. NS **53** (1), 270 (2006); See <http://www.geant4.org/geant4>.
- [32] S. Jadach , B. F. L. Ward and Z. Was, Comp. Phys. Commun. **130**, 260 (2000); S. Jadach, B. F. L. Ward and Z. Was, Phys. Rev. D **63**, 113009 (2001).
- [33] S. Jadach, Z. Was, R. Decker and J. H. Kuhn, Comput. Phys. Commun. **76**, 361 (1993).
- [34] See <http://home.thep.lu.se/~torbjorn/Pythia.html>.
- [35] D.J. Lange, Nucl. Instrum. Meth. A **462**, 152 (2001).
- [36] R. G. Ping, Chinese Physics C **32**, 8 (2008).
- [37] E. Barberio, B. van Eijk and Z. Was, Comput. Phys. Commun. **66**, 115 (1991).
- [38] J. C. Chen, G. S. Huang, X. R. Qi, D. H. Zhang and Y. S. Zhu, Phys. Rev. D **62**, 034003 (2000).
- [39] G. Bonneau and F. Martin, Nucl. Phys. B **27**, 381 (1971).
- [40] C.M. Carloni Calame, G. Montagna, O. Nicrosini, F. Piccinini, Nucl. Phys. Proc. Suppl. **131** 48-55 (2004).
- [41] See <http://www.mysql.com/about>.
- [42] R. M. Baltrusaitis *et al.* [MARK-III Collaboration], Phys. Rev. Lett. **56**, 2140 (1986).
- [43] J. Adler *et al.* [MARK-III Collaboration], Phys. Rev. Lett. **60**, 89 (1988).
- [44] D. Toth. (2014). “Measurement of Non- $D\bar{D}$ Decays of the $\psi(3770)$ Resonance at BESIII”.
- [45] L. Dong, “Center-of-mass beam energy calibration for $\psi(3770)$ data with BOSS 6.6.4,” BESIII-doc-284-v6 (2014).

- [46] A. Hafner, “Luminosity Measurement for the $\psi(3770)$ data at BESIII,” BESIII-doc-406-v2 (2015).
- [47] See <https://root.cern.ch/roofit>
- [48] D. M. Asner and W. M. Sun, Phys. Rev. D, **77**, 019901 (2008).
- [49] HFAG 2015 (*CPV*-Allowed) [http://www.slac.stanford.edu/xorg/hfag/charm/CHARM15/results_minimal.html]
- [50] T. Evans et al., Physics Letters B **757** (2016) 520527.
- [51] See <https://root.cern.ch/doc/master/classTMinuit.html>
- [52] M. Ablikim et al. [BESIII Collaboration], Chin. Phys. C, **37**, 12 (2013):12300.
- [53] G. Rong et. al, “Measurements of Branching Fractions and Form Factors for $D^0 \rightarrow K^- e^+ \nu_e, \pi^- e^+ \nu_e$ Decays”, BESIII-doc-125-v3 (2015).
- [54] B. C. Ke et al. [Carnegie Mellon University], “ π^0 Reconstruction Efficiency”, BESIII-doc-446-v4 (2015).
- [55] T. Ma, “Determination of K_S^0 Systematics”, BESIII-doc-125-v3 (2014).
- [56] R. G. Ping, Chin. Phys. C, **38**, 8 (2014):83001.
- [57] M. Abilikim et al., [BESII Collaboration], Phys. Lett. B **659**, 74 (2008).
- [58] D. Besson et al., [CLEO Collaboration], Phys. Rev. Lett. **104**, 159901 (2010) [[arXiv:1004.1358 \[hep-ex\]](https://arxiv.org/abs/1004.1358)].
- [59] N. E. Adam et al., [CLEO Collaboration], Phys. Rev. Lett. **96**, 082004 (2006) [[hep-ex/0508023](https://arxiv.org/abs/hep-ex/0508023)].
- [60] M. Ablikim et al., [BESIII Collaboration], Phys. Rev. D **88**, 023007 (2013) [[arXiv:1307.1189](https://arxiv.org/abs/1307.1189)].
- [61] M. Ablikim et al., [BESIII Collaboration], “Determination of the number of ψ' events at BESIII”, Chin. Phys. C, **37**, 6 (2013).

Appendix A

Glossary and Acronyms

Care has been taken in this thesis to minimize the use of jargon, but this cannot always be achieved. This appendix defines certain terms used in a glossary, and contains a table of acronyms and initialisms used along with their meanings.

A.1 Glossary

A.2 Acronyms / Initialisms

Table A.1: Acronyms and Initialisms

Name	Meaning
BESIII	The third Beijing Spectrometer
IHEP	Institute of High Energy Physics
BEPCII	The second Beijing Electron-Position Collider
MDC	Multi-Layer Drift Chamber
ToF	Time-of-Flight System
EMC	Electromagnetic Calorimeter
MUC	Muon Identifier
PMTs	Photomultipler Tubes

Continued on next page

Table A.1 – Continued from previous page

Acronym	Meaning
RPC	Resistive Plate Counter
ISR	Initial State Radiation
FSR	Final State Radiation
BOSS	BESIII Offline Software System
MC	Monte Carlo
ADC	Analog-to-Digital Conversion
TDC	Time-to-Digital Conversion

Appendix B

D^0 Signal Fits

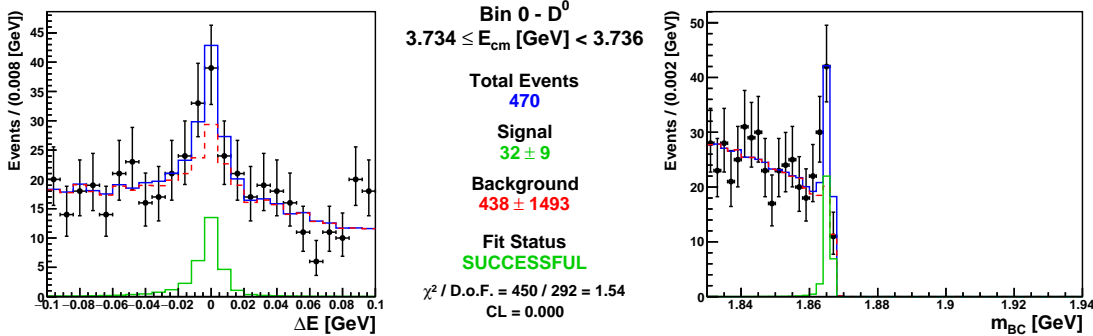


Figure B.1: Projections of the 2D signal fit (ΔE vs. m_{BC}) for D^0 in Bin 0.

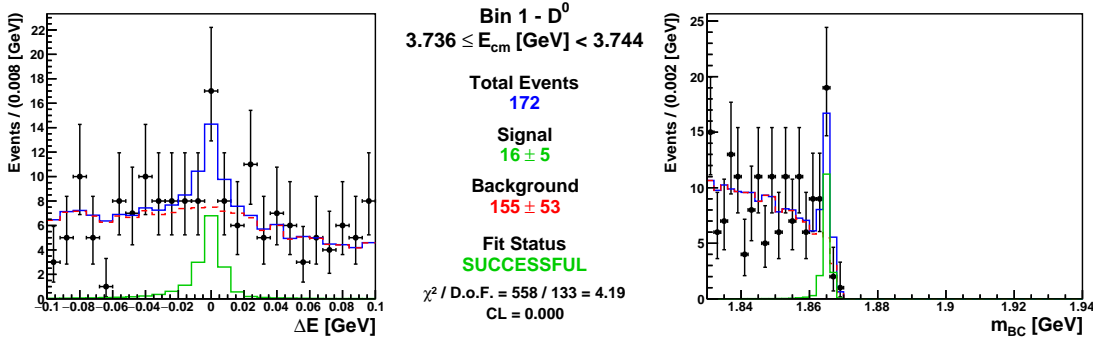
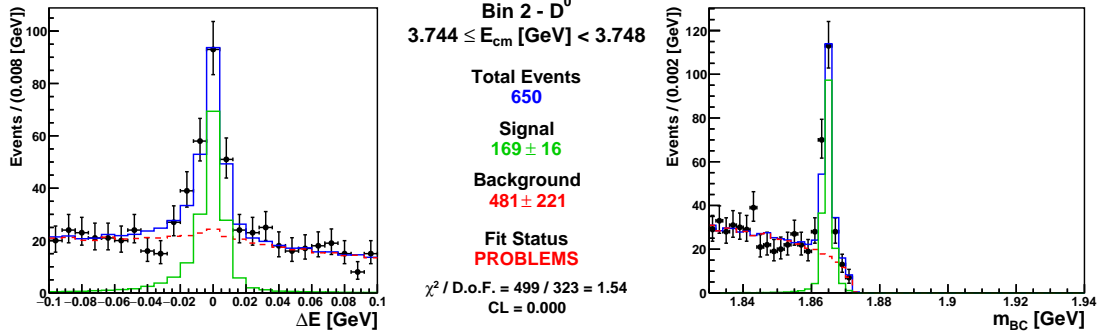
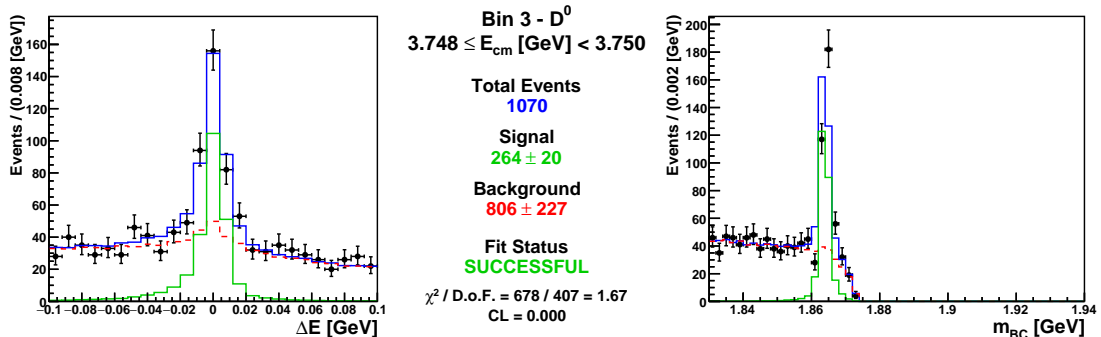
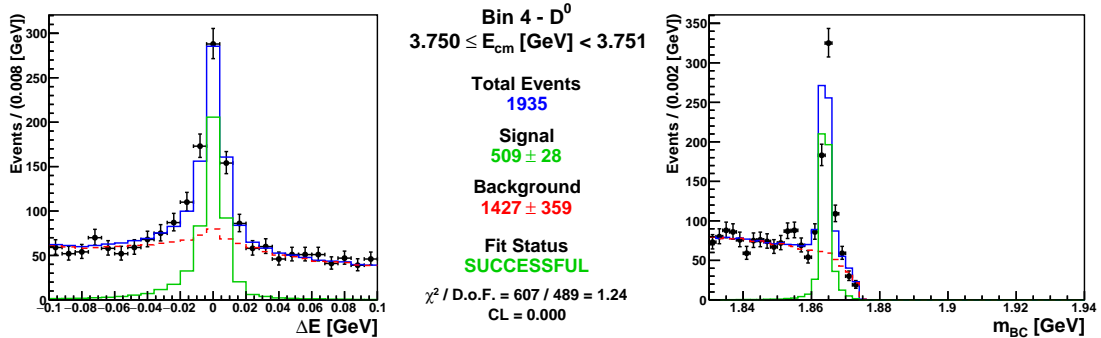
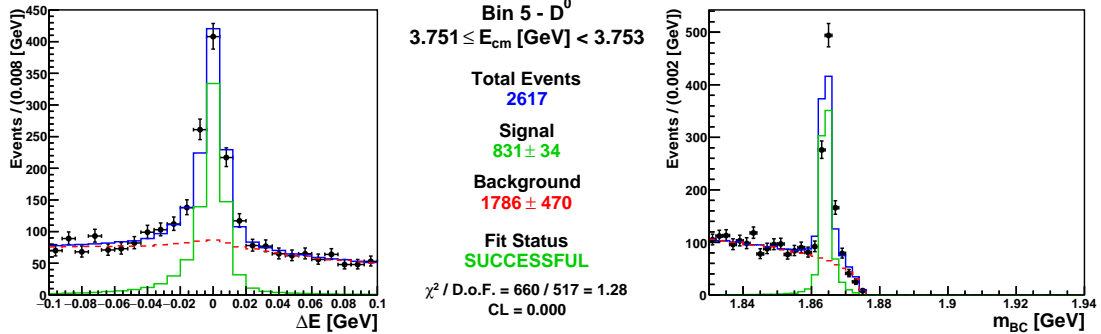
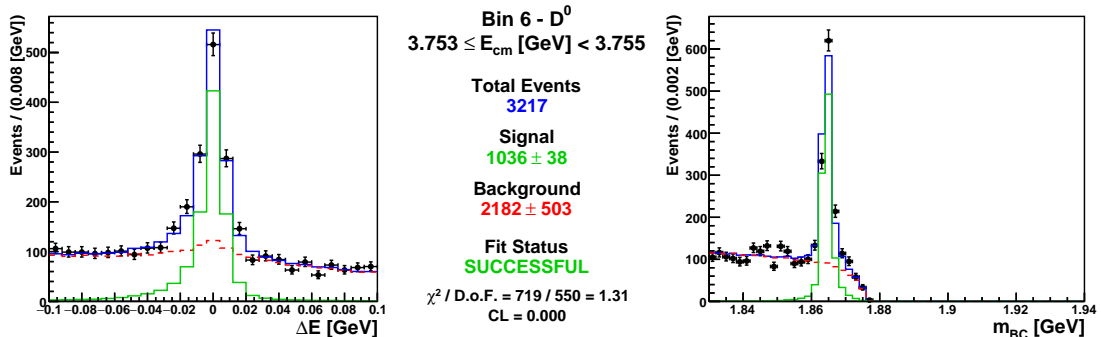
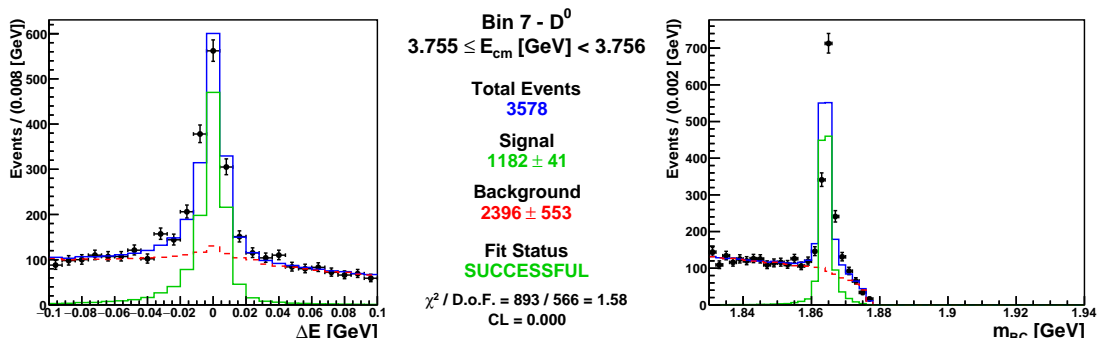
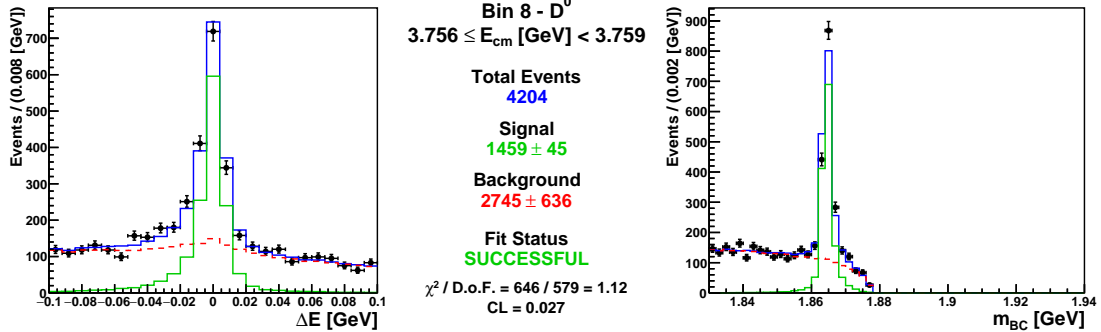
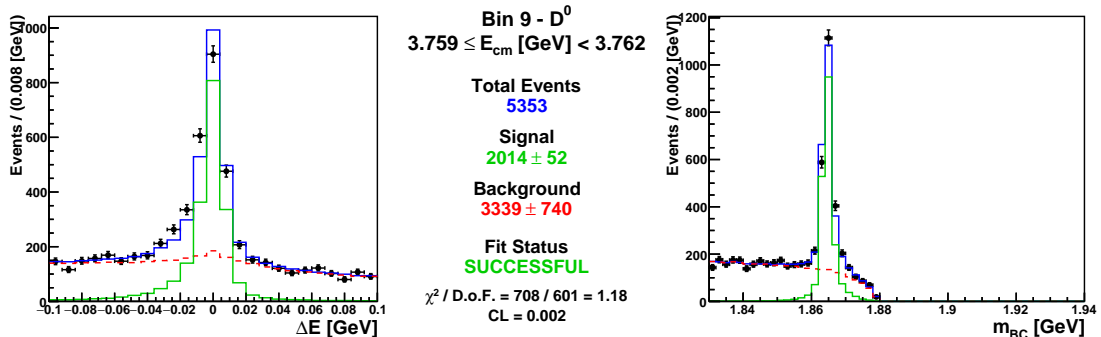
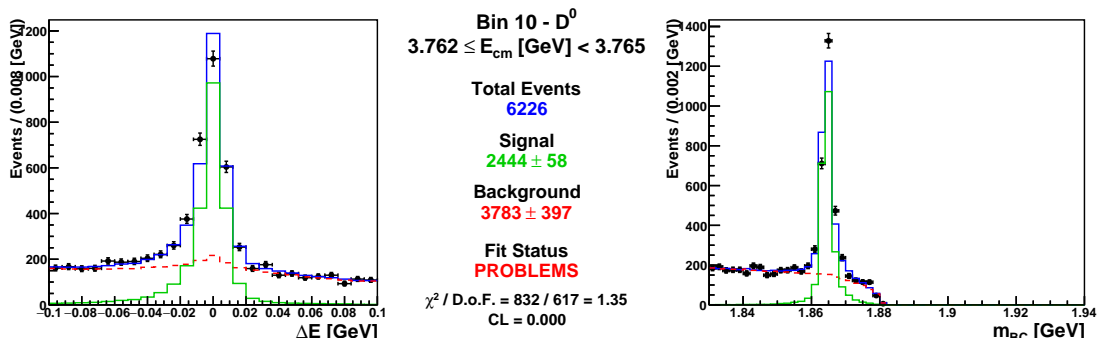
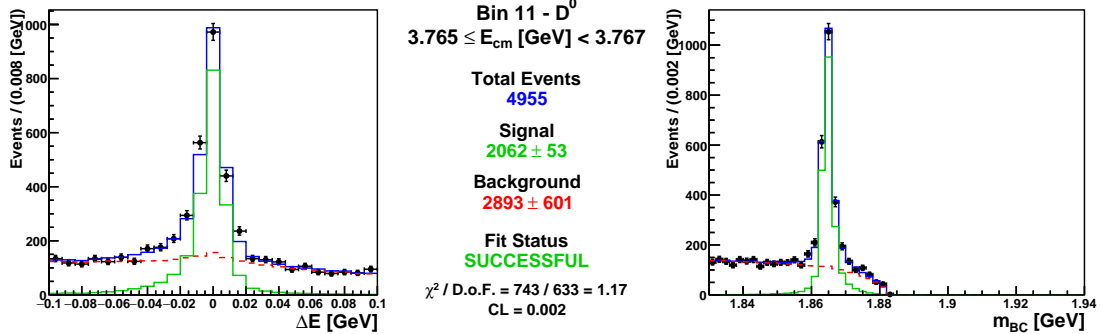
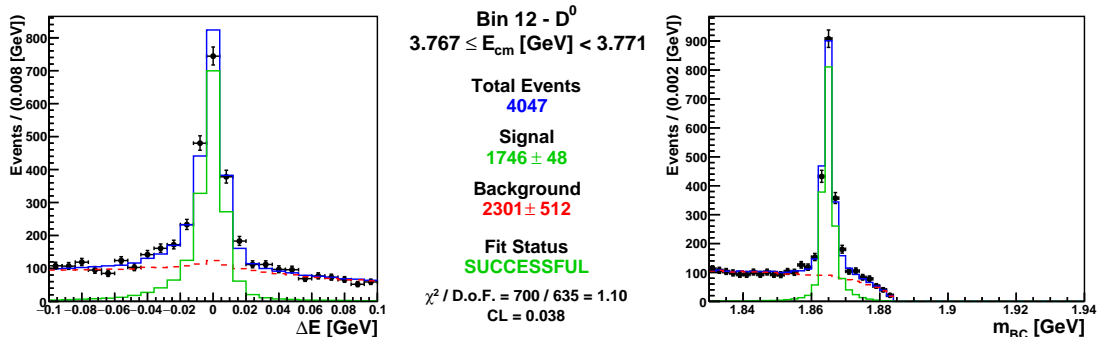
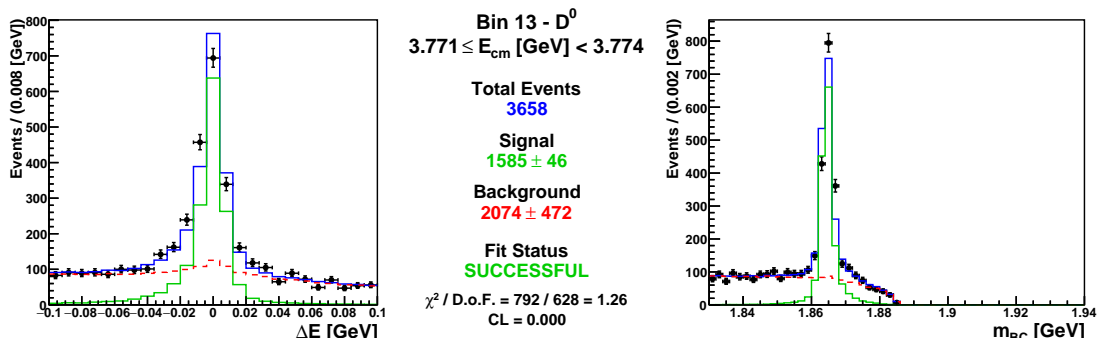


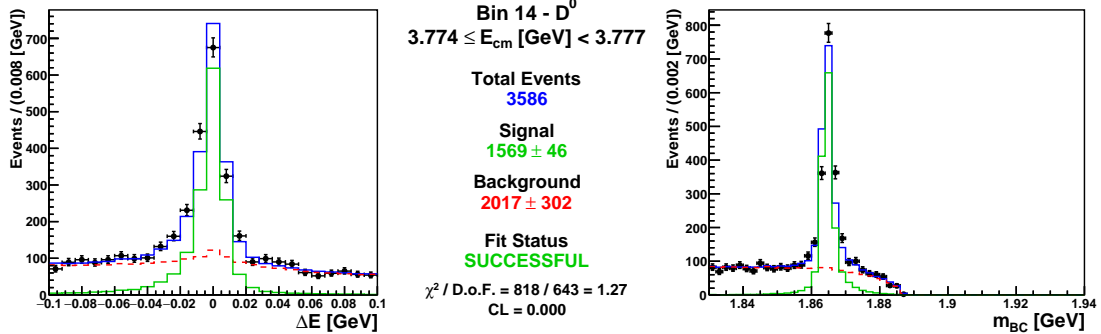
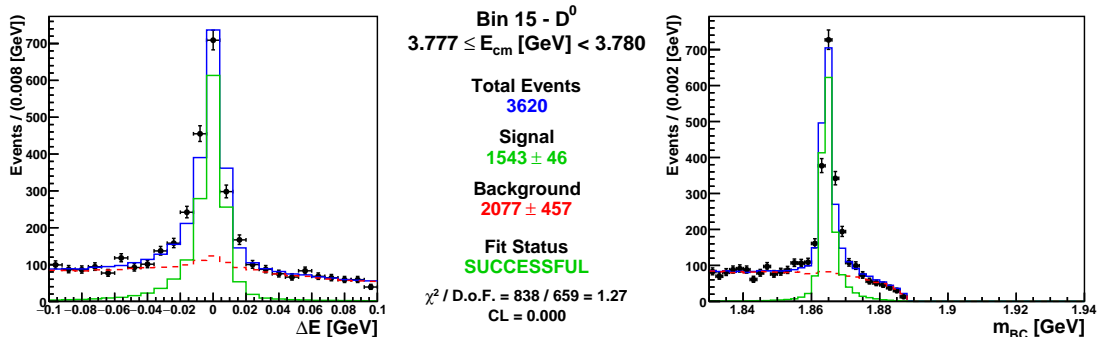
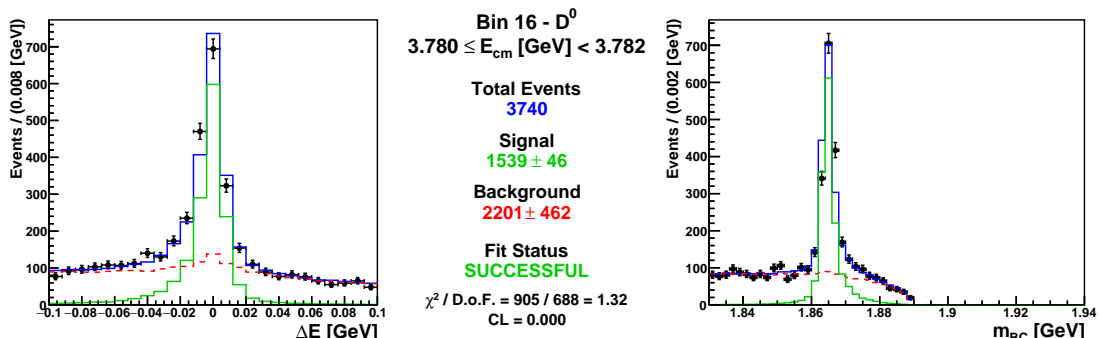
Figure B.2: Projections of the 2D signal fit (ΔE vs. m_{BC}) for D^0 in Bin 1.

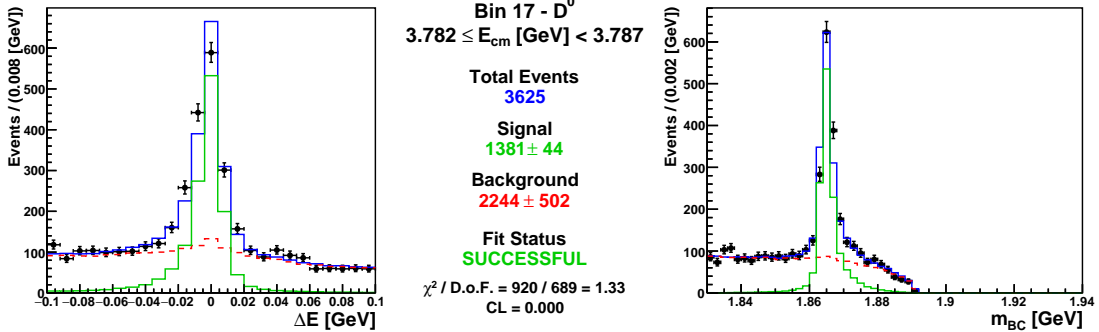
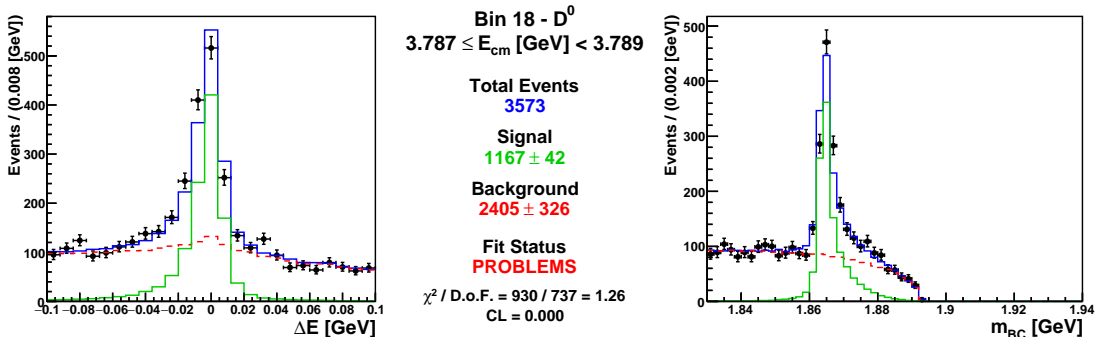
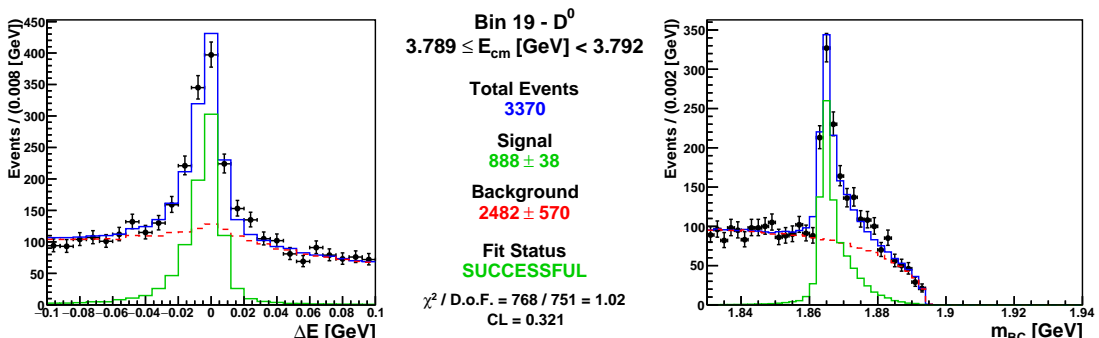
Figure B.3: Projections of the 2D signal fit (ΔE vs. m_{BC}) for D^0 in Bin 2.Figure B.4: Projections of the 2D signal fit (ΔE vs. m_{BC}) for D^0 in Bin 3.Figure B.5: Projections of the 2D signal fit (ΔE vs. m_{BC}) for D^0 in Bin 4.

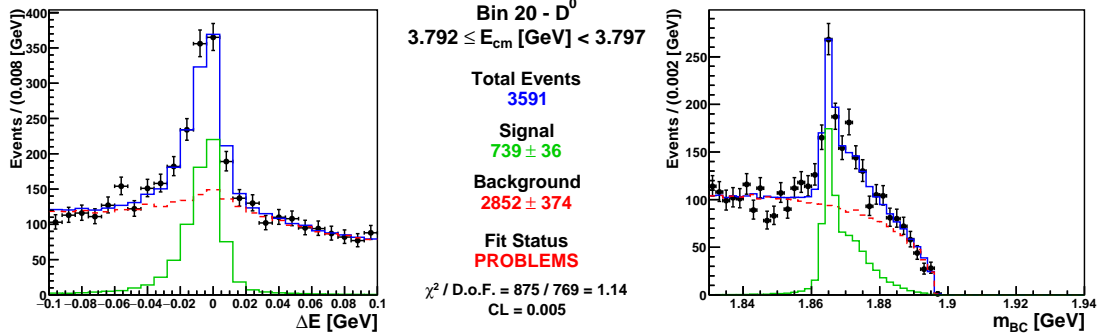
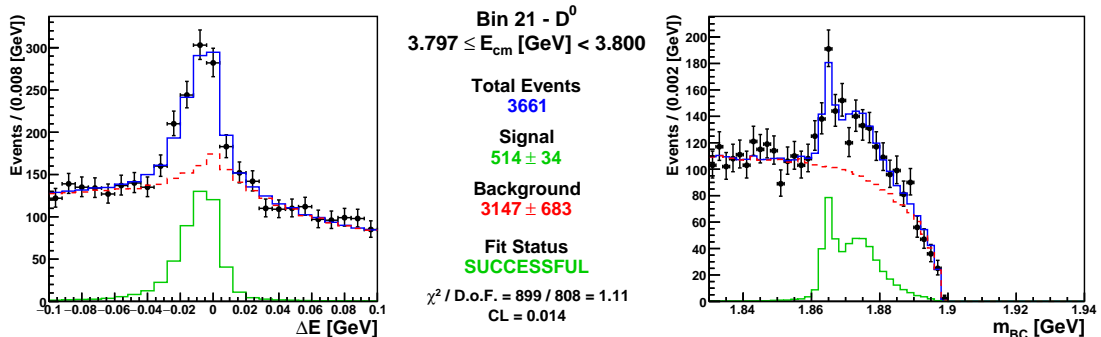
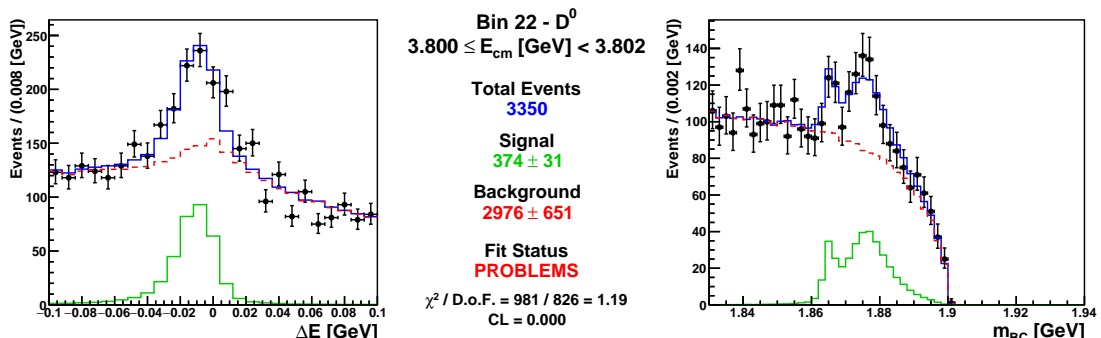
Figure B.6: Projections of the 2D signal fit (ΔE vs. m_{BC}) for D^0 in Bin 5.Figure B.7: Projections of the 2D signal fit (ΔE vs. m_{BC}) for D^0 in Bin 6.Figure B.8: Projections of the 2D signal fit (ΔE vs. m_{BC}) for D^0 in Bin 7.

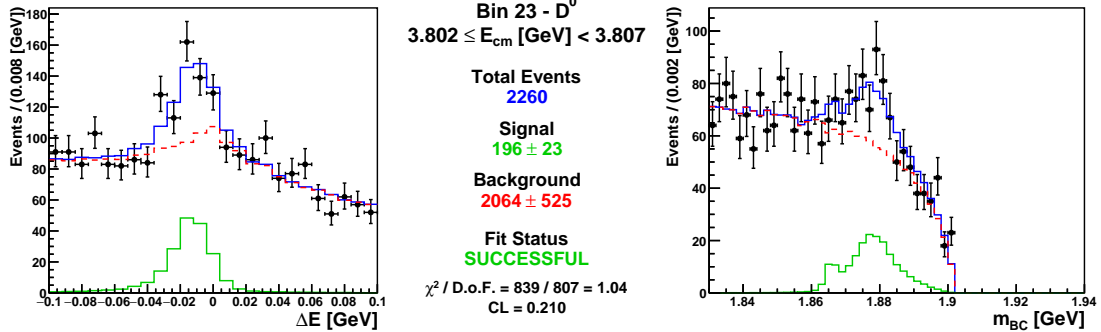
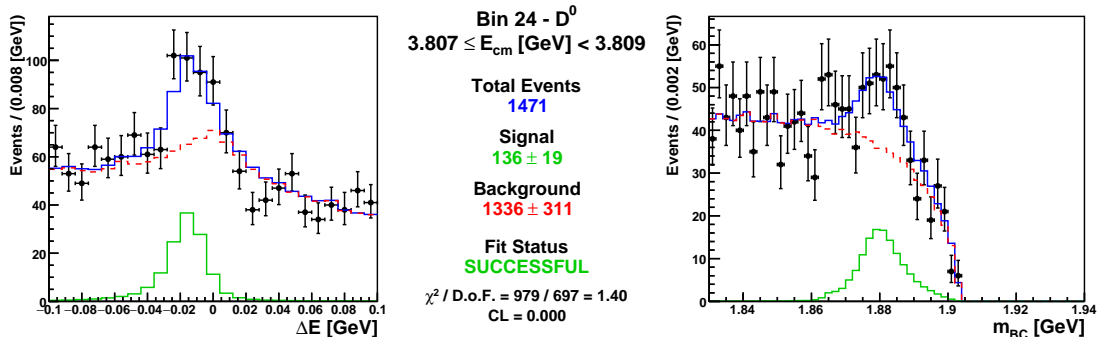
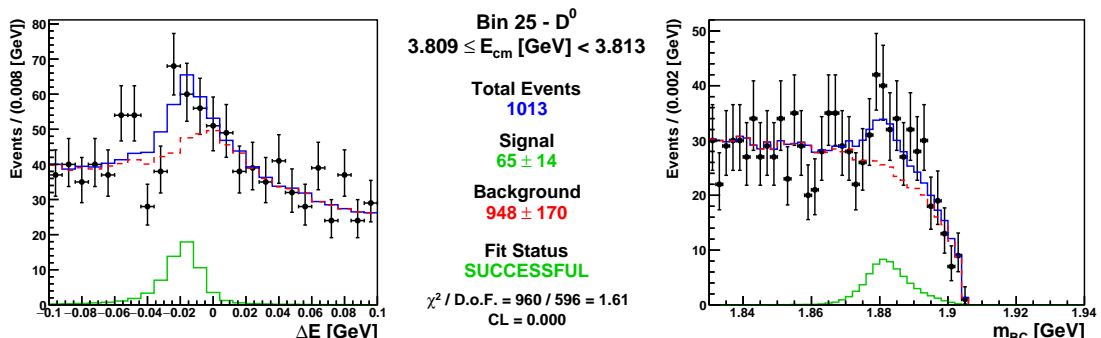
Figure B.9: Projections of the 2D signal fit (ΔE vs. m_{BC}) for D^0 in Bin 8.Figure B.10: Projections of the 2D signal fit (ΔE vs. m_{BC}) for D^0 in Bin 9.Figure B.11: Projections of the 2D signal fit (ΔE vs. m_{BC}) for D^0 in Bin 10.

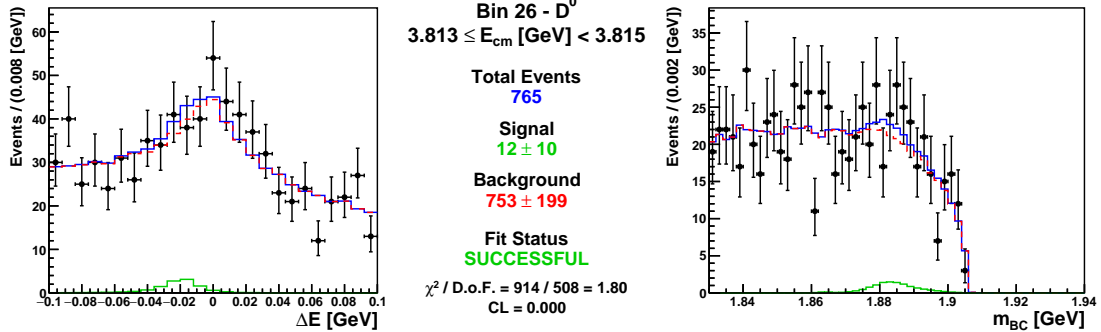
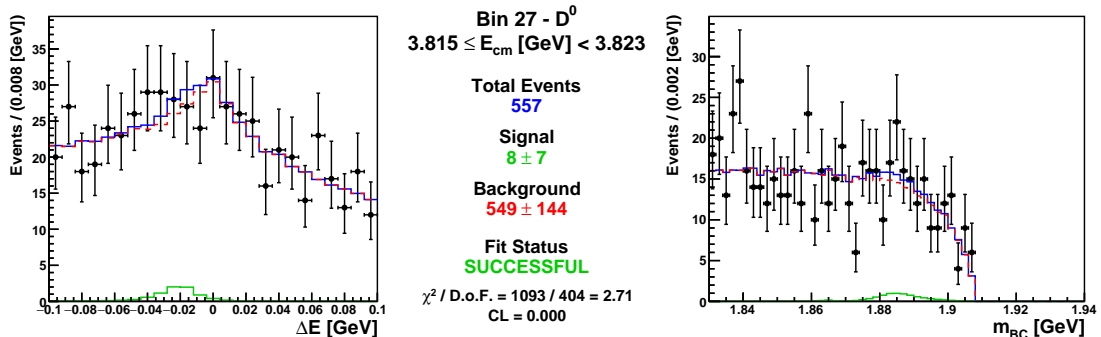
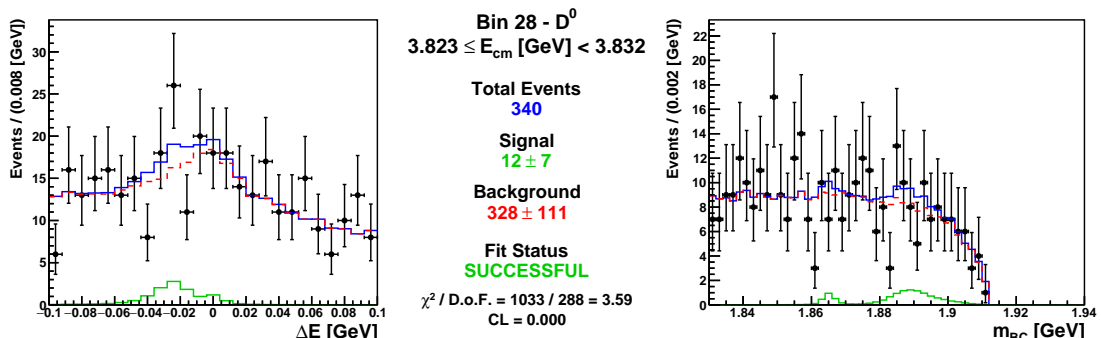
Figure B.12: Projections of the 2D signal fit (ΔE vs. m_{BC}) for D^0 in Bin 11.Figure B.13: Projections of the 2D signal fit (ΔE vs. m_{BC}) for D^0 in Bin 12.Figure B.14: Projections of the 2D signal fit (ΔE vs. m_{BC}) for D^0 in Bin 13.

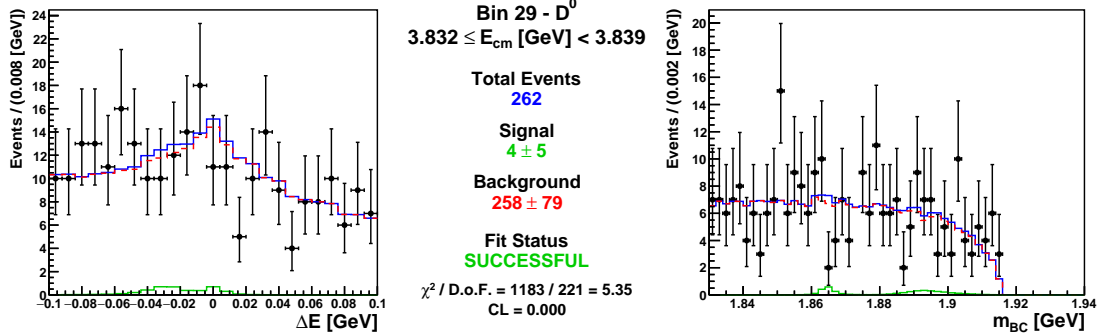
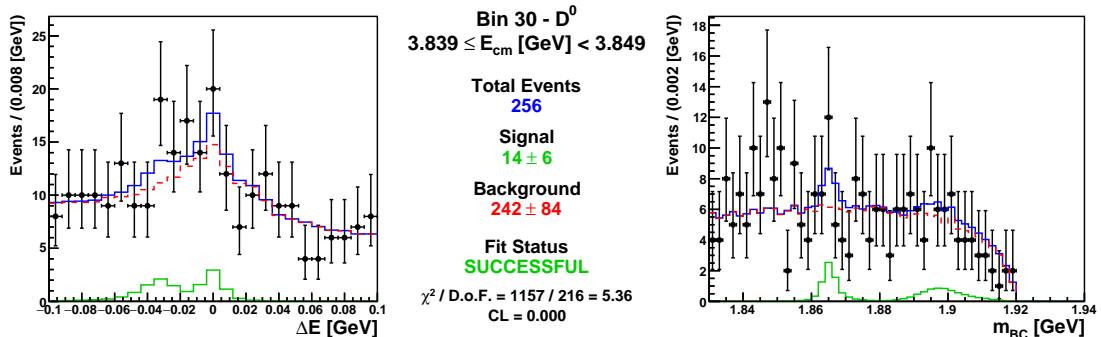
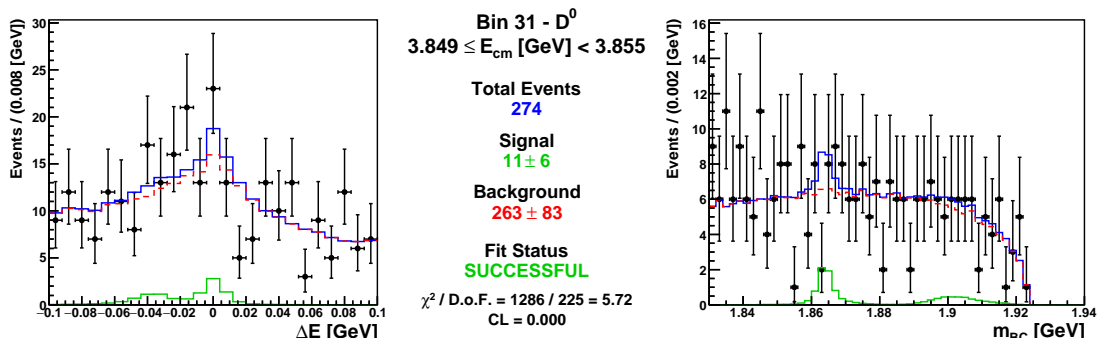
Figure B.15: Projections of the 2D signal fit (ΔE vs. m_{BC}) for D^0 in Bin 14.Figure B.16: Projections of the 2D signal fit (ΔE vs. m_{BC}) for D^0 in Bin 15.Figure B.17: Projections of the 2D signal fit (ΔE vs. m_{BC}) for D^0 in Bin 16.

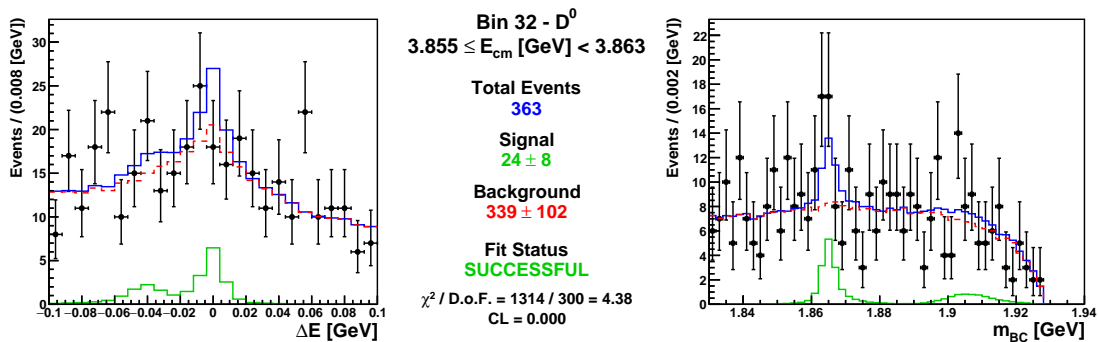
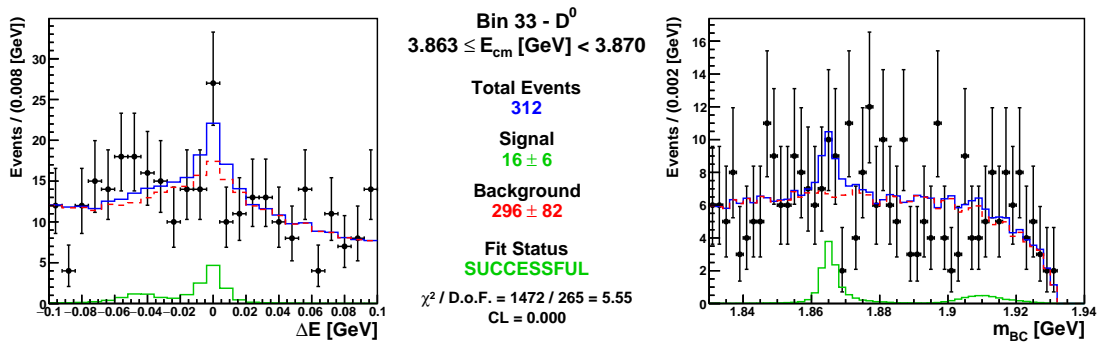
Figure B.18: Projections of the 2D signal fit (ΔE vs. m_{BC}) for D^0 in Bin 17.Figure B.19: Projections of the 2D signal fit (ΔE vs. m_{BC}) for D^0 in Bin 18.Figure B.20: Projections of the 2D signal fit (ΔE vs. m_{BC}) for D^0 in Bin 19.

Figure B.21: Projections of the 2D signal fit (ΔE vs. m_{BC}) for D^0 in Bin 20.Figure B.22: Projections of the 2D signal fit (ΔE vs. m_{BC}) for D^0 in Bin 21.Figure B.23: Projections of the 2D signal fit (ΔE vs. m_{BC}) for D^0 in Bin 22.

Figure B.24: Projections of the 2D signal fit (ΔE vs. m_{BC}) for D^0 in Bin 23.Figure B.25: Projections of the 2D signal fit (ΔE vs. m_{BC}) for D^0 in Bin 24.Figure B.26: Projections of the 2D signal fit (ΔE vs. m_{BC}) for D^0 in Bin 25.

Figure B.27: Projections of the 2D signal fit (ΔE vs. m_{BC}) for D^0 in Bin 26.Figure B.28: Projections of the 2D signal fit (ΔE vs. m_{BC}) for D^0 in Bin 27.Figure B.29: Projections of the 2D signal fit (ΔE vs. m_{BC}) for D^0 in Bin 28.

Figure B.30: Projections of the 2D signal fit (ΔE vs. m_{BC}) for D^0 in Bin 29.Figure B.31: Projections of the 2D signal fit (ΔE vs. m_{BC}) for D^0 in Bin 30.Figure B.32: Projections of the 2D signal fit (ΔE vs. m_{BC}) for D^0 in Bin 31.

Figure B.33: Projections of the 2D signal fit (ΔE vs. m_{BC}) for D^0 in Bin 32.Figure B.34: Projections of the 2D signal fit (ΔE vs. m_{BC}) for D^0 in Bin 33.

Appendix C

D^+ Signal Fits

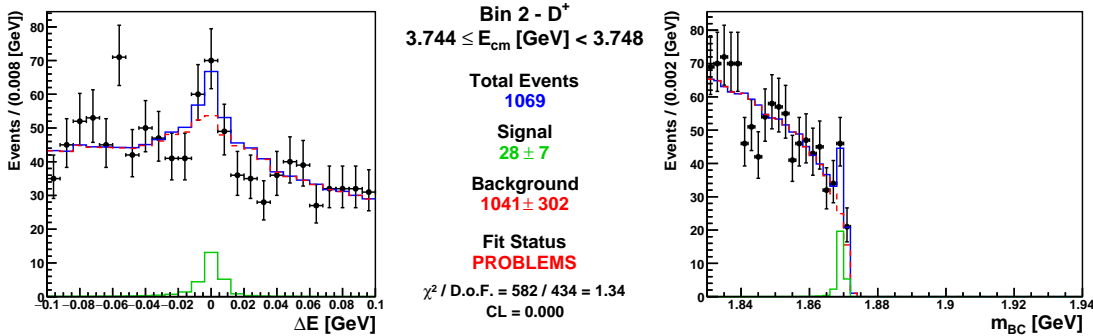


Figure C.1: Projections of the 2D signal fit (ΔE vs. m_{BC}) for D^+ in Bin 2.

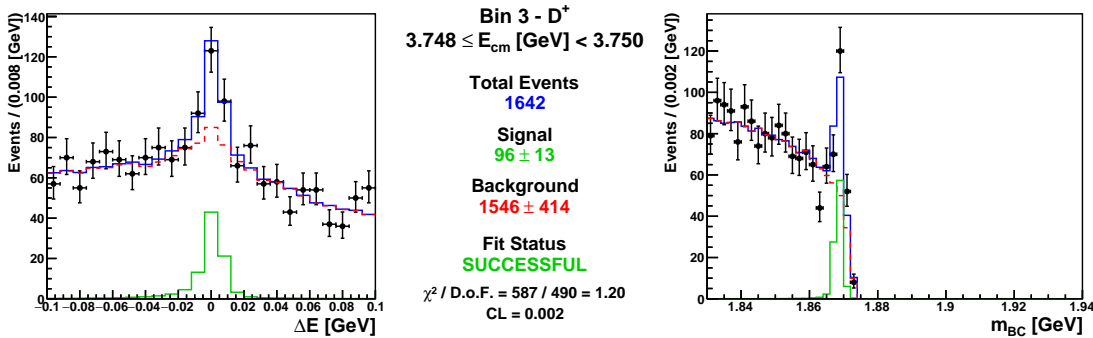
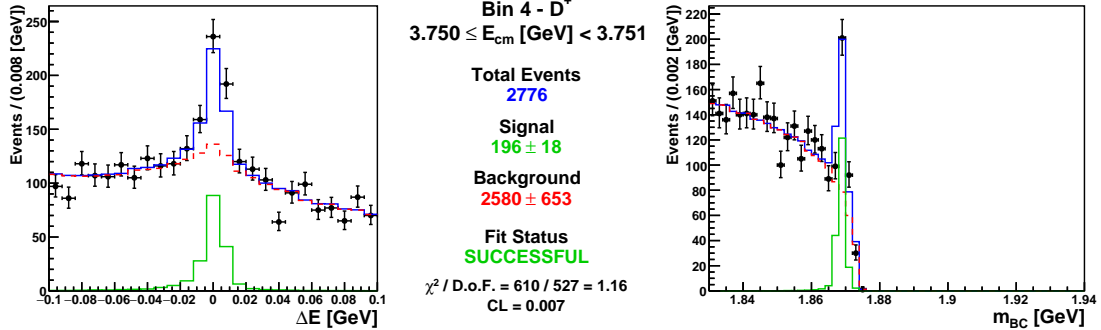
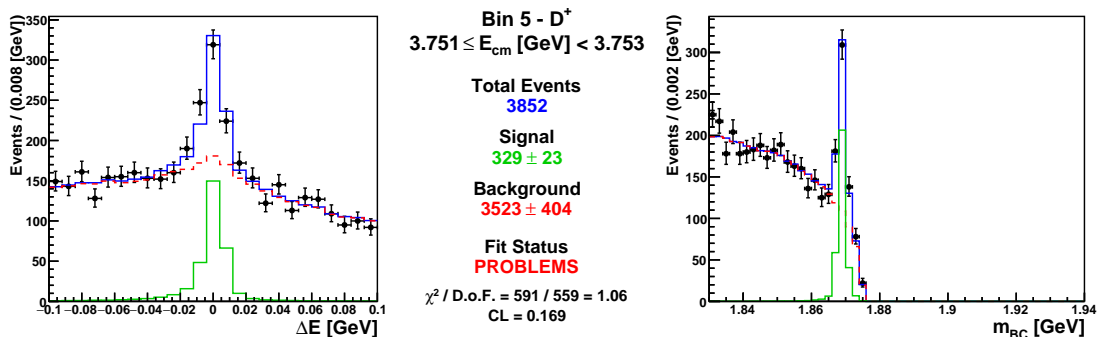
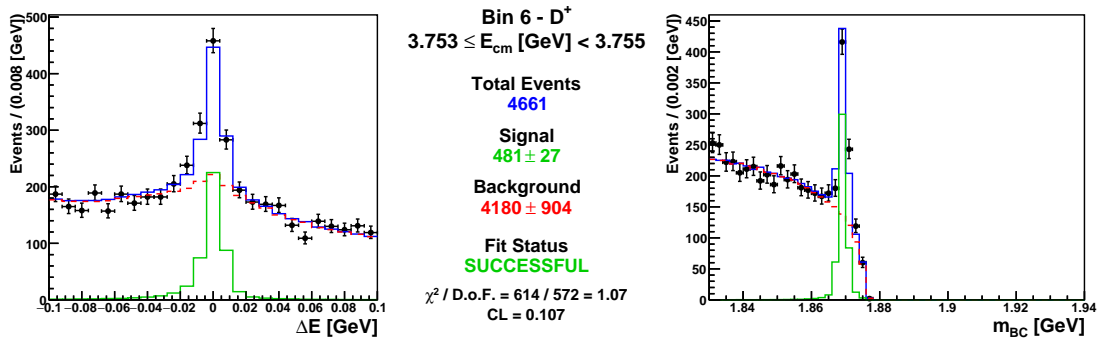
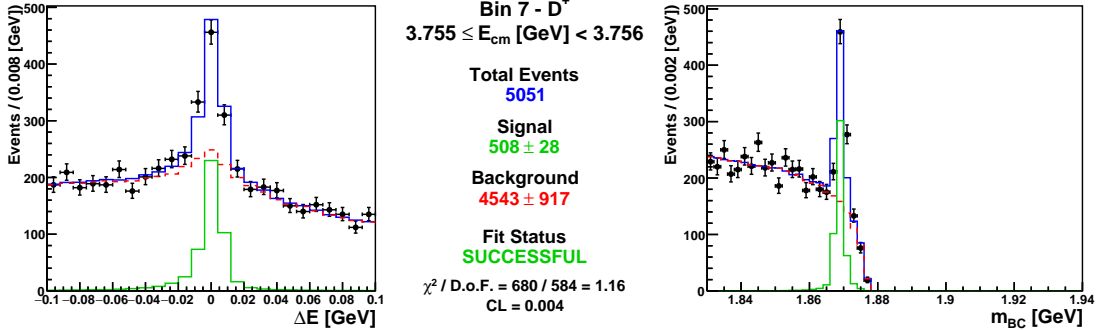
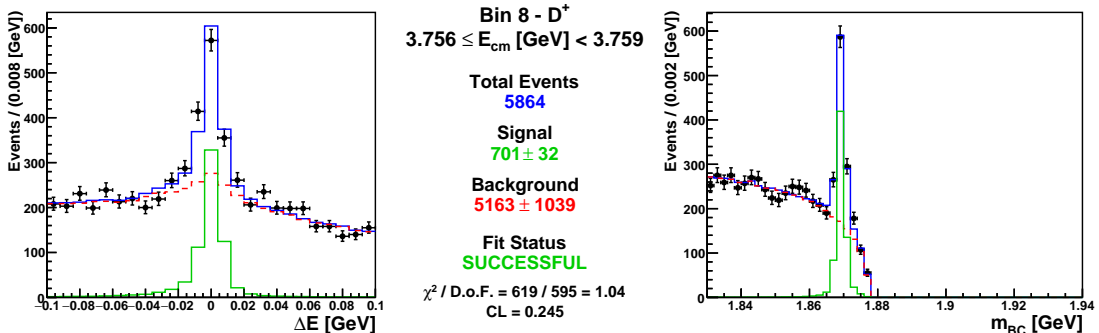
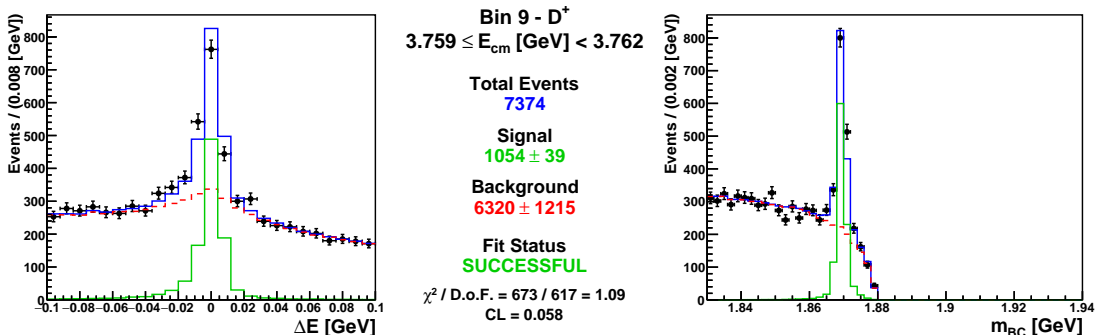
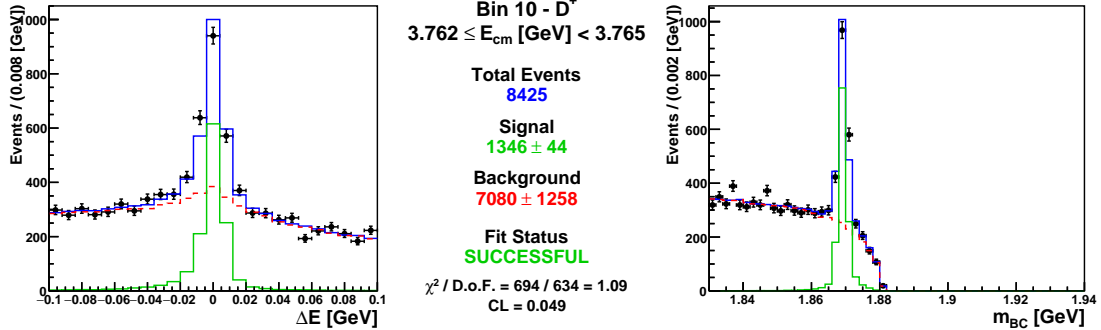
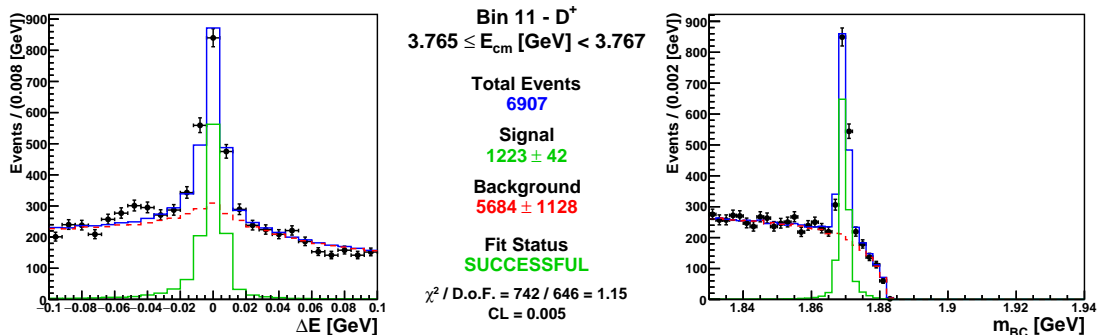
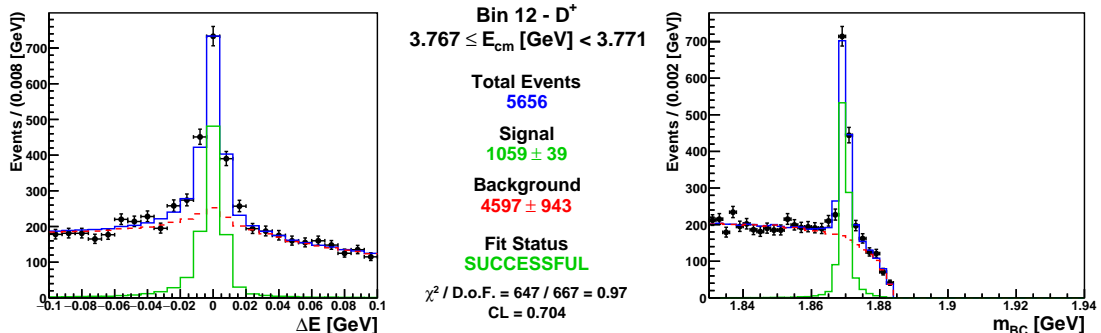


Figure C.2: Projections of the 2D signal fit (ΔE vs. m_{BC}) for D^+ in Bin 3.

Figure C.3: Projections of the 2D signal fit (ΔE vs. m_{BC}) for D^+ in Bin 4.Figure C.4: Projections of the 2D signal fit (ΔE vs. m_{BC}) for D^+ in Bin 5.Figure C.5: Projections of the 2D signal fit (ΔE vs. m_{BC}) for D^+ in Bin 6.

Figure C.6: Projections of the 2D signal fit (ΔE vs. m_{BC}) for D^+ in Bin 7.Figure C.7: Projections of the 2D signal fit (ΔE vs. m_{BC}) for D^+ in Bin 8.Figure C.8: Projections of the 2D signal fit (ΔE vs. m_{BC}) for D^+ in Bin 9.

Figure C.9: Projections of the 2D signal fit (ΔE vs. m_{BC}) for D^+ in Bin 10.Figure C.10: Projections of the 2D signal fit (ΔE vs. m_{BC}) for D^+ in Bin 11.Figure C.11: Projections of the 2D signal fit (ΔE vs. m_{BC}) for D^+ in Bin 12.

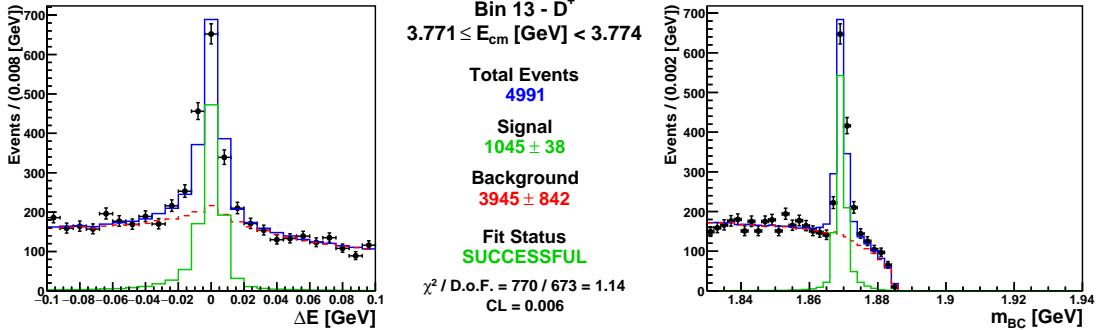


Figure C.12: Projections of the 2D signal fit (ΔE vs. m_{BC}) for D^+ in Bin 13.

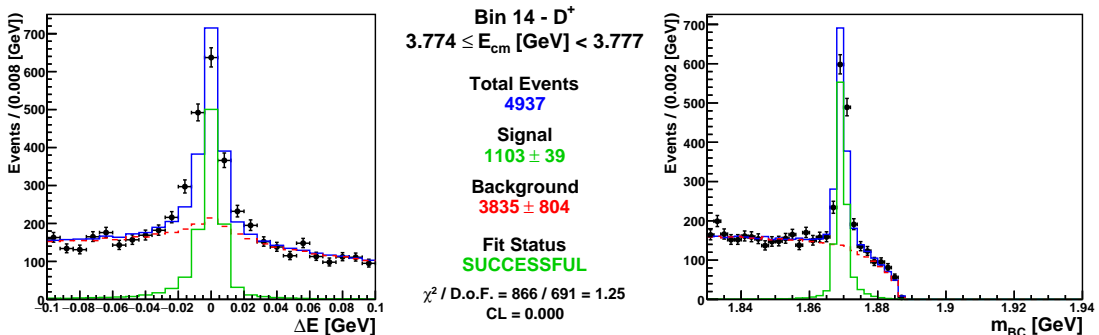


Figure C.13: Projections of the 2D signal fit (ΔE vs. m_{BC}) for D^+ in Bin 14.

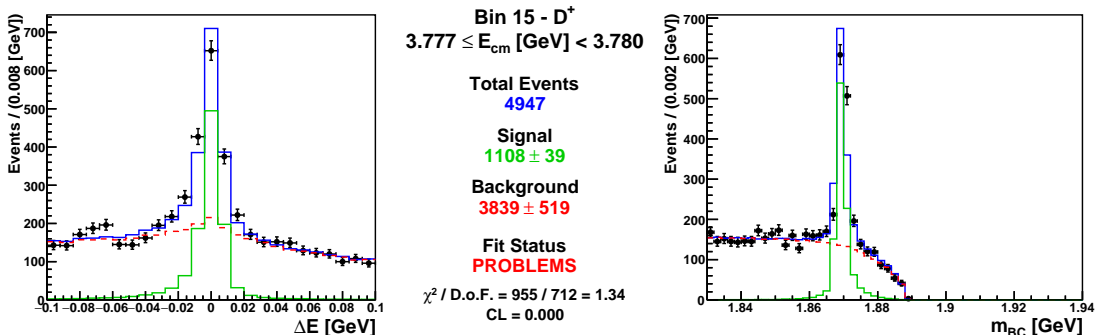
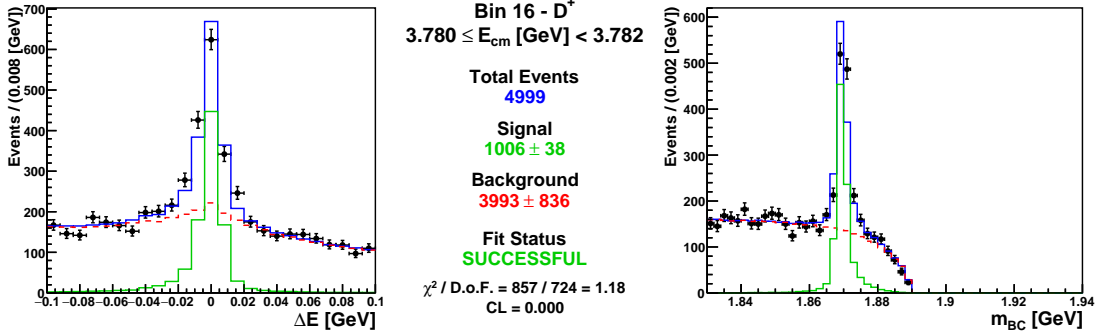
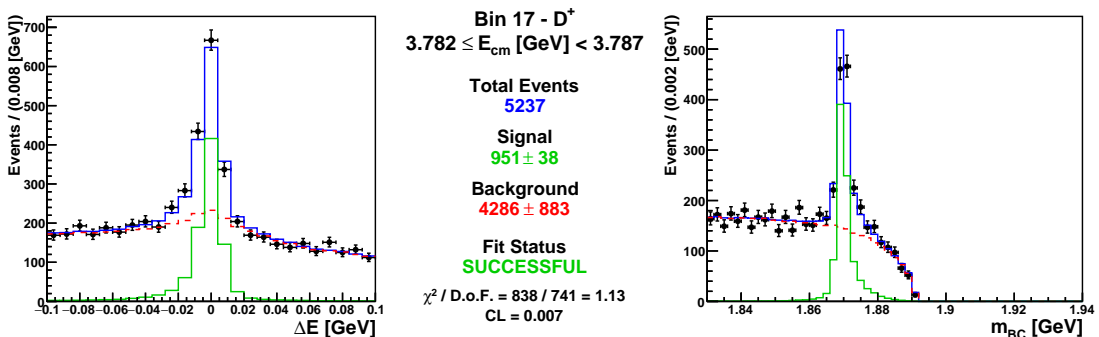
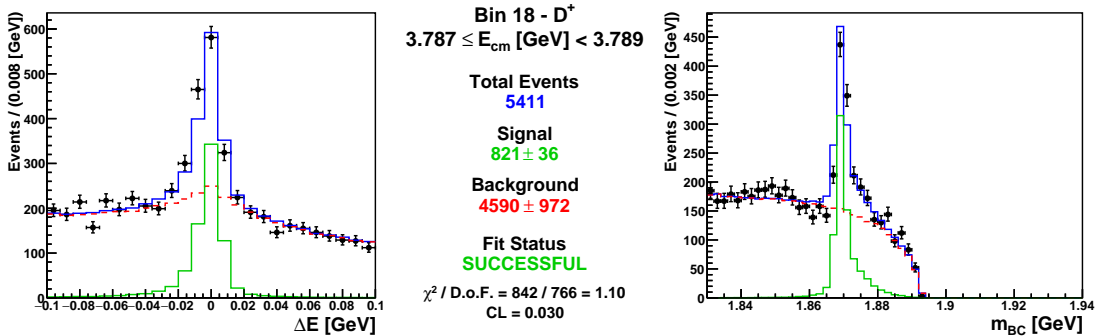
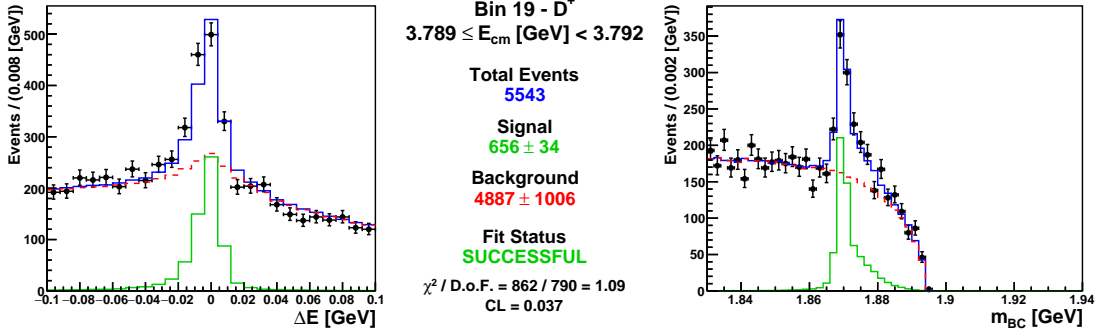
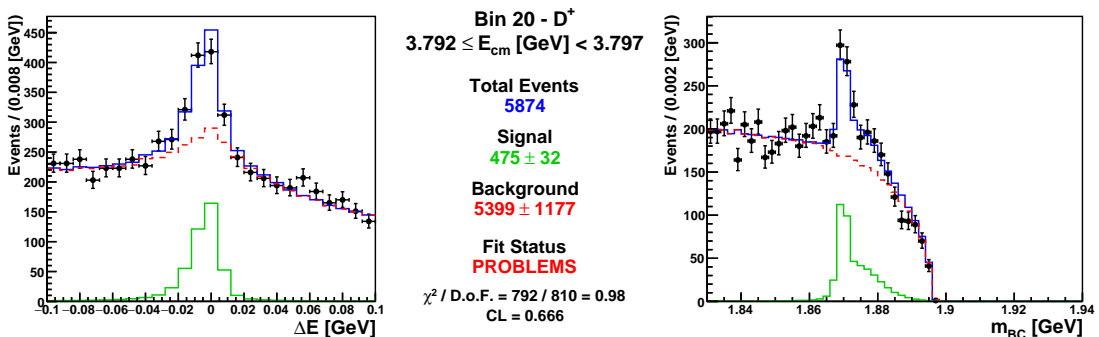
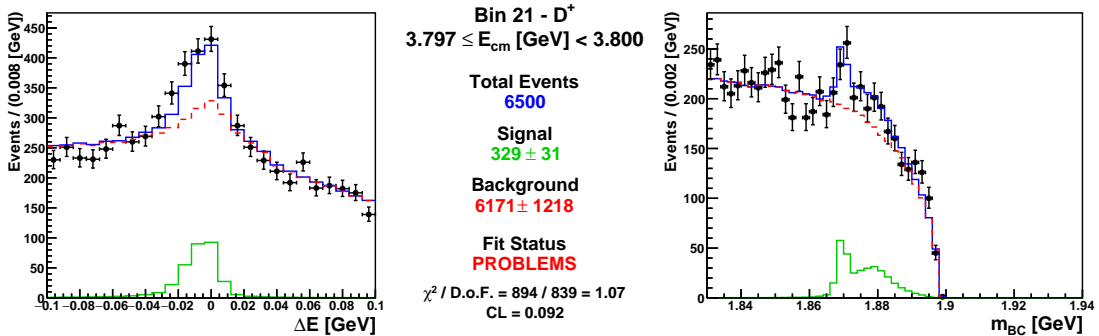
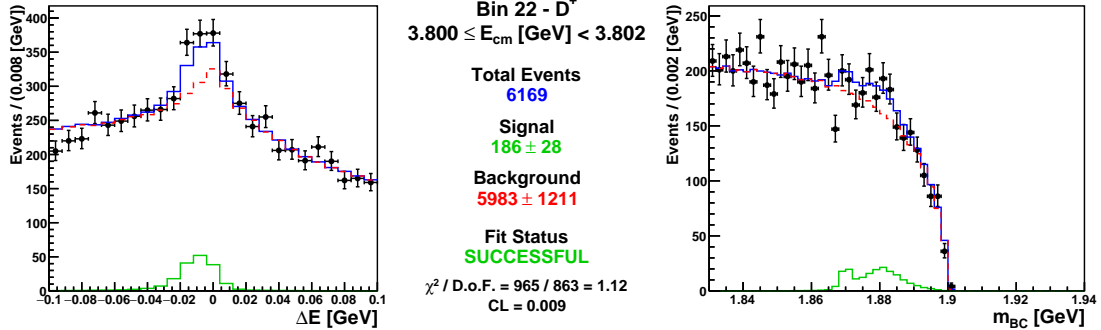
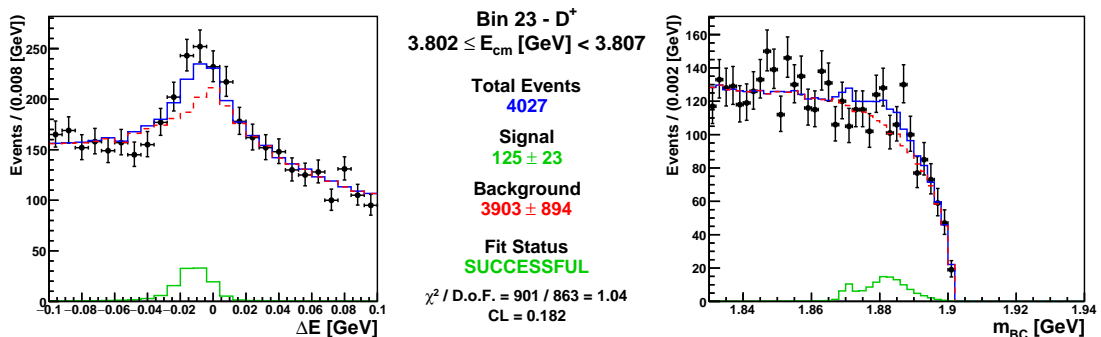
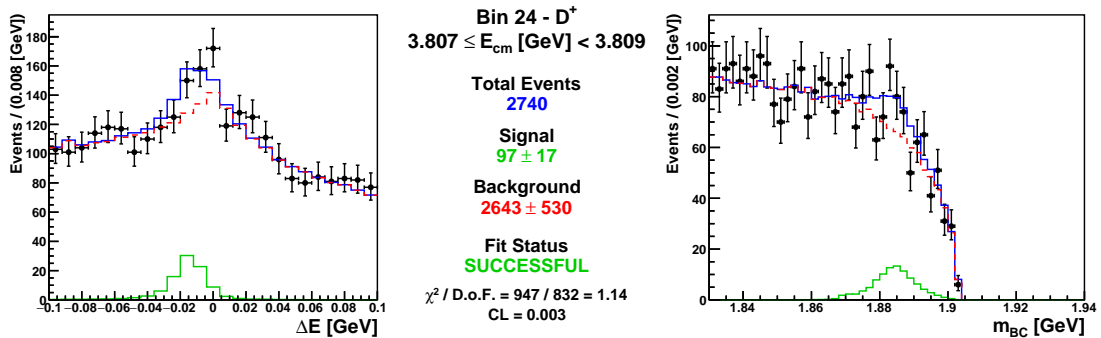
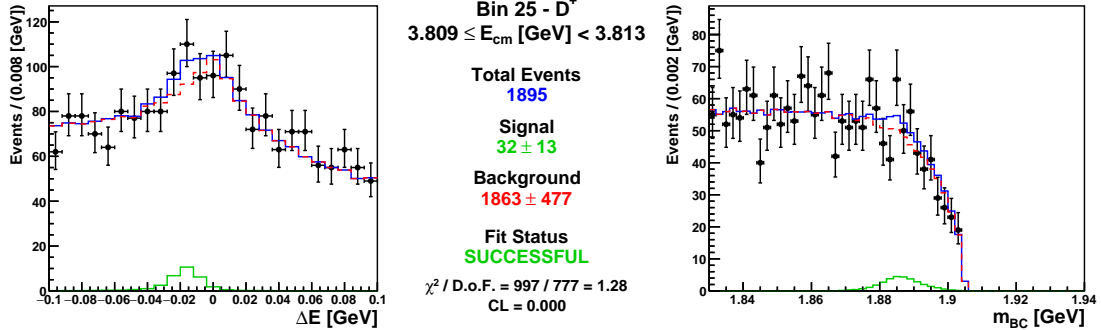
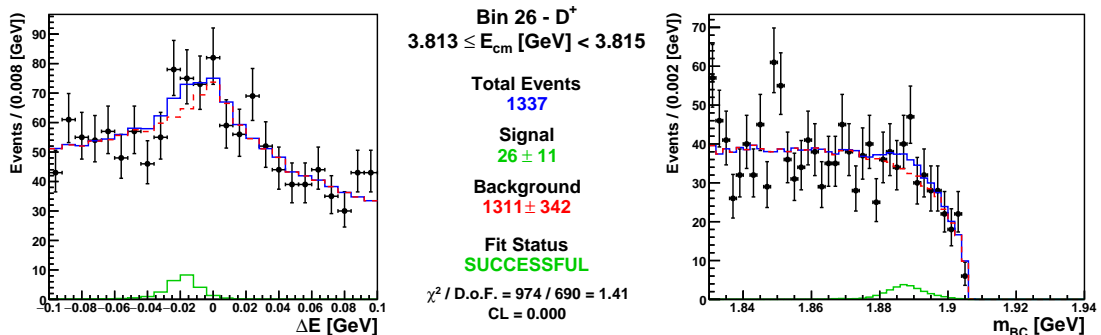
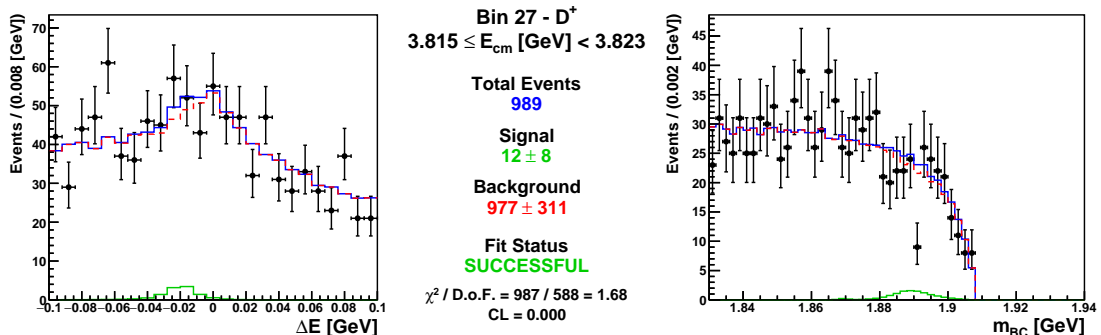


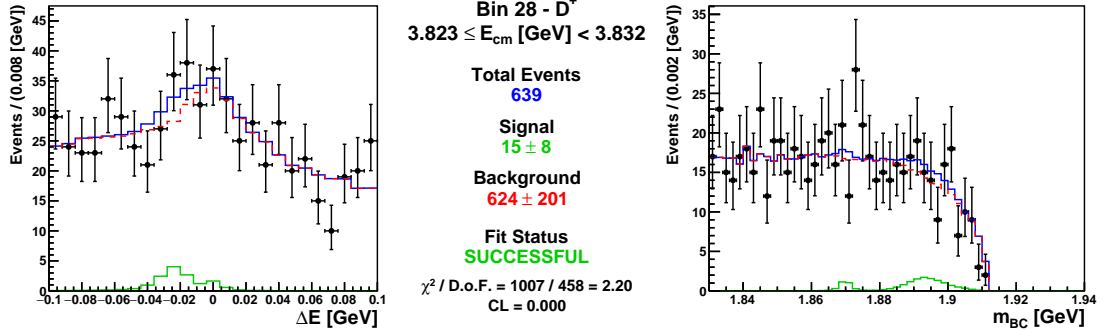
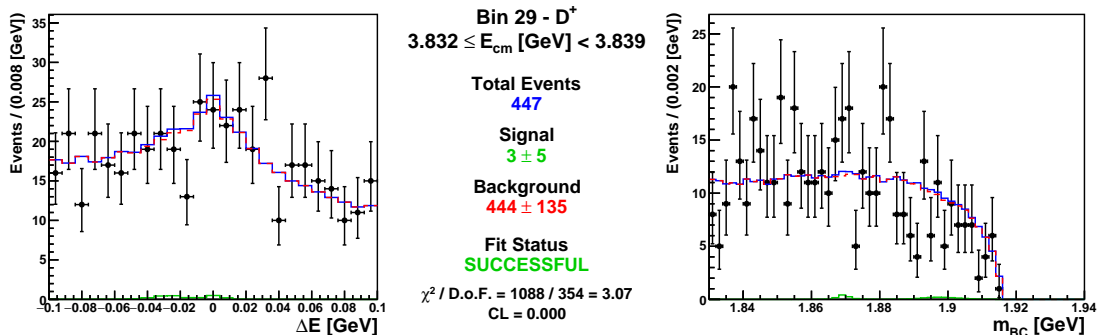
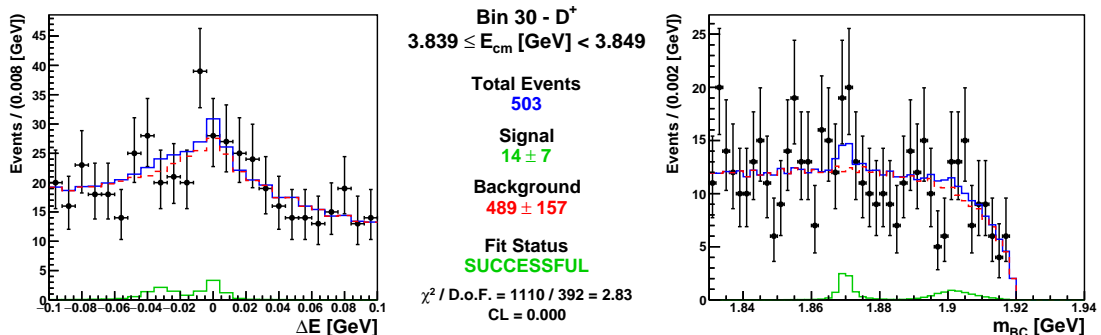
Figure C.14: Projections of the 2D signal fit (ΔE vs. m_{BC}) for D^+ in Bin 15.

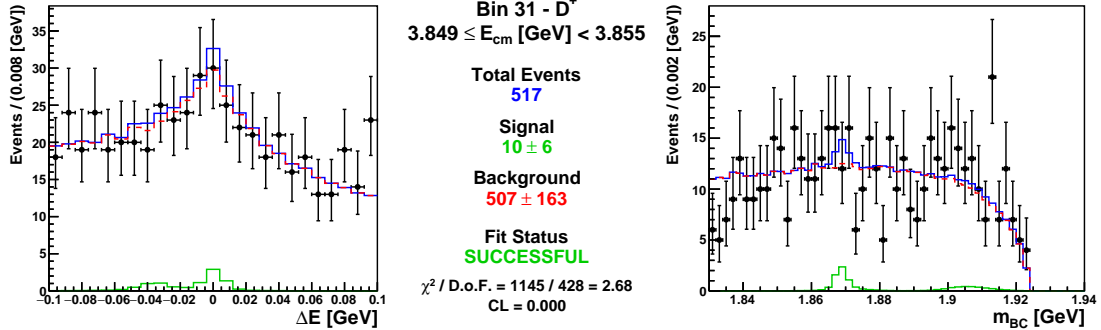
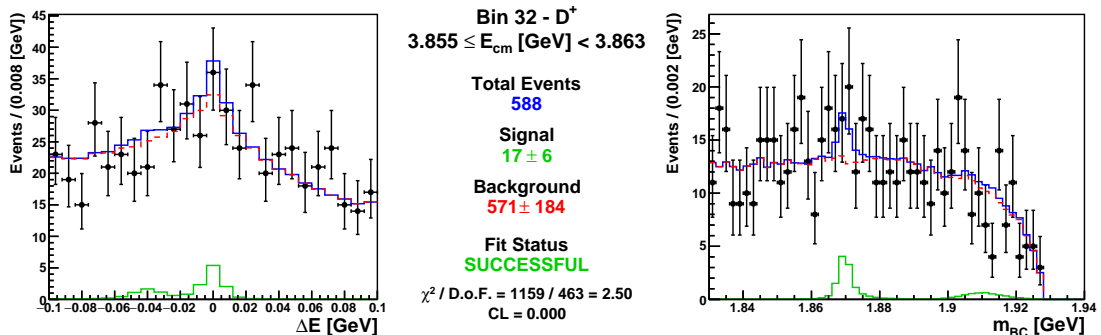
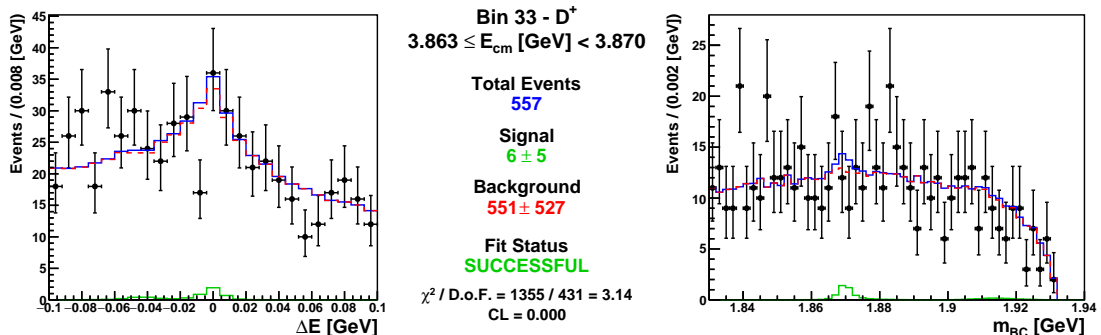
Figure C.15: Projections of the 2D signal fit (ΔE vs. m_{BC}) for D^+ in Bin 16.Figure C.16: Projections of the 2D signal fit (ΔE vs. m_{BC}) for D^+ in Bin 17.Figure C.17: Projections of the 2D signal fit (ΔE vs. m_{BC}) for D^+ in Bin 18.

Figure C.18: Projections of the 2D signal fit (ΔE vs. m_{BC}) for D^+ in Bin 19.Figure C.19: Projections of the 2D signal fit (ΔE vs. m_{BC}) for D^+ in Bin 20.Figure C.20: Projections of the 2D signal fit (ΔE vs. m_{BC}) for D^+ in Bin 21.

Figure C.21: Projections of the 2D signal fit (ΔE vs. m_{BC}) for D^+ in Bin 22.Figure C.22: Projections of the 2D signal fit (ΔE vs. m_{BC}) for D^+ in Bin 23.Figure C.23: Projections of the 2D signal fit (ΔE vs. m_{BC}) for D^+ in Bin 24.

Figure C.24: Projections of the 2D signal fit (ΔE vs. m_{BC}) for D^+ in Bin 25.Figure C.25: Projections of the 2D signal fit (ΔE vs. m_{BC}) for D^+ in Bin 26.Figure C.26: Projections of the 2D signal fit (ΔE vs. m_{BC}) for D^+ in Bin 27.

Figure C.27: Projections of the 2D signal fit (ΔE vs. m_{BC}) for D^+ in Bin 28.Figure C.28: Projections of the 2D signal fit (ΔE vs. m_{BC}) for D^+ in Bin 29.Figure C.29: Projections of the 2D signal fit (ΔE vs. m_{BC}) for D^+ in Bin 30.

Figure C.30: Projections of the 2D signal fit (ΔE vs. m_{BC}) for D^+ in Bin 31.Figure C.31: Projections of the 2D signal fit (ΔE vs. m_{BC}) for D^+ in Bin 32.Figure C.32: Projections of the 2D signal fit (ΔE vs. m_{BC}) for D^+ in Bin 33.

Appendix D

Scan Data Hadronic Counting Fits

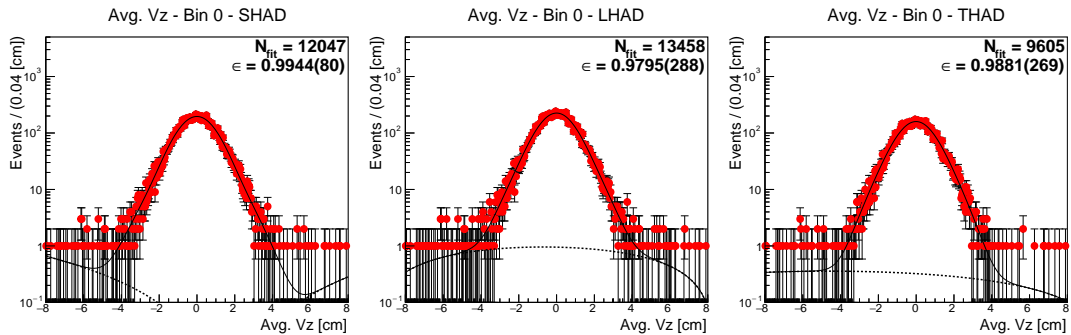


Figure D.1: Fits to determine the number of hadrons in the 3734 (Scan) data sample. This includes results for SHAD (left), LHAD (middle), and THAD (right).

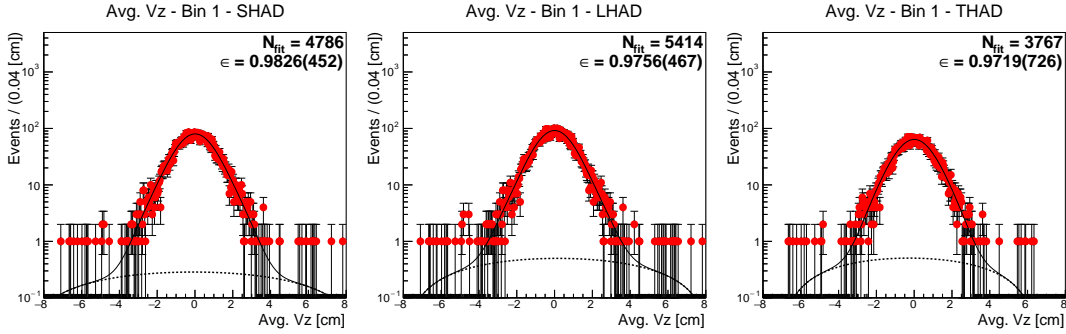


Figure D.2: Fits to determine the number of hadrons in the 3736 (Scan) data sample. This includes results for SHAD (left), LHAD (middle), and THAD (right).

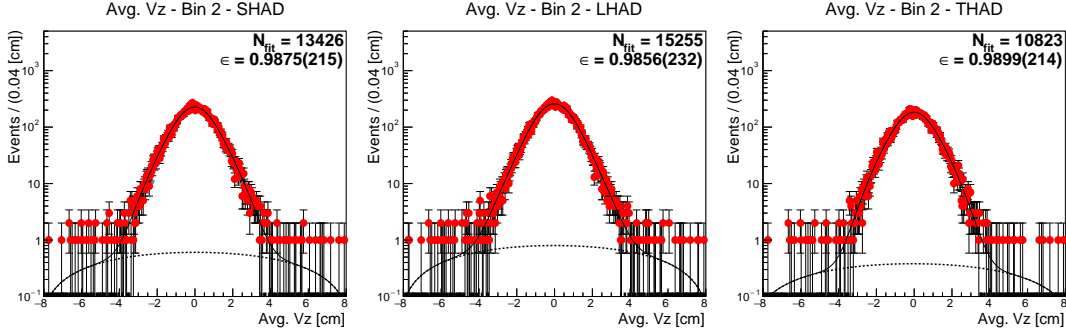


Figure D.3: Fits to determine the number of hadrons in the 3744 (Scan) data sample. This includes results for SHAD (left), LHAD (middle), and THAD (right).

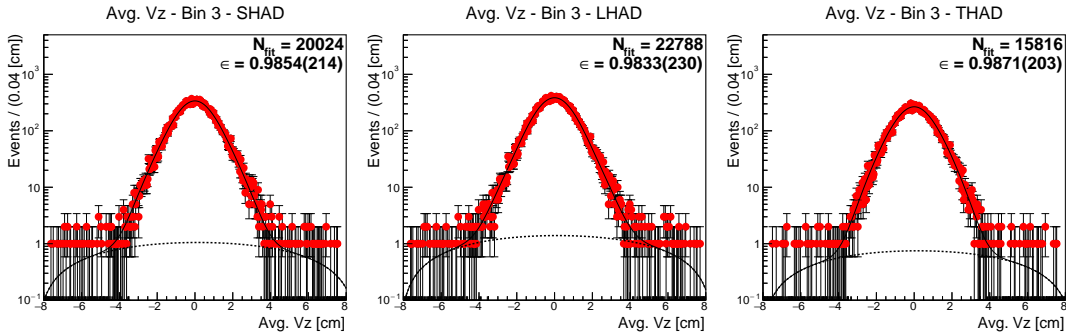


Figure D.4: Fits to determine the number of hadrons in the 3748 (Scan) data sample. This includes results for SHAD (left), LHAD (middle), and THAD (right).

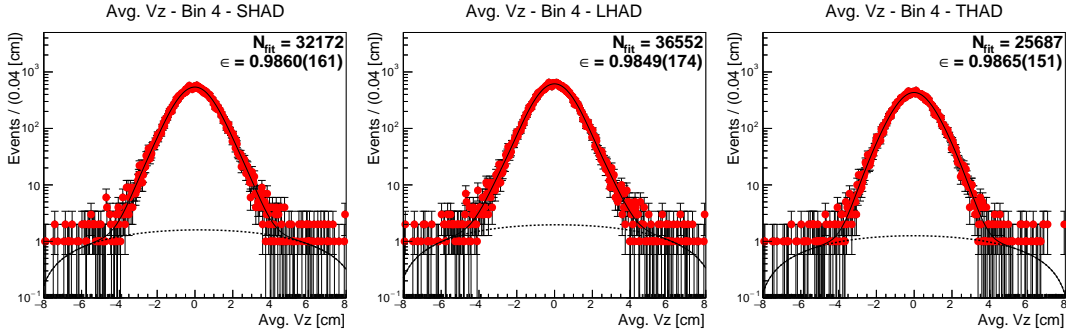


Figure D.5: Fits to determine the number of hadrons in the 3750 (Scan) data sample. This includes results for SHAD (left), LHAD (middle), and THAD (right).

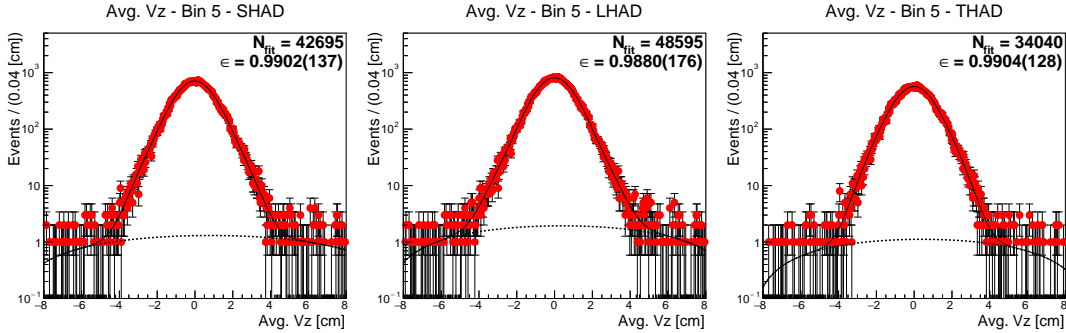


Figure D.6: Fits to determine the number of hadrons in the 3751 (Scan) data sample. This includes results for SHAD (left), LHAD (middle), and THAD (right).

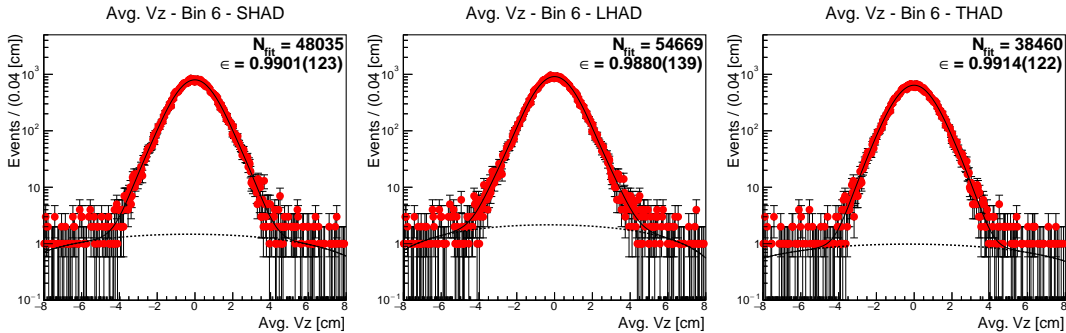


Figure D.7: Fits to determine the number of hadrons in the 3753 (Scan) data sample. This includes results for SHAD (left), LHAD (middle), and THAD (right).

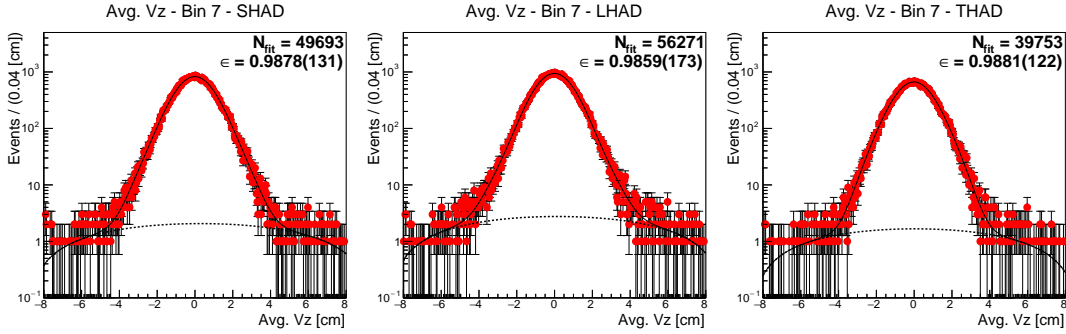


Figure D.8: Fits to determine the number of hadrons in the 3755 (Scan) data sample. This includes results for SHAD (left), LHAD (middle), and THAD (right).

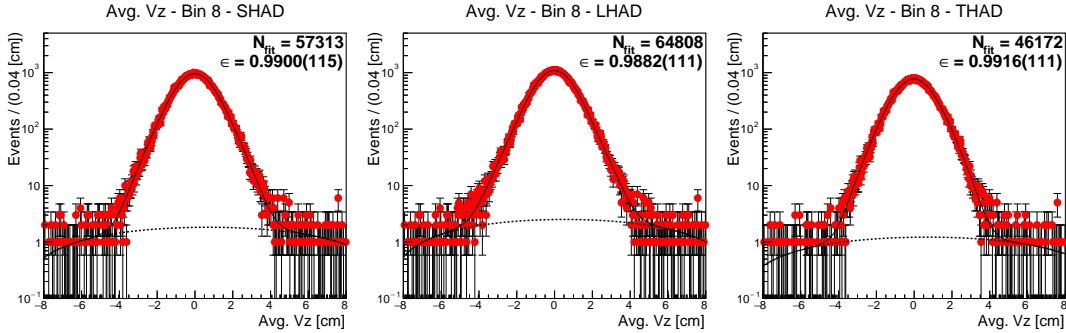


Figure D.9: Fits to determine the number of hadrons in the 3756 (Scan) data sample. This includes results for SHAD (left), LHAD (middle), and THAD (right).

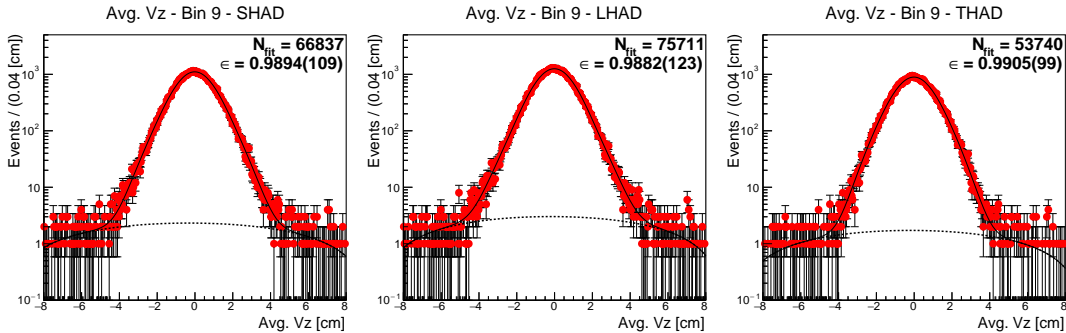


Figure D.10: Fits to determine the number of hadrons in the 3759 (Scan) data sample. This includes results for SHAD (left), LHAD (middle), and THAD (right).

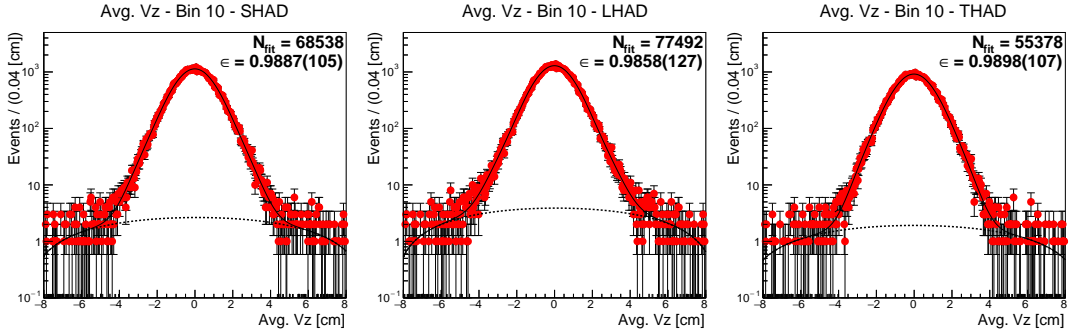


Figure D.11: Fits to determine the number of hadrons in the 3762 (Scan) data sample. This includes results for SHAD (left), LHAD (middle), and THAD (right).

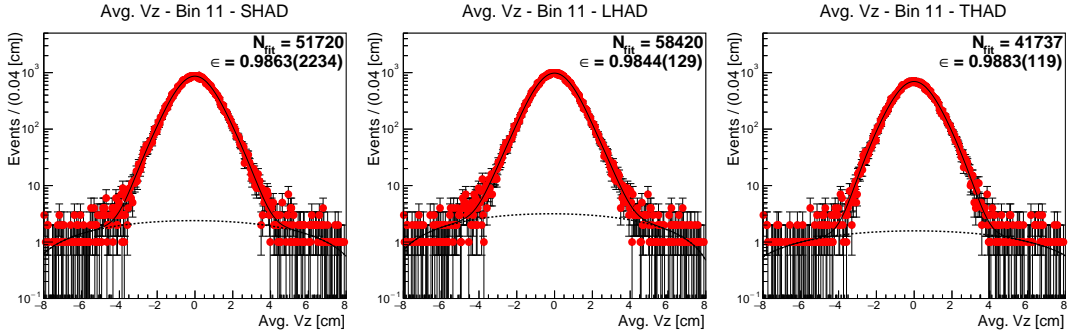


Figure D.12: Fits to determine the number of hadrons in the 3765 (Scan) data sample. This includes results for SHAD (left), LHAD (middle), and THAD (right).

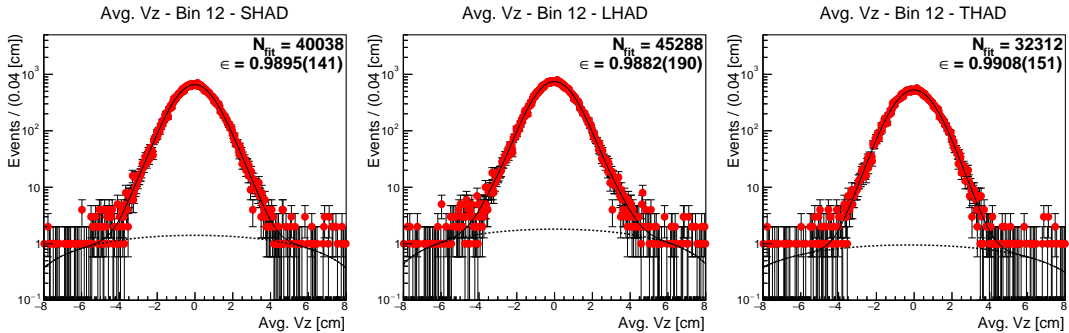


Figure D.13: Fits to determine the number of hadrons in the 3767 (Scan) data sample. This includes results for SHAD (left), LHAD (middle), and THAD (right).

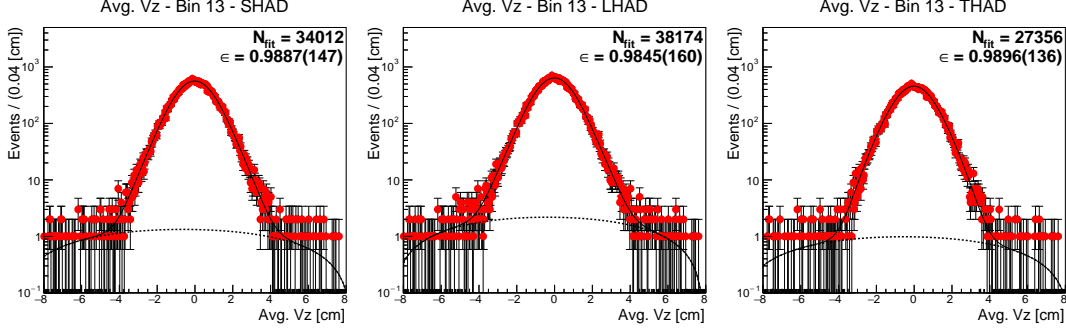


Figure D.14: Fits to determine the number of hadrons in the 3771 (Scan) data sample. This includes results for SHAD (left), LHAD (middle), and THAD (right).

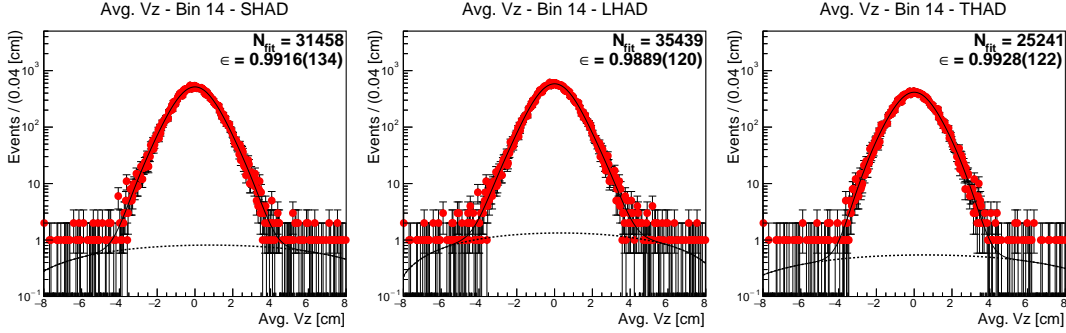


Figure D.15: Fits to determine the number of hadrons in the 3774 (Scan) data sample. This includes results for SHAD (left), LHAD (middle), and THAD (right).

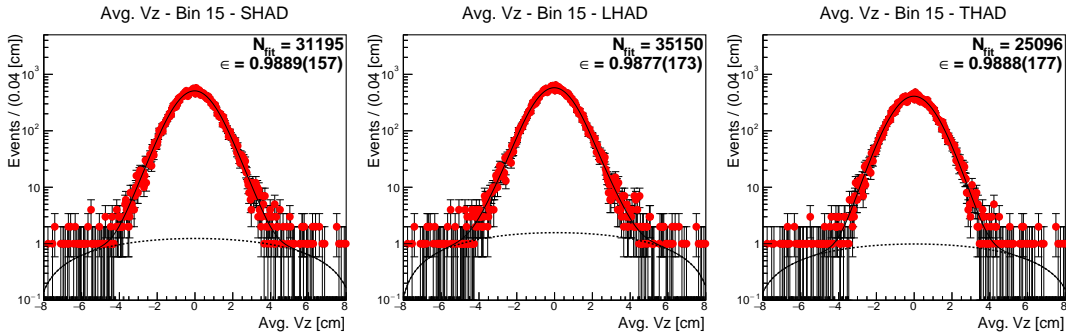


Figure D.16: Fits to determine the number of hadrons in the 3777 (Scan) data sample. This includes results for SHAD (left), LHAD (middle), and THAD (right).

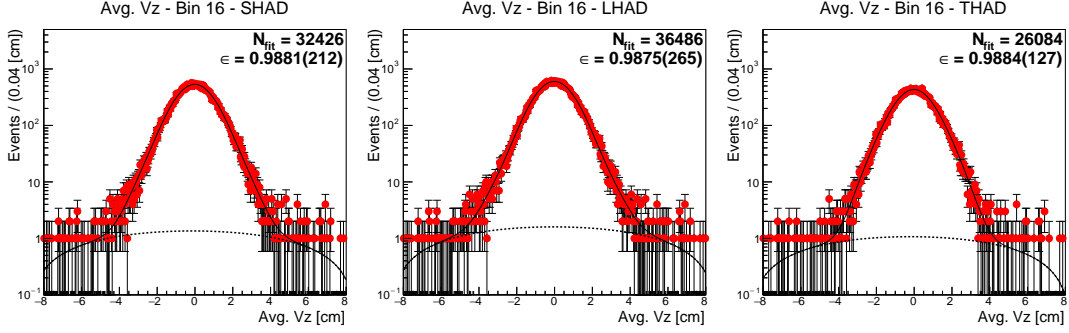


Figure D.17: Fits to determine the number of hadrons in the 3780 (Scan) data sample. This includes results for SHAD (left), LHAD (middle), and THAD (right).

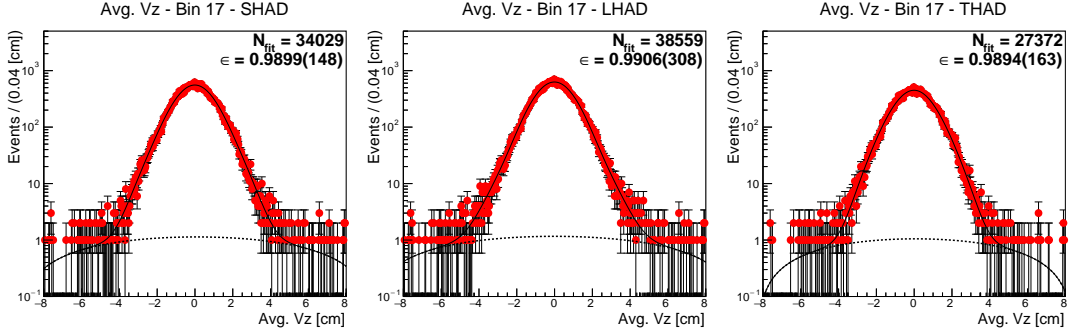


Figure D.18: Fits to determine the number of hadrons in the 3782 (Scan) data sample. This includes results for SHAD (left), LHAD (middle), and THAD (right).

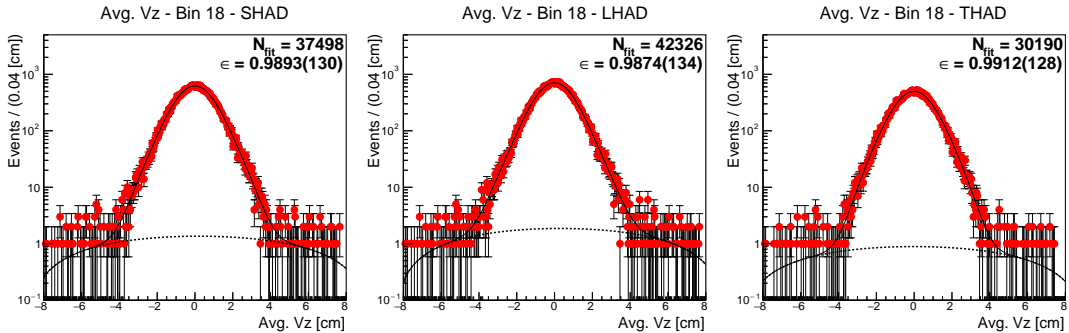


Figure D.19: Fits to determine the number of hadrons in the 3786 (Scan) data sample. This includes results for SHAD (left), LHAD (middle), and THAD (right).

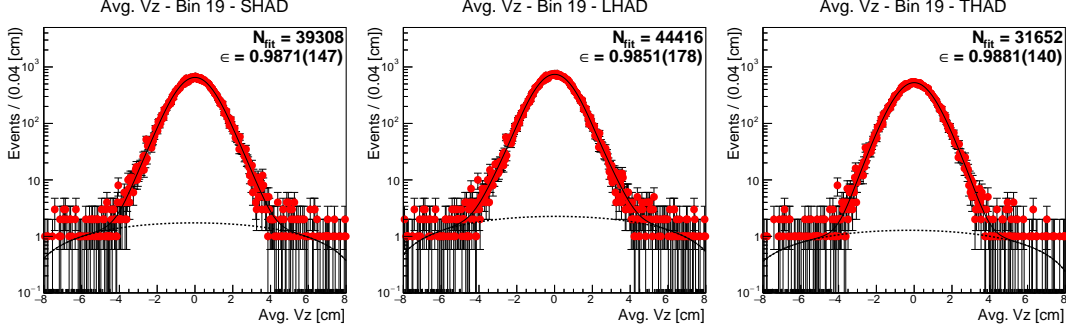


Figure D.20: Fits to determine the number of hadrons in the 3789 (Scan) data sample. This includes results for SHAD (left), LHAD (middle), and THAD (right).

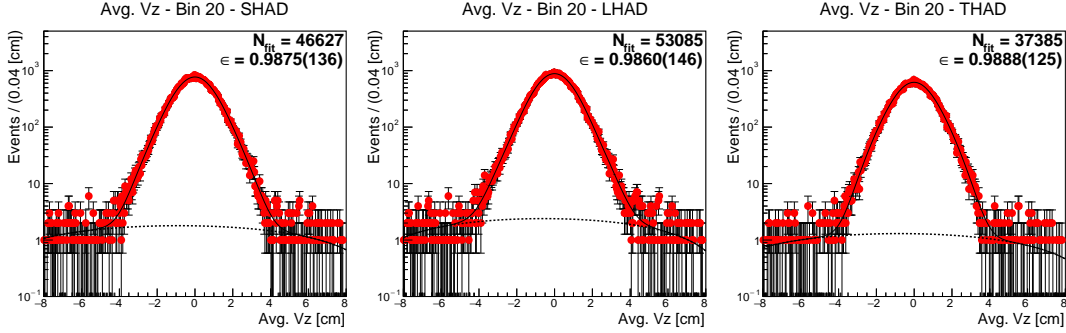


Figure D.21: Fits to determine the number of hadrons in the 3792 (Scan) data sample. This includes results for SHAD (left), LHAD (middle), and THAD (right).

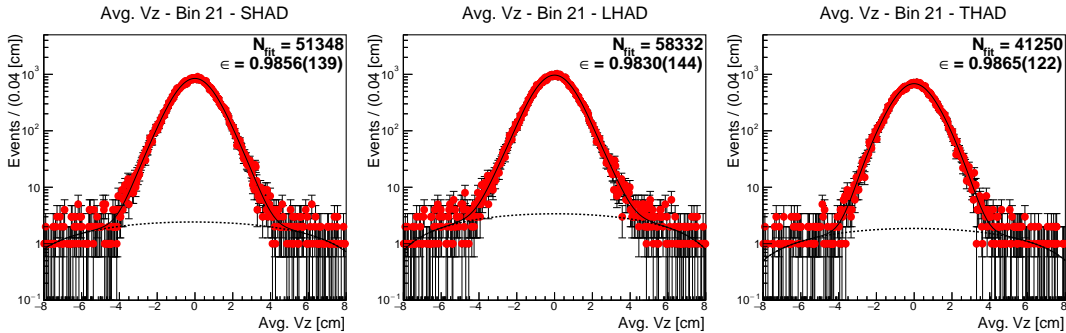


Figure D.22: Fits to determine the number of hadrons in the 3797 (Scan) data sample. This includes results for SHAD (left), LHAD (middle), and THAD (right).

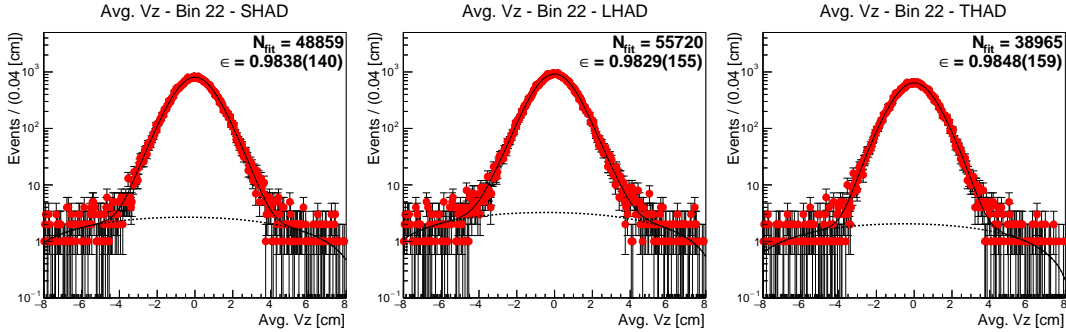


Figure D.23: Fits to determine the number of hadrons in the 3800 (Scan) data sample. This includes results for SHAD (left), LHAD (middle), and THAD (right).

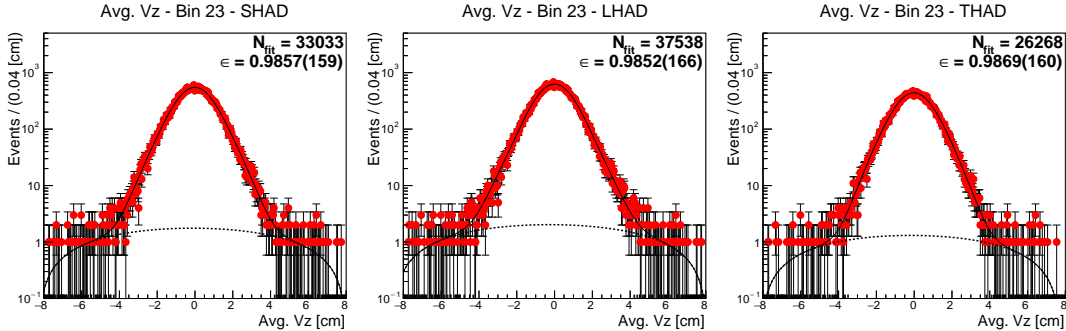


Figure D.24: Fits to determine the number of hadrons in the 3802 (Scan) data sample. This includes results for SHAD (left), LHAD (middle), and THAD (right).

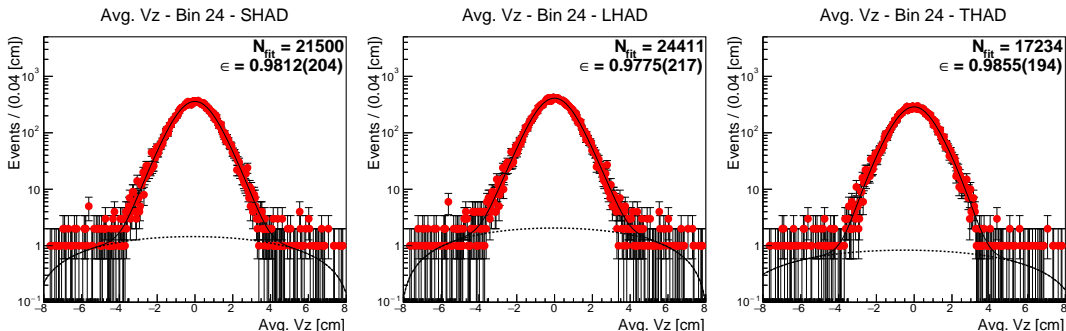


Figure D.25: Fits to determine the number of hadrons in the 3807 (Scan) data sample. This includes results for SHAD (left), LHAD (middle), and THAD (right).

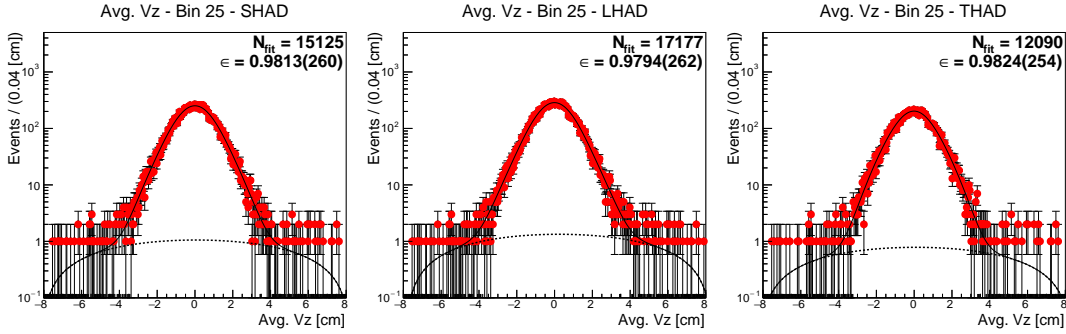


Figure D.26: Fits to determine the number of hadrons in the 3809 (Scan) data sample. This includes results for SHAD (left), LHAD (middle), and THAD (right).

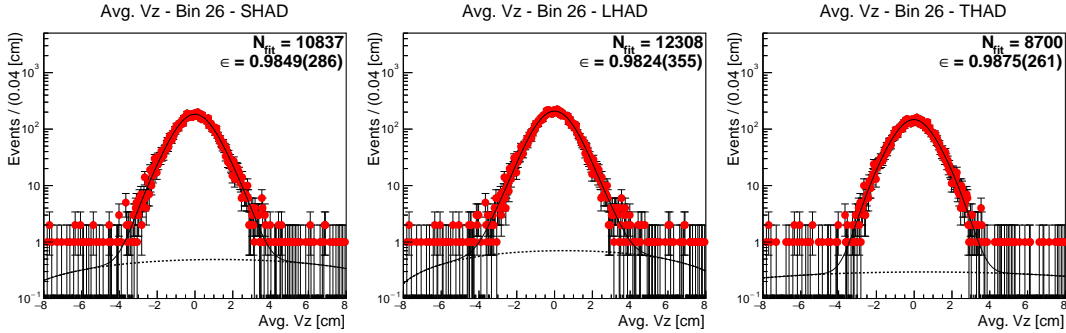


Figure D.27: Fits to determine the number of hadrons in the 3813 (Scan) data sample. This includes results for SHAD (left), LHAD (middle), and THAD (right).

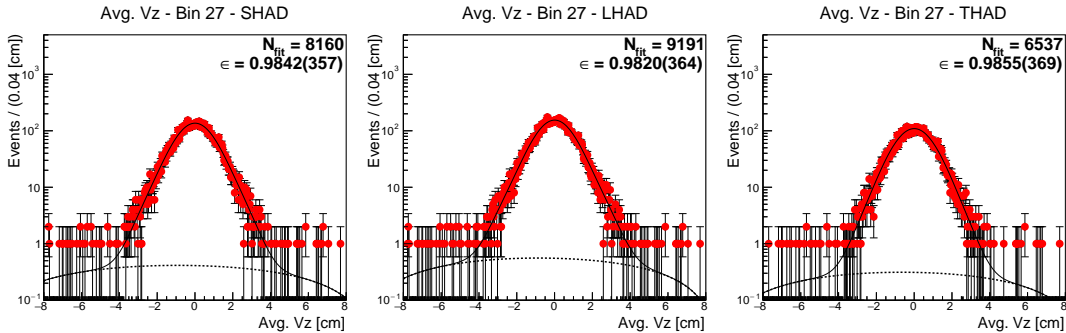


Figure D.28: Fits to determine the number of hadrons in the 3815 (Scan) data sample. This includes results for SHAD (left), LHAD (middle), and THAD (right).

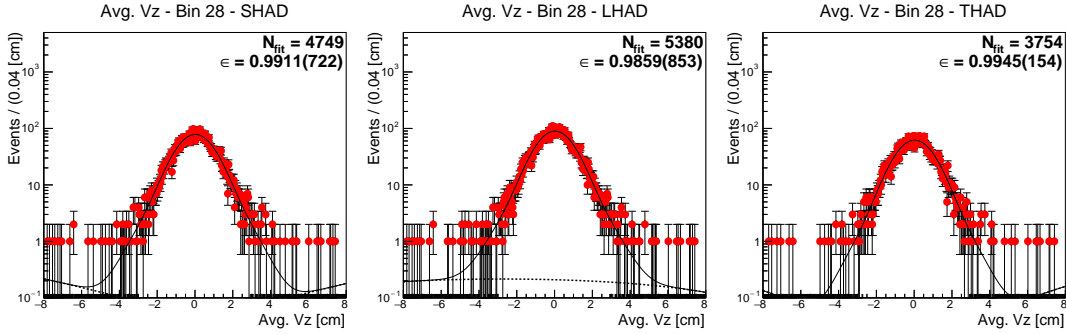


Figure D.29: Fits to determine the number of hadrons in the 3822 (Scan) data sample. This includes results for SHAD (left), LHAD (middle), and THAD (right).

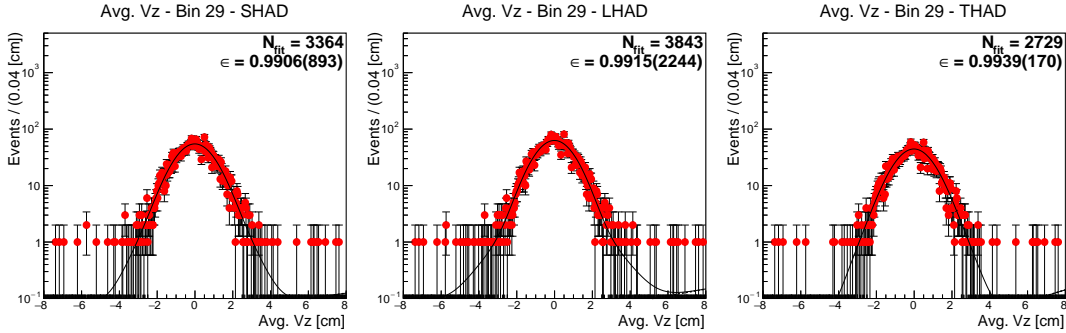


Figure D.30: Fits to determine the number of hadrons in the 3832 (Scan) data sample. This includes results for SHAD (left), LHAD (middle), and THAD (right).

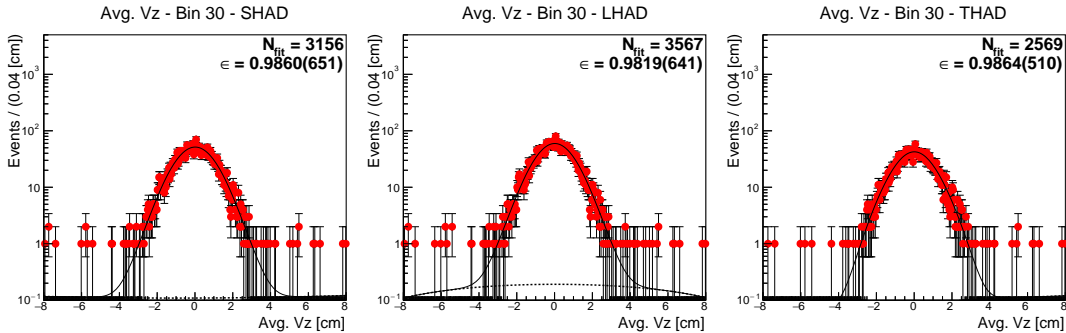


Figure D.31: Fits to determine the number of hadrons in the 3839 (Scan) data sample. This includes results for SHAD (left), LHAD (middle), and THAD (right).

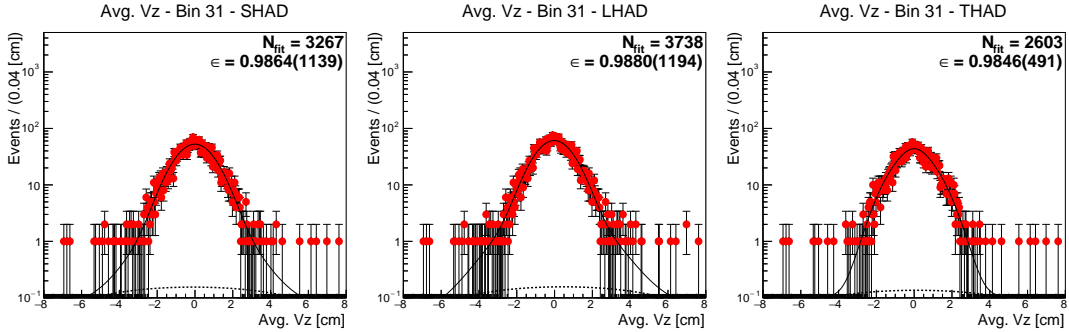


Figure D.32: Fits to determine the number of hadrons in the 3849 (Scan) data sample. This includes results for SHAD (left), LHAD (middle), and THAD (right).

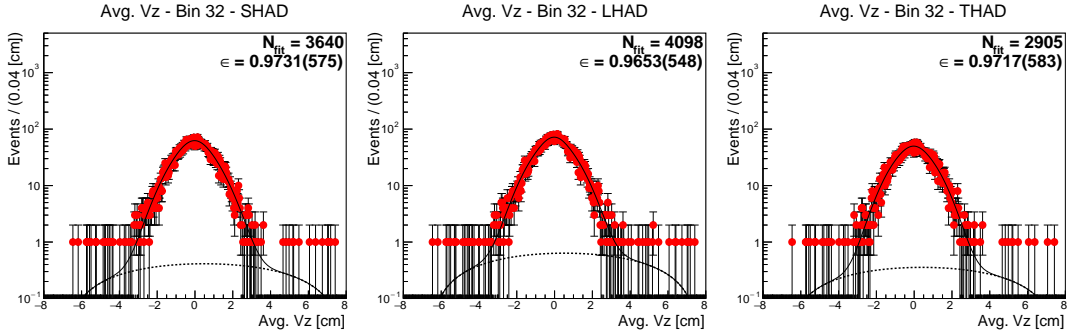


Figure D.33: Fits to determine the number of hadrons in the 3855 (Scan) data sample. This includes results for SHAD (left), LHAD (middle), and THAD (right).

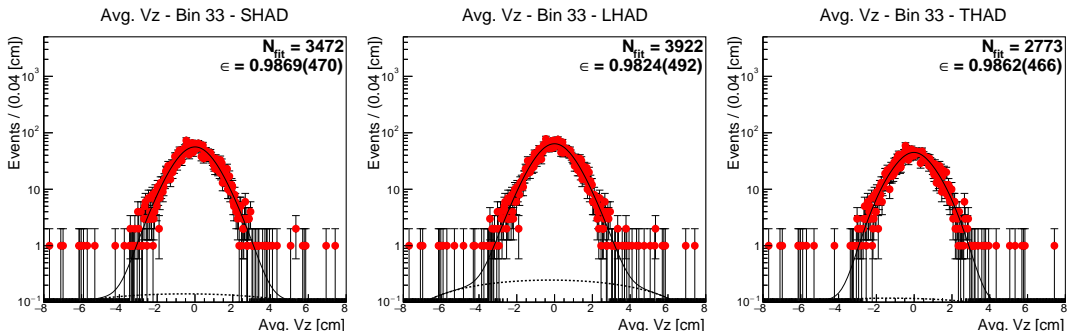


Figure D.34: Fits to determine the number of hadrons in the 3863 (Scan) data sample. This includes results for SHAD (left), LHAD (middle), and THAD (right).

Appendix E

Scan Data Reconstruction Efficiency

3734 (Scan) Reconstruction				
Sample	σ [nb]	ϵ_{MC} (SHAD) [%]	ϵ_{MC} (LHAD) [%]	ϵ_{MC} (THAD) [%]
$D^0\bar{D}^0$	0.164	0.7360 ± 0.0019	0.7956 ± 0.0020	0.6015 ± 0.0017
D^+D^-	0.000	-	-	-
$\tau^+\tau^-$	2.467	0.1284 ± 0.0008	0.2834 ± 0.0012	0.0987 ± 0.0007
$\gamma J/\psi$	1.060	0.4662 ± 0.0015	0.5625 ± 0.0017	0.3475 ± 0.0013
$\gamma\psi(2S)$	5.359	0.6305 ± 0.0018	0.6967 ± 0.0019	0.5142 ± 0.0016

Table E.1: Reconstruction of background samples for the 3734 (Scan) data.

3736 (Scan) Reconstruction				
Sample	σ [nb]	ϵ_{MC} (SHAD) [%]	ϵ_{MC} (LHAD) [%]	ϵ_{MC} (THAD) [%]
$D^0\bar{D}^0$	0.218	0.7348 ± 0.0027	0.7951 ± 0.0028	0.5995 ± 0.0024
D^+D^-	0.000	-	-	-
$\tau^+\tau^-$	2.475	0.1281 ± 0.0011	0.2815 ± 0.0017	0.0984 ± 0.0010
$\gamma J/\psi$	1.055	0.4640 ± 0.0022	0.5597 ± 0.0024	0.3429 ± 0.0019
$\gamma\psi(2S)$	5.094	0.6334 ± 0.0025	0.6995 ± 0.0026	0.5148 ± 0.0023

Table E.2: Reconstruction of background samples for the 3736 (Scan) data.

3744 (Scan) Reconstruction				
Sample	σ [nb]	ϵ_{MC} (SHAD) [%]	ϵ_{MC} (LHAD) [%]	ϵ_{MC} (THAD) [%]
$D^0\bar{D}^0$	0.765	0.7304 ± 0.0019	0.7932 ± 0.0020	0.5959 ± 0.0017
D^+D^-	0.150	0.6071 ± 0.0017	0.6838 ± 0.0018	0.4871 ± 0.0016
$\tau^+\tau^-$	2.514	0.1270 ± 0.0008	0.2812 ± 0.0012	0.0983 ± 0.0007
$\gamma J/\psi$	1.039	0.4626 ± 0.0015	0.5613 ± 0.0017	0.3431 ± 0.0013
$\gamma\psi(2S)$	4.428	0.6259 ± 0.0018	0.6938 ± 0.0019	0.5101 ± 0.0016

Table E.3: Reconstruction of background samples for the 3744 (Scan) data.

3748 (Scan) Reconstruction				
Sample	σ [nb]	ϵ_{MC} (SHAD) [%]	ϵ_{MC} (LHAD) [%]	ϵ_{MC} (THAD) [%]
$D^0\bar{D}^0$	0.838	0.7276 ± 0.0016	0.7906 ± 0.0016	0.5907 ± 0.0014
D^+D^-	0.360	0.6037 ± 0.0014	0.6800 ± 0.0015	0.4820 ± 0.0013
$\tau^+\tau^-$	2.522	0.1262 ± 0.0006	0.2781 ± 0.0010	0.0970 ± 0.0006
$\gamma J/\psi$	1.032	0.4609 ± 0.0012	0.5588 ± 0.0014	0.3427 ± 0.0011
$\gamma\psi(2S)$	4.180	0.6252 ± 0.0014	0.6928 ± 0.0015	0.5080 ± 0.0013

Table E.4: Reconstruction of background samples for the 3748 (Scan) data.

3750 (Scan) Reconstruction				
Sample	σ [nb]	ϵ_{MC} (SHAD) [%]	ϵ_{MC} (LHAD) [%]	ϵ_{MC} (THAD) [%]
$D^0\bar{D}^0$	0.968	0.7351 ± 0.0012	0.7960 ± 0.0013	0.5996 ± 0.0011
D^+D^-	0.439	0.6130 ± 0.0011	0.6879 ± 0.0012	0.4921 ± 0.0010
$\tau^+\tau^-$	2.533	0.1283 ± 0.0005	0.2812 ± 0.0007	0.0993 ± 0.0004
$\gamma J/\psi$	1.029	0.4661 ± 0.0010	0.5633 ± 0.0011	0.3470 ± 0.0008
$\gamma\psi(2S)$	4.065	0.6322 ± 0.0011	0.6986 ± 0.0012	0.5162 ± 0.0010

Table E.5: Reconstruction of background samples for the 3750 (Scan) data.

3751 (Scan) Reconstruction				
Sample	σ [nb]	ϵ_{MC} (SHAD) [%]	ϵ_{MC} (LHAD) [%]	ϵ_{MC} (THAD) [%]
$D^0\bar{D}^0$	1.237	0.7316 ± 0.0009	0.7935 ± 0.0009	0.5950 ± 0.0008
D^+D^-	0.574	0.6084 ± 0.0008	0.6841 ± 0.0009	0.4872 ± 0.0007
$\tau^+\tau^-$	2.542	0.1274 ± 0.0004	0.2805 ± 0.0006	0.0983 ± 0.0003
$\gamma J/\psi$	1.025	0.4629 ± 0.0007	0.5606 ± 0.0008	0.3439 ± 0.0006
$\gamma\psi(2S)$	3.969	0.6279 ± 0.0008	0.6959 ± 0.0009	0.5098 ± 0.0008

Table E.6: Reconstruction of background samples for the 3751 (Scan) data.

3753 (Scan) Reconstruction				
Sample	σ [nb]	ϵ_{MC} (SHAD) [%]	ϵ_{MC} (LHAD) [%]	ϵ_{MC} (THAD) [%]
$D^0\bar{D}^0$	1.377	0.7342 ± 0.0010	0.7955 ± 0.0010	0.5973 ± 0.0009
D^+D^-	0.748	0.6103 ± 0.0009	0.6855 ± 0.0009	0.4888 ± 0.0008
$\tau^+\tau^-$	2.553	0.1267 ± 0.0004	0.2798 ± 0.0006	0.0976 ± 0.0003
$\gamma J/\psi$	1.022	0.4636 ± 0.0008	0.5606 ± 0.0008	0.3443 ± 0.0007
$\gamma\psi(2S)$	3.871	0.6290 ± 0.0009	0.6964 ± 0.0009	0.5112 ± 0.0008

Table E.7: Reconstruction of background samples for the 3753 (Scan) data.

3755 (Scan) Reconstruction				
Sample	σ [nb]	ϵ_{MC} (SHAD) [%]	ϵ_{MC} (LHAD) [%]	ϵ_{MC} (THAD) [%]
$D^0\bar{D}^0$	1.566	0.7322 ± 0.0009	0.7931 ± 0.0009	0.5961 ± 0.0008
D^+D^-	0.797	0.6080 ± 0.0008	0.6832 ± 0.0009	0.4883 ± 0.0007
$\tau^+\tau^-$	2.562	0.1276 ± 0.0004	0.2808 ± 0.0006	0.0986 ± 0.0003
$\gamma J/\psi$	1.018	0.4632 ± 0.0007	0.5603 ± 0.0008	0.3450 ± 0.0006
$\gamma\psi(2S)$	3.752	0.6272 ± 0.0008	0.6946 ± 0.0009	0.5104 ± 0.0008

Table E.8: Reconstruction of background samples for the 3755 (Scan) data.

3756 (Scan) Reconstruction				
Sample	σ [nb]	ϵ_{MC} (SHAD) [%]	ϵ_{MC} (LHAD) [%]	ϵ_{MC} (THAD) [%]
$D^0\bar{D}^0$	1.629	0.7410 ± 0.0010	0.7995 ± 0.0011	0.6067 ± 0.0009
D^+D^-	0.914	0.6150 ± 0.0009	0.6889 ± 0.0010	0.4960 ± 0.0008
$\tau^+\tau^-$	2.573	0.1293 ± 0.0004	0.2821 ± 0.0006	0.1002 ± 0.0004
$\gamma J/\psi$	1.017	0.4686 ± 0.0008	0.5645 ± 0.0009	0.3507 ± 0.0007
$\gamma\psi(2S)$	3.721	0.6347 ± 0.0010	0.7011 ± 0.0010	0.5184 ± 0.0009

Table E.9: Reconstruction of background samples for the 3756 (Scan) data.

3759 (Scan) Reconstruction				
Sample	σ [nb]	ϵ_{MC} (SHAD) [%]	ϵ_{MC} (LHAD) [%]	ϵ_{MC} (THAD) [%]
$D^0\bar{D}^0$	1.948	0.7415 ± 0.0009	0.8000 ± 0.0009	0.6076 ± 0.0008
D^+D^-	1.192	0.6162 ± 0.0008	0.6894 ± 0.0008	0.4967 ± 0.0007
$\tau^+\tau^-$	2.584	0.1286 ± 0.0004	0.2826 ± 0.0005	0.0999 ± 0.0003
$\gamma J/\psi$	1.011	0.4688 ± 0.0007	0.5652 ± 0.0008	0.3507 ± 0.0006
$\gamma\psi(2S)$	3.572	0.6351 ± 0.0008	0.7010 ± 0.0008	0.5194 ± 0.0007

Table E.10: Reconstruction of background samples for the 3759 (Scan) data.

3762 (Scan) Reconstruction				
Sample	σ [nb]	ϵ_{MC} (SHAD) [%]	ϵ_{MC} (LHAD) [%]	ϵ_{MC} (THAD) [%]
$D^0\bar{D}^0$	2.385	0.7420 ± 0.0008	0.8004 ± 0.0009	0.6078 ± 0.0007
D^+D^-	1.534	0.6154 ± 0.0007	0.6891 ± 0.0008	0.4964 ± 0.0007
$\tau^+\tau^-$	2.598	0.1285 ± 0.0003	0.2819 ± 0.0005	0.0998 ± 0.0003
$\gamma J/\psi$	1.005	0.4680 ± 0.0007	0.5642 ± 0.0007	0.3496 ± 0.0006
$\gamma\psi(2S)$	3.426	0.6359 ± 0.0008	0.7017 ± 0.0008	0.5199 ± 0.0007

Table E.11: Reconstruction of background samples for the 3762 (Scan) data.

3765 (Scan) Reconstruction				
Sample	σ [nb]	ϵ_{MC} (SHAD) [%]	ϵ_{MC} (LHAD) [%]	ϵ_{MC} (THAD) [%]
$D^0\bar{D}^0$	2.715	0.7425 ± 0.0010	0.8006 ± 0.0011	0.6085 ± 0.0009
D^+D^-	1.882	0.6168 ± 0.0009	0.6905 ± 0.0010	0.4978 ± 0.0008
$\tau^+\tau^-$	2.613	0.1281 ± 0.0004	0.2819 ± 0.0006	0.0997 ± 0.0004
$\gamma J/\psi$	1.000	0.4693 ± 0.0008	0.5649 ± 0.0009	0.3519 ± 0.0007
$\gamma\psi(2S)$	3.315	0.6376 ± 0.0010	0.7035 ± 0.0010	0.5219 ± 0.0009

Table E.12: Reconstruction of background samples for the 3765 (Scan) data.

3767 (Scan) Reconstruction				
Sample	σ [nb]	ϵ_{MC} (SHAD) [%]	ϵ_{MC} (LHAD) [%]	ϵ_{MC} (THAD) [%]
$D^0\bar{D}^0$	3.102	0.7432 ± 0.0011	0.8008 ± 0.0012	0.6090 ± 0.0010
D^+D^-	2.200	0.6171 ± 0.0010	0.6908 ± 0.0011	0.4978 ± 0.0009
$\tau^+\tau^-$	2.627	0.1286 ± 0.0005	0.2818 ± 0.0007	0.0999 ± 0.0004
$\gamma J/\psi$	0.995	0.4693 ± 0.0009	0.5653 ± 0.0010	0.3511 ± 0.0008
$\gamma\psi(2S)$	3.212	0.6369 ± 0.0010	0.7025 ± 0.0011	0.5214 ± 0.0009

Table E.13: Reconstruction of background samples for the 3767 (Scan) data.

3771 (Scan) Reconstruction				
Sample	σ [nb]	ϵ_{MC} (SHAD) [%]	ϵ_{MC} (LHAD) [%]	ϵ_{MC} (THAD) [%]
$D^0\bar{D}^0$	3.406	0.7440 ± 0.0014	0.8021 ± 0.0014	0.6098 ± 0.0012
D^+D^-	2.634	0.6179 ± 0.0012	0.6913 ± 0.0013	0.4987 ± 0.0011
$\tau^+\tau^-$	2.641	0.1284 ± 0.0006	0.2821 ± 0.0008	0.1003 ± 0.0005
$\gamma J/\psi$	0.989	0.4700 ± 0.0011	0.5661 ± 0.0012	0.3528 ± 0.0009
$\gamma\psi(2S)$	3.075	0.6356 ± 0.0013	0.7020 ± 0.0013	0.5206 ± 0.0011

Table E.14: Reconstruction of background samples for the 3771 (Scan) data.

3774 (Scan) Reconstruction				
Sample	σ [nb]	ϵ_{MC} (SHAD) [%]	ϵ_{MC} (LHAD) [%]	ϵ_{MC} (THAD) [%]
$D^0\bar{D}^0$	3.714	0.7429 ± 0.0014	0.8009 ± 0.0014	0.6084 ± 0.0012
D^+D^-	3.067	0.6172 ± 0.0012	0.6903 ± 0.0013	0.4975 ± 0.0011
$\tau^+\tau^-$	2.656	0.1286 ± 0.0006	0.2819 ± 0.0008	0.0996 ± 0.0005
$\gamma J/\psi$	0.983	0.4695 ± 0.0011	0.5657 ± 0.0012	0.3509 ± 0.0009
$\gamma\psi(2S)$	2.975	0.6365 ± 0.0013	0.7028 ± 0.0013	0.5194 ± 0.0011

Table E.15: Reconstruction of background samples for the 3774 (Scan) data.

3777 (Scan) Reconstruction				
Sample	σ [nb]	ϵ_{MC} (SHAD) [%]	ϵ_{MC} (LHAD) [%]	ϵ_{MC} (THAD) [%]
$D^0\bar{D}^0$	3.692	0.7436 ± 0.0016	0.8016 ± 0.0016	0.6090 ± 0.0014
D^+D^-	3.078	0.6171 ± 0.0014	0.6904 ± 0.0015	0.4978 ± 0.0013
$\tau^+\tau^-$	2.669	0.1299 ± 0.0007	0.2837 ± 0.0010	0.1012 ± 0.0006
$\gamma J/\psi$	0.978	0.4702 ± 0.0013	0.5662 ± 0.0014	0.3537 ± 0.0011
$\gamma\psi(2S)$	2.870	0.6362 ± 0.0015	0.7024 ± 0.0015	0.5204 ± 0.0013

Table E.16: Reconstruction of background samples for the 3777 (Scan) data.

3780 (Scan) Reconstruction				
Sample	σ [nb]	ϵ_{MC} (SHAD) [%]	ϵ_{MC} (LHAD) [%]	ϵ_{MC} (THAD) [%]
$D^0\bar{D}^0$	3.444	0.7460 ± 0.0014	0.8036 ± 0.0014	0.6126 ± 0.0012
D^+D^-	2.599	0.6194 ± 0.0012	0.6925 ± 0.0013	0.5003 ± 0.0011
$\tau^+\tau^-$	2.683	0.1285 ± 0.0006	0.2824 ± 0.0008	0.1000 ± 0.0005
$\gamma J/\psi$	0.973	0.4703 ± 0.0011	0.5665 ± 0.0012	0.3530 ± 0.0009
$\gamma\psi(2S)$	2.788	0.6380 ± 0.0013	0.7043 ± 0.0013	0.5228 ± 0.0011

Table E.17: Reconstruction of background samples for the 3780 (Scan) data.

3782 (Scan) Reconstruction				
Sample	σ [nb]	ϵ_{MC} (SHAD) [%]	ϵ_{MC} (LHAD) [%]	ϵ_{MC} (THAD) [%]
$D^0\bar{D}^0$	2.791	0.7441 ± 0.0012	0.8019 ± 0.0013	0.6101 ± 0.0011
D^+D^-	2.206	0.6195 ± 0.0011	0.6923 ± 0.0012	0.5004 ± 0.0010
$\tau^+\tau^-$	2.696	0.1281 ± 0.0005	0.2814 ± 0.0008	0.0995 ± 0.0004
$\gamma J/\psi$	0.968	0.4706 ± 0.0010	0.5663 ± 0.0011	0.3531 ± 0.0008
$\gamma\psi(2S)$	2.712	0.6377 ± 0.0011	0.7046 ± 0.0012	0.5210 ± 0.0010

Table E.18: Reconstruction of background samples for the 3782 (Scan) data.

3786 (Scan) Reconstruction				
Sample	σ [nb]	ϵ_{MC} (SHAD) [%]	ϵ_{MC} (LHAD) [%]	ϵ_{MC} (THAD) [%]
$D^0\bar{D}^0$	1.995	0.7460 ± 0.0012	0.8037 ± 0.0013	0.6122 ± 0.0011
D^+D^-	1.627	0.6194 ± 0.0011	0.6923 ± 0.0012	0.5013 ± 0.0010
$\tau^+\tau^-$	2.709	0.1289 ± 0.0005	0.2810 ± 0.0007	0.1007 ± 0.0004
$\gamma J/\psi$	0.961	0.4698 ± 0.0010	0.5652 ± 0.0011	0.3524 ± 0.0008
$\gamma\psi(2S)$	2.605	0.6380 ± 0.0011	0.7044 ± 0.0012	0.5223 ± 0.0010

Table E.19: Reconstruction of background samples for the 3786 (Scan) data.

3789 (Scan) Reconstruction				
Sample	σ [nb]	ϵ_{MC} (SHAD) [%]	ϵ_{MC} (LHAD) [%]	ϵ_{MC} (THAD) [%]
$D^0\bar{D}^0$	1.361	0.7457 ± 0.0010	0.8035 ± 0.0011	0.6118 ± 0.0009
D^+D^-	1.178	0.6188 ± 0.0009	0.6918 ± 0.0010	0.5002 ± 0.0008
$\tau^+\tau^-$	2.722	0.1284 ± 0.0004	0.2805 ± 0.0006	0.1003 ± 0.0004
$\gamma J/\psi$	0.957	0.4700 ± 0.0008	0.5655 ± 0.0009	0.3526 ± 0.0007
$\gamma\psi(2S)$	2.550	0.6379 ± 0.0010	0.7040 ± 0.0010	0.5225 ± 0.0009

Table E.20: Reconstruction of background samples for the 3789 (Scan) data.

3792 (Scan) Reconstruction				
Sample	σ [nb]	ϵ_{MC} (SHAD) [%]	ϵ_{MC} (LHAD) [%]	ϵ_{MC} (THAD) [%]
$D^0\bar{D}^0$	0.920	0.7440 ± 0.0010	0.8019 ± 0.0011	0.6094 ± 0.0009
D^+D^-	0.680	0.6176 ± 0.0009	0.6905 ± 0.0010	0.4989 ± 0.0008
$\tau^+\tau^-$	2.739	0.1286 ± 0.0004	0.2800 ± 0.0006	0.0998 ± 0.0004
$\gamma J/\psi$	0.951	0.4677 ± 0.0008	0.5637 ± 0.0009	0.3498 ± 0.0007
$\gamma\psi(2S)$	2.467	0.6364 ± 0.0010	0.7027 ± 0.0010	0.5196 ± 0.0009

Table E.21: Reconstruction of background samples for the 3792 (Scan) data.

3797 (Scan) Reconstruction				
Sample	σ [nb]	ϵ_{MC} (SHAD) [%]	ϵ_{MC} (LHAD) [%]	ϵ_{MC} (THAD) [%]
$D^0\bar{D}^0$	0.562	0.7444 ± 0.0010	0.8025 ± 0.0010	0.6102 ± 0.0009
D^+D^-	0.414	0.6183 ± 0.0009	0.6916 ± 0.0009	0.4998 ± 0.0008
$\tau^+\tau^-$	2.755	0.1280 ± 0.0004	0.2796 ± 0.0006	0.0998 ± 0.0004
$\gamma J/\psi$	0.944	0.4688 ± 0.0008	0.5646 ± 0.0008	0.3512 ± 0.0007
$\gamma\psi(2S)$	2.370	0.6380 ± 0.0009	0.7042 ± 0.0009	0.5218 ± 0.0008

Table E.22: Reconstruction of background samples for the 3797 (Scan) data.

3800 (Scan) Reconstruction				
Sample	σ [nb]	ϵ_{MC} (SHAD) [%]	ϵ_{MC} (LHAD) [%]	ϵ_{MC} (THAD) [%]
$D^0\bar{D}^0$	0.424	0.7417 ± 0.0009	0.8004 ± 0.0009	0.6068 ± 0.0008
D^+D^-	0.241	0.6161 ± 0.0008	0.6894 ± 0.0009	0.4965 ± 0.0007
$\tau^+\tau^-$	2.771	0.1281 ± 0.0004	0.2803 ± 0.0006	0.0994 ± 0.0003
$\gamma J/\psi$	0.938	0.4671 ± 0.0007	0.5633 ± 0.0008	0.3492 ± 0.0006
$\gamma\psi(2S)$	2.301	0.6358 ± 0.0008	0.7029 ± 0.0009	0.5183 ± 0.0008

Table E.23: Reconstruction of background samples for the 3800 (Scan) data.

3802 (Scan) Reconstruction				
Sample	σ [nb]	ϵ_{MC} (SHAD) [%]	ϵ_{MC} (LHAD) [%]	ϵ_{MC} (THAD) [%]
$D^0\bar{D}^0$	0.325	0.7421 ± 0.0011	0.8008 ± 0.0012	0.6075 ± 0.0010
D^+D^-	0.236	0.6157 ± 0.0010	0.6892 ± 0.0011	0.4959 ± 0.0009
$\tau^+\tau^-$	2.784	0.1285 ± 0.0005	0.2806 ± 0.0007	0.0995 ± 0.0004
$\gamma J/\psi$	0.935	0.4676 ± 0.0009	0.5635 ± 0.0010	0.3496 ± 0.0008
$\gamma\psi(2S)$	2.260	0.6362 ± 0.0010	0.7034 ± 0.0011	0.5195 ± 0.0009

Table E.24: Reconstruction of background samples for the 3802 (Scan) data.

3807 (Scan) Reconstruction				
Sample	σ [nb]	ϵ_{MC} (SHAD) [%]	ϵ_{MC} (LHAD) [%]	ϵ_{MC} (THAD) [%]
$D^0\bar{D}^0$	0.352	0.7407 ± 0.0012	0.8000 ± 0.0013	0.6049 ± 0.0011
D^+D^-	0.289	0.6132 ± 0.0011	0.6876 ± 0.0012	0.4941 ± 0.0010
$\tau^+\tau^-$	2.795	0.1286 ± 0.0005	0.2800 ± 0.0007	0.0995 ± 0.0004
$\gamma J/\psi$	0.927	0.4666 ± 0.0010	0.5628 ± 0.0011	0.3480 ± 0.0008
$\gamma\psi(2S)$	2.174	0.6344 ± 0.0011	0.7024 ± 0.0012	0.5175 ± 0.0010

Table E.25: Reconstruction of background samples for the 3807 (Scan) data.

3809 (Scan) Reconstruction				
Sample	σ [nb]	ϵ_{MC} (SHAD) [%]	ϵ_{MC} (LHAD) [%]	ϵ_{MC} (THAD) [%]
$D^0\bar{D}^0$	0.233	0.7430 ± 0.0016	0.8019 ± 0.0016	0.6092 ± 0.0014
D^+D^-	0.132	0.6170 ± 0.0014	0.6907 ± 0.0015	0.4977 ± 0.0013
$\tau^+\tau^-$	2.807	0.1281 ± 0.0007	0.2803 ± 0.0010	0.0998 ± 0.0006
$\gamma J/\psi$	0.923	0.4676 ± 0.0012	0.5632 ± 0.0014	0.3511 ± 0.0011
$\gamma\psi(2S)$	2.133	0.6375 ± 0.0015	0.7046 ± 0.0015	0.5216 ± 0.0013

Table E.26: Reconstruction of background samples for the 3809 (Scan) data.

3813 (Scan) Reconstruction				
Sample	σ [nb]	ϵ_{MC} (SHAD) [%]	ϵ_{MC} (LHAD) [%]	ϵ_{MC} (THAD) [%]
$D^0\bar{D}^0$	0.060	0.7393 ± 0.0019	0.7994 ± 0.0020	0.6045 ± 0.0017
D^+D^-	0.153	0.6128 ± 0.0018	0.6879 ± 0.0019	0.4923 ± 0.0016
$\tau^+\tau^-$	2.819	0.1272 ± 0.0008	0.2783 ± 0.0012	0.0980 ± 0.0007
$\gamma J/\psi$	0.917	0.4679 ± 0.0015	0.5634 ± 0.0017	0.3488 ± 0.0013
$\gamma\psi(2S)$	2.063	0.6341 ± 0.0018	0.7020 ± 0.0019	0.5160 ± 0.0016

Table E.27: Reconstruction of background samples for the 3813 (Scan) data.

3815 (Scan) Reconstruction				
Sample	σ [nb]	ϵ_{MC} (SHAD) [%]	ϵ_{MC} (LHAD) [%]	ϵ_{MC} (THAD) [%]
$D^0\bar{D}^0$	0.056	0.7424 ± 0.0019	0.8022 ± 0.0020	0.6068 ± 0.0017
D^+D^-	0.089	0.6157 ± 0.0018	0.6887 ± 0.0019	0.4969 ± 0.0016
$\tau^+\tau^-$	2.829	0.1287 ± 0.0008	0.2809 ± 0.0012	0.0999 ± 0.0007
$\gamma J/\psi$	0.914	0.4675 ± 0.0015	0.5635 ± 0.0017	0.3494 ± 0.0013
$\gamma\psi(2S)$	2.034	0.6381 ± 0.0018	0.7048 ± 0.0019	0.5202 ± 0.0016

Table E.28: Reconstruction of background samples for the 3815 (Scan) data.

3822 (Scan) Reconstruction				
Sample	σ [nb]	ϵ_{MC} (SHAD) [%]	ϵ_{MC} (LHAD) [%]	ϵ_{MC} (THAD) [%]
$D^0\bar{D}^0$	0.140	0.7442 ± 0.0019	0.8038 ± 0.0020	0.6097 ± 0.0017
D^+D^-	0.197	0.6176 ± 0.0018	0.6919 ± 0.0019	0.4992 ± 0.0016
$\tau^+\tau^-$	2.859	0.1295 ± 0.0008	0.2813 ± 0.0012	0.1003 ± 0.0007
$\gamma J/\psi$	0.902	0.4676 ± 0.0015	0.5651 ± 0.0017	0.3497 ± 0.0013
$\gamma\psi(2S)$	1.920	0.6401 ± 0.0018	0.7064 ± 0.0019	0.5234 ± 0.0016

Table E.29: Reconstruction of background samples for the 3822 (Scan) data.

3832 (Scan) Reconstruction				
Sample	σ [nb]	ϵ_{MC} (SHAD) [%]	ϵ_{MC} (LHAD) [%]	ϵ_{MC} (THAD) [%]
$D^0\bar{D}^0$	0.069	0.7469 ± 0.0027	0.8037 ± 0.0028	0.6122 ± 0.0025
D^+D^-	0.046	0.6209 ± 0.0025	0.6924 ± 0.0026	0.5009 ± 0.0022
$\tau^+\tau^-$	2.887	0.1290 ± 0.0011	0.2796 ± 0.0017	0.1003 ± 0.0010
$\gamma J/\psi$	0.888	0.4678 ± 0.0022	0.5634 ± 0.0024	0.3500 ± 0.0019
$\gamma\psi(2S)$	1.799	0.6366 ± 0.0025	0.7046 ± 0.0027	0.5206 ± 0.0023

Table E.30: Reconstruction of background samples for the 3832 (Scan) data.

3839 (Scan) Reconstruction				
Sample	σ [nb]	ϵ_{MC} (SHAD) [%]	ϵ_{MC} (LHAD) [%]	ϵ_{MC} (THAD) [%]
$D^0\bar{D}^0$	0.237	0.7435 ± 0.0027	0.8017 ± 0.0028	0.6102 ± 0.0025
D^+D^-	0.254	0.6168 ± 0.0025	0.6902 ± 0.0026	0.4991 ± 0.0022
$\tau^+\tau^-$	2.914	0.1270 ± 0.0011	0.2759 ± 0.0017	0.0983 ± 0.0010
$\gamma J/\psi$	0.877	0.4676 ± 0.0022	0.5631 ± 0.0024	0.3502 ± 0.0019
$\gamma\psi(2S)$	1.716	0.6374 ± 0.0025	0.7059 ± 0.0027	0.5231 ± 0.0023

Table E.31: Reconstruction of background samples for the 3839 (Scan) data.

3849 (Scan) Reconstruction				
Sample	σ [nb]	ϵ_{MC} (SHAD) [%]	ϵ_{MC} (LHAD) [%]	ϵ_{MC} (THAD) [%]
$D^0\bar{D}^0$	0.186	0.7440 ± 0.0027	0.8028 ± 0.0028	0.6087 ± 0.0025
D^+D^-	0.186	0.6195 ± 0.0025	0.6921 ± 0.0026	0.5007 ± 0.0022
$\tau^+\tau^-$	2.939	0.1289 ± 0.0011	0.2773 ± 0.0017	0.1001 ± 0.0010
$\gamma J/\psi$	0.862	0.4679 ± 0.0022	0.5612 ± 0.0024	0.3496 ± 0.0019
$\gamma\psi(2S)$	1.604	0.6357 ± 0.0025	0.7041 ± 0.0027	0.5206 ± 0.0023

Table E.32: Reconstruction of background samples for the 3849 (Scan) data.

3855 (Scan) Reconstruction				
Sample	σ [nb]	ϵ_{MC} (SHAD) [%]	ϵ_{MC} (LHAD) [%]	ϵ_{MC} (THAD) [%]
$D^0\bar{D}^0$	0.337	0.7467 ± 0.0019	0.8046 ± 0.0020	0.6116 ± 0.0017
D^+D^-	0.273	0.6188 ± 0.0018	0.6917 ± 0.0019	0.5006 ± 0.0016
$\tau^+\tau^-$	2.967	0.1290 ± 0.0008	0.2785 ± 0.0012	0.1000 ± 0.0007
$\gamma J/\psi$	0.853	0.4676 ± 0.0015	0.5621 ± 0.0017	0.3498 ± 0.0013
$\gamma\psi(2S)$	1.545	0.6374 ± 0.0018	0.7049 ± 0.0019	0.5207 ± 0.0016

Table E.33: Reconstruction of background samples for the 3855 (Scan) data.

3863 (Scan) Reconstruction				
Sample	σ [nb]	ϵ_{MC} (SHAD) [%]	ϵ_{MC} (LHAD) [%]	ϵ_{MC} (THAD) [%]
$D^0\bar{D}^0$	0.340	0.7476 ± 0.0019	0.8040 ± 0.0020	0.6123 ± 0.0017
D^+D^-	0.099	0.6191 ± 0.0018	0.6916 ± 0.0019	0.5006 ± 0.0016
$\tau^+\tau^-$	2.988	0.1280 ± 0.0008	0.2763 ± 0.0012	0.1001 ± 0.0007
$\gamma J/\psi$	0.843	0.4667 ± 0.0015	0.5620 ± 0.0017	0.3499 ± 0.0013
$\gamma\psi(2S)$	1.476	0.6370 ± 0.0018	0.7054 ± 0.0019	0.5210 ± 0.0016

Table E.34: Reconstruction of background samples for the 3863 (Scan) data.

Appendix F

Scan Data Signal Counts

3734 (Scan) Results			
Sample	N_{had} (SHAD)	N_{had} (LHAD)	N_{had} (THAD)
Data	12047 ± 109	13458 ± 116	9605 ± 98
$q\bar{q}$	7942 ± 62	8743 ± 66	6314 ± 52
$D^0\overline{D^0}$	100 ± 1	108 ± 1	81 ± 1
D^+D^-	0 ± 0	0 ± 0	0 ± 0
$\tau^+\tau^-$	262 ± 1	579 ± 3	201 ± 1
$\gamma J/\psi$	409 ± 2	494 ± 2	305 ± 1
$\gamma\psi(2S)$	2802 ± 12	3096 ± 13	2285 ± 10
Hadrons	529 ± 126	435 ± 134	416 ± 111

Table F.1: Hadronic events selected in the 3734 (Scan) data.

3736 (Scan) Results			
Sample	N_{had} (SHAD)	N_{had} (LHAD)	N_{had} (THAD)
Data	4786 ± 69	5413 ± 73	3767 ± 61
$q\bar{q}$	3144 ± 28	3460 ± 30	2500 ± 23
$D^0\overline{D^0}$	52 ± 1	56 ± 1	42 ± 1
D^+D^-	0 ± 0	0 ± 0	0 ± 0
$\tau^+\tau^-$	104 ± 1	229 ± 1	80 ± 1
$\gamma J/\psi$	160 ± 1	194 ± 1	118 ± 1
$\gamma\psi(2S)$	1060 ± 7	1171 ± 8	861 ± 6
Hadrons	263 ± 75	301 ± 80	162 ± 66

Table F.2: Hadronic events selected in the 3736 (Scan) data.

3744 (Scan) Results			
Sample	N_{had} (SHAD)	N_{had} (LHAD)	N_{had} (THAD)
Data	13426 ± 115	15255 ± 123	10823 ± 104
$q\bar{q}$	9082 ± 72	9984 ± 78	7226 ± 61
$D^0\bar{D}^0$	532 ± 2	577 ± 2	434 ± 1
D^+D^-	86 ± 1	97 ± 1	69 ± 1
$\tau^+\tau^-$	304 ± 2	673 ± 3	235 ± 1
$\gamma J/\psi$	457 ± 2	555 ± 2	339 ± 1
$\gamma\psi(2S)$	2639 ± 11	2925 ± 12	2151 ± 9
Hadrons	322 ± 137	440 ± 146	366 ± 121

Table F.3: Hadronic events selected in the 3744 (Scan) data.

3748 (Scan) Results			
Sample	N_{had} (SHAD)	N_{had} (LHAD)	N_{had} (THAD)
Data	20024 ± 141	22788 ± 150	15815 ± 125
$q\bar{q}$	13384 ± 105	14706 ± 113	10651 ± 90
$D^0\bar{D}^0$	857 ± 3	931 ± 3	695 ± 2
D^+D^-	305 ± 1	344 ± 1	243 ± 1
$\tau^+\tau^-$	447 ± 2	985 ± 4	343 ± 2
$\gamma J/\psi$	668 ± 2	810 ± 2	497 ± 2
$\gamma\psi(2S)$	3672 ± 13	4069 ± 14	2984 ± 11
Hadrons	688 ± 177	940 ± 189	398 ± 155

Table F.4: Hadronic events selected in the 3748 (Scan) data.

3750 (Scan) Results			
Sample	N_{had} (SHAD)	N_{had} (LHAD)	N_{had} (THAD)
Data	32171 ± 179	36551 ± 191	25686 ± 160
$q\bar{q}$	21617 ± 168	23746 ± 180	17205 ± 144
$D^0\bar{D}^0$	1616 ± 4	1750 ± 4	1318 ± 3
D^+D^-	611 ± 1	686 ± 1	490 ± 1
$\tau^+\tau^-$	738 ± 3	1618 ± 5	571 ± 2
$\gamma J/\psi$	1089 ± 3	1316 ± 3	810 ± 2
$\gamma\psi(2S)$	5838 ± 16	6451 ± 17	4767 ± 14
Hadrons	659 ± 246	982 ± 263	522 ± 216

Table F.5: Hadronic events selected in the 3750 (Scan) data.

3751 (Scan) Results			
Sample	N_{had} (SHAD)	N_{had} (LHAD)	N_{had} (THAD)
Data	42694 ± 206	48594 ± 220	34040 ± 184
$q\bar{q}$	28246 ± 219	31021 ± 234	22483 ± 188
$D^0\bar{D}^0$	2687 ± 6	2915 ± 6	2186 ± 5
D^+D^-	1037 ± 2	1166 ± 2	830 ± 2
$\tau^+\tau^-$	961 ± 3	2117 ± 5	742 ± 2
$\gamma J/\psi$	1409 ± 3	1707 ± 4	1047 ± 2
$\gamma\psi(2S)$	7401 ± 17	8204 ± 18	6010 ± 14
Hadrons	948 ± 301	1461 ± 322	739 ± 264

Table F.6: Hadronic events selected in the 3751 (Scan) data.

3753 (Scan) Results			
Sample	N_{had} (SHAD)	N_{had} (LHAD)	N_{had} (THAD)
Data	48035 ± 219	54668 ± 233	38460 ± 196
$q\bar{q}$	31437 ± 244	34517 ± 262	25027 ± 210
$D^0\bar{D}^0$	3344 ± 7	3623 ± 7	2720 ± 6
D^+D^-	1510 ± 3	1696 ± 3	1209 ± 2
$\tau^+\tau^-$	1069 ± 3	2363 ± 6	824 ± 3
$\gamma J/\psi$	1567 ± 3	1895 ± 4	1164 ± 3
$\gamma\psi(2S)$	8055 ± 18	8918 ± 20	6547 ± 15
Hadrons	1049 ± 329	1652 ± 352	967 ± 288

Table F.7: Hadronic events selected in the 3753 (Scan) data.

3755 (Scan) Results			
Sample	N_{had} (SHAD)	N_{had} (LHAD)	N_{had} (THAD)
Data	49692 ± 222	56270 ± 237	39753 ± 199
$q\bar{q}$	32437 ± 254	35604 ± 272	25826 ± 219
$D^0\bar{D}^0$	3917 ± 8	4242 ± 9	3188 ± 7
D^+D^-	1655 ± 3	1860 ± 4	1329 ± 3
$\tau^+\tau^-$	1116 ± 3	2457 ± 6	862 ± 3
$\gamma J/\psi$	1610 ± 3	1948 ± 4	1199 ± 3
$\gamma\psi(2S)$	8039 ± 17	8903 ± 19	6541 ± 15
Hadrons	915 ± 339	1253 ± 362	803 ± 296

Table F.8: Hadronic events selected in the 3755 (Scan) data.

3756 (Scan) Results			
Sample	N_{had} (SHAD)	N_{had} (LHAD)	N_{had} (THAD)
Data	57313 ± 239	64807 ± 254	46172 ± 214
$q\bar{q}$	36748 ± 288	40333 ± 309	29261 ± 248
$D^0\bar{D}^0$	4672 ± 10	5042 ± 10	3825 ± 8
D^+D^-	2176 ± 4	2437 ± 5	1754 ± 4
$\tau^+\tau^-$	1287 ± 4	2809 ± 7	997 ± 4
$\gamma J/\psi$	1844 ± 4	2222 ± 5	1380 ± 3
$\gamma\psi(2S)$	9141 ± 20	10098 ± 22	7466 ± 17
Hadrons	1441 ± 375	1863 ± 401	1485 ± 328

Table F.9: Hadronic events selected in the 3756 (Scan) data.

3759 (Scan) Results			
Sample	N_{had} (SHAD)	N_{had} (LHAD)	N_{had} (THAD)
Data	66837 ± 258	75711 ± 275	53739 ± 231
$q\bar{q}$	42080 ± 333	46166 ± 357	33513 ± 287
$D^0\bar{D}^0$	6410 ± 12	6916 ± 13	5253 ± 10
D^+D^-	3260 ± 6	3647 ± 7	2627 ± 5
$\tau^+\tau^-$	1474 ± 4	3241 ± 7	1145 ± 4
$\gamma J/\psi$	2103 ± 4	2536 ± 5	1573 ± 3
$\gamma\psi(2S)$	10067 ± 20	11112 ± 21	8234 ± 17
Hadrons	1439 ± 422	2090 ± 451	1391 ± 369

Table F.10: Hadronic events selected in the 3759 (Scan) data.

3762 (Scan) Results			
Sample	N_{had} (SHAD)	N_{had} (LHAD)	N_{had} (THAD)
Data	68538 ± 261	77492 ± 278	55377 ± 235
$q\bar{q}$	42513 ± 341	46621 ± 365	33866 ± 294
$D^0\bar{D}^0$	7945 ± 15	8570 ± 16	6508 ± 12
D^+D^-	4238 ± 8	4746 ± 9	3418 ± 7
$\tau^+\tau^-$	1499 ± 4	3288 ± 7	1164 ± 3
$\gamma J/\psi$	2111 ± 4	2545 ± 5	1577 ± 3
$\gamma\psi(2S)$	9779 ± 19	10791 ± 20	7995 ± 16
Hadrons	449 ± 431	927 ± 460	846 ± 377

Table F.11: Hadronic events selected in the 3762 (Scan) data.

3765 (Scan) Results			
Sample	N_{had} (SHAD)	N_{had} (LHAD)	N_{had} (THAD)
Data	51719 ± 227	58419 ± 241	41736 ± 204
$q\bar{q}$	31053 ± 253	34042 ± 272	24741 ± 218
$D^0\bar{D}^0$	6617 ± 15	7135 ± 16	5423 ± 12
D^+D^-	3810 ± 9	4265 ± 9	3075 ± 7
$\tau^+\tau^-$	1098 ± 4	2417 ± 7	854 ± 3
$\gamma J/\psi$	1540 ± 3	1854 ± 4	1155 ± 3
$\gamma\psi(2S)$	6939 ± 16	7656 ± 17	5679 ± 14
Hadrons	657 ± 341	1046 ± 364	804 ± 299

Table F.12: Hadronic events selected in the 3765 (Scan) data.

3767 (Scan) Results			
Sample	N_{had} (SHAD)	N_{had} (LHAD)	N_{had} (THAD)
Data	40038 ± 200	45288 ± 212	32311 ± 179
$q\bar{q}$	23074 ± 192	25285 ± 206	18387 ± 165
$D^0\bar{D}^0$	5629 ± 14	6065 ± 15	4613 ± 12
D^+D^-	3314 ± 8	3711 ± 9	2673 ± 7
$\tau^+\tau^-$	825 ± 3	1808 ± 5	640 ± 2
$\gamma J/\psi$	1140 ± 3	1374 ± 3	853 ± 2
$\gamma\psi(2S)$	4994 ± 13	5509 ± 14	4088 ± 11
Hadrons	1058 ± 278	1534 ± 297	1053 ± 244

Table F.13: Hadronic events selected in the 3767 (Scan) data.

3771 (Scan) Results			
Sample	N_{had} (SHAD)	N_{had} (LHAD)	N_{had} (THAD)
Data	34012 ± 184	38173 ± 195	27356 ± 165
$q\bar{q}$	19014 ± 161	20825 ± 173	15156 ± 138
$D^0\bar{D}^0$	5106 ± 15	5504 ± 16	4185 ± 12
D^+D^-	3279 ± 10	3668 ± 11	2647 ± 8
$\tau^+\tau^-$	683 ± 3	1501 ± 5	533 ± 2
$\gamma J/\psi$	936 ± 3	1127 ± 3	702 ± 2
$\gamma\psi(2S)$	3938 ± 12	4349 ± 13	3225 ± 10
Hadrons	1053 ± 246	1194 ± 262	904 ± 216

Table F.14: Hadronic events selected in the 3771 (Scan) data.

3774 (Scan) Results			
Sample	N_{had} (SHAD)	N_{had} (LHAD)	N_{had} (THAD)
Data	31457 ± 177	35438 ± 188	25241 ± 158
$q\bar{q}$	17211 ± 148	18843 ± 159	13721 ± 127
$D^0\bar{D}^0$	5038 ± 15	5431 ± 16	4126 ± 13
D^+D^-	3456 ± 10	3865 ± 12	2786 ± 9
$\tau^+\tau^-$	623 ± 3	1367 ± 5	483 ± 2
$\gamma J/\psi$	843 ± 2	1015 ± 3	630 ± 2
$\gamma\psi(2S)$	3458 ± 10	3818 ± 11	2822 ± 9
Hadrons	825 ± 232	1095 ± 247	671 ± 204

Table F.15: Hadronic events selected in the 3774 (Scan) data.

3777 (Scan) Results			
Sample	N_{had} (SHAD)	N_{had} (LHAD)	N_{had} (THAD)
Data	31195 ± 176	35150 ± 187	25095 ± 158
$q\bar{q}$	17165 ± 150	18785 ± 161	13688 ± 129
$D^0\bar{D}^0$	5006 ± 16	5397 ± 17	4100 ± 13
D^+D^-	3464 ± 11	3875 ± 12	2794 ± 9
$\tau^+\tau^-$	632 ± 3	1380 ± 5	492 ± 3
$\gamma J/\psi$	838 ± 3	1009 ± 3	630 ± 2
$\gamma\psi(2S)$	3329 ± 11	3675 ± 12	2723 ± 9
Hadrons	758 ± 233	1026 ± 248	665 ± 205

Table F.16: Hadronic events selected in the 3777 (Scan) data.

3780 (Scan) Results			
Sample	N_{had} (SHAD)	N_{had} (LHAD)	N_{had} (THAD)
Data	32426 ± 180	36485 ± 191	26084 ± 161
$q\bar{q}$	18339 ± 161	20062 ± 173	14627 ± 138
$D^0\bar{D}^0$	5011 ± 14	5398 ± 15	4114 ± 12
D^+D^-	3139 ± 9	3510 ± 10	2536 ± 8
$\tau^+\tau^-$	672 ± 3	1477 ± 5	523 ± 2
$\gamma J/\psi$	892 ± 2	1074 ± 3	669 ± 2
$\gamma\psi(2S)$	3469 ± 10	3830 ± 11	2843 ± 9
Hadrons	900 ± 242	1130 ± 258	768 ± 213

Table F.17: Hadronic events selected in the 3780 (Scan) data.

3782 (Scan) Results			
Sample	N_{had} (SHAD)	N_{had} (LHAD)	N_{had} (THAD)
Data	34028 ± 184	38558 ± 196	27372 ± 165
$q\bar{q}$	20194 ± 179	22082 ± 192	16109 ± 154
$D^0\bar{D}^0$	4464 ± 12	4812 ± 13	3660 ± 10
D^+D^-	2938 ± 8	3283 ± 9	2373 ± 7
$\tau^+\tau^-$	742 ± 3	1631 ± 5	576 ± 2
$\gamma J/\psi$	979 ± 3	1178 ± 3	734 ± 2
$\gamma\psi(2S)$	3717 ± 10	4107 ± 11	3037 ± 9
Hadrons	991 ± 258	1462 ± 275	878 ± 226

Table F.18: Hadronic events selected in the 3782 (Scan) data.

3786 (Scan) Results			
Sample	N_{had} (SHAD)	N_{had} (LHAD)	N_{had} (THAD)
Data	37498 ± 193	42325 ± 205	30190 ± 173
$q\bar{q}$	23901 ± 214	26122 ± 229	19072 ± 184
$D^0\bar{D}^0$	3793 ± 10	4086 ± 10	3112 ± 8
D^+D^-	2568 ± 7	2870 ± 7	2078 ± 5
$\tau^+\tau^-$	890 ± 3	1940 ± 6	695 ± 3
$\gamma J/\psi$	1150 ± 3	1384 ± 3	863 ± 2
$\gamma\psi(2S)$	4236 ± 11	4677 ± 12	3468 ± 9
Hadrons	957 ± 289	1241 ± 309	898 ± 253

Table F.19: Hadronic events selected in the 3786 (Scan) data.

3789 (Scan) Results			
Sample	N_{had} (SHAD)	N_{had} (LHAD)	N_{had} (THAD)
Data	39308 ± 198	44415 ± 210	31651 ± 177
$q\bar{q}$	26534 ± 239	28991 ± 256	21176 ± 206
$D^0\bar{D}^0$	2874 ± 6	3096 ± 7	2358 ± 5
D^+D^-	2064 ± 5	2308 ± 5	1668 ± 4
$\tau^+\tau^-$	989 ± 3	2162 ± 6	773 ± 3
$\gamma J/\psi$	1273 ± 3	1532 ± 3	955 ± 2
$\gamma\psi(2S)$	4607 ± 11	5084 ± 12	3773 ± 9
Hadrons	964 ± 311	1238 ± 332	944 ± 272

Table F.20: Hadronic events selected in the 3789 (Scan) data.

3792 (Scan) Results			
Sample	N_{had} (SHAD)	N_{had} (LHAD)	N_{had} (THAD)
Data	46626 ± 215	53085 ± 230	37384 ± 193
$q\bar{q}$	33038 ± 300	36079 ± 322	26373 ± 259
$D^0\bar{D}^0$	2416 ± 5	2604 ± 5	1979 ± 4
D^+D^-	1482 ± 3	1657 ± 3	1197 ± 2
$\tau^+\tau^-$	1243 ± 4	2707 ± 7	964 ± 4
$\gamma J/\psi$	1570 ± 3	1893 ± 4	1174 ± 3
$\gamma\psi(2S)$	5543 ± 12	6120 ± 13	4526 ± 11
Hadrons	1330 ± 370	2020 ± 396	1166 ± 323

Table F.21: Hadronic events selected in the 3792 (Scan) data.

3797 (Scan) Results			
Sample	N_{had} (SHAD)	N_{had} (LHAD)	N_{had} (THAD)
Data	51348 ± 226	58331 ± 241	41249 ± 203
$q\bar{q}$	37808 ± 349	41264 ± 373	30191 ± 300
$D^0\bar{D}^0$	1693 ± 3	1825 ± 3	1388 ± 3
D^+D^-	1036 ± 2	1158 ± 2	837 ± 1
$\tau^+\tau^-$	1427 ± 5	3118 ± 8	1112 ± 4
$\gamma J/\psi$	1790 ± 4	2156 ± 4	1341 ± 3
$\gamma\psi(2S)$	6119 ± 13	6755 ± 14	5005 ± 11
Hadrons	1471 ± 416	2050 ± 445	1372 ± 363

Table F.22: Hadronic events selected in the 3797 (Scan) data.

3800 (Scan) Results			
Sample	N_{had} (SHAD)	N_{had} (LHAD)	N_{had} (THAD)
Data	48859 ± 221	55719 ± 236	38965 ± 197
$q\bar{q}$	36644 ± 342	39976 ± 367	29268 ± 295
$D^0\bar{D}^0$	1235 ± 2	1333 ± 2	1010 ± 2
D^+D^-	583 ± 1	652 ± 1	470 ± 1
$\tau^+\tau^-$	1395 ± 4	3051 ± 7	1081 ± 4
$\gamma J/\psi$	1721 ± 3	2076 ± 4	1286 ± 3
$\gamma\psi(2S)$	5748 ± 12	6354 ± 13	4686 ± 10
Hadrons	1530 ± 408	2273 ± 436	1160 ± 355

Table F.23: Hadronic events selected in the 3800 (Scan) data.

3802 (Scan) Results			
Sample	N_{had} (SHAD)	N_{had} (LHAD)	N_{had} (THAD)
Data	33032 ± 181	37538 ± 193	26268 ± 162
$q\bar{q}$	25099 ± 238	27373 ± 255	20050 ± 205
$D^0\bar{D}^0$	649 ± 1	700 ± 1	531 ± 1
D^+D^-	391 ± 1	438 ± 1	315 ± 1
$\tau^+\tau^-$	963 ± 3	2103 ± 6	746 ± 3
$\gamma J/\psi$	1177 ± 3	1418 ± 3	880 ± 2
$\gamma\psi(2S)$	3871 ± 10	4280 ± 10	3161 ± 8
Hadrons	880 ± 300	1223 ± 320	582 ± 261

Table F.24: Hadronic events selected in the 3802 (Scan) data.

3807 (Scan) Results			
Sample	N_{had} (SHAD)	N_{had} (LHAD)	N_{had} (THAD)
Data	21499 ± 146	24410 ± 156	17234 ± 131
$q\bar{q}$	16378 ± 159	17850 ± 171	13087 ± 137
$D^0\bar{D}^0$	459 ± 1	495 ± 1	374 ± 1
D^+D^-	311 ± 1	349 ± 1	251 ± 1
$\tau^+\tau^-$	632 ± 2	1377 ± 5	489 ± 2
$\gamma J/\psi$	761 ± 2	918 ± 2	567 ± 1
$\gamma\psi(2S)$	2427 ± 7	2688 ± 8	1980 ± 6
Hadrons	527 ± 217	729 ± 232	482 ± 190

Table F.25: Hadronic events selected in the 3807 (Scan) data.

3809 (Scan) Results			
Sample	N_{had} (SHAD)	N_{had} (LHAD)	N_{had} (THAD)
Data	15124 ± 122	17177 ± 131	12089 ± 109
$q\bar{q}$	11655 ± 116	12699 ± 124	9315 ± 99
$D^0\bar{D}^0$	217 ± 1	234 ± 1	177 ± 1
D^+D^-	102 ± 1	114 ± 1	82 ± 1
$\tau^+\tau^-$	450 ± 2	986 ± 4	351 ± 2
$\gamma J/\psi$	541 ± 2	652 ± 2	406 ± 1
$\gamma\psi(2S)$	1705 ± 6	1885 ± 7	1395 ± 5
Hadrons	451 ± 169	605 ± 181	360 ± 148

Table F.26: Hadronic events selected in the 3809 (Scan) data.

3813 (Scan) Results			
Sample	N_{had} (SHAD)	N_{had} (LHAD)	N_{had} (THAD)
Data	10836 ± 104	12308 ± 110	8700 ± 93
$q\bar{q}$	8323 ± 85	9063 ± 91	6653 ± 73
$D^0\overline{D^0}$	39 ± 1	43 ± 1	32 ± 1
D^+D^-	84 ± 1	94 ± 1	67 ± 1
$\tau^+\tau^-$	321 ± 2	703 ± 3	247 ± 1
$\gamma J/\psi$	384 ± 1	463 ± 2	286 ± 1
$\gamma\psi(2S)$	1173 ± 5	1298 ± 5	954 ± 4
Hadrons	509 ± 135	641 ± 144	456 ± 118

Table F.27: Hadronic events selected in the 3813 (Scan) data.

3815 (Scan) Results			
Sample	N_{had} (SHAD)	N_{had} (LHAD)	N_{had} (THAD)
Data	8159 ± 90	9190 ± 95	6536 ± 80
$q\bar{q}$	6308 ± 66	6868 ± 71	5044 ± 56
$D^0\overline{D^0}$	28 ± 1	30 ± 1	23 ± 1
D^+D^-	37 ± 1	41 ± 1	30 ± 1
$\tau^+\tau^-$	247 ± 1	540 ± 3	192 ± 1
$\gamma J/\psi$	290 ± 1	350 ± 1	217 ± 1
$\gamma\psi(2S)$	883 ± 4	975 ± 4	719 ± 3
Hadrons	363 ± 112	383 ± 119	309 ± 99

Table F.28: Hadronic events selected in the 3815 (Scan) data.

3822 (Scan) Results			
Sample	N_{had} (SHAD)	N_{had} (LHAD)	N_{had} (THAD)
Data	4748 ± 68	5379 ± 73	3754 ± 61
$q\bar{q}$	3695 ± 41	4019 ± 44	2956 ± 35
$D^0\overline{D^0}$	41 ± 1	44 ± 1	34 ± 1
D^+D^-	48 ± 1	54 ± 1	39 ± 1
$\tau^+\tau^-$	147 ± 1	321 ± 2	114 ± 1
$\gamma J/\psi$	168 ± 1	203 ± 1	126 ± 1
$\gamma\psi(2S)$	491 ± 2	542 ± 3	401 ± 2
Hadrons	154 ± 80	193 ± 86	81 ± 70

Table F.29: Hadronic events selected in the 3822 (Scan) data.

3832 (Scan) Results			
Sample	N_{had} (SHAD)	N_{had} (LHAD)	N_{had} (THAD)
Data	3364 ± 58	3842 ± 61	2729 ± 52
$q\bar{q}$	2622 ± 31	2848 ± 34	2098 ± 26
$D^0\overline{D}^0$	14 ± 1	15 ± 1	12 ± 1
D^+D^-	8 ± 1	9 ± 1	6 ± 1
$\tau^+\tau^-$	105 ± 1	229 ± 1	82 ± 1
$\gamma J/\psi$	118 ± 1	142 ± 1	88 ± 1
$\gamma\psi(2S)$	326 ± 2	360 ± 2	266 ± 2
Hadrons	168 ± 66	236 ± 70	174 ± 58

Table F.30: Hadronic events selected in the 3832 (Scan) data.

3839 (Scan) Results			
Sample	N_{had} (SHAD)	N_{had} (LHAD)	N_{had} (THAD)
Data	3156 ± 56	3567 ± 59	2569 ± 50
$q\bar{q}$	2574 ± 31	2793 ± 34	2061 ± 27
$D^0\overline{D}^0$	49 ± 1	53 ± 1	40 ± 1
D^+D^-	43 ± 1	49 ± 1	35 ± 1
$\tau^+\tau^-$	103 ± 1	225 ± 1	80 ± 1
$\gamma J/\psi$	114 ± 1	138 ± 1	86 ± 1
$\gamma\psi(2S)$	306 ± 2	339 ± 2	251 ± 1
Hadrons	-36 ± 64	-32 ± 68	13 ± 57

Table F.31: Hadronic events selected in the 3839 (Scan) data.

3849 (Scan) Results			
Sample	N_{had} (SHAD)	N_{had} (LHAD)	N_{had} (THAD)
Data	3266 ± 57	3738 ± 61	2603 ± 51
$q\bar{q}$	2529 ± 32	2740 ± 34	2027 ± 27
$D^0\overline{D}^0$	38 ± 1	41 ± 1	31 ± 1
D^+D^-	31 ± 1	35 ± 1	25 ± 1
$\tau^+\tau^-$	104 ± 1	225 ± 1	81 ± 1
$\gamma J/\psi$	111 ± 1	133 ± 1	83 ± 1
$\gamma\psi(2S)$	281 ± 2	312 ± 2	230 ± 1
Hadrons	168 ± 65	249 ± 70	123 ± 57

Table F.32: Hadronic events selected in the 3849 (Scan) data.

3855 (Scan) Results			
Sample	N_{had} (SHAD)	N_{had} (LHAD)	N_{had} (THAD)
Data	3640 ± 60	4097 ± 64	2905 ± 53
$q\bar{q}$	2910 ± 36	3151 ± 39	2333 ± 31
$D^0\overline{D^0}$	80 ± 1	86 ± 1	65 ± 1
D^+D^-	53 ± 1	60 ± 1	43 ± 1
$\tau^+\tau^-$	122 ± 1	263 ± 1	94 ± 1
$\gamma J/\psi$	127 ± 1	152 ± 1	95 ± 1
$\gamma\psi(2S)$	314 ± 2	347 ± 2	256 ± 1
Hadrons	32 ± 70	35 ± 75	16 ± 62

Table F.33: Hadronic events selected in the 3855 (Scan) data.

3863 (Scan) Results			
Sample	N_{had} (SHAD)	N_{had} (LHAD)	N_{had} (THAD)
Data	3472 ± 58	3921 ± 62	2773 ± 52
$q\bar{q}$	2732 ± 35	2955 ± 38	2191 ± 30
$D^0\overline{D^0}$	76 ± 1	82 ± 1	62 ± 1
D^+D^-	18 ± 1	20 ± 1	14 ± 1
$\tau^+\tau^-$	114 ± 1	247 ± 1	89 ± 1
$\gamma J/\psi$	118 ± 1	142 ± 1	88 ± 1
$\gamma\psi(2S)$	282 ± 1	312 ± 2	230 ± 1
Hadrons	129 ± 68	160 ± 73	94 ± 60

Table F.34: Hadronic events selected in the 3863 (Scan) data.